Université du Québec

INRS Institut national de la recherche scientifique

Centre Énergie Matériauxet Télécommunications

Development of High-performance Bi-functional Oxygen Electrocatalysts for Rechargeable Zn-air Batteries

Par

Mingjie Wu

Thèse présentée pour l'obtention du grade de
Philosophiae doctor (Ph.D.)
en sciences de l'énergie et des matériaux

Jury d'évaluation

Président du jury et examinateur interne	Prof. Andreas Ruediger INRS-EMT, Canada
Examinateur externe	Prof. Jian Liu The University of British Columbia, Canada
Examinateur externe	Prof. Sasha Omanovic McGill University, Canada
Directeur de recherché examinateur interne	Prof. Shuhui Sun INRS-EMT, Canada

Acknowledgment

First, my profound gratitude goes to my supervisor, Professor Shuhui Sun, for his helpful guidance, valuable suggestions, and constant encouragement both in my study and in my life. His profound insights and accurateness about my research taught me so much that they are engraved on my heart. He provided me with the best patient guidance and give me the greatest freedom to explore various research ideas. Without these, I could not accomplish so much work.

I would also like to express my gratitude to my jury members, including Prof. Andreas Ruediger, Prof. Sasha Omanovic, and Prof. Jian Liu, for their invested time and effort as the jury committee.

I want to thank Dr. Gaixia Zhang for her great instructions and encouragement throughout my Ph.D. study. Guided by her rigorous academic attitude, I have gained more confidence and achieved personal goals. I also thank my fellow members of Prof. Sun's research group for their collaborations and supports. Special thanks to Zhangsen Chen, Yang Gao, Diane Rawach, Xiaohua Yang, Zonghua Pu, Lei Du, Amir Hasanpour, Hongliu Dai, Xin Tong, Fang Dong, Jun Zhang and so on. I would also like to express my sincere gratitude to all the professors who have taught me at INRS that greatly broadened my horizon and enriched my knowledge in my study. Their inspirational and conscientious teaching has provided me with a firm basis for the composing of this thesis and will always be of great value to my future academic research. I thank all the administrative staff at INRS for their help and support. I am grateful to the beam scientists of Canadian Light Source, especially to Dr. Ning Chen, Dr. Jian Wang, Dr. Yongfeng Hu, Dr. Weifeng Chen, Tianxiao Sun, and Dr. Tom Regier for their technical assistance and guidance. I am also indebted to many of my colleagues and friends whom I received friendship and unconditional support over the years.

I also would like to acknowledge the funding source, including Fonds de Recherche du Québec-Nature et Technologies (FRQNT), China Scholarship Council (CSC), and INRS for the financial support.

Finally, I would like to extend my deep gratefulness to my family and friends, especially my wife, Danjie Meng, whose encouragement and support have made my accomplishments possible.

Abstract

Rechargeable zinc-air batteries (ZABs) are considered one of the most promising candidates as power sources for portable electronic devices, electric vehicles (EVs), and grid storage, due to their high energy density (1218 Wh kg^{-1}), environmentally benignity, safe operational characteristics, and low production cost. One of the biggest challenges and the bottleneck in developing high-performance rechargeable ZABs is the design of suitable bifunctional air electrodes, with controlled chemical compositions and well-designed architectures that can efficiently catalyze the key oxygen reduction reaction (ORR) and oxygen evolution reaction (OER). Air electrodes with bifunctional catalytic activity (ORR and OER) are the most significant and complicated part of the rechargeable ZABs that inevitably determine the electrochemical performance and cycling stability. This thesis describes facile synthetic strategies for the fabrication of bifunctional oxygen electrodes for rechargeable ZABs.

In the first study, we developed a facile method to fabricate graphitic-shell encapsulated binary FeNi alloy/nitride nanocrystals and biomass-derived N-doped carbon (NC) hybrid (Fe_xNi_yN@C/NC) structures. The porous architecture can provide abundant accessible active sites and improved mass transfer. Benefitting from the high graphitization of the carbon layer and strong metal-support interactions between the graphite-coated Fe_xNi_yN nanocrystals and the N-doped porous carbon, the hybrid material (Fe_xNi_yN@C/NC) can take full advantage of the unique structures to promote the electrocatalytic reaction kinetics and stability for both ORR and OER. As expected, the obtained Fe_xNi_yN@C/NC catalyst exhibits high bifunctional ORR/OER activity, indicated by the small potential gap (ΔE) of 0.67 V between $E_{j=10}$ (1.54 V) and $E_{1/2}$ (0.87 V) in 1.0 M KOH. The electrochemical tests and X-ray absorption spectroscopy (XAS) analyses revealed that there is almost no change in the bulk structure of the Fe_xNi_yN nanocrystals after

suffering the harsh OER electrochemical corrosion process. When integrated into an air electrode for the rechargeable ZAB, the hybrid catalyst demonstrated high stability over 400 hours at 5.0 mA cm^{-2}.

To further improve the graphitization extents of carbon and reduce the part of the amorphous carbon, a facile two-step strategy has been developed to synthesize diphasic metal/metal phosphide nanoparticles encapsulated in the bamboo-shape N-doped CNTs (M/M_2P@NCNTs). Among them, the unique heterojunction structure of the Co/Co_2P greatly induces the construction of highly ordered NCNTs with rich pyridinic-N and graphitic-N active sites. This straightforward strategy is a valid measure to avoid the destruction of ORR active sites due to the high potential oxidation conditions. Typically, the Co/Co_2P@NCNTs ($E_{1/2}$=0.90 V) has exhibited outstanding ORR performance with an $E_{1/2}$ of 0.87 V versus RHE after suffering high potential oxidation condition, which to the best of our knowledge, is record-level among previously reported ORR catalysts. Meanwhile, deep self-reconstruction of heterojunction Co/Co_2P confined in NCNTs shows increasing OER performance owing to the dynamic active state generation of plentiful $CoO_x(OH)_y$ active species. This is different from the previously reported structural transformation that occurred only in the near-surface region of cobalt oxides. Benefiting from the high oxidation potentials resistance of the NCNT and the transformation from the heterojunction Co/Co_2P into Co^{3+} containing $CoO_x(OH)_y$ active species, the Co/Co_2P@NCNTs can be used as an efficient bifunctional precatalyst for rechargeable zinc-air flow batteries. The assembled zinc-air flow battery with the developed catalyst displays high cell efficiency with an unprecedented cycle life of 1000 h in an ambient environment, indicating the promising application of these catalysts in metal-air batteries.

Further, a facile bimetal coupling approach was used to synthesize Fe/Co double hydroxide/oxide nano-sheets cladding layer on N-doped multiwall carbon nanotubes (FeCo-

DHO/NCNTs). Through the direct nucleation, growth, and anchoring, the Fe/Co double hydroxide/oxide nano-sheets (FeCo-DHO) with crystalline and amorphous phases are uniformly inlaid on the surface of NCNTs, which provide high electrical contact area and strong adhesion on the conductive carbon support. The strong interactions of the FeCo-DHO nano-sheets with NCNTs (possibly due to the formation of M-O-C (M = Co, Fe) chemical bonding) not only greatly facilitate the charge transfer and mass transport but also lead to high chemical stability to resist the corrosion during charge and discharge operation. Consequently, the as-synthesized FeCo-DHO/NCNTs exhibits high bifunctional ORR/OER activity and stability, with a potential gap of 0.7 V between $E_{j=10}$ (OER, potential at 10.0 mA cm^{-2}) and $E_{1/2}$ (ORR, half-wave potential). In addition, outstanding charging-discharging performance and long cycling lifetime were achieved in liquid and quasi-solid-state ZABs. The high electrochemical performance of such catalysts thereby makes it very promising to replace the noble-metal catalysts (Pt group metals for ORR and Ir/Ru group metals for OER) in metal-air batteries.

Finally, a self-supported electrode as a high-performance binder- and carbon-free cathode for rechargeable hybrid zinc batteries are explored. In this work, The Ni foam (NF) in this work not only acts as a substrate but also serves as a nickel precursor for the formation of the $Co_{3-x}Ni_xO_4$ catalyst. Meanwhile, combining the 3D porous structure of NF and intrinsic high OER activity of the stainless steel (SS), the assembled porous air electrode can take full advantage of the sandwich structure to promote the electrocatalytic reaction kinetics. This novel nanostructure demonstrates a very high reversible Faradaic redox reaction of CoNi-O ↔ CoNi-O-OH and high bifunctional activity toward both ORR and OER. Moreover, the air cathode, prepared by pressing the stainless steel SS@Co_3O_4 sandwiched between two NF@$Co_{3-x}Ni_xO_4$, possesses a dense and interconnected structure with a high loading of active catalyst. The rechargeable hybrid battery system, assembled from this NS@$Co_{3-x}Ni_xO_4$/Co_3O_4 electrode based on both Zn-$Co_{3-x}Ni_xO_4$ and

Zn-air electrochemical reactions, exhibits much higher energy efficiency and durability than those of commercial Pt/C and RuO_2 electrocatalysts. This protocol opens a new avenue for the rational design of highly efficient and stable self-supported air electrodes for metal-air batteries.

Keywords:

Rechargeable zinc-air battery; hybrid zinc batteries, bifunctional electrocatalysts; defects; FeNi alloy/nitrides; heterojunction structure; self-supported; degree of graphitization;

Table of Contents

List of Figures

List of Tables

List of Abbreviations

ADT	Accelerated durability test
BE	Binding energy
CV	Cyclic voltammetry
$E_{1/2}$	Half-wave potential
EDS	Energy dispersive X-ray spectroscopy
E_{onset}	Onset potential
GC	Glassy carbon
HER	Hydrogen evolution reaction
HRTEM	High-resolution transmission electron microscope
LSV	Linear sweeping voltammetry
ORR	Oxygen reduction reaction
OER	Oxygen evolution reaction
ECSA	Electrochemical surface area
RDE	Rotating ring-disk electrode
RHE	Reversible hydrogen electrode
rpm	Revolutions per minute
RRDE	Rotating ring-disk electrode
SAED	Selected area electron diffraction
SCE	Saturated calomel electrode
SEM	Scanning electron microscopy
TEM	Transmission electron microscopy
XPS	X-ray photoelectron spectroscopy

XRD	X-ray diffraction
XAS	X-ray absorption spectroscopy
XANES	X-ray absorption near-edge structure
XAFS	X-ray absorption fine structure
Pt/C	Carbon support platinum catalyst
EV	Electric vehicles
GDL	Gas diffusion layer
Ru/C	Carbon support ruthenium catalyst
NCNT	N-doped carbon nanotube
SS	Stainless steel
NF	Nickle foam

List of Publications

1. **Mingjie Wu**, Gaixia Zhang, Ning Chen, Tom Regier, Yongfeng Hu, Diane Rawach, Shuhui Sun, Self-Reconstruction of Co/Co_2P Heterojunctions Confined in N-Doped Carbon Nanotubes for Zinc-Air Flow Batteries. ***ACS Energy Letters***, 6 (2021) 1153-1161.
2. **Mingjie Wu**, Gaixia Zhang, Hui Tong, Xianhu Liu, Lei Du, Ning Chen, Jian Wang, Tianxiao Sun, Tom Regier, Shuhui Sun, Cobalt (II) oxide nanosheets with rich oxygen vacancies as highly efficient bifunctional catalysts for ultra-stable rechargeable Zn-air flow battery. ***Nano Energy***, 79 (2021) 105409.
3. **Mingjie Wu**, Gaixia Zhang, Lei Du, Dachi Yang, Huaming Yang, Shuhui Sun, Defect Electrocatalysts and Alkaline Electrolyte Membranes in Solid-state Zinc-air Battery: Recent Advances, Challenges and Future Perspectives. ***Small Methods***, 5 (2021) 2000868.
4. **Mingjie Wu**, Gaixia Zhang, Ning Chen, Mohamed Cherif, Fu-Kuo Chiang, Yuren Wen, Xiaohua Yang, Weifeng Chen, François Vidal, Shuhui Sun, Active sites engineering and identification of atomically dispersed metal catalysts along with crystalline particles with tunable electrocatalytic activities. To be submitted.
5. **Mingjie Wu**, Gaixia Zhang, Huaming Yang, Xianhu Liu, Marc Dubois, Shuhui Sun, Aqueous Zn-based Rechargeable Batteries: Recent Progress and Future Perspectives. ***InfoMat***, 2021, accepted.
6. Hongliu Dai, Jing Dong, **Mingjie Wu**, Dongniu Wang, Lucia Zuin, Ning Chen, Chao Lai, Gaixia Zhang, Shuhui Sun, Cobalt Phthalocyanine Derived Molecular Isolation Layer for Highly Stable Lithium Anode. ***Angewandte Chemie International Edition***, 2021, in press.
7. Zonghua Pu, Tingting Liu, Zhangsen Chen, **Mingjie Wu**, Ning Chen, Weifeng Chen, Dewen Zheng, Shanyu Wang, Gaixia Zhang, Zhangxin Chen, Shuhui Sun, In-situ

Electrochemical Synthesis of Atomically Dispersed Metal Sites for Efficient Hydrogen Evolution Reaction. To be submitted.

8. **Mingjie Wu**, Gaixia Zhang, Ning Chen, Weifeng Chen, Jinli Qiao, Shuhui Sun. Graphitic-shell encapsulation of NiFe-based nanocrystals decorated on biomass-derived N-doped porous carbon for enhanced oxygen evolution and reduction catalysis. ***Carbon Energy***, 3 (2020) 176-187.
9. **Mingjie Wu**, Gaixia Zhang, Ning Chen, Weifeng Chen, Jinli Qiao, Shuhui Sun. A Self-supported Electrode as a High-Performance Binder- and Carbon-Free Cathode for Rechargeable Hybrid Zinc Batteries. ***Energy Storage Materials***, 24 (2020) 272-280.
10. Fang Dong, **Mingjie Wu**, Gaixia Zhang, Xianhu Liu, Diane Rawach, Ana C Tavares, Shuhui Sun, Defect Engineering of Carbon-based Electrocatalysts for Rechargeable Zinc-air Batteries. ***Chem Asian J.*** 15 (2020) 3737-3751.
11. Nathanael Komba, Gaixia Zhang, Zonghua Pu, **Mingjie Wu**, Federico Rosei, Shuhui Sun, MoS_2-supported on free-standing TiO_2-nanotubes for efficient hydrogen evolution reaction. ***International Journal of Hydrogen Energy***, 45 (2020) 4468-4480.
12. **Mingjie Wu**, Gaixia Zhang, Ning Chen, Weifeng Chen, Jinli Qiao, Shuhui Sun. Ultra-long life rechargeable zinc-air battery based on high-performance trimetallic nitride and NCNT hybrid bifunctional electrocatalysts. ***Nano Energy*** 61 (2019) 86-95.
13. **Mingjie Wu**, Gaixia Zhang, J. Prakash, Shuhui Sun, Rational design of multifunctional air electrodes for rechargeable Zn-Air batteries: Recent progress and future perspectives, ***Energy Storage Materials***, 21 (2019) 253-286.
14. QiliangWei, Mohamed Cherif, Gaixia Zhang, Ali Almesrati, Jiatang Chen, **Mingjie Wu**, Nathanael Komba, Yongfeng Hu, Tom Regier, Tsun-KongSham, FrançoisVidal, Shuhui Sun. Transforming reed waste into a highly active metal-free catalyst for oxygen

reduction reaction. ***Nano Energy*** 62 (2019), 700-708.

15. **Mingjie Wu**, Gaixia Zhang, Ning Chen, Weifeng Chen, Jinli Qiao, Shuhui Sun. Fe/Co Double Hydroxide/Oxide Nanoparticles on N-Doped CNTs as Highly Efficient Electrocatalyst for Rechargeable Liquid and Quasi-Solid-State Zinc-Air Batteries. ***Advanced Energy Materials***, 8 (2018) 1801836.
16. Meng Yu, Qiliang Wei, **Mingjie Wu**, Jie Wu, Jieyu Liu, Gaixia Zhang, Shuhui Sun, Weichao Wang. Morphology controlled synthesis of $SmMn_2O_5$ nanocrystals via a surfactant-free route for Zn-air batteries. ***Journal of Power Source***, 396 (2018) 754-763.

Statement of Contributions

The body of this thesis is based upon a combination of published works. Chapters 3,4,5,6 are adapted from the following list of publications.

Chapter 3 is based on a research article "*Graphitic-shell encapsulated FeNi alloy/nitride nanocrystals on biomass-derived N-doped carbon as an efficient electrocatalyst for rechargeable Zn-air battery, Carbon Energy, (2020) 1-12", authored by M. Wu, G. Zhang, Y. Hu, J. Wang, T. Sun, T. Regier, J. Qiao, S. Sun.*

Contributions: M. Wu, G. Zhang and S. Sun conceived the project and oversaw all the research phases. I designed and carried out the experiment, collected and analyzed the data, and drafted the manuscript. Dr. Zhang, Dr. Hu and Dr. Sun assisted with the writing of the manuscript. Dr. Zhang, Dr. Wang, Dr. Sun and Dr. Regier helped with the analysis of the data. All authors discussed and corrected the manuscript.

Chapter 4 is based on a research article *"Self-reconstruction of Co/Co_2P heterojunction confined in N-doped carbon nanotubes for high-performance rechargeable zinc-air flow battery, ACS Energy Letters, 6 (2021) 1153-1161", authored by M. Wu, G. Zhang, N. Chen, Y. Hu, T. Regier, D. Rawach, S. Sun.*

Contributions: M. Wu, G. Zhang and S. Sun conceived the project and oversaw all the research phases. I designed and carried out the experiment, collected and analyzed the data, and drafted the manuscript. Dr. Zhang and Dr. Sun helped with the writing of the paper. Dr. Zhang, Dr. Chen, Dr. Hu and Dr. Regier helped with the analysis of the data. All authors discussed and corrected the manuscript.

Chapter 5 is based on a research article *"Fe/Co Double Hydroxide/Oxide Nanoparticles on N-Doped CNTs as Highly Efficient Electrocatalyst for Rechargeable Liquid and Quasi-Solid-State*

Zinc-Air Batteries, Advanced Energy Materials, 8 (2018) 1801836" authored by M. Wu, Q. Wei, G. Zhang, J. Qiao, M. Wu, J. Zhang, Q. Gong, S. Sun.

Contributions: M. Wu, G. Zhang and S. Sun conceived the project and oversaw all the research phases. I designed and carried out the experiment, collected and analyzed the data, and drafted the manuscript. Dr. Zhang assisted with the writing of the manuscript. J. Zhang helped with drawing a schematic illustration of the ZAB configuration. All authors discussed and corrected the manuscript.

Chapter 6 is based on a research article *"A self-supported electrode as a high-performance binder- and carbon-free cathode for rechargeable hybrid zinc batteries, Energy Storage Materials, 24 (2020) 272-280", authored by M. Wu, G. Zhang, N. Chen, W. Chen, J. Qiao, S. Sun.*

Contributions: M. Wu, Dr. G. Zhang and S. Sun conceived the project and oversaw all the research phases. I designed and carried out the experiment, collected and analyzed the data, and drafted the manuscript. Dr. Zhang and Dr. Sun helped with the writing of the paper. Dr. Zhang and Dr. Chen helped with the analysis of the data. All authors discussed and corrected the manuscript.

Chapter 1 Introduction

1.1 Motivation

Due to the aggravating energy crisis and environmental issues, the ever-increasing sustainable energy demands in the fast-growing modern society, have prompted a great deal of interest in electrochemical energy conversions and/or storage technologies.[1] To meet the growing global requirements in terms of energy conversion and distribution, it is reasonable and urgent to expect a more volatile energy economy in the near future. Highly efficient energy storage devices play a critical role in portable electronics and electric vehicles (EVs), which can facilitate the electrification of transportation, reducing demand for fossil fuels and promoting a low carbon economy.[2]

For centuries, batteries have been showing huge advantages in converting and storing chemical energies. Compared with traditional forms of energy storage, their capacity, to be easily scaled down to small sizes, has made them indispensable for portable electronic devices. To date, the Li-ion battery is one of the most promising electrochemical energy technologies, which nearly dominates the whole rechargeable battery market since its advent in the late 1990s.[3] Nowadays, most EVs use Li-ion batteries. However, their limitations of insufficient energy density, blemished safety, and high cost, have restricted the large-scale applications in the automobile industry to some extent. In this regard, many alternative rechargeable battery technologies, such as Li-S, Na-ion, and metal-air batteries have been proposed which have attracted significant attention in the scientific community as well as industries.

Metal-air batteries have become a promising power source based on the nature of considerably high energy densities due to free-oxygen fuel from the atmosphere. The theoretical specific energies, volumetric energy densities, and cell voltages of various metal anodes in metal-

air batteries are shown in Figure 1-1. For rechargeable Li-air batteries, Li suffers many unconquerable limitations, such as rechargeability, inherent instability, and cost issues, which make them hard to be commercialized. Recently, zinc-air batteries (ZABs) have received far more attention in this field due to their high energy density, cell voltage, innate safety, and relatively suitable reduction potentials within aqueous metal-air batteries.[4-5] Zinc can be charged more efficiently with slow self-discharge and high Coulombic charging efficiency in aqueous electrolytes as compared with magnesium and aluminum-air batteries. Additionally, zinc as one of the most abundant elements in the earth's crust (Zn is the fourth most abundant in the Earth's crust, which is about 300 times greater than that of lithium) is inexpensive and available for large-scale production. Therefore, among all metal-air systems, ZABs have frequently been advocated as the most practically viable option, both technically and economically for future EVs applications.[6]

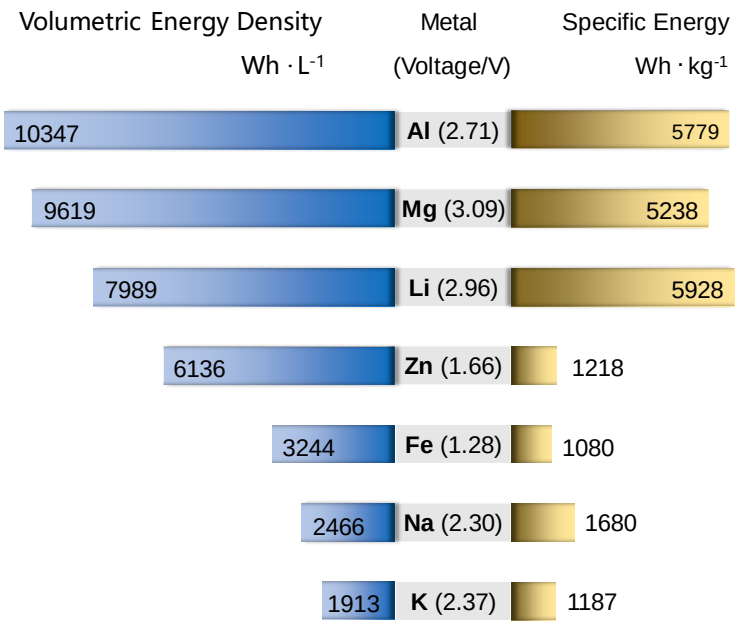

Figure 1-1 Theoretical specific energies, volumetric energy densities, and nominal cell voltages for various metal-air batteries.

There are two types of rechargeable ZABs; mechanically and electrically rechargeable forms. The difference between them is that the mechanically rechargeable ZABs are charged by replacing the discharged zinc anodes and removing products such as zinc oxides and zincates, while the electrically rechargeable ZABs are charged by converting electrical energy to chemical energy that takes place within battery configuration. However, due to the high costs of setting up a network of zinc recharging and supplying stations, the concept of mechanically rechargeable forms was never widely adopted. Electrically rechargeable forms can be divided into two types; two-electrode and tri-electrode configuration (Figure 1-2).[7] The difference between them is that the oxygen electrochemical processes (oxygen reduction/evolution reaction, ORR/OER) happen at two separated air electrodes (tri-electrode configuration) or one single air electrode (two-electrode configuration). Although the tri-electrode configuration provides a higher battery cycling durability and much more loose requirements of catalysts preparation than the two-electrode configuration. It unavoidably pays the price of increasing the volume and weight of batteries, ending up with reduced volumetric energy as well as power density. The basic structure of a rechargeable ZAB is schematically shown in Figure 1-2, which is typically composed of four main components: a zinc anode, membrane separator, alkaline electrolyte (6 mol KOH or 25-30 wt% KOH), and bifunctional air cathode. During battery discharge, the zinc anode is oxidized and liberates electrons, which travel through an external load to the air electrode. While inexhaustible O_2 from the atmosphere diffuses into the porous air electrode, which is reduced to hydroxyl ions via the oxygen reduction at a triple-phase boundary (the interface of O_2, liquid electrolyte, and solid electrocatalysts). These hydroxyl ions migrate into the anode and react with Zn to yield soluble zincate ions ($Zn(OH)_4^{2-}$). When these $Zn(OH)_4^{2-}$ ions reach supersaturated concentrations in the electrolyte, they spontaneously decompose to insoluble zinc oxide (ZnO). Additionally, because Zn/ZnO standard reduction potential ($Zn + 2H_2O \rightarrow ZnO + H_2$, -1.26 V vs

standard hydrogen electrode (SHE) at pH 14) is below that of the hydrogen evolution reaction (HER) ($H_2O + 2e^- \rightarrow 2OH^- + H_2$, -0.83 V vs SHE at pH 14). Therefore, self-corrosion of the zinc may occur in parallel with the generation of explosive hydrogen gas during discharge, which lowers the zinc utilization and Coulombic efficiency. During charging, ZABs carry on electrical energy storage through the OER occurring at the electrode-electrolyte interface, whereas zinc is deposited at the cathode surface through the reduction of zincate ions.[8-9]

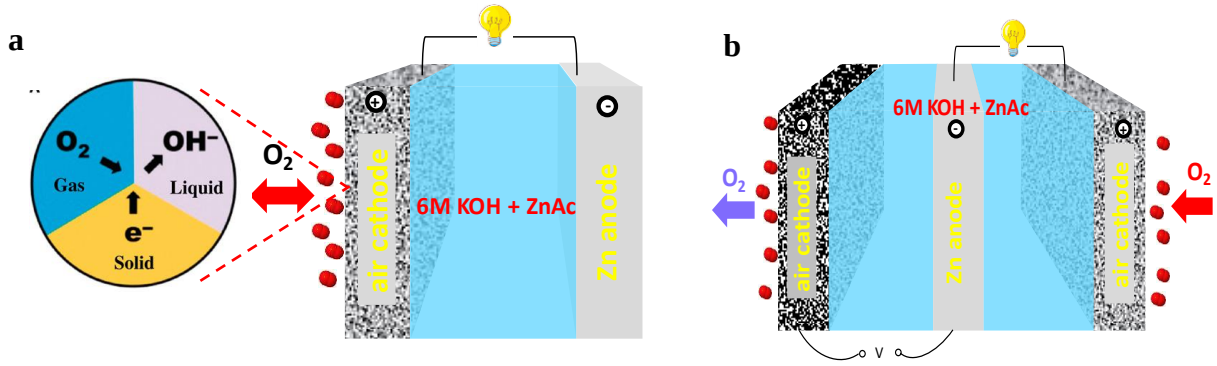

Figure 1-2 A schematic of the two-electrode (a) and tri-electrode (b) configuration ZABs.[7]

The chemical reactions involved are summarized as follows:

Cathode:

$$O_2 + 4e^- + 2H_2O \leftrightarrow 4OH^-, \quad E_0 = 0.4\ V \text{ vs SHE} \tag{1}$$

Anode:

$$\left.\begin{array}{l} Zn + 4OH^- \leftrightarrow Zn(OH)_4^{2-} + 2e^- \\ Zn(OH)_4^{2-} \leftrightarrow ZnO + 2OH^- + H_2O \end{array}\right\} \; Zn + 2OH^- \leftrightarrow ZnO + H_2O + 2e^-,\ E_0 = -1.26\ V \text{ vs SHE} \tag{2}$$

$$\text{Overall reaction: } 2Zn + O_2 \leftrightarrow 2ZnO, \quad E_0 = 1.66\ V \text{ vs SHE} \tag{3}$$

Up to date, the biggest challenge and bottleneck in developing rechargeable ZABs are rationally designing suitable bifunctional air electrodes with controlled chemical compositions and well-designed architectures that can efficiently catalyze the OER.[10-11] The air electrode materials must also have excellent stability under the wide working range of potentials during the discharge and charge process for practical ZABs. The development of highly stable air electrodes is quite challenging due to the harsh truth of suffering highly oxidative conditions upon OER as well as strong reducing conditions under ORR at high current rates. The use of highly active and cost-effective catalysts plays a vital role in realizing their wide distribution, to facilitate the sluggish oxygen electrochemical reaction kinetics of the air electrodes. To date, carbon-supported platinum (Pt) exhibits a superior activity for the ORR, but rather poor performance for the OER due to the formation of a stable oxide layer with low electrical conductivity. Instead, noble-metal oxides such as ruthenium (Ru) and iridium (Ir) oxides show excellent OER performance, but rather low activity for the ORR.[12-13] In particular, the stability of these precious metal-based catalysts is still far from being satisfied under rechargeable ZABs operation. It remains challenging to achieve both efficient and stable ORR and OER bifunctionality on a single catalyst. Moreover, the scarcity and resultant high cost of noble metals hinder their large-scale implementation in the ZABs systems. Therefore, the exploration of alternative air electrode materials with high oxygen electrocatalytic activity and long-term stability will be an ongoing task to achieve a dramatic performance enhancement. A large variety of highly efficient oxygen electrocatalysts have been developed so far and greatly promoted the kinetics of ORR/OER. Meanwhile, a profound understanding of the nature of relevant electrocatalytic processes and advances in materials science and nanotechnology greatly accelerates the commercialization of rechargeable ZABs.

1.2 Oxygen Electrochemistry

Rechargeable ZABs can be performed through electrochemical processes involving ORR and OER that require bifunctional air electrodes to accelerate their sluggish reaction rates. Below, we briefly introduce these two reactions and the electrocatalysts used for them.

1.2.1 Oxygen reduction reaction (ORR)

The ORR process in an air electrode contains a few steps: O_2 diffusion through the breathable air electrode, O_2 surface adsorption on the catalyst, weakening and breaking of the O-O bond. The high O=O bond energy (498 kJ mol^{-1}) makes ORR difficult to proceed with, which requires four coupled electron and proton transfers involving a series of complicated reactions.[14] Two main possible pathways have been generally accepted (Figure 1-3): one involves a direct $4e^-$ pathway to produce water (k_1), and the other gains 2 e^- to produce H_2O_2 (k_2). To obtain maximum energy capacity, it is highly desirable to reduce O_2 via the $4e^-$ pathway. The behavior of ORR can be different depending on the chemical composition and structure of catalysts. It is widely believed that the ORR proceeds mainly via a direct $4e^-$ pathway on noble metal catalysts. For other promising alternative materials, such as transition-metal oxides, $2e^-$ pathways may involve in the ORR process, because of their specific crystal structure and molecular composition. However, the two-electron reduction path involves intermediates of peroxide that not only reduce the efficiency of ORR but also corrode carbon-based catalysts or carbon support materials due to their high oxidizability.

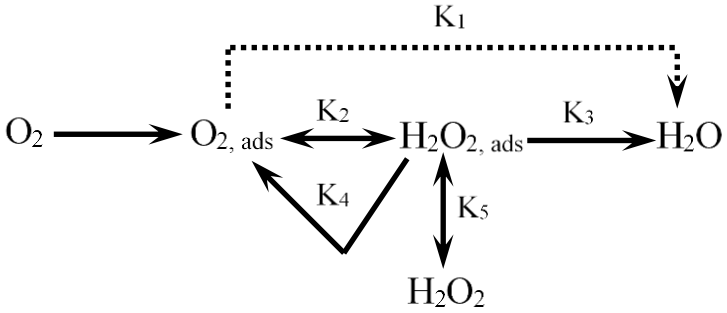

Figure 1-3 Mechanism and pathways for the oxygen reduction reaction.

1.2.2 Oxygen evolution reaction (OER)

The OER, as the reverse reaction of ORR, also plays a key part in rechargeable ZABs. Same as ORR, the OER is a complex process involving the transfer of 4 protons and $4e^-$; it proceeds far from the equilibrium potential (1.23 V vs RHE) which causes large energy loss in the charging process of ZABs. In addition, the easy peeling of the coated catalysts from the electrodes during the evolution of a large amount of O_2, greatly weakens their electrochemical performance and cycling stability. Moreover, corrosion of the air electrodes, due to being oxidized by the highly reactive O_2 generated from the OER, is another critical issue. Thus, to meet the requirements in rechargeable ZABs, the development of air electrodes with advanced electrocatalysts and configurations is urgently needed for efficiently catalyzing OER/ORR with high-performance activity and strong stability.

1.3 Challenges and Mechanisms Proposed for Bifunctional Oxygen Electrocatalysis

The majority of the energy loss in ZABs is due to the slow kinetics of the ORR and OER (Figure 1-4a).[15] The use of highly active and cost-effective catalysts to lower the free energy of

the potential-determining step(s) plays a pivotal role in widely distributing these devices (Figure 1-4b).[16] To achieve high power density and stability for the rechargeable ZABs, the bifunctional air electrodes with high catalytic ORR and OER activity and superior durability play a significant role.[17] However, the development of a desired bifunctional air electrode that can withstand the harsh conditions during repetitive discharge and charge in alkaline electrolytes is quite challenging. Both ORR and OER processes require high overpotentials.[18]

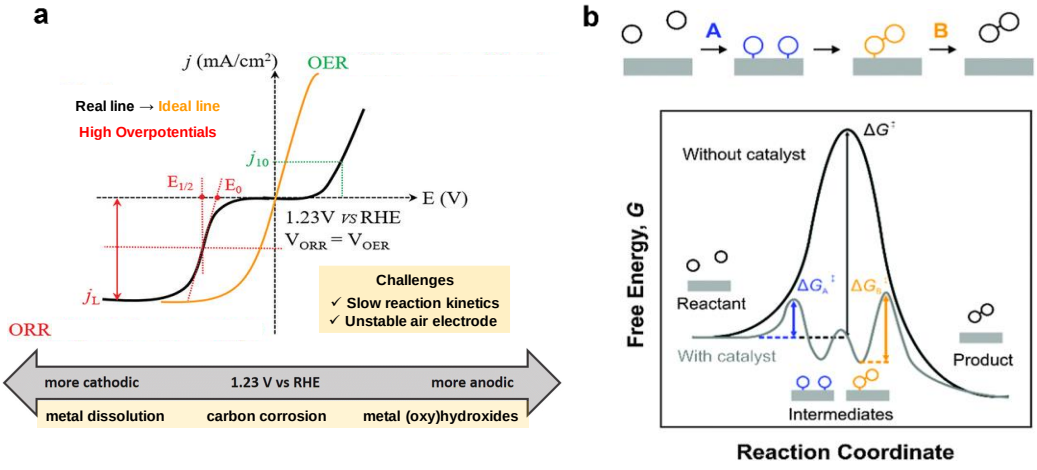

Figure 1-4 (a) Schematic of the overpotentials and challenges associated with oxygen electrocatalysis (OER, ORR).[15] (b) Schematic illustrations of a prototypical reaction mechanism, transition state theory, and its associated linear free energy relationships.[16]

The overall reaction (ORR and OER) of oxygen electrocatalysis consists of a sequence of elementary oxygen redox steps as shown in Figure 1-5a,b, which explicitly show the most widely accepted reaction mechanisms.[19] In an alkaline environment, the four reaction steps of the ORR/OER can be written as:

$$\text{Step 1:} \quad O_2 + H_2O + e^- \leftrightarrow 2OOH^* + OH^- \tag{4}$$

$$\text{Step 2:} \quad OOH^* + 2e^- \leftrightarrow O^* + OH^- \tag{5}$$

$$\text{Step 3:} \quad O^* + H_2O + e^- \leftrightarrow OH^* + OH^- \tag{6}$$

$$\text{Step 4:} \quad OH^* + e^- \leftrightarrow OH^- \tag{7}$$

where * represents the active site on the catalysts. The adsorption free energies of ORR/OER intermediates at selected potentials (E vs. RHE) on precious metal platinum are shown in Figure 1-5c. At the equilibrium voltage of 1.23 V, the formation of OOH* from O_2 (step 1) with the largest barrier is the thermodynamically potential-determining step for the ORR while the formation of OOH* from O* (step 2) is the potential-determining step for the OER. Figure 1-5d provides an overview of the activity trends for both OER and ORR. The activity volcano curves using the same activity descriptor make a clear comparison between OER and ORR. The scaling relationship results in a mismatch in oxygen adsorption energy for OER and ORR.[19] Searching bifunctional catalysts has mainly focused on nonprecious alternatives such as transition metal compounds (e.g., oxides, sulfides, nitrides, carbides, and macrocycles), carbon-based materials, and the hybrid composites of the former two.[20-23] However, most of the non-precious metal catalysts still underperform precious metal counterparts, although researchers tried to develop some kinetic models and electronic structure parameters that can potentially govern the adsorbate binding strength to predict catalysts with enhanced activity.[16, 24-26] The effective and versatile synthetic methodology to controllably regulate the intrinsic activity of catalysts is still a significant challenge for both ORR and OER processes.

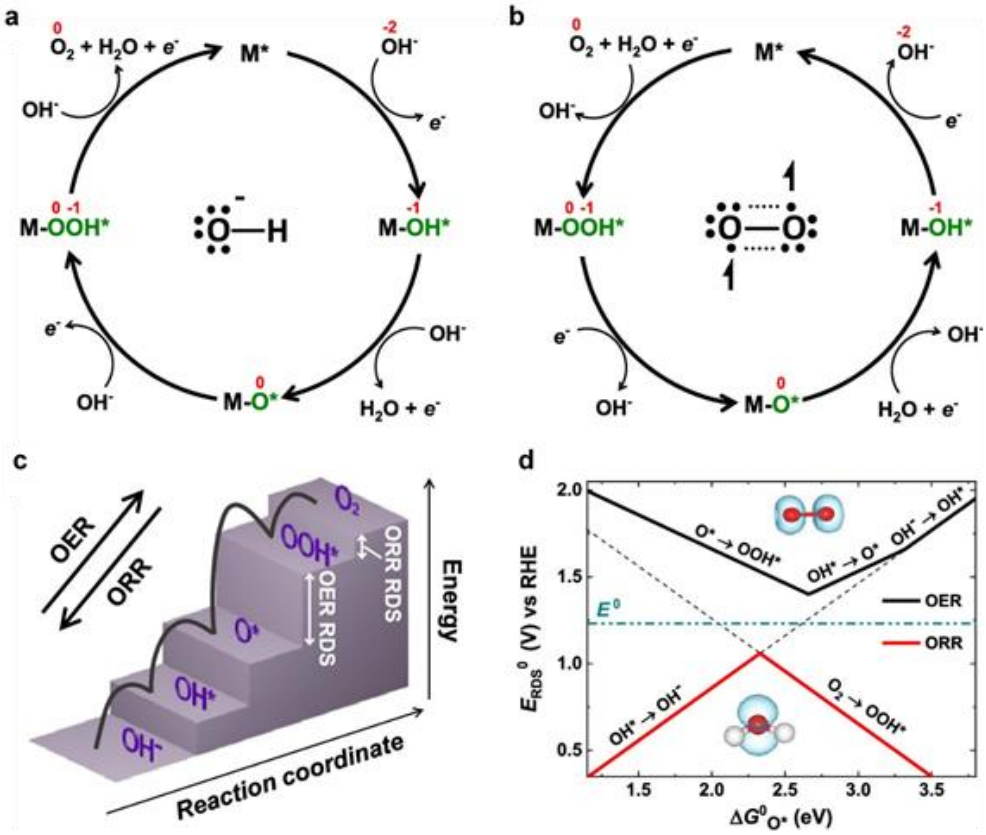

Figure 1-5 (a, b) Elementary reactions (alkaline) involved in the catalytic cycle of OER and ORR, respectively, where M* refers to the adsorption site on the catalyst surface. (c) Potential energy diagram of a typical catalyst under applied potential E = 0 V vs RHE. (d) Activity volcano plot for OER and ORR.[19]

Moreover, the performance of bifunctional air electrodes must be stable in a wide working potential range from ~0.6 V (versus reversible hydrogen electrode (RHE), pH = 14) during discharge to ~2.0 V during charging.[27-28] Particularly for the carbon-based materials, the structure and morphology changes due to the carbon corrosion under highly oxidative conditions easily induce the significant increase of the charge- and mass-transport resistances, which significantly limit their power density.[29] The critical issues related to the air electrode corrosion during the charging reaction slowed down ZAB development and remarkably made it less competitive to Li-ion battery at the end of the 20th century. The use of carbon-free air electrodes or carbon

substrates with a high graphitization degree has been reported to improve battery cycling stability.[30-32] In the following sections, the advanced materials as the bifunctional catalysts and their design strategies will be discussed.

1.4 Defect Chemistry of Bifunctional Electrocatalyst

The search for bifunctional catalysts has mainly focused on nonprecious alternatives, such as transition metal compounds (e.g., metal oxides, hydroxides, sulfides, carbides, phosphides, macrocycles, perovskites, and spinels), carbon-based materials, and their hybrids materials. Based on the change of materials composition, bifunctional catalysts can be roughly classified into three categories: i) Carbon-based metal-free bifunctional catalysts, ii) Metal-based carbon-free catalysts, iii) Metal-carbon-based hybrid materials. Through tuning the structure and composition of powdery catalysts, efficient O_2 electrocatalysts with desired properties can be obtained, including 1) high active site density and uniform distribution; 2) high surface area, sufficient porous structure for the sufficient mass transfer pathways and consequently avoiding the issue of peeling off during continuous O_2 evolution; 3) enhanced robust architecture for the chemical and mechanical stability for high cycling durability of ZABs. There are generally two strategies to improve the activity and selectivity of the oxygen electrocatalysts: (i) increasing the catalysts loading on a given electrode or optimizing catalyst structure to expose more active sites per gram; (ii) increasing the intrinsic activity of each active site.[33] In practice, to obtain high-performance catalysts, these two strategies are usually applied simultaneously. The improvement of intrinsic activity and active site density will directly lead to increases in electrode activity and can mitigate transport issues arising from excessive catalyst loadings.[34] The intrinsic ORR and OER activity and active site density highly depend on the properties of the catalysts, which can be improved by a variety of factors, such as morphology, composition, size, supports, shape,

crystallographic structure, active sites, and defects structure.[35-38]

As promising bifunctional oxygen electrocatalysts for both the ORR and OER, cost-effective transition-metal (TM)-based compounds are expected to substitute for noble-metal-based catalysts in ZABs.[11] The catalytic activity of transition-metal compounds toward the ORR/OER strongly depends on their TM active center and chemical composition. For instance, by engineering the composition of spinel oxides, their properties, such as crystalline and electronic structure, which play vital roles in ORR/OER catalysis, can be well-tuned.[39-42] In addition, varying the composition of the hybrid nano-composites (e.g., chemical attachment and electrical coupling between ORR- and OER-active materials) could be an efficient strategy to develop bifunctional electrocatalysts.[43-45] The particle size of the catalysts is also highly relevant to their catalytic activities.[46-49] When the catalyst size is reduced from micron-scale to nanoscale, the physical and chemical properties of the catalysts change significantly due to quantum effects and consequently affect the behavior and properties of catalysts such as electrochemically catalytic reactivity, surface area, electrical conductivity, and structures. Seo et al.[50] synthesized carbon nanotube-supported cobalt oxide nanoparticles (CoO_x/CNTs) with the size distribution of 3-10 nm, and investigated their size dependency for bifunctional oxygen catalysis. The particle size-dependent catalytic activity was observed, where OER activities increased with the decreased CoO_x particle sizes. The OER enhancement was related to the increased oxidation state of the cobalt species and greater specific activity in smaller-sized CoO_x nanoparticles. Besides, the morphology control (e.g., nanowire/plate/pillar/flower arrays, 3D mesoporous structure, 2D nanosheets) can also influence a catalyst's properties, such as the specific surface area, charge-transport, exposed active sites, which, in turn, tune the catalytic behaviors.[51-53] Here, the key intrinsic properties of oxygen electrocatalysts influencing their bifunctional electrocatalytic activity will be thoroughly discussed in terms of defect engineering strategies, including directly

controllable strategies: (1) atomically dispersed metal sites control, (2) vacancy defects control, (3) lattice-strain control, and the indirect strategies: (4) crystallographic structure control, (5) metal-carbon support interaction control. Table 1 presents a summary of some recently reported representatives for rechargeable ZABs. It should be noted that the defect properties are often tangled together. For example, some exposed crystal planes can lead to O-vacancy defects on the surfaces.[54] The formation of O-vacancy defects will cause an increase in lattice strain.[55-56] Apart from these types of surface defects, other lattice defects, for example, lattice dislocations, expansion, and distortion, may also change their physicochemical properties.[57] Therefore, the lattice strain, the oxygen defect, lattice deformation are strongly coupled with each other. These defects can further improve the electrical conductivity and create extra active sites for electrochemical reactions.

1.4.1 Atomically dispersed metal sites control

Atomically dispersed metal catalysts (ADMCs) have recently emerged as a new frontier in catalysis science and have attracted extensive research attention.[58-61] Traditional heterogeneous catalysts with a broad size distribution of metal particles suffer from a low metal utilization efficiency and poor selectivity. Homogeneous catalysts with well-defined active sites and tunable coordination environments exhibit excellent activity and exclusive selectivity for a specific reaction.[62] ADMCs inherit the merits of both heterogeneous and homogeneous catalysts and exhibit the great potential to bridge the gap between heterogeneous and homogeneous catalysis. As illustrated in Figure 1-6, the size reduction causes the increase of the surface free energy of the metal species. In the extreme case of single-atom catalysts, the surface free energy of metal species reaches a maximum due to the highly active valence electrons, the quantum confinement of electrons, and the sparse quantum level of metal atoms.[63] Due to the promoted chemical

interactions, the activity will increase with reduced particle sizes until atomic dispersion is reached. Metal-organic frameworks (MOFs) with 3D ordered porous structures have been widely utilized to prepare ADMCs materials.[64-65] Atomically dispersed metal ions can be easily introduced in the metal nodes, organic ligands, or pores of MOFs because of their unique characteristics, including organic-inorganic hybrid nature, large surface area, well-defined porosity, tunable chemical composition, and adjustable functionality.[66] Moreover, the uniformly distributed metal ions in pristine MOFs can be converted into ADMCs through simple heat treatment, forming the atomically dispersed metal sites anchored in MOF-derived carbon materials. Owing to the high surface energy of atomically dispersed metal atoms, stabilizing the as-formed single atoms against migration and agglomeration becomes the key challenge in the synthesis of ADMCs.[67] The ADMCs have high electrical conductivity and consequently better performance for electrocatalytic energy conversion. Although many researchers have discussed the important roles of ADMCs for many applications, including the oxygen reduction reaction (ORR), oxygen evolution reaction (OER), hydrogen evolution reaction (HER), and CO_2 reduction reaction (CO_2RR),[68-70] ADMCs as the bifunctional oxygen electrocatalysts is still challenging. The principal reason is the limitations of ADMCs such as poor stability and bad recyclability persisting in the wide working potential range of ZABs. The structure and morphology of the amorphous carbon obtained by high-temperature pyrolysis can change due to the carbon corrosion under highly oxidative conditions, which will significantly limit the ORR and OER performance. Therefore, the development of synthetic strategies plays a fundamental role in practical applications of ADMCs with bifunctional ORR/OER activity (Figure 1-6).

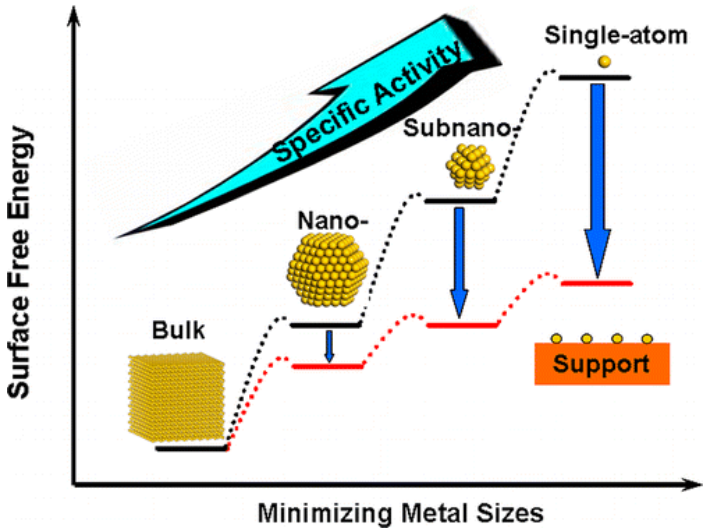

Figure 1-6 Schematic illustration of the changes of surface free energy and specific activity per metal atom with metal particle size, and the support effects on stabilizing single atoms.[63]

1.4.2 Vacancy defects control

Anion/cation defects are generally observed in transition metal-based materials, which have a great impact on the material properties such as the electronic structure, ionic/electronic conductivities.[71-73] The representative anion/cation defects existing in transition metal-based materials mainly include anion/cation substitution, anion/cation vacancy, and interstitial impurity atom.[74] Traditionally, anions in the transition metal oxides are considered as active sites for surface electrochemical processes. In addition to the classically studied mechanisms on surface metal sites, Grimaud et al.[75] provided direct experimental evidence that lattice oxygen can be activated for the OER and promote new reaction pathways. The O_2 generated during the OER comes from lattice oxygen as confirmed by in situ ^{18}O isotope labeling mass spectrometry. Increasing studies have shown the critical roles of the anion redox process in electrochemical processes. Here, we give an introduction to commonly used transition metal oxide catalysts for the ORR and OER, emphasizing the effects of anion/cation vacancy defects on catalytic activities. Vacancies are the simplest defects that exist in the materials above absolute zero (0 K), which

correspond to the absence of atoms at the lattice sites. Anion/cation vacancy defects can exist separately or concurrently in one material to reach the minimum free energy (Figure 1-7).[74] In the case of nonstoichiometric compounds, they may contain a high concentration of vacancies far above the thermal equilibrium. The presence of vacancies will change the entropy and enthalpy of the material system.[76] A large number of diverse compounds with abundant vacancy have been developed, which significantly improve the electrochemical efficiency.

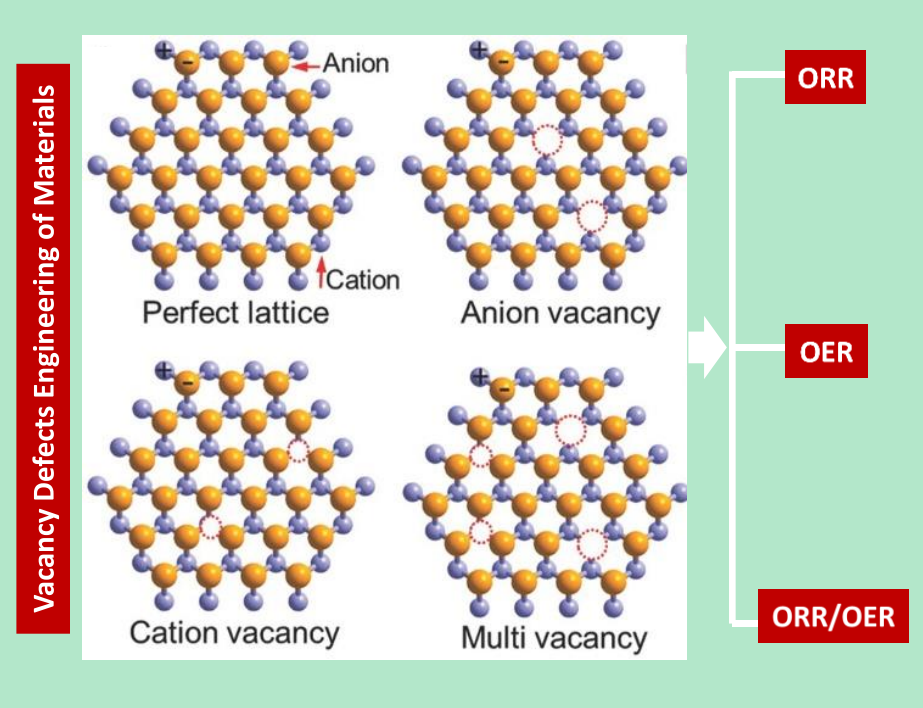

Figure 1-7 The types of vacancies in transition-metal-based electrocatalysts.[74]

Cation vacancies can have a significant effect on electrocatalytic activity, owing to their various electron and orbital distributions.[77] However, the formation of cation vacancies is more difficult than anion vacancies due to the large formation energy of metal cation vacancies in perovskites.[78-79] Developing effective synthetic methods to prepare materials containing well-defined metal-cation vacancies is highly pursued to further understand the effects of cation

vacancies on the ORR/OER performance. Recently, Wang et al.[78] introduced abundant Sn vacancies on the surface of the layered SnCoFe perovskite hydroxide precursors by energetic Ar plasma. Sn vacancies could be preferentially controlled owing to the lower lattice energy and weaker chemical bonds of $Sn(OH)_4$. The prior formation of Sn vacancies promoted the exposure of active CoFe sites, resulting in an amorphous surface layer, modulated the conductivity, and thus enhanced the OER performance. Notably, the electrocatalysts with abundant metal cation vacancies are limitedly reported as the bifunctional ORR/OER catalysts, which may be attributed to the challenges regarding cation vacancies formation. In this sense, researchers need to put more effort into developing effective methods to prepare materials containing metal-cation vacancies.

In addition to cation vacancies, the anion vacancies such as oxygen vacancies in the transition metal oxides have been extensively reported to enhance electrocatalysis performance.[80-82] The oxygen vacancies can be obtained more easily by various techniques, such as thermal annealing, cation doping, and solution processing, due to the relatively low formation energy. The presence of oxygen vacancies can tailor the surface electronic properties and gap states, which will significantly improve the conductivity and facilitate the absorption and desorption of reactant and reaction intermediates.[83] For instance, Co_3O_4, which is a typical spinel-type oxide with mixed oxidation states of Co^{2+} at the tetrahedral site and Co^{3+} at the octahedral site, has been widely demonstrated for the facile formation of oxygen vacancies.[84-85] However, it is still challenging to introduce oxygen vacancies controllably, and understand their intrinsic reaction mechanisms and evolution during the OER. Apart from the oxygen vacancy, sulfur vacancies are another commonly reported anion vacancy, which is frequently observed in the metal chalcogenides electrocatalysts.[86-88]

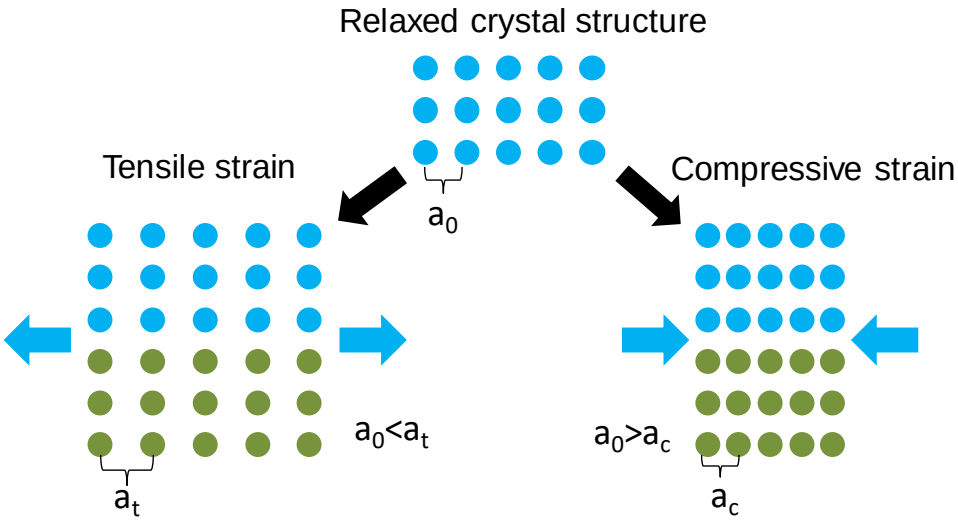

Figure 1-8 Schematic illustration of the strain effect on the crystal structure.[16]

1.4.3 Lattice-strain control

In the past two decades, density-functional theory (DFT) has accelerated the establishment of design principles and activity descriptors based on surface electronic structure features.[16, 89-91] The structural effects related to tensile and compressive strain can modify the electronic bandwidth, which will alter electronic features, e.g., the metal d-band and O 2p-band centers (Figure 1-8).[92-93] The d-band center of metal relative to the Fermi level is considered to govern the binding energy of adsorbates on the metal catalyst surfaces, such as *OOH, *O, and *OH.[94] ORR activity of metals follows a volcano trend vs. the metal d-band center relative to the Fermi level or the calculated binding energy of oxygenated species, assuming ORR follows the conventional mechanisms involving four proton-coupled electron transfer reaction steps.[95-96] The O 2p-band center is also an effective electronic structure descriptor for surface reactivity trends.[97-98] The O2p-band center has a linear relationship with the adsorption energy of oxygen, as well as oxygenated adsorbates (*OH, *OOH, *O).[99] The lower O 2p-band center indicates a higher interstitial-mediated ORR surface exchange rates and lower oxygen interstitial formation

energy for the Ruddlesden-Popper oxides,[100] whereas a higher O 2p-band center corresponds to a higher vacancy-mediated ORR surface exchange rate and lower oxygen vacancy formation energy for the ABO_3 perovskites.[75] In addition, modification of electronic structure by strain can also alter oxygen vacancy formation and migration energetics of oxide catalysts, which is key to influencing oxygen vacancy transport, oxygen surface exchange rate, and oxygen vacancy ordering.[101-103] The reasonable tuning of electronic structure by strain effects can modify surface adsorption of rate-limiting intermediates, as well as the nature of the proton-electron transfer for key elementary reaction steps. For instance, lowering the d-band center of Pt relative to the Fermi level through compressive strain is an effective route to weaken the binding strength of OH intermediate and thus increase ORR activity. The extensive study of strain-engineering Pt-based metals has been conducted, including subsurface metal solute incorporation, epitaxial growth of varied metal thicknesses on oxide substrates, metal deposition on Li-ion intercalation materials, and synthesis of core-shell nanoparticles to tune the surface lattice strain for ORR.[1, 93, 104]

1.4.4 Crystallographic structure control

For the design of efficient transition metal-based (e.g., Mn, Co, Ni, and Fe) bifunctional catalysts, the precise control of the exposed preferential crystal planes and appropriate surface energies is one of the most promising routes to improve their catalytic selectivity and activity (Figure 1-9).[105-109] Their unique facet-controlled geometry with different low-index facets (e.g., {111}, {110}, and/or {100}) in different proportions significantly determines their catalytic activity. The importance of the exposed lattice facets for the oxygen electrocatalytic activity has been widely investigated in the Mn-based nanocrystals.[110] For example, Chen et al.[111] found that MnO_2 catalysts exhibit different ORR activities, which strongly depend on the crystallographic structures, following an order of α->β->γ-MnO_2. L. Suib et al.[112] systematically investigated the

relationships between the structures of manganese oxides (α-, β-, and δ-MnO_2 and amorphous MnO_2) and OER/ORR activities in alkaline media. It was indicated that both OER and ORR activities had similar structure-determined activity trends, i.e., an order of α-MnO_2 > amorphous MnO_2 > β-MnO_2 > δ-MnO_2. Kuo et al.[113] found that the OER and ORR activities of MnO nanocrystals were strongly correlated with exposed lattice facets. In comparison with (111) planes, the preferentially exposed (100) planes with a higher adsorption energy of O species (e.g., OH^- and O_2) could largely promote the activity. The facet-dependent electrochemical performances of Co-based materials were also reported. For example, Liu et al.[114] synthesized Co_3O_4 cubes with an exposed (001) plane and octahedrons with an exposed (111) plane. They found that Co_3O_4 octahedrons showed much higher specific capacity and cycling performance in ZABs than Co_3O_4 cubes. DFT-based first-principle calculations indicated that Co_3O_4 (111) had a lower activation barrier than Co_3O_4 (001) for the O_2 desorption step in OER, which is of great significance to recover active sites of catalyst and generate a better cyclic performance. Recently, Qiao et al.[54] developed a high-performance bifunctional electrocatalyst, namely single-crystal (SC) CoO nanorods (NRs), through the surface structure engineering. The introduction of desired oxygen-vacancy-rich {111} nanofacets in the pyramidal crystals greatly influence the electronic structure. Consequently, the engineering of the electronic structure of CoO optimized the adsorption energies for ORR/OER intermediates, and enabled great improvements in the electrocatalytic activity of CoO. Therefore, the crystallographic structure control can indirectly introduce defect sites, which is a promising route as well to improve the catalytic activity.

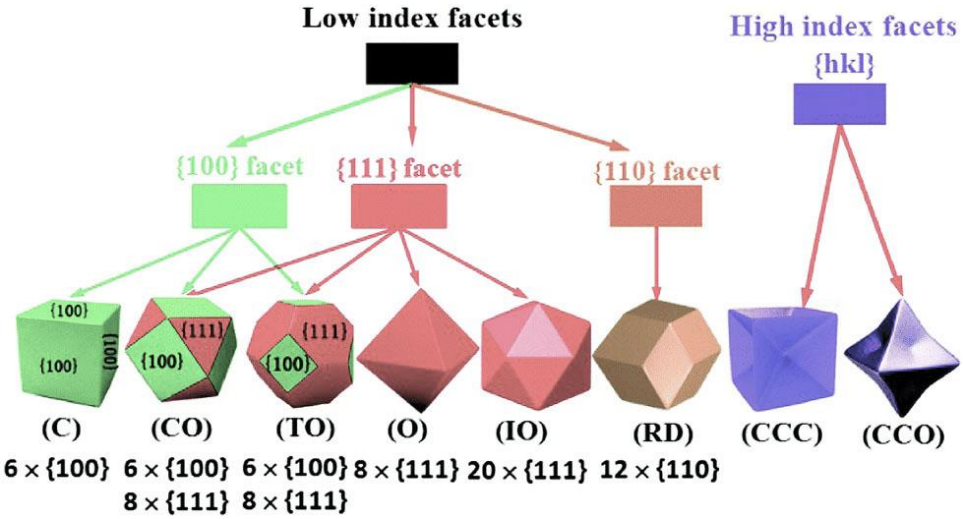

Figure 1-9 Illustration of various 3D polyhedral configurations shown as a function of low index {100}, {111}, and/or {110} facets and high index {hkl} facets [notes: C = cube, CO = cuboctahedron, TO = truncated octahedron, O = octahedron, IO = icosahedron, RD = rhombic dodecahedron, CCC = concave cube, CCO = concave octahedron].[115]

1.4.5 Metal-carbon support interaction control

To date, carbon-supported metal catalysts are one of the most investigated multifunctional electrocatalysts because of their outstanding and tunable catalytic behavior.[43] The metal-support interaction can influence the catalytic performances of metal catalysts in different ways, including (i) geometric effects of the metal (e.g., NP size, morphology, or strain),[116-117] (ii) electronic effects (e.g., charge transfer between metal and support),[118-119] (iii) interfacial reactivity (specific sites at the metal-support interface),[120] and (iv) directly serving as fast electron and mass transfer media for the metal catalysts[121-122] (carbon supports present several advantages, such as high specific surface area, porous structure, and high conductivity). Electronic, geometric, and ligand effects are interrelated and always work together to affect the catalytic performances. Based on these, significant efforts have been devoted to revealing metal-carbon support interactions during catalyst synthesis or catalytic reactions by XRD, electron microscopy, and X-

ray absorption spectroscopy methods. It has been reported that carbon support can influence the chemical state of metal nanoparticles (NPs) other than simply acting as a substrate for the deposition and dispersion of the metallic phase.[123] Moreover, the catalytic performance of carbon-supported metal catalysts is significantly dependent on the size of highly dispersed metal nanoparticles on the carbon support. A tremendous number of works have been devoted to tuning the anchoring modes of supported metallic catalysts (atomically dispersed metal atom, nanocluster, or even NPs) on nanostructured carbon-based materials.[124] In addition, searching for stable carbon support materials is necessary to suppress the loss of catalyst surface area caused by carbon support corrosion. Carbon materials as catalyst support present several advantages, such as (i) the good resistance to acids and bases; (ii) the stable structure to high temperatures (even above 1023 K under inert atmosphere); (iii) the low cost and easy availability; and (iv) various physical forms (carbon tube, graphene, carbon fibers, carbon sheet, porous carbon, etc).[125] To further improve the multifunctional catalytic activity, the modified carbon materials are used not only as supports but also as kinetics accelerators due to their catalytic activity. The catalytic activity and selectivity of carbon-based catalysts are strongly related to their surface chemistry and electronic properties.[126] Meanwhile, the anchoring of supported metallic catalysts is related to the surface physicochemical properties of the carbon support.[45, 127] For the sp^2 type carbon material, the basal/edge carbon atoms and point-defects such as structural carbon vacancies or nonaromatic rings can be the potential active sites or anchoring sites for the single TM atoms (Figure 1-10a,b).[128-130] Nowadays, the reinforcement of metal-carbon interaction is mainly realized by the structural surface defects, substitutional-doping and/or chemical functionalization of the carbon surfaces. For instance, the heteroatoms (N, B, P, and S)-doped carbon materials as highly efficient electrocatalysts for ORR are widely used as support. The introduction of heteroatom dopants usually increases the carbon sites' reactivity upon functionalization, making

them efficient as localized sites for metallic catalysts (atomically dispersed metal, nanoclusters or even NPs) anchoring. The metallic catalysts, especially the nanoclusters and NPs, have been widely investigated as promising candidates as efficient and stable OER catalysts. When considering both ORR and OER chemical processes, we can distinguish between (i) bifunctional catalysis, such as the nanoclusters or even NPs supported by heteroatoms (N, B, P, and S)-modified carbon materials, where the surface functional groups ensure one catalytic function (usually the ORR) and the metal catalysts for another one (usually OER), and (ii) cooperative catalysis, especially atomically dispersed metal catalysts, where the functional groups and the metals operate concertedly during a single chemical transformation (Figure 1-10c).[43] In addition, to improve the stability of the carbon materials under high oxidation potentials, carbon supports with a high degree of graphitization, such as CNT and graphene, have been extensively considered.[131-133] The higher degree of graphitization would result in higher stability due to a lower density of edge and defect sites. Other supports with the tailorable graphitization degree and support microstructure have been considered as well, such as nanofibers, hierarchical carbon, aerogels, and ordered mesoporous carbon.[5, 134-136] The surface chemistry and the broad spectrum of structures of different carbon materials offer interesting perspectives to modify the catalytic performances. Functionalized and chemically modified carbon nanomaterials have been getting more attention over the past few years.[137] In these materials, surface functional groups can stabilize the carbon structure and, at the same time, can provide bonding sites for metal catalysts to increase the dispersion and stability.

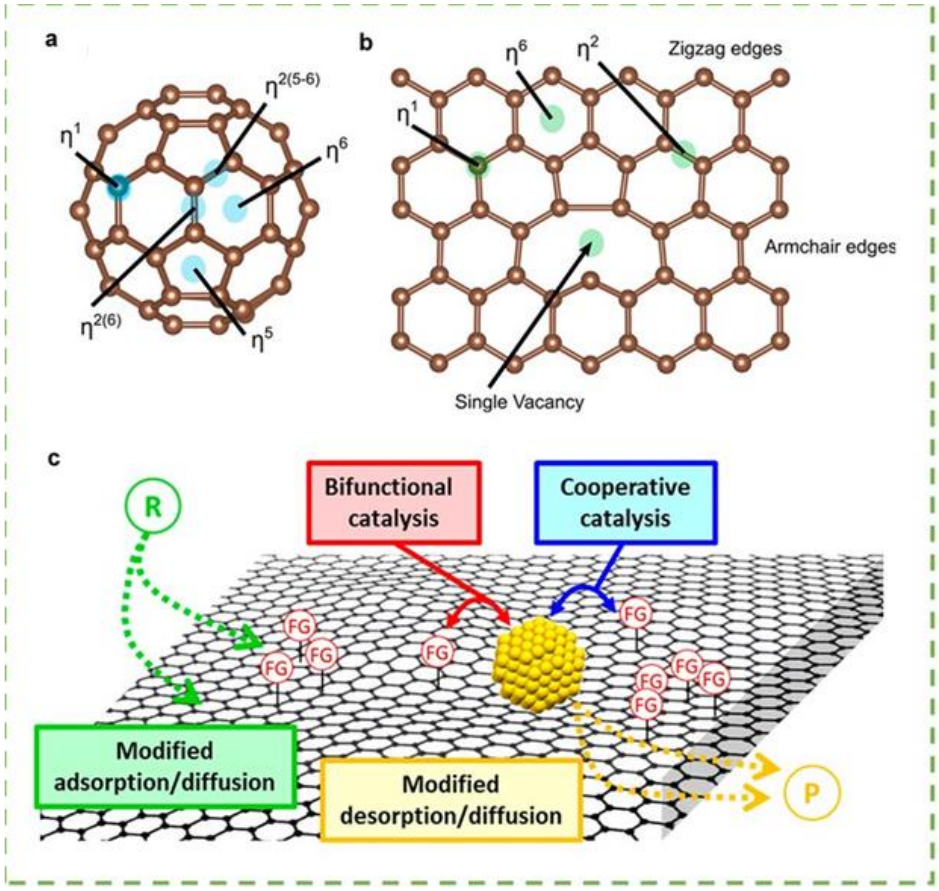

Figure 1-10 Typical adsorption modes on (a) C60 and (b) the graphene layer presenting also an armchair and zigzag edges as well as single vacancy. (c) Direct effects of surface functional groups on catalysis.[43]

1.5 Configurations of Air Electrodes

Since the O_2 bubbles generated from the OER are intrinsically insulative, which seriously blocks the transfer of electrons/ions from the air electrode. Therefore, designing high throughput gas-breathing air electrodes becomes indispensable. In the past decade, multitudes of strategies have been investigated to improve electrocatalytic activity and stability of bifunctional air electrodes. These strategies have been organized into three categories, aiming at controlling their chemical composition and architecture. 1) The conventional or common strategy is to synthesize powdery catalysts by high-temperature pyrolysis, calcination, or hydrothermal methods followed

by electrode fabrication through physical deposition (e.g., drop-casting, spray-coating) of an active material onto a carbon gas diffusion layer (GDL) with the assistance of polymeric binders and extra conductive additives. 2) Electrocatalysts are *in situ* grown on conductive substrates (e.g., carbon paper, carbon cloth, Ni foam, stainless steel (SS) mesh, indium tin oxide (ITO), metal foils) by methods such as hydrothermal process, electro-deposition (ED), chemical vapor deposition (CVD) and atomic layer deposition (ALD) technologies. 3) The last one is known as freestanding catalyst films or wires, which are composed of graphene sheets and their analogs (e.g., MoS_2, WS_2, g-C_3N_4) as the active species.

1.5.1 Powdery electrocatalysts physically deposited on GDL

Conventional air electrode always consists of three main components: current collector, GDL, and active catalyst layer (powdery O_2 electrocatalyst). The current collector usually uses conductive metal mesh such as nickel foam and stainless steel. The GDL should have a highly effective surface area which is preferable for the gas transfer and must be hydrophobic for the air contact while avoiding leakage and alleviate the evaporation loss of electrolytes. The hydrophobicity can be realized by impregnating the GDL with hydrophobic agents PTFE and high-temperature calcining.[138] Besides these, it should also meet other stringent requirements, such as enough mechanical strength, high electrical conductivity, superior corrosion resistance to oxidation, and strong alkaline environments. In the case of flexible devices, undoubtedly, they should also have optimum bending stiffness. Currently, two types of commercially carbon-based GDLs are commonly used in ZABs: nonwoven carbon paper (e.g., Toray, Freudenberg, and Sigracet) and woven carbon cloth (e.g., Zoltek, GDL-CT, and ELATTM). These carbon-based GDLs typically have double layers, consisting of a macro-porous gas-diffusion substrate and a thin microporous layer (MPL). The MPL is made of relatively hydrophilic carbon with fine

porosity (e.g., carbon black), which allows efficient air diffusion to the active catalysts, and minimizes the contact resistance between the substrate and catalyst layer.[139] Air electrodes are fabricated by casting and pressing the mixture of the catalysts and binder (e.g., PTFE, Nafion) into the carbon-based GDLs. The polymer binders are used to make the catalysts layer tightly stick to GDL. Although these carbon-based GDLs have been widely used in rechargeable ZABs, the carbon corrosion towards high oxidation potentials during long-term charging as well as exposure to strong alkaline electrolytes are still urgent issues to be resolved.[140] Additionally, porous supporting carbon materials or metal powders in the active layer have large specific surface areas, which effectively promote the diffusion of O_2. Therefore, the GDL is usually absent from the composition of the air electrode in some cases. One typical approach is to mix active catalyst material, porous carbon or metal powders, and polymer binder (PTFE), then press the obtained slurry onto a current collector (nickel foam or other metal grids).[141] In this design, these metal substrates (stainless-steel/nickel mesh and nickel/copper foam) known for their higher electrical conductivity and better electrochemically oxidative stability not only play a role in collecting current but also in gas diffusion. However, the different wettability of the GDL and active catalyst layer is of great importance and the absence of a gas diffusion layer would inevitably affect the battery performance. Porous carbon materials or metal powders act more like an MPL, providing a porous structure in the catalyst layer, which can effectively optimize the distribution of air throughout the catalyst layer, contributing to comparable performance to carbon-based GDLs in ZABs.[140, 142-143]

The active catalyst layer as the most important part of the triple-phase boundary plays a key role in improving the performance of ZABs. O_2 has low solubility and diffusivity in the strong alkaline electrolytes, thus, in the ORR process, O_2 is mainly in the form of the gas phase. The active catalyst layer with a high surface area is therefore very crucial for an air electrode.

Moreover, the excellent conductivity, stability, and corrosion/oxidation resistance are very important for the active catalyst layer during the long-term harsh charge/discharge process. Consequently, high porous and conductive carbon materials (e.g., carbon nanotubes (CNTs), graphene, and porous carbon) have been most widely used as supporting materials, because of their distinctive physical and chemical advantages.[144-145] Meanwhile, to meet the rigorous requirements of ORR/OER, the excellent contact of O_2 and electrolyte on the surface of the electrocatalyst is necessary and significant. Therefore, the wettability of the active catalyst layer with the electrolyte should be excellent to ensure a sufficient contact area. To realize the optimized wettability, the side of the air electrode contacting with electrolyte (active catalyst layer) should be hydrophilic. Compared with self-supported air electrodes, although this process of electrode fabrication using binders results in some undesirable results, it is still the mainstream technic currently own to its high feasibility and maturity.

1.5.2 Electrocatalysts in situ grown on conductive substrates

Recently, flexible electronic devices have gained increasing popularity because of their special properties such as being bendable, portable, crumpled, and lightweight.[146] Especially, flexible ZABs have emerged as one of the most promising electrochemical energy storage technologies. However, this technology is still in the prototype stage. For both theory and the practical application of flexible ZABs, there still exist many scientific and technological challenges to be overcome.[147] First and foremost, it is very urgent to design and fabricate mechanically robust, flexible, electrochemically stable, and highly effective air electrodes toward flexible ZABs batteries.[148] Recently, self-supported electrocatalysts directly growing on conductive substrates (e.g., carbon cloth, Ni foam, stainless steel (SS) mesh, ITO, metal foils) or forming freestanding films or wires, have attracted considerable interest.[149-153] Conventional

electrode fabrication, by casting or coating procedure with the assistance of polymeric binders, is always tedious and time-consuming. Moreover, the inevitable introduction of low conductive binders will result in some undesirable consequences, such as limited active surface areas, microstructures destruction, decreased volumes, and undesirable interface, which greatly limits electron conductance and mass transport.[154] Meanwhile, binders inevitably suffer degradation over long charge/discharge cycling operation under oxidizing conditions. Consequently, it will gradually degrade, eventually leading to the detachment of catalysts from carbon supports.[155-156] Electrocatalysts *in situ* grown on conductive substrates with advanced architectures like nanowire/plate/pillar/flower arrays as binder-free air electrodes have many structural advantages, in comparison with their powdery counterparts, [153, 157] such as 1) greatly simplifying the design and fabrication procedure of air electrodes; 2) allowing highly practical and scalable preparation of the self-supported electrodes; 3) effectively avoiding catalysts' mechanical shedding from supporting substrates during continuous O_2 evolution, due to the strong adhesion between the electrocatalysts and conductive substrates; 4) assuring good electron conductivity by *in situ* growth on highly conductive substrates; 5) affording large electroactive surface area, plenty of exposed active sites, and efficient mass transport, consequently promoting reaction kinetics. For the fabrication of flexible ZABs, it may require a flexible current collector, a flexible electrolyte membrane, and a flexible encapsulating material. To maintain stable electrochemical performance under deformation, each component must be carefully designed. Meanwhile, the structural and mechanical stability of the fabricated electrodes is critical to meet the requirement of long-term and cyclic use. For this reason, the interaction between active materials and substrates need to be further enhanced by optimizing preparation condition.

1.5.3 Freestanding electrocatalyst films and wires

Very recently, a new class of freestanding films and wires as bifunctional air electrodes of ZABs have been reported.[158-160] Compared with conventional powdery catalysts coated on conductive substrates, their ordered assembly can generate oriented transport channels with interconnected porosities which are beneficial to O_2 evolution. Currently, freestanding electrocatalyst electrodes are generally produced mainly by three strategies. 1) By self-assembly of the dispersive mixture of functionalized carbon (e.g., graphene oxide, carbon nanotubes, and g-C_3N_4) and metal-based active species to prepare films or wires. 2) By electrospinning technique combined with a thermal annealing process to prepare carbon nanofiber (CNF) films encapsulating metal active compositions. 3) By ED, CVD and their derivative technologies (e.g., floating catalyst CVD (FCCVD), plasma-enhanced CVD (PECVD)) to prepare freestanding films decorated with metal active species. For the freestanding catalyst films or wires, this technology is still in the prototype stage. For flexible ZABs in both theory and practical application, many scientific and technological challenges need to be overcome.

1.6 Objectives and Structure of this Thesis

The main objectives are to i) develop high-performance cathode materials for rechargeable ZABs, ii) reveal the relationship between nanostructure/composition and electrochemical performance, iii) track the structural evolution during electrocatalytic operation and understanding real active state, and iv) offer an innovative and valuable solution for the development of low-cost, highly durable and efficient electrocatalysts for rechargeable ZABs. Therefore, in this thesis work, different types of bifunctional oxygen electrocatalysts or electrodes were designed and investigated; their relevant structure properties and electrochemical performance were improved, and then contribute to high-performance rechargeable ZABs. Figure

1-11 illustrates all work conducted throughout this thesis.

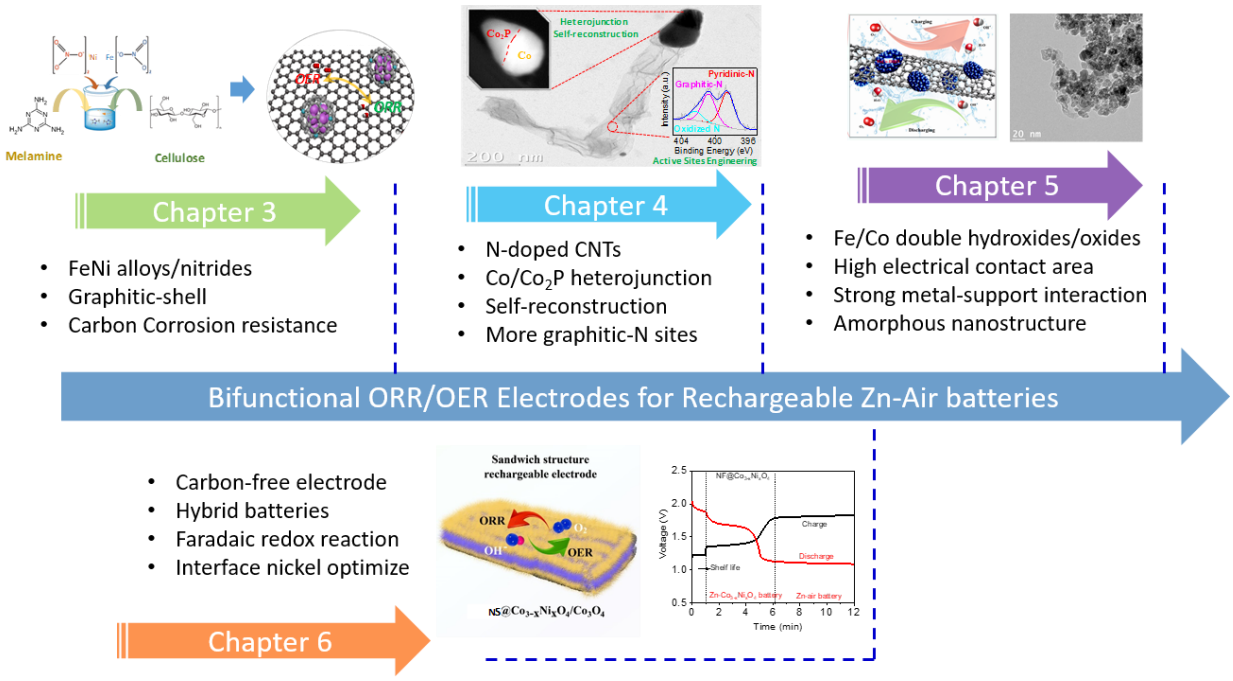

Figure 1-11 Schematic illustration of the research topics of the thesis.

This thesis comprises seven chapters. **Chapter 1** introduces a general background, the current research progress and challenges of ZABs. Especially, the crucial defect engineering strategies to tune the ORR/OER catalysts are elucidated. **Chapter 2** describes some key physical and electrochemical characterization techniques used throughout the thesis. **Chapter 3** a facile template-free method to fabricate binary FeNi alloy/nitride nanocrystals with graphitic-shell supported on the N-doped porous carbon (Fe_xNi_yN@C/NC). Such a novel nanostructure exhibits strong interactions, which contribute to improved electrocatalytic performance. The crucial structure properties optimized by graphitic-shell encapsulation provide several advantages in the rechargeable ZABs. **Chapter 4** focuses on the design of a high degree of graphitization of NCNTs with optimized N species, and in particular the investigation of the dynamic structural

evolution of Co/Co_2P heterojunctions. The highly ordered NCNTs with rich pyridinic-N and graphitic-N active sites are valid to avoid the destruction of ORR active sites due to the high potential oxidation conditions required for the OER process. In addition, the triggered cross-linked $CoO_x(OH)_y$ active species contribute to increased OER activity, which can be used as a highly active bifunctional pre-catalyst for rechargeable zinc-air flow batteries. **Chapter 5** presents an effort to design an efficient hybrid bifunctional oxygen electrocatalyst by strong interactions of the FeCo hydroxide/oxide nano-particles with NCNTs. This hybrid catalyst provides a high electrical contact area, which greatly facilitates the sluggish oxygen reaction kinetics. In addition to the powder catalyst development, **Chapter 6** highlights the development of a self-supported sandwich-structured electrode. Such a carbon-free electrode with $Co_{3-x}Ni_xO_4/Co_3O_4$ nanowire arrays can take full advantage of the sandwich structure to promote the oxygen reaction kinetics and redox electrochemical performance, providing a Zn-based battery. This strategy provides a new avenue to design high-efficiency and stable self-supported air electrodes for the rechargeable hybrid zinc batteries. Finally, **Chapter 7** summarizes the important results and gives some discussion for the future direction.

Chapter 2 Key Performance Measurement Techniques

2.1 Overview

In this work, the bifunctional ORR/OER electrocatalysts mentioned in Chapters 3-6 were synthesized in different methods, including hydrothermal, high-temperature pyrolysis, chemical vapor deposition, and ball-milling. The detailed experimental procedures, characterization of each synthesized material are described within the proceeding chapters. In this chapter, some key performance measurement techniques and characterization techniques related to the evaluation and study of the structure, morphology, and composition of bifunctional electrocatalysts are briefly presented.

2.2 Physical Characterization Methods

Some important physical characterization methods used in this thesis include X-ray photoelectron spectroscopy (XPS), transmission electron microscopy (TEM), scanning electron microscopy (SEM), X-ray Diffraction (XRD), and X-ray absorption spectroscopy (XAS).

2.2.1 X-ray photoelectron spectroscopy

XPS is a surface-sensitive quantitative analysis method to accurately obtain the elemental composition of solid materials.[161] This technique is the most extended tool for the chemical characterization due to: 1) the non-destructive; 2) the broad analysis window that covers all the elements unless H and He; and 3) the high sensitivity. Considering the low escape depth of the photoelectrons inspection (≈ 1-3 nm), this technique is the most suitable for the thin-film and surface applications and processes. Its working principle is based upon the photoelectric effect shown in Figure 2-1. The photon energy can be absorbed completely by the electronic cloud of

the atoms. According to the Einstein equation: $E_{kinetic} = h\nu - E_{binding}$, if the photon energy ($h\nu$) is high enough, this can cause the ejection of the so-called photoelectrons with kinetic energy ($E_{kinetic}$). The photon energy and electron binding energy ($E_{binding}$) of the ejected electron determine the kinetic energy of photoelectrons. In this work, the XPS will be conducted to detect the surface structure and composition of prepared catalysts.

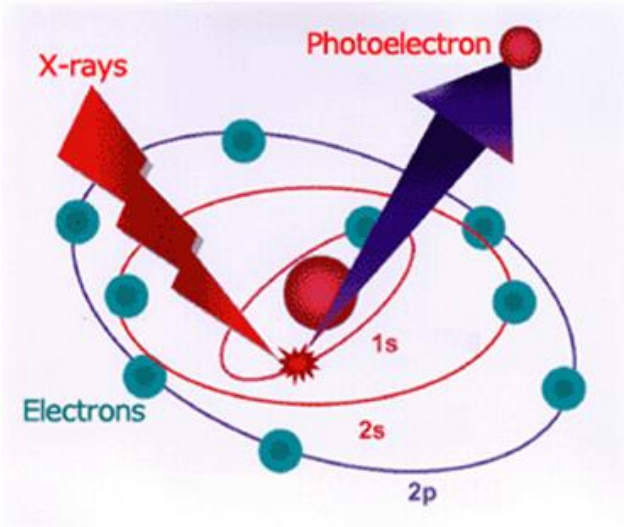

Figure 2-1 XPS working principle. (refer to wpo-altertechnology)

2.2.2 Transmission electron microscopy

TEM is a microscopy technique in which a beam of electrons is transmitted through a specimen to form an image (Figure 2-2).[162] It operates on the same basic principles as the light microscope but uses electrons instead of light. The specimen is most often an ultrathin section less than 100 nm thick or a suspension on a grid. An image is formed from the interaction of the electrons with the sample as the beam is transmitted through the specimen. The higher resolution of TEM than light microscopes is owing to the smaller de Broglie wavelength of electrons, which enables TEM to capture the fine detail of materials, such as particle size, shape, interparticle

interaction, crystallinity, number of layers, and morphology. In addition, different types of diffraction patterns obtained from TEM suggest different crystallization structures. For instance, dotted, center-circled and diffuse-circled diffraction patterns correspond to mono-crystalline, polycrystalline and amorphous structures, respectively. This type of characterization of materials is essential on a length scale from atoms to hundreds of nanometers. TEM instruments can be performed with many operating modes, including conventional imaging, scanning TEM imaging (STEM), diffraction, etc. For conventional imaging, contrast may be due to the differences in the thickness or density, atomic number, crystal structure or orientation, etc. In addition, dark-field and light field images of TEM are used to characterize the size, morphology, and crystal lattice of the sample. A bright-field image is the most commonly used image. In the bright field mode, the transmitted or unscattered electron beam is selected with the aperture, and the scattered electrons are blocked. Therefore, areas with crystalline or high mass materials will appear dark. In the dark field mode, the scattered electrons are selected, and the unscattered electron beam is excluded. Hence, the areas with materials will appear bright, and the areas with no samples will be black. This technique can be used to enhance contrast when the bright field image is not clear enough, especially when imaging crystalline features that are too small or are drowned out of view.

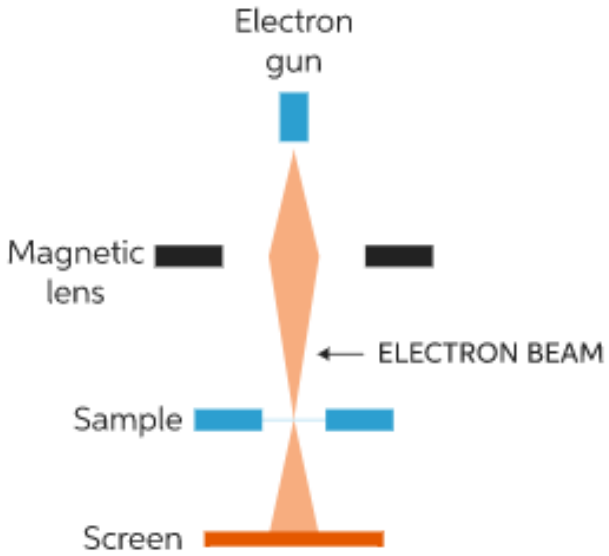

Figure 2-2 Simple diagram of a typical TEM.[162]

2.2.3 Scanning electron microscopy

SEM is an electron microscope technique that forms images of a sample by scanning its surface with a focused beam of electrons (Figure 2-3).[163] When the electrons interact with the sample, it will produce various signals that contain information about the surface topography and composition of the sample. These signals produced include secondary electrons (SE), back-scattered electrons (BSE), characteristic X-rays and light (cathodoluminescence) (CL), etc. The SEs with low energy less than 50 eV only escape from the surface (few nanometers) of a sample, which makes them useful for the examination of surface morphology. This mode also has the highest resolution. In contrast, BSE is a high-energy electron re-emitted from the sample due to elastic scattering. BSEs are most used to reveal chemical compositional differences (atomic number contrast). Compared with SE, BSE originating from deeper locations within the specimen shows poor resolution of images.

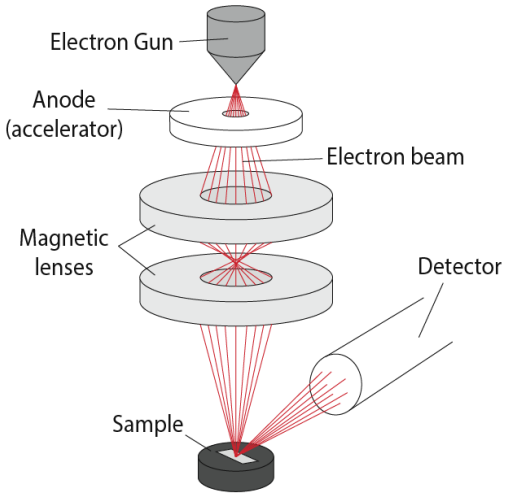

Figure 2-3 Simple diagram of a typical SEM. (refer to eng-atoms.msm.cam.ac.uk)

2.2.4 X-ray diffraction

XRD techniques are used for the identification of crystalline phases of various materials and quantitative phase analysis.[164] Crystal atoms scatter incident X-rays, primarily through interaction with the atoms' electrons. This phenomenon is known as elastic scattering. In the majority of directions, these waves cancel each other out through destructive interference, however, they add constructively in a few specific directions (Figure 2-4), as determined by Bragg's law:

$$n\lambda = 2d\sin\theta \quad (1)$$

where n is an integer, λ is the characteristic wavelength of the X-rays impinging on the crystalline sample, d is the interplanar spacing between rows of atoms, and θ is the angle of the X-ray beam with respect to these planes. When this equation is satisfied, X-rays scattered by the atoms in the plane of a periodic structure are in phase and diffraction occurs in the direction defined by the angle θ. This diffraction pattern can be thought of as a chemical fingerprint, and chemical identification can be performed by comparing this diffraction pattern to a database of known patterns.

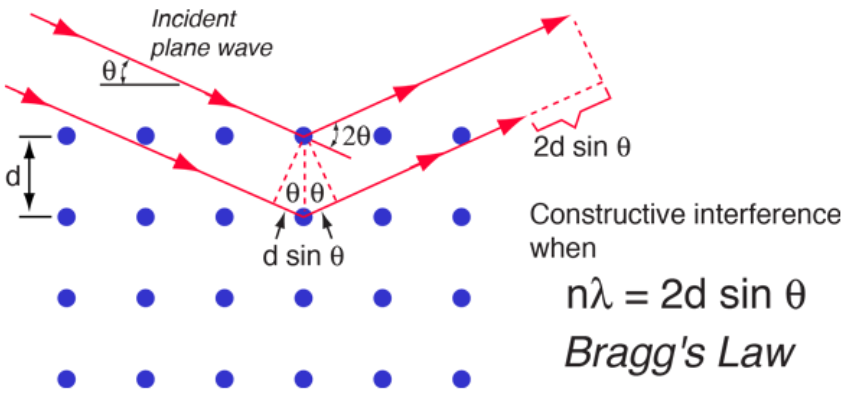

Figure 2-4 Simple diagram of an XRD. (refer to h-and-m-analytical)

2.2.5 X-ray absorption spectroscopy

XAS is a technique for determining the local geometric and/or electronic structure of the target element.[165] XAS data is obtained by tuning the photon energy, using a crystalline monochromator, to a range where core electrons can be excited (0.1-100 keV). The edges are, in part, named by which core electron is excited: the principal quantum numbers n = 1, 2, and 3, correspond to the K-, L-, and M-edges, respectively (Figure 2-5a). The operation is usually performed at synchrotron radiation facilities, which provide intense and tunable X-ray beams (Figure 2-5b). The most intense features are due to electric-dipole allowed transitions to unoccupied final states. For example, the most intense features of a K-edge are due to core transitions from 1s→p-like final states, while the most intense features of the L_3-edge are due to 2p→d-like final states (Figure 2-5c). There are four main regions found on an x-ray absorption spectrum: 1) pre-edge ($E < E_0$); 2) x-ray absorption near edge structure (XANES) ($E_0 - 10 < E < E_0 + 50$ eV); and 3) extended x-ray absorption fine structure (EXAFS), ($E_0 + 50 < E < E_0 + 1000$ eV). In the pre-edge region, the electron transitions from the core level to the higher unfilled or

half-filled orbitals occur. In the XANES region, transitions of core electrons to non-bound levels with close energy happen. Because of the high probability of such transition, a sudden raise in absorption is observed. In the EXAFS region, due to the high kinetic energy ($E-E_0$) of the photoelectrons, single scattering by the nearest neighboring atoms normally dominates.

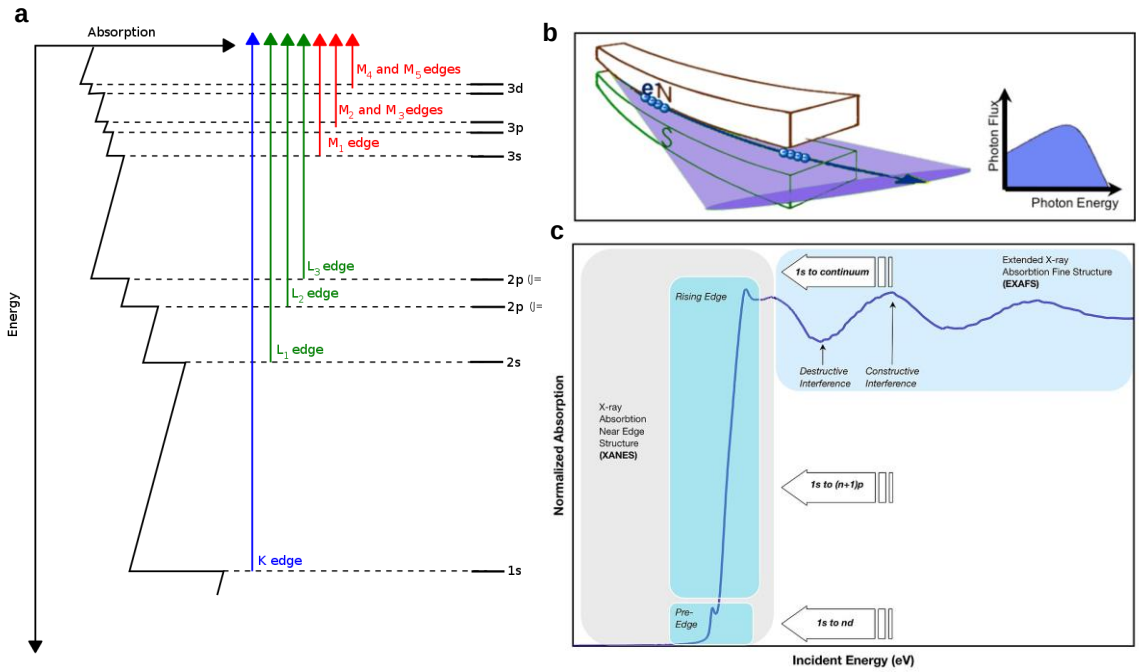

Figure 2-5 (a) Transitions that contribute to XAS edges. (b) Schematic diagrams of the generation of synchrotron radiation by injecting electron bunches into one group of bending magnets. The photon spectra on the right show the broad energy distribution of the radiation based on bending magnets. (c) Three regions of XAS data for the K-edge. (refer to en.wikipedia)

2.3 Electrochemical Characterizations

Some important electrochemical characterization methods used in this thesis mainly involve three-electrode cell and single-cell battery performance evaluation.

2.3.1 Three-electrode cell

Rotating disk or ring-disk electrode (RDE or RRDE) is a well-established technique to

provide quantitative information on the electrochemical reaction kinetics of catalyst materials, by taking advantage of the steady-state laminar flow conditions during rotating. The RRDE is a double working electrode, very similar to the RDE (Figure 2-6a). Catalyst powder cast on the RDE or RRDE was used as the working electrode. The electrocatalytic measurements for ORR, OER, and electrochemical impedance spectroscopy (EIS) are all carried out in a standard three-electrode cell in 0.1 or 1.0 M KOH electrolyte (Figure 2-6b). The electrochemical test system of a half-reaction comprises a working electrode (WE), a reference electrode (RE), a counter electrode (CE), and an electrolyte. A Pt wire and a Hg/HgO electrode were used as the counter and reference electrodes, respectively.

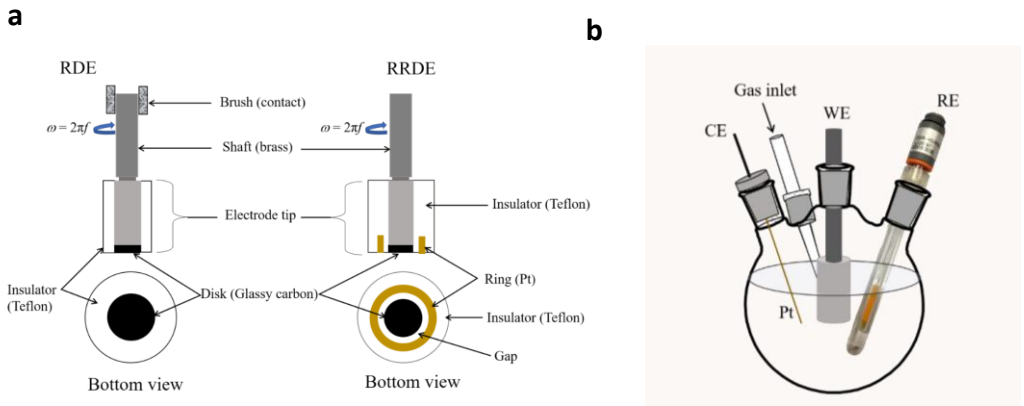

Figure 2-6 (a) Schematic presentation of the rotating disk electrode and rotating ring-disk electrode. (b) Three-electrode electrochemical cell system.[20]

In this work, the catalyst's activity concerning both ORR and OER are investigated by using cyclic voltammetry (CV) and linear sweep voltammetry (LSV) methods. CV is performed by cycling the potential of a working electrode and measuring the resulting current. In a typical LSV measurement of ORR, the electrode potential is swept from 1.0 to 0.1 V with a scan rate of 5 mV s^{-1} in an oxygen-saturated KOH solution at a certain rotation speed (e.g., 1600 rpm). For the OER, the electrode potential is swept from 0 to 20 V vs. RHE with the same scan rate and rotation

speed in an oxygen-saturated KOH solution. During this LSV experiment, current versus potential data is plotted, as shown in Figure 2-7. An efficient bifunctional electrocatalyst means low overpotential for both the ORR and OER.

The peroxide percentage ($H_2O_2\%$) was determined from RRDE measurements based on the disk current (I_d) and ring current (I_r) via the following Equation (2):

$$H_2O_2\% = 100 \times \frac{2I_r / N}{I_d + I_r / N} \tag{2}$$

The ORR electron transfer number (n) was based on the following Equation (3):

$$n = \frac{4I_d}{I_d + I_r / N} \tag{3}$$

where N (= 0.37) is the current collection efficiency of the Pt ring, which was calibrated with an N_2-saturated 10 mM $K_3Fe(CN)_6$ + 0.1 M KOH electrolyte solution.

ECSA was calculated using ECSA= $C_{dl}/(40*m_{loading})$, where $m_{loading}$ is the loading mass of catalyst per geometrical area of the electrode. The C_{dl} (double-layer capacitance) was determined by measuring the capacitive current associated with double-layer charging from the scan-rate dependence of CV stripping. For this, the potential window of CV stripping was about 1.1 V to 1.19 V versus RHE (1.0 M KOH solution). The scan rates were 5 mV s^{-1}, 10 mV s^{-1}, 15 mV s^{-1}, 20 mV s^{-1} and 25 mV s^{-1}. The C_{dl} was estimated by plotting the j_a at 0.59 V (where j_a are the c anodic current densities) versus RHE against the scan rate, in which the slope was the C_{dl}.

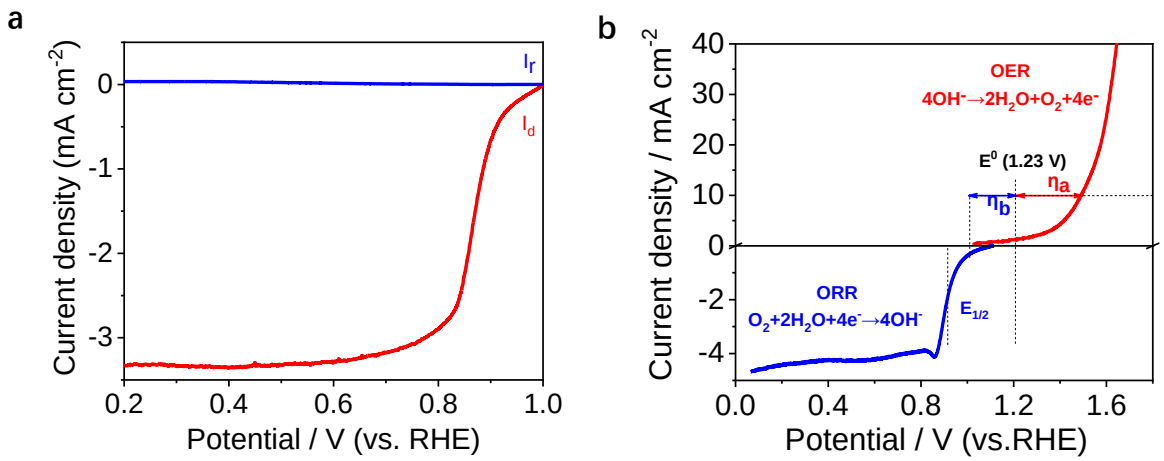

Figure 2-7 Linear sweep voltammetry for the (a) ORR and (b) OER in 1.0 M KOH solution.

Electrochemical impedance spectroscopy (EIS) can reveal charge transfer and mass-transport resistance of catalysts, providing a better understanding of the possible factors affecting ORR/OER performance. Generally, EIS studies also utilize a three-electrode mode which is comprised of a working electrode (the sample material), a counter electrode (commonly graphite or platinum), and a reference electrode. Typical EIS spectra (i.e., Nyquist plots) of different catalysts in a standard three-electrode cell, as well as the corresponding equivalent circuit, are shown in Figure 2-8. The Nyquist plot is modeled by the provided equivalent circuit including five elements: R1, C1, Rct, and W1. R1 is the electrolyte resistance. Rct represents the charge-transfer resistance during the electrochemical reaction, which is directly related to the electrocatalytic activity of the catalysts. C1 is the capacitor resistance, and W1 is the Warburg impedance related to ion diffusion into electrodes. The field of semicircle belongs to kinetic control, and the right belongs to the mass-transfer control field. In terms of the general analysis of the results, a smaller charge-transfer resistance indicates higher ORR and OER activities, and smaller W1 suggests a faster mass-transfer process.

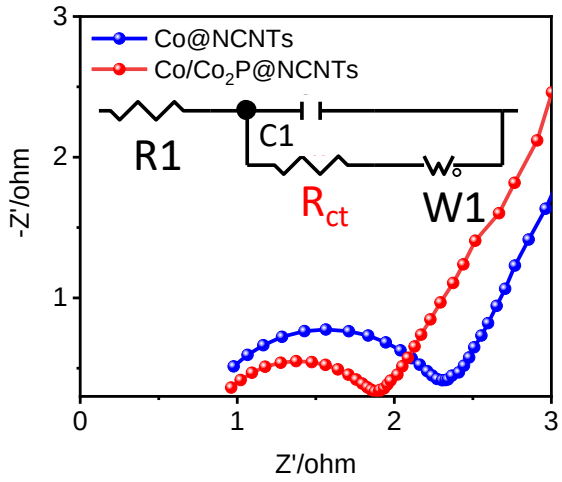

Figure 2-8 Nyquist plots obtained by EIS using different catalysts in a standard three-electrode cell. Inset: Equivalent circuit.

2.3.2 Battery performance evaluation

Some important parameters, such as working voltage, energy efficiency, specific capacity, power density, and cyclic stability are used to evaluate the performance of zinc-air batteries. These parameters can be obtained through galvanodynamic polarization and galvanostatic measurements. The galvanodynamic polarization is generally carried out by gradually increasing negative (discharging) or positive (charging) currents density relative to the battery cathode, meanwhile, the potential responses are recorded to obtain discharge and charge polarization curves. Figure 2-9 shows a typical example of discharge and charge polarization plots (black and brown solid lines, respectively) of a rechargeable zinc-air battery obtained by the galvanodynamic polarization method. For the initial discharge polarization curve, the sharp voltage drop part is referred to as activation polarization, which is mostly caused by the limit electron transfer of oxygen reactions at the air electrode. When the current is further increased, the gradual voltage drop part is dominated by ohmic polarization, which mostly comes from the internal electrolyte resistance and the interfacial resistances. The voltage drop at the end is

referred to as mass-transfer polarization, which is associated with the limited mass transfer of reactants (i.e., oxygen or OH-) to the electrodes. In addition, the energy efficiency can also be obtained by simply dividing the discharge voltage by the charge voltage.

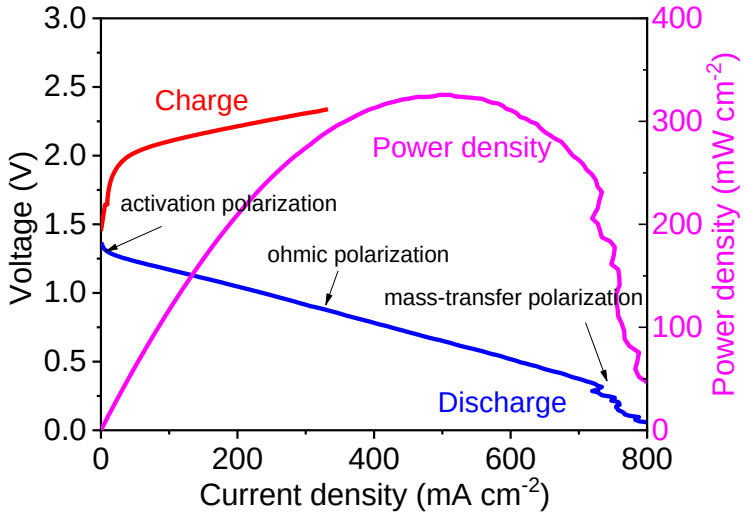

Figure 2-9 Galvanodynamic discharge and charge polarization curves and the corresponding power density plot of the zinc-air batteries.

In addition, the capacity of the Zn-air battery is decided by the zinc electrode, and the capacity is often normalized by the mass of the zinc electrode. The galvanostatic full-discharge test by applying a fixed discharge current (Figure 2-10a) was used to evaluate the real capacity of the zinc-air battery by making the comparison to the theoretical specific zinc capacity of 820 mAh g^{-1}. In addition, the galvanostatic discharge/charge cycling test is performed at fixed negative and positive currents (Figure 2-10b), which is used to investigate the stability of zinc-air batteries. The galvanostatic cycling test can be measured in different conditions, in terms of different discharge/charge current density, cycling number, and cycling period. In addition, the voltage gap (charge potential-discharge potential) and energy efficiency (determined by dividing the discharge potential by the charge potential) can be obtained from galvanostatic cycling.

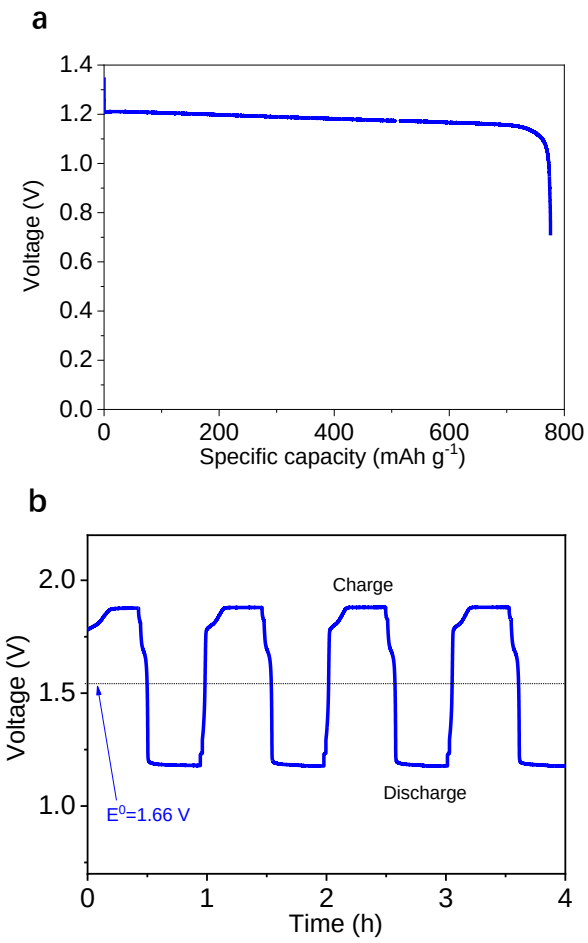

Figure 2-10 (a) Specific capacity curves of the zinc-air battery under fixed current densities. (b) Galvanostatic discharge/charge cycling test.

Chapter 3 Graphitic-shell Encapsulated FeNi Alloy/Nitride Nanocrystals on N-doped Carbon for Rechargeable Zn-air battery

3.1 Introduction

The growing concerns over climate change and the fast increasing global energy demand have promoted rapid development in renewable energy technologies, such as fuel cells, metal-air batteries, and water-splitting H_2 production.[11, 166-167] However, the sluggish kinetics of the electrochemical oxygen reactions (i.e., oxygen reduction reaction (ORR) and oxygen evolution reaction (OER)) significantly hinder the large-scale applications of these sustainable energy technologies.[28, 168] For the rechargeable Zn-air batteries, the involved multistep electron transfer processes in the reversible electrochemical reactions of oxygen require highly efficient bifunctional catalysts to catalyze both ORR and OER.[169-171] To date, carbon-supported platinum (Pt) is one of the most efficient catalysts for the ORR but always exhibits poor performance for the OER due to the formation of a stable oxide layer with low electrical conductivity.[172] Instead, noble-metal oxides such as ruthenium (Ru) and iridium (Ir) oxides could efficiently catalyze the OER process, but show quite low activity for the ORR.[172-173] To realize the rechargeability of the Zn-air batteries, combining them in a certain proportion is an attainable approach, unfortunately, these noble-metal-based catalysts are always plagued by high cost and scarcity.[174]

Porous carbon materials have attracted much attention due to their unique structures and properties, such as good conductivity and large surface area.[135, 144-145, 175] The incorporation of heteroatoms (Fe, Ni, Co, Mn, Cu, N, S, B, P, etc.) into the porous carbon matrix can effectively adjust the charge density and electronic distribution of carbon materials, and consequently improve the electrocatalytic performance.[5, 176] The porous carbon is usually synthesized by

complicated routes, such as the electrospinning technique, the soft template method, the hard template method, the dual template method, or the strong alkali etching method.[14, 168, 175, 177-178] The as-synthesized heteroatoms-doped porous carbon catalysts normally show excellent ORR performance, sometimes even outperform the Pt/C catalyst, in alkaline medium. However, the OER activities of these types of materials are still far from satisfactory due to their intrinsic properties and the carbon corrosion issue under high potential.[179-180] To enhance the OER activity and stability of the carbon materials without sacrificing the activity of ORR, introducing certain transition metal compounds (e.g., metal oxides, nitrides, hydroxides, sulfides, carbides, phosphides) and their derivatives into porous carbon materials is an effective strategy.[122, 181-184] Recently, metal/metallic compound nanoparticles with Mott-Schottky contacts have been synthesized, which can efficiently enhance the synergistic effect between the metal and metallic compounds in carbon frameworks.[185] In addition, the synergistic effects between carbonaceous materials and transition metal compounds (oxides, carbides, nitrides, or alloys) can significantly enhance catalytic performance.[121, 186-188]

Herein, we developed a facile method to fabricate the graphitic-shell encapsulated binary FeNi alloy/nitride nanocrystals and biomass-derived N-doped carbon hybrid (Fe_xNi_yN@C/NC) structure. This novel structure has several advantages. First, the N-doped graphitic carbon layers can protect the metallic cores from harsh electrochemical corrosion. Second, this unique morphological architecture could also provide a direct electron transfer pathway, enhance the structure stability, and then improve the catalytic activity. As expected, the obtained Fe_xNi_yN@C/NC catalyst exhibits excellent bifunctional ORR/OER activity, indicated by the small potential gap ($\triangle E$) of 0.67 V between $E_{j=10}$ (1.54 V) and $E_{1/2}$ (0.87 V) in 1.0 M KOH. Moreover, the catalyst displays a high positive onset potential of 0.98 V vs RHE for ORR. The electrochemical tests and XAS analyses revealed that the binary FeNi alloy/nitride nanocrystals

exhibit strong antioxidant ability and stability for OER. Importantly, a Zn-air battery device using Fe_xNi_yN@C/NC catalyst as an air electrode exhibits outstanding charging and discharging performance and cycling ability. This strategy provides a facile route to design a new type of metal alloy/nitrides with graphitic-shell and N-doped porous carbon hybrid structure for highly efficient bifunctional oxygen electrocatalyst in metal-air batteries.

3.2 Experimental Section

3.2.1 Synthesis of Fe_xNi_yN@C/NC and Fe_xNi_yN/NC

To prepare Fe_xNi_yN@C/NC, firstly, 1 g of cellulose and 1 g of melamine were dispersed in 30 mL deionized water with vigorous stirring at room temperature. Then, 0.61 g $Ni(CH_3COO)_2 \cdot 6H_2O$ and 0.68 g $FeSO_4 \cdot 7H_2O$ were dissolved in 20 ml distilled water under stirring for 10 min. Subsequently, the solutions obtained above were mixed under stirring for 1 h. Finally, the solution was transferred to a 100 ml Teflon container, sealed in an autoclave, and hydrothermally reacted at 180 ºC for 6 h. The precipitate was collected, washed, and centrifuged with distilled water 3 times. The product was dried at 80 °C for 12 h and collected as the FeNi carbonate hydroxide precursor (Fe_xNi_yCH). Finally, the precursor was heated to 900 ºC under Ar and then kept at 900 °C for 10 min under NH_3. The Fe_xNi_yN/NC was synthesized following the identical procedure used for Fe_xNi_yN@C/NC synthesis except that no melamine was used.

3.2.2 Synthesis of Fe_xNi_yO and Fe_xNi_y/C

The precursor was synthesized following the similar procedure used for Fe_xNi_yN/NC synthesis. The only difference is that Fe_xNi_yO was obtained by pyrolyzing the precursor at 500 ºC for 1 h under air, and the Fe_xNi_y/C was synthesized by heating the precursor to 900 ºC for 1 h

under Ar.

3.2.3 Fabrication of the liquid and quasi-solid-state Zn-air battery

The liquid Zn-air batteries were tested in home-built electrochemical cells; the electrolyte was 1.0 or 6.0 M KOH with a 0.2 M Zn acetate solution. The Liquid rechargeable Zn-air battery was assembled with current collectors (nickel foam for cathode), a polished Zn plate, and a catalyst layer (CL) coated gas diffusion electrode (GDE). To prepare the air electrode, a definite volume of homogeneous catalyst ink consisting of Fe_xNi_yN@C/NC catalyst, Nafion solution (5 wt.%), and isopropanol were dropped onto a gas diffusion layer (GDL) (loading: 2 mg cm^{-2}) with an exposed active area of 1.0 cm^2. Then Ni foam, GDE, and hydrophobic and breathable membrane were pressed together to form the integrated air electrode. For the quasi-solid-state Zn-air battery**,** a glass microfiber membrane soaked in 6.0 M KOH with a 0.2 M Zn acetate solution was used as the quasi-solid-state electrolyte. Then the flexible solid-state Zn-air battery was assembled with air electrode (loading: 2 mg cm^{-2}) and Zn foil anode (1.0 cm^2) placed on the two sides of the glass microfiber membrane, and a piece of iron mesh was used as a current collector.

3.2.4 Material characterizations

The morphologies of the as-prepared catalysts were observed by a scanning electron microscope (SEM, Quanta 450 ESEM, FEI) and a transmission electron microscope (HRTEM, JEM-2100). The surface properties were analyzed by X-ray photoelectron spectroscopy (XPS, VG ESCALAB 220i-XL) equipped with a hemispherical analyzer for a Twin Anode X-ray Source. The crystal structure of the catalysts was analyzed by X-ray diffraction (XRD) (40 kV, 25 mA, Cu Kα radiation, λ=1.5418 Å). The X-ray absorption spectroscopy (XAS) measurements

were performed at the Canadian Light Source (CLS) located at the University of Saskatchewan, a 2.9 GeV third-generation synchrotron source.

3.2.5 Electrochemical measurements

The ORR and OER performance of as-prepared catalysts were measured on an electrochemical workstation (Pine, Model PGSTAT-72637) and a rotating ring disk electrode apparatus (RRDE-3A, ALS) in a three-electrode cell by using a platinum wire as counter electrode and Hg/HgO (KOH, (20%)) as the reference electrode. The working electrode was a rotating ring/disk electrode with a glass carbon disk (0.2475 cm^2 in area). To prepare the catalyst slurry, 2.0 mg of electrocatalyst was dispersed in 0.2 mL isopropanol and 0.01 mL Nafion solution (5.0 wt%, Sigma Aldrich) and ultrasonicated for 60 min. 0.02 mL of the ink was dropped onto the glassy carbon electrode to give a catalyst loading of 0.8 mg cm^{-2} and dried in air. In this work, all potentials were converted to the reversible hydrogen electrode (RHE). Tafel plots calculation and electron transfer number calculation are based on the previously reported method.

3.3 Results and discussion

The fabrication of the Fe_xNi_yN@C/NC involves a general two-step process, including hydrothermal and pyrolysis (Figure 3-1a). In the first step, FeNi carbonated hydroxide precursor was grown on cellulose carbon substrate by hydrolysis and oxidation at 160 ^oC. Controlled nucleation of FeNi alloy/nitride (Fe_xNi_yN) nanocrystals on NC was achieved by tuning the metal salts/cellulose ratio and reaction time. Subsequently, the pyrolysis reaction at 900 ^oC led to direct nucleation of Fe_xNi_yN and reduction of cellulose to form the Fe_xNi_yN@C/NC hybrid. Melamine was also added in the synthesis steps to provide the nitrogen source. The graphitic-shell encapsulated Fe_xNi_yN nanocrystals on N-doped carbon were confirmed by transmission electron

microscopy (TEM). As shown in Figure 3-1b, Fe_xNi_yN nanoparticles with two particle size distributions (i.e., 10-20 nm and 100-200 nm in diameters, respectively) are embedded in the porous carbon framework. Figure 3-1c indicates that the Fe_xNi_yN nanoparticles are covered by a thin graphitic shell, which could effectively reduce their agglomeration or detachment from the carbon support under highly oxidizing conditions. It has been proven that the metallic cores can significantly tune the electronic structure of graphitic-shell on the surface. In addition, the core-

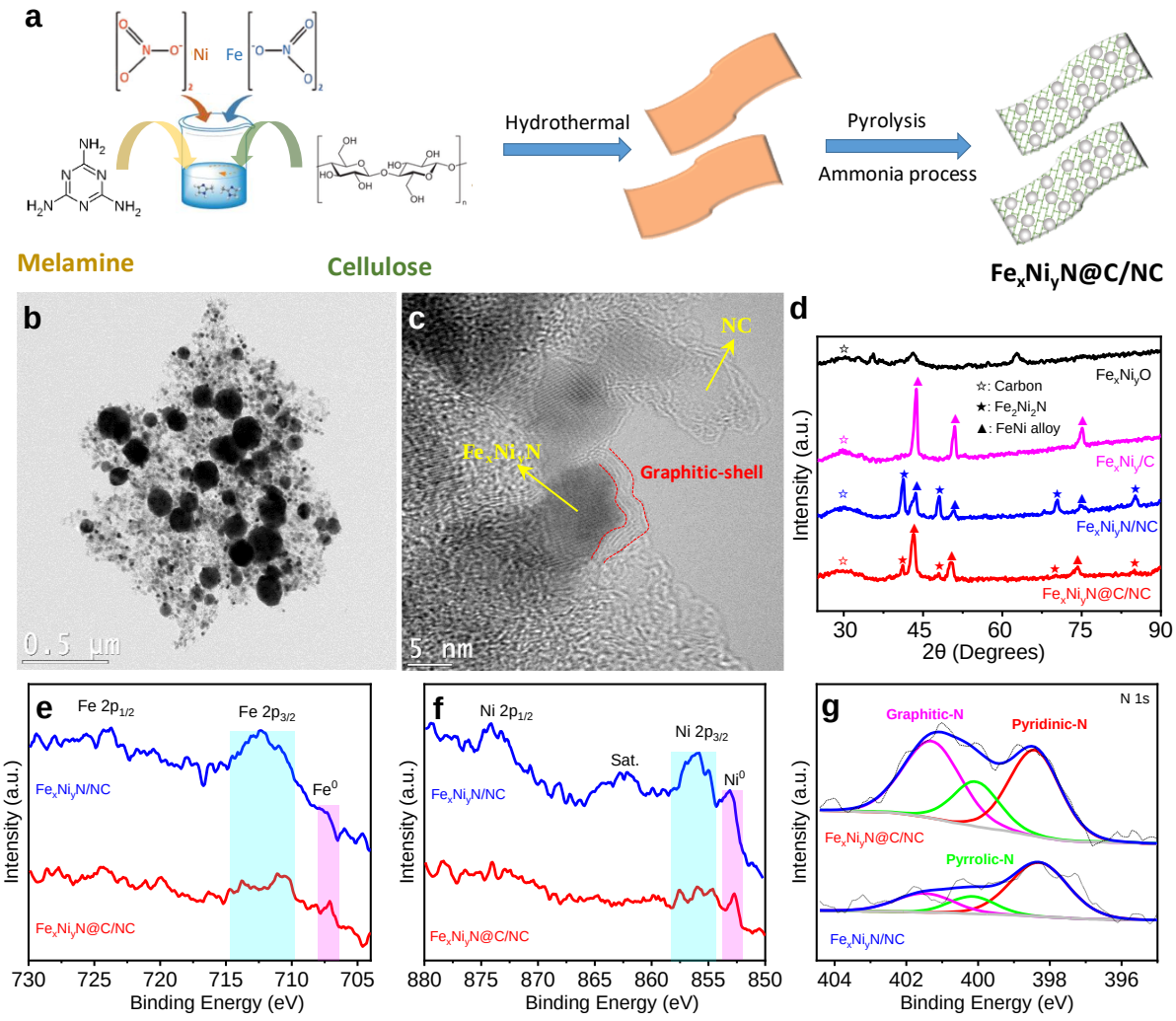

Figure 3-1 (a) Schematic illustration of the synthesis of Fe_xNi_yN@C/NC. (b, c) TEM images of Fe_xNi_yN@C/NC catalyst. (d) The XRD of the Fe_xNi_yN@C/NC, Fe_xNi_yN/NC, Fe_xNi_y/C, and Fe_xNi_yO catalysts (☆: Carbon, ★: Fe_2Ni_2N, ▲: FeNi alloy). High-resolution (e) Fe 2p, (f) Ni 2p and (g) N 1s of Fe_xNi_yN@C/NC and Fe_xNi_yN/NC.

shell structure can tune the surface lattice strain for efficient ORR.[1, 93, 104] Electron transfer from metal nanoparticles can result in an alteration of the binding energies of reaction intermediates (i.e., OH*, OOH*, O*, and H*) on the graphene surface.[189] The metal-based compounds wrapped by the conductive ultrathin heteroatom-doped carbon layer could provide a direct electron transfer pathway, enhance the structure stability, and then improve the catalytic activity.[181, 190] To probe the chemical composition evolution of the catalysts, the obtained catalysts were also characterized using X-ray diffraction (XRD) (Figure 3-1d). The XRD patterns of Fe_xNi_yO indicate the two main phases of Fe_3O_4 (PDF#65-3107) and NiO (PDF#65-2901). For the Fe_xNi_y/C, three major peaks centered at 43.60°, 50.79°, and 74.68° are attributed to the (111), (200), and (220) planes of the $Fe_{0.64}Ni_{0.36}$ alloy (PDF#47-1405), respectively. In addition, the peaks at 43.28°, 50.40°, and 74.05° are the characteristics of the (111), (200), and (220) reflections of $CFe_{15.1}$ (PDF#52-0512), respectively. After ammonia post-treatment, the metallic $Fe_{0.64}Ni_{0.36}$ alloy nanoparticles were further transformed into Fe_2Ni_2N (PDF#50-1350) nanoparticles in the sample Fe_xNi_yN/NC.[121] The Fe_xNi_yN@C/NC sample shows similar XRD patterns as that of the Fe_xNi_yN/NC, but with significantly decreased peaks intensity of Fe_2Ni_2N. This could be that the graphitic-shell protective layer prevented the formation of FeNi nitride to some extent or the reduced size of Fe_xNi_yN particles. X-ray photoelectron spectroscopy (XPS) was used to investigate the surface chemical composition of the catalysts. In the Fe 2p XPS spectra (Figure 3-1e), the peak at around 707.8 eV is assigned to the metallic Fe^0 species. The Ni 2p XPS spectrum (Figure 3-1f) also showed a sharp peak at 853.2 eV, which can be assigned to the metallic Ni species. The sharp peaks of the metallic Fe^0 and Ni^0 species suggest the presence of FeNi alloy. The presence of broad Fe $2p_{3/2}$ and Ni $2p_{3/2}$ peaks for the Fe_xNi_yN/NC could be attributed to the presence of a small number of metal oxide species on the surface. The peak intensities of the Ni and Fe for the Fe_xNi_yN@C/NC significantly decreased after introducing

melamine as the nitrogen source, which should be attributed to the graphitic-shell and the size-reduced Fe_xNi_yN nanocrystals. The graphitic-shell structure can effectively protect the surface of Fe_xNi_yN nanocrystals from oxidation. Meanwhile, the XPS survey spectrum revealed the ~ 2.6 at.% nitrogen in Fe_xNi_yN@C/NC, which is much higher than that of Fe_xNi_yN/NC (~ 0.2 at.%). The elemental quantifications of different N determined from N 1s XPS spectra are summarized in Table 3-1. Three dominant peaks correspond to the graphitic-, pyridinic- and pyrrolic-N, respectively (Figure 3-1g). The percentage of graphitic-N increased from 21.87% to 40.49%, after introducing melamine as the nitrogen source.

Table 3-1. The elemental quantifications of different N.

Types	Graphitic-N (%)	Pyridinic-N (%)	Pyrrolic-N (%)
Fe_xNi_yN/NC	21.87	62.31	15.82
Fe_xNi_yN@C/NC	**40.49**	**40.89**	**18.62**

X-ray absorption spectroscopy (XAS) measurements were performed to further study the electronic structure and bulk composition of the samples. First, a selected sample region of the Fe_xNi_yN@C/NC on a holey carbon film-coated TEM grid was characterized by the scanning transmission X-ray microscopy (STXM) at the Spectromicrosopy (SM) beamline at Canadian Light Source (CLS), for the C, N, and O K-edges, and Fe and Ni L-edges through image stacks. Figure 3-2a-f show the chemical imaging of the Fe_xNi_yN@C/NC sheet derived from the stacks at the C, O, and N K-edges to image the NC substrate, as well as at the Fe and Ni L-edges to image the Fe_xNi_yN nanocrystals, as shown in. Interestingly, the C, N, Fe, and Ni thickness distribution in terms of optical density (od, i.e., linear X-ray absorbance) shows a high correlation between C and N, and a linear relationship between Fe and Ni, implying the Fe:Ni of 2:1 based on their

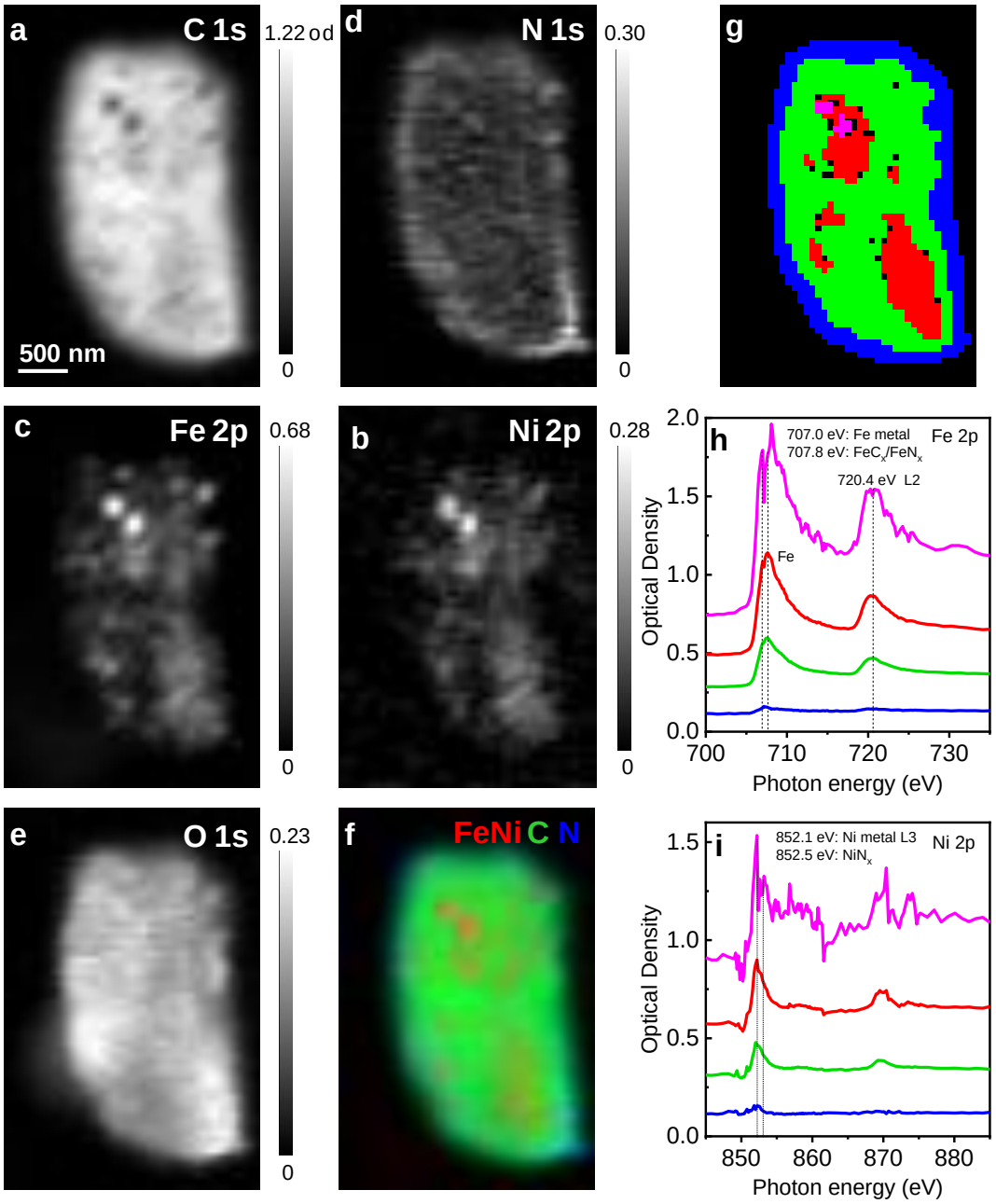

Figure 3-2 STXM chemical imaging and spatially-resolved XANES spectra of a single sheet of Fe_xNi_yN@C/NC, elemental optical density thickness maps derived from the (a) C K-edge, (b) N K-edge, (c) Fe L-edge, (d) Ni L-edge, and (e) O K-edge. (f) The color composite map of a-d, green: C, blue: N, red: Fe/Ni; spatially-resolved STXM-XANES spectra extracted from selected regions on the Fe_xNi_yN@C/NC sheet. (g) The selected regions with green, blue, and red referring to different thickness regions and the pink highlights of hotspots of Fe/Ni. (h) Fe 2p and (i) Ni 2p STXM-XANES spectra of the Fe_xNi_yN@C/NC sheet for the selected regions of interest as shown in (g).

optical density values. This suggests that the nitrogen doping into the carbon substrate is very uniform and the Fe_xNi_yN nanocrystals are implanted inside the NC substrate. Figure 3-2f displays

the color composite image of C 1s, N 1s, Fe 2p, and Ni 2p derived Fe_xNi_yN@C/NC thickness maps. The color image intensity was rescaled in each color channel for a better view of all components. On the NC sheet, except for some obvious spots, there are many blurred bright spots/patches that can be barely resolved by STXM, which are the nanoscaled Fe_xNi_yN nanocrystals grown on the NC sheet. A detailed XANES comparison among different thickness regions of Fe_xNi_yN@C/NC is presented in Figure 3-2h-i at individual elemental edges. The feature at around 707 eV for the Fe L-edge spectra and 852.1 eV for the Ni L-edge spectra are due to metallic Fe and Ni, respectively. Meanwhile, the features at 707.8 eV for the Fe L-edge and 852.5 eV for the Ni L-edge should be due to the formation of FeNi carbides or FeNi nitrides. Moreover, the Fe and Ni K-edge in the Fe_xNi_yN@C/NC, Fe_xNi_yN/NC, Fe_xNi_y/C, Fe_xNi_yO, Fe_xNi_yCH, as well as reference samples (Fe foil, Ni foil, $Fe(NO_3)_3$ and $Ni((NO_3)_2)$ were also characterized by the Soft X-ray micro characterization beamline (SXRMB), as shown in Figure 3-3a,b. The position of the adsorption edge is sensitive to the oxidation state of the transition metals.[191] It could be observed that the position of the Fe and Ni K-edge XANES spectra for the Fe_xNi_yN@C/NC, Fe_xNi_yN/NC, Fe_xNi_y/C, Fe_xNi_yO, Fe foil, and Ni foil are very close, confirming that Fe and Ni in the Fe_xNi_yN@C/NC, Fe_xNi_yN/NC, and Fe_xNi_y/C mainly exist in the forms of metallic Fe and Ni. The Fourier-transformed (FT) k^3-weighted EXAFS data in Figure 3-3c,d also shows the lack of the peak corresponding to Fe/Ni and O/N interaction (around 1.4 and 1.5 Å) in Fe_xNi_yN@C/NC, Fe_xNi_yN/NC, and Fe_xNi_y/C with the simultaneous appearance of the peak for Fe/Ni-Ni/Fe interaction (around 2.2 Å). These results further reveal that Fe and Ni ions in the samples treated by high-temperature annealing were reduced to metallic Fe and Ni. By contrast, the FT-EXAFS of Fe_xNi_yN@C/NC, Fe_xNi_yN/NC unraveled Fe-N/C and Ni-N/C peaks located at about 1.5 Å and 1.4 Å, respectively, suggesting the presence of FeNi nitride.

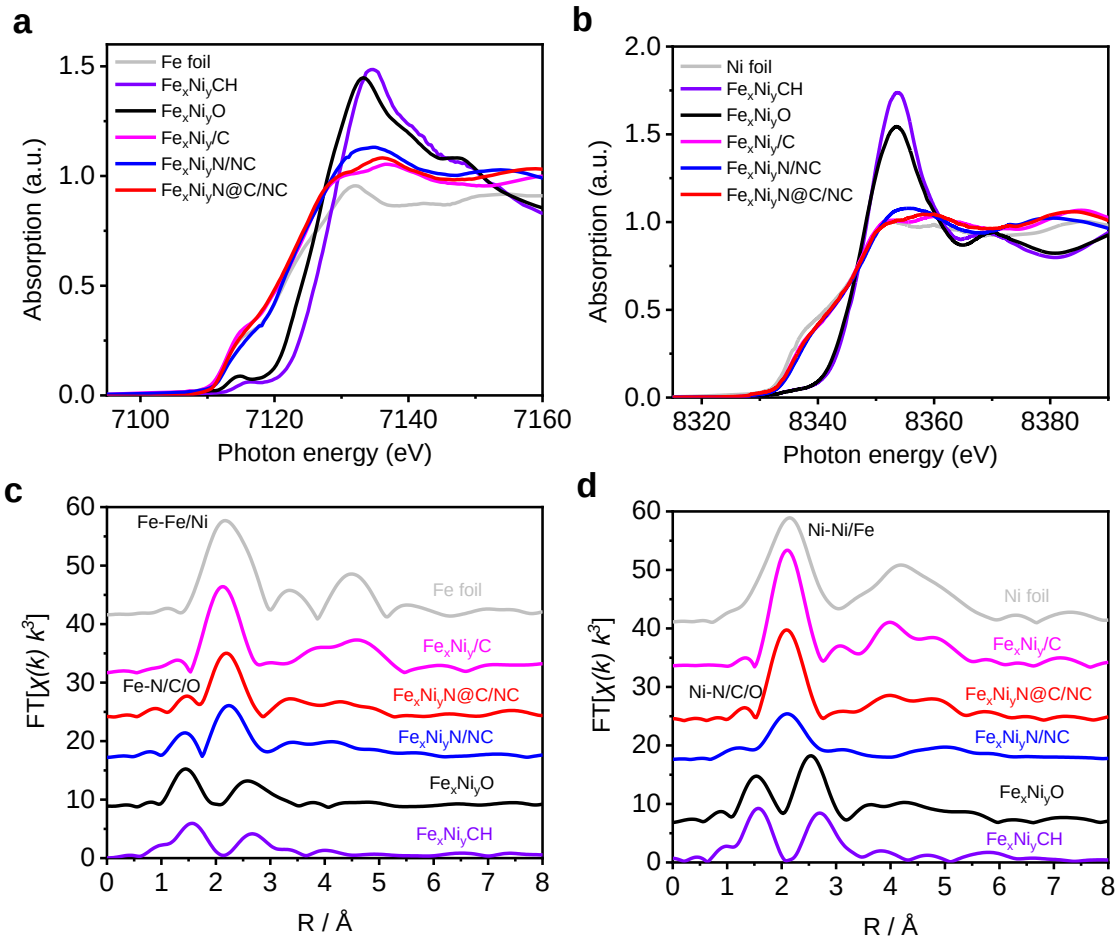

Figure 3-3 The normalized (a) Fe and (b) Ni K-edge XANES spectra of Fe_xNi_yN@C/NC, Fe_xNi_yN/NC, Fe_xNi_y/C, Fe_xNi_yO, and Fe_xNi_yCH. The corresponding Fourier transforms of (c) Fe K-edge and (d) Ni K-edge EXAFS oscillations $k^3\chi(k)$.

The electrocatalytic performances of the samples were evaluated. The ORR activity of the Fe_xNi_yN@C/NC was measured in 1.0 M KOH via the rotating disk electrode (RDE) method. The Fe_xNi_yN@C/NC catalyst shows an $E_{1/2}$ of 0.87 V and an onset potential of 0.98 V, which are much better than those of Fe_xNi_yN/NC, Fe_xNi_y/C, and Fe_xNi_yO (Figure 3-4a). To assess the ORR pathway of Fe_xNi_yN@C/NC, the rotating ring disk electrode (RRDE) measurements were also carried out. The RRDE test revealed that the H_2O_2 yield of Fe_xNi_yN@C/NC remains below 6% in the potential range 0.2-0.9 V, indicating a high electron-transfer number of 3.88-3.99 (Figure 3-4c). These results confirm that Fe_xNi_yN@C/NC undergoes a high-efficiency catalytic process via

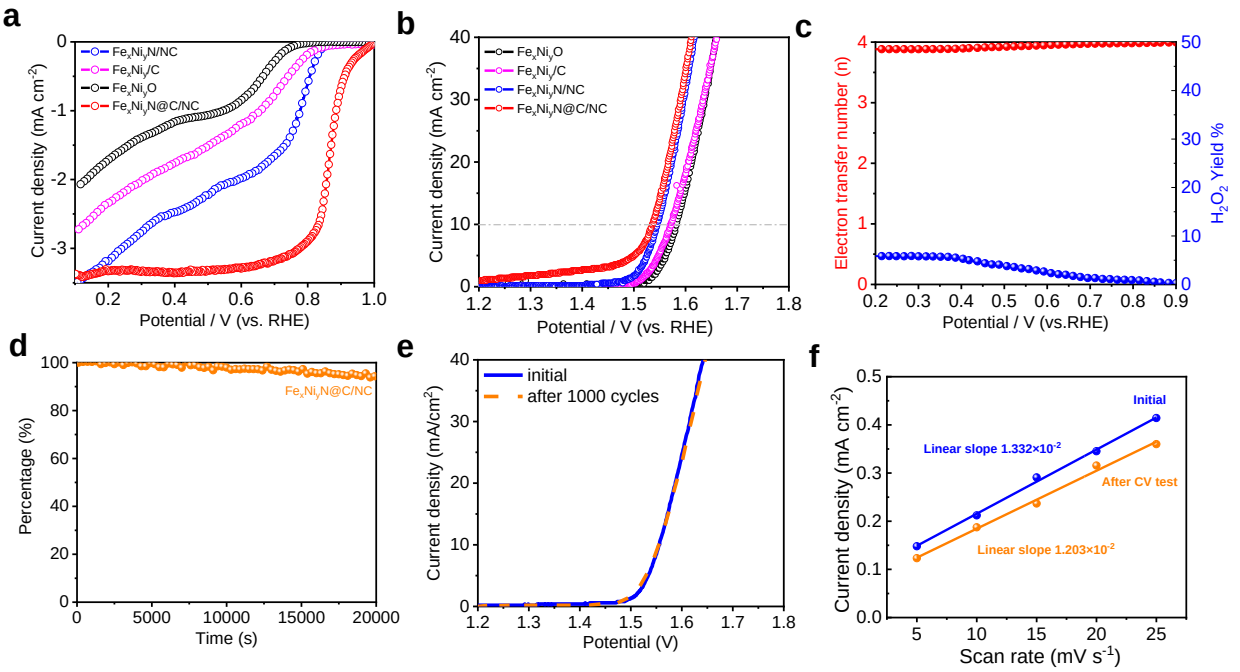

Figure 3-4 (a) ORR and (b) OER polarization plots of Fe_xNi_yN@C/NC, Fe_xNi_yN/NC, Fe_xNi_y/C, and Fe_xNi_yO in O_2-saturated 1.0 M KOH (rotation rate: 1600 rpm). (c) Percentages of H_2O_2 produced and ORR electron transfer numbers catalyzed by Fe_xNi_yN@C/NC in 1.0 M KOH solution. The corresponding electrochemical impedance spectra (EIS) at a three-electrode system. (d) Chronoamperometric responses of Fe_xNi_yN@C/NC at 0.7 V in an O_2-saturated 1.0 M KOH solution. (e) OER of Fe_xNi_yN@C/NC before and after 1000 cycles of CV between 1.3 V and 1.6 V. (f) The capacitive current of Fe_xNi_yN@C/NC before and after the OER process measured at 1.15 V versus RHE as a function of scan rate.

a $4e^-$ ORR pathway. As shown in Figure 3-4d, at a setting potential of 0.8 V, a steady current density was retained with no obvious decay for 20,000 s (94%), which indicates much better ORR stability than Pt/C. The OER performance of the Fe_xNi_yN@C/NC catalyst was further compared with that of the other reference catalysts in a 1.0 M KOH electrolyte. Figure 3-4b shows the OER polarization curves for the Fe_xNi_yN@C/NC, Fe_xNi_yN/NC, Fe_xNi_y/C, and Fe_xNi_yO. Specifically, the Fe_xNi_yN@C/NC shows an overpotential (305 mV) at the current density of 10 mA cm^{-2}, which is lower than that for Fe_xNi_yN/NC (315 mV), Fe_xNi_y/C (341 mV), and Fe_xNi_yO (353 mV). It is noticeable, however, that Fe_xNi_yN@C/NC and Fe_xNi_yN/NC exhibit a significantly enhanced OER activity compared to Fe_xNi_y/C and Fe_xNi_yO, which is mainly due to the formation

of abundant FeNi nitride. It has been reported that metal nitrides show very promising catalytic properties toward OER.[192] Fortunately, the unique structure of small Fe_xNi_yN nanocrystals encapsulated in N-doped carbon layers (Fe_xNi_yN@C/NC) contributes to higher ORR and OER activity than that of Fe_xNi_yN/NC. Due to the strong electrical coupling effect, this unique architecture could provide a direct electron transfer pathway, and then improve the kinetics of the electrochemical oxygen reactions. Consequently, Fe_xNi_yN@C/NC exhibited an outstanding overall electrode activity, reflected by a lower value ($\triangle E$ = 0.67 V) of the difference between the ORR and OER metrics ($\triangle E = E_{j=10} - E_{1/2}$). Moreover, the accelerated durability test reveals that Fe_xNi_yN@C/NC demonstrates outstanding stability with nearly no change in $E_{j=10}$ after 1,000 cycles (Figure 3-4e). The direct nucleation, growth, and anchoring of Fe_xNi_yN nanocrystals on the NC with N-rich active sites could afford strong chemical attachment and electrical coupling between the nanocrystals and carbon substrate, leading to improved activity and durability for the ORR and OER.

The high oxidation condition required for the OER process (charging process) in a Zn-air battery inevitably would result in structural changes in the carbon-based materials. Therefore, minimizing the influence of the high oxidation condition on the carbon-based hybrid materials (e.g., carbon corrosion, metal compounds oxidation, and hydroxylation) will significantly improve the life span, energy efficiency, and output power density of the Zn-air battery. To characterize and observe the structural changes of Fe_xNi_yN@C/NC in the discharge/charge (ORR/OER) process, the continuous cyclic voltammetry (CV) test was performed in a large potential window ranging from about 0.0 to 1.54 V versus RHE (1.0M KOH solution) (Figure 3-5). After 100 cycles of CV scans, there was a negative shift in the ORR peak potential, which could be attributed to the change of the high electrochemically active surface area (ECSA) after suffering from high oxidation conditions. It is reported that the electronic properties of the

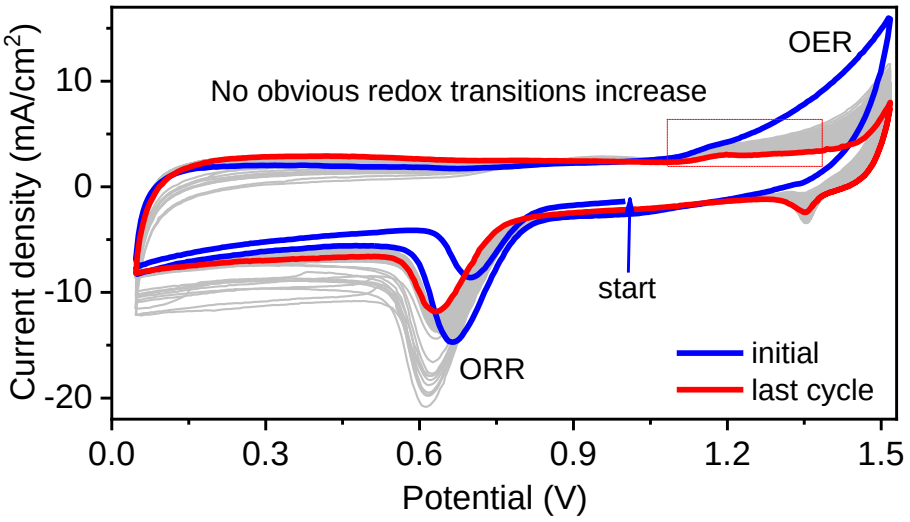

Figure 3-5 CV curves (100 cycles) of Fe_xNi_yN@C/NC with wide potential window (0.05 V-1.5 V versus RHE at 50 mV s^{-1}).

graphitic-shell could be modified by metallic cores, which prevent their exfoliation under continuous high oxidation conditions.[189] The double-layer capacitance (C_{dl}) proportional to ECSA was determined by measuring the CV curves at different scan rates before and after the CV test. As shown in Figure 3-4f, there is only a slight drop of C_{dl} after 1000 cycles, suggesting nearly 90% of the initial ECSA remains. To further investigate the impact of the harsh electrochemical conditions, electrochemical impedance spectra (EIS) analyses were performed in the half-cell to determine the kinetic change of the electrode reactions. After the OER process (1.0 V-2.0 V vs RHE at a scan rate of 5 mV s^{-1}), there was very little change in electrochemical impedance Z (Figure 3-6a). Furthermore, Fe K-edge EXAFS and N K-edge XAS were carried out to investigate the electronic structure of FeNi alloy/nitride nanocrystals and C-N active sites, respectively. The Fe K-edge EXAFS spectra show a slightly positive shift after the OER process (Figure 3-6b), which might be ascribed to the oxidation of the few metallic nanocrystals without the graphitic shell. As shown in Figure 3-6c, there was no obvious change to the Fe bonding

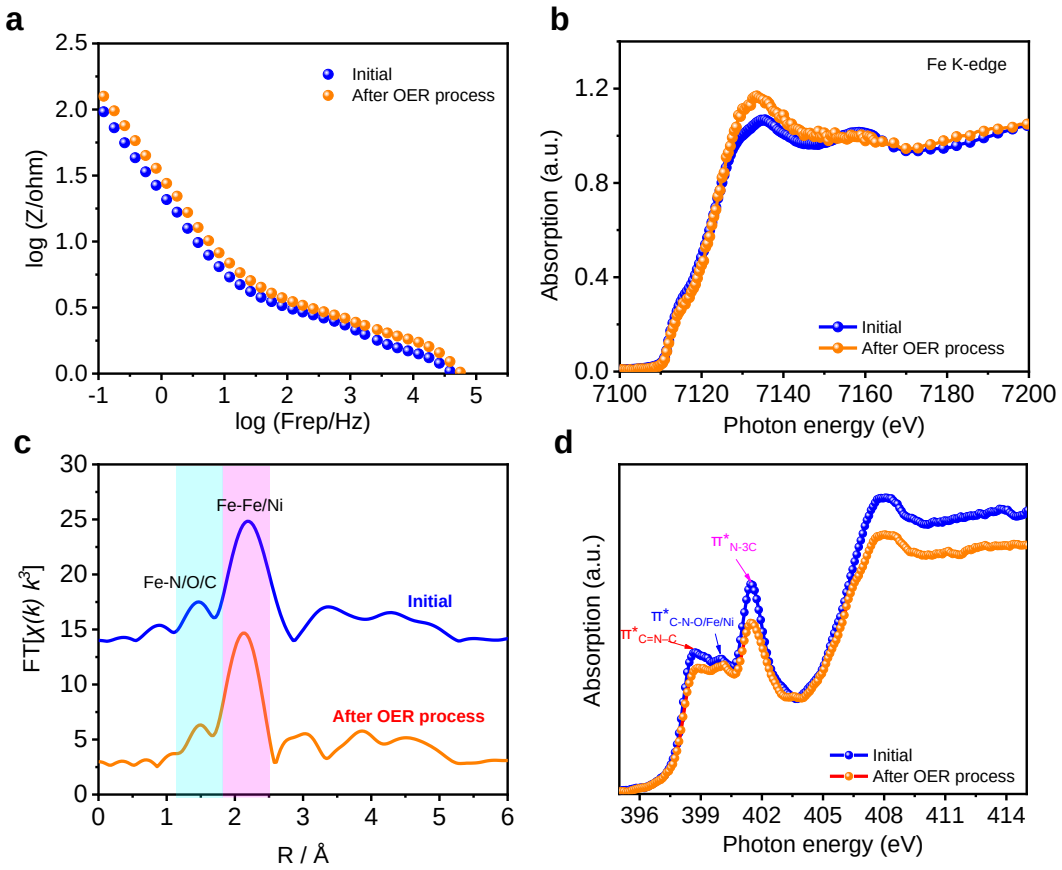

Figure 3-6 (a) Electrochemical impedance spectra (EIS) at a three-electrode system of Fe_xNi_yN@C/NC before and after the OER process. (b) The normalized Fe K-edge XANES spectra of Fe_xNi_yN@C/NC before and after the OER process. (c) The Fourier transforms of Fe K-edge EXAFS oscillations $k^3\chi(k)$ of Fe_xNi_yN@C/NC before and after the OER process (k-weight: 3). (d) The N K-edge XAS spectra of Fe_xNi_yN@C/NC before and after the OER process.

environment after the OER measurement as evidenced by the Fourier transforms of Fe K-edge EXAFS oscillations $k^3\chi(k)$ of Fe_xNi_yN@C/NC, further indicating that the Fe_xNi_yN nanocrystals with graphitic-shell encapsulation are being protected during the OER process. In addition, the N K-edge XANES curves of Fe_xNi_yN@C/NC before and after the OER measurement present a similar feature (Figure 3-6d). XAS spectra show four main characteristic peaks at 398.6, 400.1, 401.47, and 405~412 eV, which correspond to the pyridinic-N ($\pi^*_{C=N-C}$), pyrrolic-N ($\pi^*_{C-N-O/Fe/Ni}$) graphitic-N (π^*_{N-3C}) and 1s-σ_{N-C} transition, respectively.[193] Compared to the initial N K-edge XANES curve, there is a slightly reduced peak area for the sample after the OER measurement,

especially for the $\pi^*_{C=N-C}$ and $\pi^*_{N-C,}$ suggesting that the number of C=N bonds was reduced, which could result in the ORR activity loss.

Finally, the liquid rechargeable Zn-air battery devices were assembled using a gas diffusion layer dropped with Fe_xNi_yN@C/NC as the air electrode. Figure 3-7a shows a schematic illustration of the liquid Zn-air battery. Figure 3-7b displays discharge and charge polarization curves of the rechargeable Zn-air battery using the Fe_xNi_yN@C/NC catalyst as the air electrode. It reveals that the Fe_xNi_yN@C/NC exhibited a smaller voltage gap between charge and discharge than that reported for Pt/C+RuO_2, which means higher energy efficiency and better rechargeable ability.[194] The discharge-charge voltage gap at 60 mA cm^{-2} is only 0.93 V, contributing to energy efficiency of 54.0%. In addition, the peak power density could be as high as ~350 mW cm^{-2}, which is much higher than that of Pt/C (250 mW cm^{-2})[121], and also much superior to those reported for Zn-air primary batteries[60, 195-197]. Moreover, the excellent rechargeability of the Fe_xNi_yN@C/NC was demonstrated by more than 400 discharge/charge cycles over 400 h (Figure 3-7c). After more than 400 cycles, the final discharge-charge voltage gap is only 0.80 V, which remains nearly unchanged. We further demonstrated its potential application in a quasi-solid-state Zn-air battery, which was fabricated using the Fe_xNi_yN@C/NC catalyst coated carbon cloth as the air electrode, a flexible Zn plate as the anode, and a glass microfiber membrane wetted by electrolyte. A schematic illustration of the quasi-solid-state Zn-air battery with Fe_xNi_yN@C/NC catalyst is demonstrated in Figure 3-7d inset. To examine the stability of the assembled rechargeable battery, it was cycled at a current density of 2.0 mA cm^{-2} with each cycle lasting 20 min. As shown in Figure 3-7d, the initial discharge-charge voltage gap is about 0.85 V. After 60 cycles (20 h of operation time), the battery exhibited a slight increase for the charge and discharge overpotential due to the desiccation of the membrane. After wetting the membrane again, the charge and discharge performance almost returned to their original positions. These

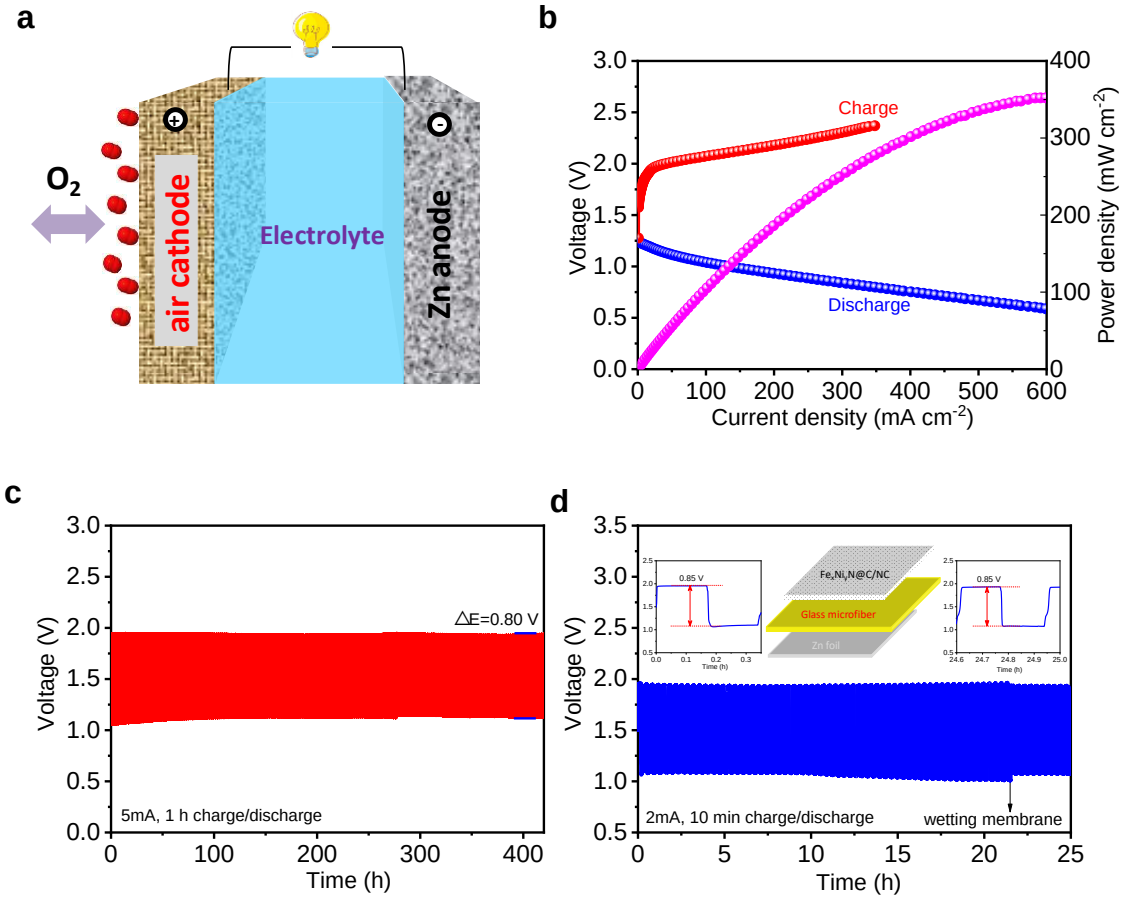

Figure 3-7 (a) Schematic illustration of the liquid Zn-air battery configuration. (b) Discharge and charge polarization curves of Fe_xNi_yN@C/NC catalyst and the corresponding power density plot of the liquid Zn-air battery. Galvanostatic discharge and charge cycling stability of Fe_xNi_yN@C/NC in (c) liquid and (d) quasi-solid-state Zn-air battery.

results indicate the potential application of the Fe_xNi_yN@C/NC catalyst for the quasi-solid-state Zn-air battery.

3.4 Conclusions

In summary, a facile template-free approach was developed to fabricate the graphitic-shell encapsulated FeNi alloy/nitride nanocrystals and biomass-derived N-doped porous carbon (Fe_xNi_yN@C/NC) hybrid composite. The porous architecture can provide abundant accessible

active sites and improved mass transfer. Benefitting from the strong catalyst-support interactions between the graphite-coated Fe_xNi_yN nanocrystals and the N-doped porous carbon, the hybrid material (Fe_xNi_yN@C/NC) can take full advantage of the unique structures to promote the electrocatalytic reaction kinetics and stability for both ORR and OER. The XAS analysis showed that there is almost no change in the bulk structure of the Fe_xNi_yN nanocrystals after suffering the harsh OER electrochemical corrosion process. When integrated into an air electrode for the rechargeable Zn-air batteries, the hybrid catalyst demonstrated excellent high stability over 400 h at 5.0 mA cm^{-2}. These findings pave a new way of designing highly efficient bifunctional electrocatalysts, via a simple and low-cost method, for metal-air batteries and beyond.

Chapter 4 Self-reconstruction of Co/Co_2P Heterojunctions Confined in N-doped Carbon Nanotubes for Zinc-air Flow Batteries

4.1 Introduction

Rechargeable metal-air batteries are among the most promising energy storage systems benefiting from their high theoretical energy density and sustainable energy conversion.[1] Oxygen evolution reaction (OER) and oxygen reduction reaction (ORR) are the two essential electrochemical reactions in rechargeable metal-air batteries.[2] Platinum (Pt)-based catalysts are highly efficient for ORR, and Ru/Ir-based catalysts are highly active toward the OER process.[3] However, these precious metal catalysts are severely limited by their scarcity and high cost, which make it imperative to develop low-cost and high-performance bifunctional catalysts for rechargeable metal-air batteries.[4]

Improving bifunctional ORR and OER catalytic activity and accelerating their kinetics on the electrode is highly desired to achieve high-performance rechargeable zinc-air batteries. To this end, some non-precious metal catalysts can effectively catalyze the ORR and OER processes, respectively. Among them, promising bifunctional electrocatalytic activity has been achieved using the transition metal-based nanomaterials strongly coupled with heteroatom-doped carbon materials.[5] So far, synthesizing highly active electrocatalysts for rechargeable zinc-air batteries remains crucial, but meanwhile, more effort should be devoted to tracking the structural evolution during electrocatalytic operation and understanding their dynamic active state generation.[6] A deeper understanding of the properties determining activity and stability and the exploration of real-time active sites under operational conditions are essential to developing high-performance rechargeable zinc-air battery electrocatalysts. Most transition metal-based nanomaterials as

highly active OER pre-catalysts in alkaline electrolytes undergo slow and incomplete self-reconstructions on the surface.[7] In situ generated (oxy)hydroxides during OER are usually regarded as real active sites for the OER.[8] Therefore, the rational design of pre-catalysts that can deeply generate active OER species is highly desirable. In addition, under the OER process with high potential, most carbon materials easily suffer from serious carbon corrosion issues, which inevitably result in the sharp decline of discharge performance.[9] Recently, Li et al. developed a catalyst with atomic iron sites supported on a hollow carbon.[10] Although the obtained catalyst exhibited high ORR activity in alkaline media, the discharge potential at 5 mA cm^{-2} is only 1.1 V caused by the poor corrosion resistance under high oxidation conditions. Usually, improving the graphitization extents of carbon substrates by high-temperature treatment is expected to effectively enhance the carbon corrosion resistance, thus contributing to improved durability for both ORR and OER.[5, 11]

Herein, we report a facile strategy to synthesize diphasic metal/metal phosphide nanoparticles encapsulated in the bamboo-shape N-doped CNTs (M/M_2P@NCNTs). Among them, the unique heterojunction structure of the Co/Co_2P greatly induces the construction of highly ordered NCNTs with rich pyridinic-N and graphitic-N active sites. This straightforward strategy is a valid measure to avoid the destruction of ORR active sites due to the high potential oxidation conditions required for the OER process. Typically, the Co/Co_2P@NCNTs ($E_{1/2}$=0.90 V) exhibited high ORR activity with a half-wave potential ($E_{1/2}$) of 0.87 V after suffering a high potential oxidation condition. To our knowledge, this is record-level among previously reported ORR catalysts. Meanwhile, deep self-reconstruction of heterojunction Co/Co_2P confined in NCNTs shows increasing OER performance owing to the dynamic active state generation of plentiful $CoO_x(OH)_y$ active species, which is different from previously reported structural

transformation that appeared only in the surface of cobalt oxides.[8] Benefiting from the optimized N active sites of the NCNT with high oxidation potentials resistance and the transformation from the heterojunction Co/Co_2P into Co^{3+} Oh-containing $CoO_x(OH)_y$ active species, the Co/Co_2P@NCNTs can be used as a highly active bifunctional pre-catalyst for rechargeable zinc-air flow batteries. The assembled battery with the developed catalyst displays high cell efficiency with an unprecedented cycle life of 1000 h in an ambient environment, demonstrating its promising application in metal-air batteries.

4.2 Experimental Section

4.2.1 Synthesis of catalysts

For the Co/Co_2P@NCNTs synthesis, 0.25 g $Co(NO_3)_2{\cdot}6H_2O$, 0.5 g triphenylphosphine (TPP), and 1.5 g melamine were mixed uniformly using a ball-milling treatment for 20 min. Then, the mixture was heated up to 900 °C under Ar flow and maintained for 1 h to obtain the gram-scale Co/Co_2P@NCNTs. The phase of formed Co_2P acts as the catalyst for NCNTs growth during the heat treatment process. The Fe/Fe_2P@NCNTs and Ni/Ni_2P@NCNTs were synthesized following a similar procedure with the use of different metal salts including ($Fe(NO_3)_2{\cdot}6H_2O$ for Fe/Fe_2P@NCNTs and $Ni(NO_3)_2{\cdot}6H_2O$ for the Ni/Ni_2P@NCNTs). The Co@NCNTs were also synthesized following the same procedure used for the Co/Co_2P@NCNTs synthesis aside from not using triphenylphosphine. The N,P-C was synthesized following the same procedure used for the Co/Co_2P@NCNTs synthesis with the $Zn(NO_3)_2{\cdot}6H_2O$ as the metal source instead.

4.2.2 Electrochemical measurements and Fabrication of zinc-air flow battery

The ORR and OER performances of the as-prepared catalysts were measured on an electrochemical workstation (Pine, Model PGSTAT-72637) and a rotating ring disk electrode

apparatus (RRDE-3A, ALS) in a three-electrode cell by using a platinum wire as the counter electrode and Hg/HgO (KOH, (20%)) as the reference electrode. The working electrode was a rotating ring/disk electrode with a glass carbon disk (0.2475 cm^2 in area). To prepare the catalyst slurry, 2.0 mg of electrocatalyst was dispersed in 0.2 mL isopropanol and 0.01 mL Nafion solution (5.0 wt%, Sigma Aldrich) and ultrasonicated for 60 min. 0.02 mL of the ink was dropped onto the glassy carbon electrode to give a catalyst loading of 0.8 ug cm^{-2} and was dried in air. In this paper, all potentials were converted to a reversible hydrogen electrode (RHE). To subtract the background capacitive current, linear sweep voltammetry was conducted under the same conditions in an N_2-saturated electrolyte. For the battery, stainless steel meshes were used as both current collector and support for the air cathodes. The Co/Co_2P@NCNTs catalyst was used as the bifunctional electroactive material to fabricate the air cathode. Homogeneous catalyst ink consisting of Co/Co_2P@NCNTs catalyst, binder (Nafion solution, 5 wt%), and isopropanol was dropped onto the stainless steel meshes with a catalyst loading of 0.5 mg cm^{-2}. The air cathode was then paired with a Zn plate anode and assembled in a battery prototype. The electrolyte was composed of 6.0 M KOH and 0.20 M $Zn(CH_3COO)_2$, and continuously pumped to the battery.

4.2.3 Material characterizations

The morphology of the as-prepared M/M_2P@NCNTs was observed by a scanning electron microscope (SEM, Quanta 450 ESEM, FEI) and a transmission electron microscope (HRTEM, JEM-2100). The surface properties were analyzed by X-ray photoelectron spectroscopy (XPS, VG ESCALAB 220i-XL) equipped with a hemispherical analyzer for a Twin Anode X-ray Source. The crystal structure of the catalysts was analyzed by X-ray diffraction (XRD) (40 kV, 25 mA, Cu Kα radiation, λ=1.5418 Å). Raman spectroscopy (Renishaw Imaging Microscope Wire™) was performed using the 785 nm laser radiation with circular polarization. The X-ray absorption

spectroscopy (XAS) measurements were performed at the Canadian Light Source (CLS) located at the University of Saskatchewan with a 2.9 GeV third-generation synchrotron source. The Co K-edge X-ray absorption near-edge structure (XANES) and Extended X-ray Absorption Fine Structure (EXAFS) were collected on the 06ID-1 Hard X-ray MicroAnalysis (HXMA) beamline. The experiment was performed in fluorescence mode by using a Canberra 32 Ge germanium array detector.[198] The P K-edge XAS was collected on the soft X-ray micro characterization beamline (SXRMB) beamline. The powder samples were spread onto double-sided conducting carbon tape. The XANES at the N and O K-edge were obtained at the spherical grating monochromator (SGM) beamline 11ID-1 with an energy resolution of $E/\Delta E \geq 5000$. The fine powder of obtained catalysts and reference materials were spread on double-sided carbon tape on a Cu sample holder.

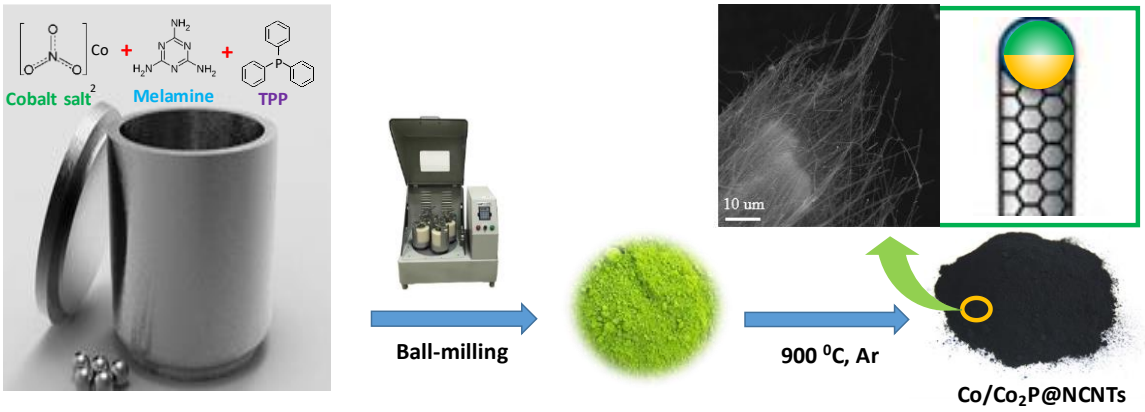

Figure 4-1 Schematic procedure of synthesizing the gram-scale Co/Co_2P@NCNTs.

4.3 Results and discussion

The preparation process of the M/M_2P@NCNTs is shown in Figure 4-1. Briefly, the melamine acts as the source of both nitrogen and carbon for the growth of the N-doped carbon nanotubes (NCNTs). The triphenylphosphine provides the phosphorus source for the synthesis of

phase M_2P. During the growth of NCNTs process for the Co/Co_2P@NCNTs, the Co nanoparticles located at the edge or the tip are easier to transform into Co_2P, and the Co nanoparticles located in the central section of NCNTs are difficult to be phosphatized, thus forming the biphasic structure of Co/Co_2P heterojunction.[12] Then, the formed heterojunction M/M_2P directly catalyzes the growth of highly ordered NCNTs. During the heat treatment process, the gram-scale Co/Co_2P@NCNTs is obtained at 900 °C along with the g-C_3N_4 intermediate that is obtained at 550 °C.[13] For the NCNT formation mechanism, firstly, generating surface carbide by thermal decomposition of melamine and then dissolving in the surface of the metal nanoparticles. Subsequently, carbon will reach oversaturation, and then forms a semi-fullerene cap. Finally, the continuous supply of carbon to the catalyst particles facilitates the growth of nanotubes.[14] The type of nitrogen active sites of the NCNTs are determined by the metal catalyst particle. The growth of the NCNTs encapsulating diphasic M/M_2P nanocrystals was demonstrated by scanning electron microscopy (SEM) for the M/M_2P@NCNTs (Figure 4-2a). The bright-field and dark-field high-resolution transmission electron microscopy (HRTEM) images illustrate diphasic Co/Co_2P nanocrystal and orderly NCNTs in the Co/Co_2P@NCNTs (~150 nm in diameter, Figure 4-2b). The construction of the highly ordered NCNTs is induced by the unique heterojunction structure of the Co/Co_2P. Moreover, HRTEM images show that the surface of Co_2P phases are coated tightly with NCNTs layer with high crystallinity (thickness: 2.8 nm), and the lattice fringe of 0.34 nm corresponds to the (002) lattice plane of graphitic carbon (Figure 4-2c). Figure 4-3 shows Raman spectra of the Co/Co_2P@NCNTs and N,P-C. The intensity ratio of the ID/IG peaks of the Co/Co_2P@NCNTs and N,P-C reveal their degree of graphitization and was calculated to be 1.62 and 1.91, respectively. The ratio decreases significantly for the Co/Co_2P@NCNTs, which further indicates the great improvement of the degree of graphitization.[15] Generally, the changes in the carbon lattice structures and morphologies under high oxidation potentials can significantly

increase charge- and mass-transport resistances. The relatively high degree of graphitization is vital to enhance the corrosion resistance of the carbon under high oxidation potentials.[16]

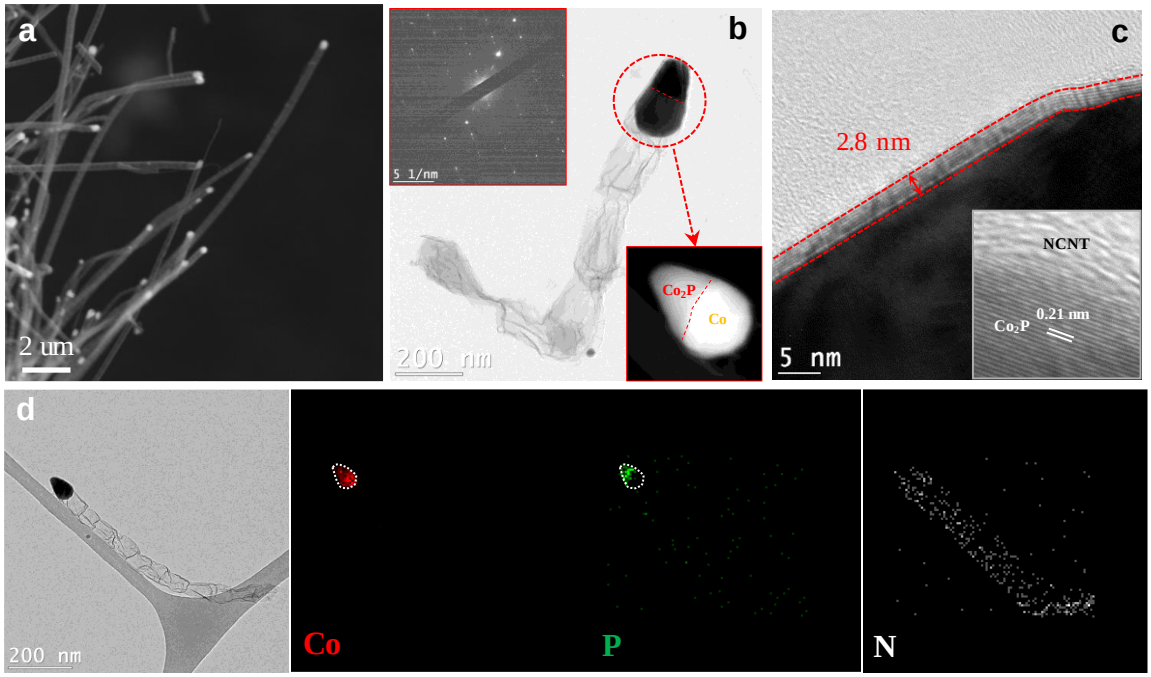

Figure 4-2 (a) SEM image of Co/Co_2P@NCNTs. (b, c) TEM images of the Co/Co_2P@NCNTs. (d) TEM image of the Co/Co_2P@NCNTs and the elemental mapping of Co, P, and N.

The insets of Figure 4-2b, c showed the crystalline structure of the Co/Co_2P nanocrystals, consistent with X-ray diffraction (XRD) results (Figure 4-4a). The spatial distribution of N, P, and Co atoms in CNT was further identified by energy-dispersive X-ray spectrometry (EDX) mappings. As shown in Figure 4-2e, nitrogen atoms overlap well with CNT, suggesting the uniform nitrogen distribution in the bamboo-like NCNT. The P only disperses on the tip of the nanocrystals, but Co disperses in the entire architecture of the nanocrystals, further demonstrating the unique structure of the diphasic Co/Co_2P nanocrystals confined in the NCNTs. In addition, a high nitrogen concentration of 5.12 at.% of NCNTs was measured by X-ray photoelectron spectroscopy (XPS), which is much higher than that of the Co@NCNTs (2.36 at.%) (Table 4-1). The contents of oxygen further decrease from 5.1 at.% (Co@NCNTs) to 3.49 at.%

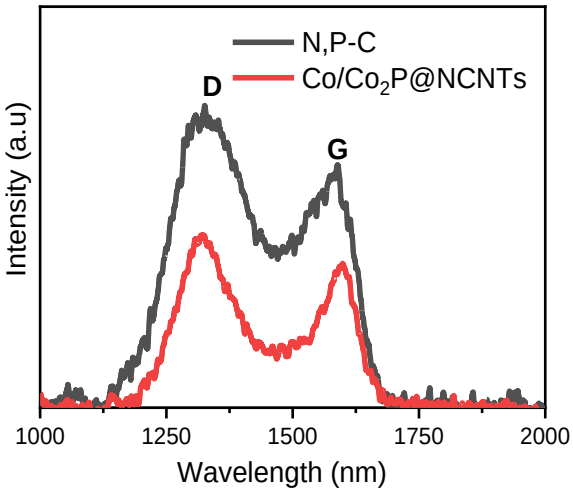

Figure 4-3 Raman spectra of N,P-C and Co/Co_2P@NCNTs. A distinguished D band peak of Raman spectra appears near 1350 cm^{-1} which indicates the presence of defects, disordered or amorphous carbon. A pronounced G band peak (at 1580 cm^{-1}) originating from the graphitic nature of the NCNTs is also displayed.

(Co/Co_2P@NCNTs). The high-resolution XPS spectra of the N 1s region reveal four types of nitrogen environments in the Co@NCNTs and N,P-C (Figure 4-4b), namely, pyridinic-N, pyrrolic-N, graphitic-N, and oxidized N. The percentage of graphitic-N of the Co/Co_2P@NCNTs increases by about 152% and 30% compared with the N,P-C and Co@NCNTs, respectively, likely due to the improvement of graphitization extents of carbon materials (Table 4-1). Meanwhile, the formation of inactive species of pyrrolic-N is inhibited effectively. The high percentage of the graphitic-N and larger diameter of CNTs of the Co/Co_2P@NCNTs with rich active sites can greatly promote catalytic reaction kinetics, mass transport efficiency, and catalyst stability. For the N,P-C, the P 2p XPS spectrum (Figure 4-4c) shows one broad peak with binding energies at 132.6 eV corresponding to the P-C bond.[17] However, the Co/Co_2P@NCNTs only shows one peak at around 129.5 eV which is attributed to Co-P,[18] and the absence of the P-C peak indicates that the NCNTs only contains N atoms in the carbonaceous framework.

Table 4-1: Percentage content of four types of N relative to total N.

Samples	Graphitic-N (%)	Pyridinic-N (%)	Pyrrolic-N (%)	Oxidized N (%)
N,P-C	15.71	73.7	7.77	2.82
Co@NCNTs	30.59	55.71	4.54	9.16
Co/Co_2P@NCNTs	**39.57**	**48.02**	**0**	**12.41**

X-ray absorption near-edge structure (XANES) and extended X-ray absorption fine structure (EXAFS) spectra were performed to further probe the bonding configuration and electronic structure of the Co atoms in the Co/Co_2P@NCNTs (Figure 4-4d-e). Moreover, the Co XANES spectra of the Co/Co_2P@NCNTs and Co@NCNTs closely resemble the spectra collected from the Co reference foil, indicating that Co exists in the form of metallic species in both Co/Co_2P@NCNTs and Co@NCNTs (Figure 4-4d). This difference was further confirmed by the corresponding magnitude of Fourier transform (FT) k^3-weighted EXAFS spectra (Figure 4-4e). The Co@NCNTs and Co foil show one strong peak at 2.17 Å, corresponding to the Co-Co coordination shells. Moreover, much lower intensity and broadened full width at half maximum (FWHM) of the Co-Co peak for Co/Co_2P@NCNTs was observed, which is due to the unique heterojunction structure of the well-dispersed Co/Co_2P nanoparticles. The normalized P K-edge XANES spectra of the Fe/Fe_2P@NCNTs, Co/Co_2P@NCNTs, and Ni/Ni_2P@NCNTs all exhibit a strong peak at 2144 eV, which mainly arises from P atoms and metal atoms (Figure 4-4f). Notably, the peak at 2152 eV observed in the curve of the N,P-C (corresponded to the P-C bond)[17] disappears in the Fe/Fe_2P@NCNTs, Co/Co_2P@NCNTs, and Ni/Ni_2P@NCNTs, indicating that the phosphorus elements are not doped in the NCNTs skeleton. This result agrees well with the XPS and EDS results.

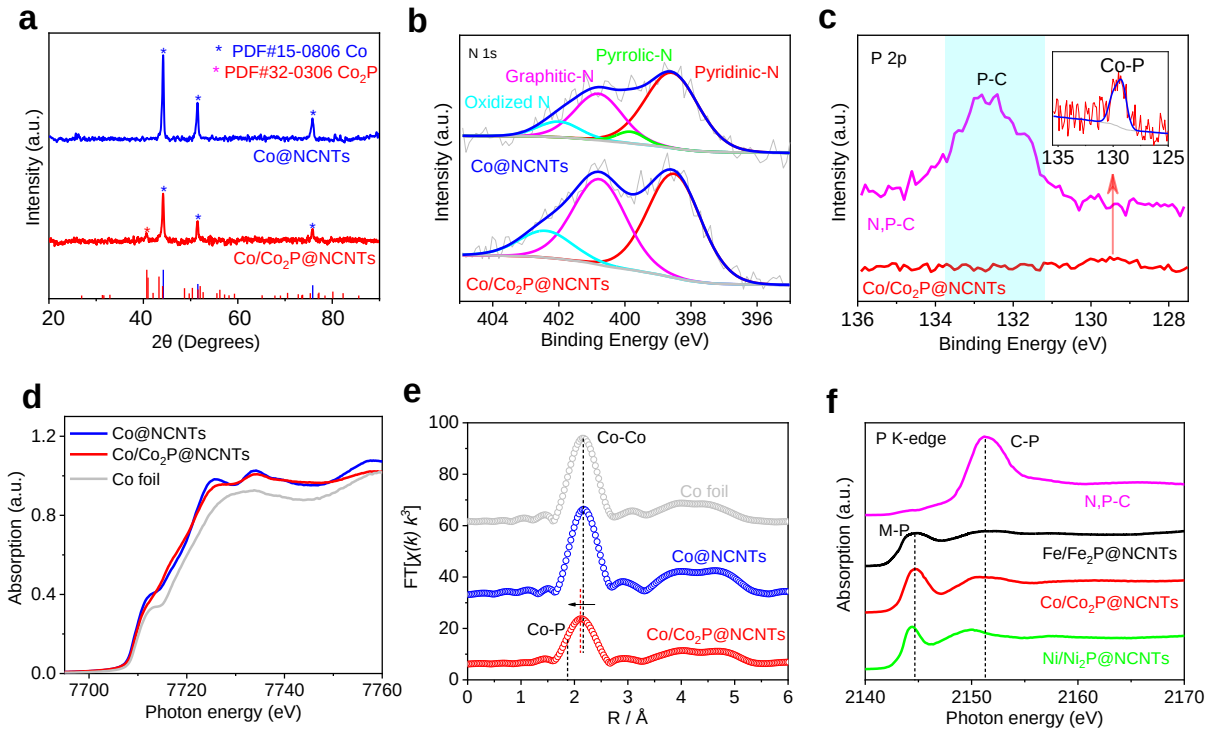

Figure 4-4 (a) The XRD spectra of the Co/Co_2P@NCNTs and Co@NCNTs. (b) High-resolution XPS of N 1s of the Co@NCNTs and Co/Co_2P@NCNTs. (c) High-resolution XPS of P 2p of the Co/Co_2P@NCNTs and N,P-C. (d) The normalized Co K-edge XANES spectra of the Co/Co_2P@NCNTs, Co@NCNTs, and the standard Co foil. (e) The magnitude of Fourier transforms of Co K-edge EXAFS oscillations $k^3\chi(k)$. (f) The normalized P K-edge XAS spectra of the M/M_2P@NCNTs (M= Co, Ni, Fe) and N,P-C.

The analyses above indicate that the Co/Co_2P@NCNTs maintain a high crystallinity of the NCNTs with rich active sites and a unique bamboo-like wrinkling structure. These features enable the Co/Co_2P@NCNTs as an ideal bifunctional catalyst for ORR and OER. The ORR and OER properties were evaluated by steady-state linear sweep voltammetry (LSV) on a rotating disk electrode (RDE) in 1.0 M KOH (Figure 4-5). For comparison, the Fe/Fe_2P@NCNTs, Co/Co_2P@NCNTs, Ni/Ni_2P@NCNTs, and N,P-C were measured to evaluate the importance of metal effects (Figure 4-5a). It has been reported that the different metal salts not only affect the structure but also have a great influence on the chemical state of N in the carbon materials.[19] This

as-prepared N,P-C material with a large amount of pyridinic-N exhibits relatively poor ORR activity, indicating that the activity of the M/M_2P@NCNTs catalysts is largely ascribed to graphitic-N sites rather than pyridinic-N and pyrrolic-N sites. Their activities follow the trend graphitic-N > pyridinic-N > pyrrolic-N, which is consistent with the results reported in the literature.[20] Moreover, the Co/Co_2P@NCNTs exhibits the highest ORR activity ($E_{1/2}$ = 0.90 V vs RHE). The rotating ring disk electrode (RRDE) test demonstrates that the H_2O_2 yield of the Co/Co_2P@NCNTs remains below 15% in the potential range 0.2-0.9 V, achieving a high electron-transfer number of 3.8-4.0 (Figure 4-5c). The outstanding ORR kinetics of the Co/Co_2P@NCNTs was further reflected by the small Tafel slope of 48.6 mV dec^{-1} (Figure 4-5b). Fe/Fe_2P@NCNTs exhibited comparable ORR activity with the Co/Co_2P@NCNTs in terms of onset potential (0.98 V vs RHE). However, its diffusion-controlled and the mixed kinetic-diffusion-controlled regions were limited compared with that of the Co/Co_2P@NCNTs. It confirms that Co/Co_2P@NCNTs shows faster reaction kinetics and higher mass transport efficiency for the ORR. Furthermore, the Co/Co_2P@NCNTs has shown superior ORR ($E_{1/2}$ = 0.90 V vs RHE) and OER ($E_{j=10}$ = 1.58 V vs RHE) activities than those of the Co@NCNTs ($E_{1/2}$ = 0.85 V vs RHE, $E_{j=10}$ = 1.62 V vs RHE) (Figure 4-5d). It indicates that the presence of rich graphitic-N/pyridinic-N active sites and Co/Co_2P active sites in the Co/Co_2P@NCNTs can greatly promote catalytic activity.

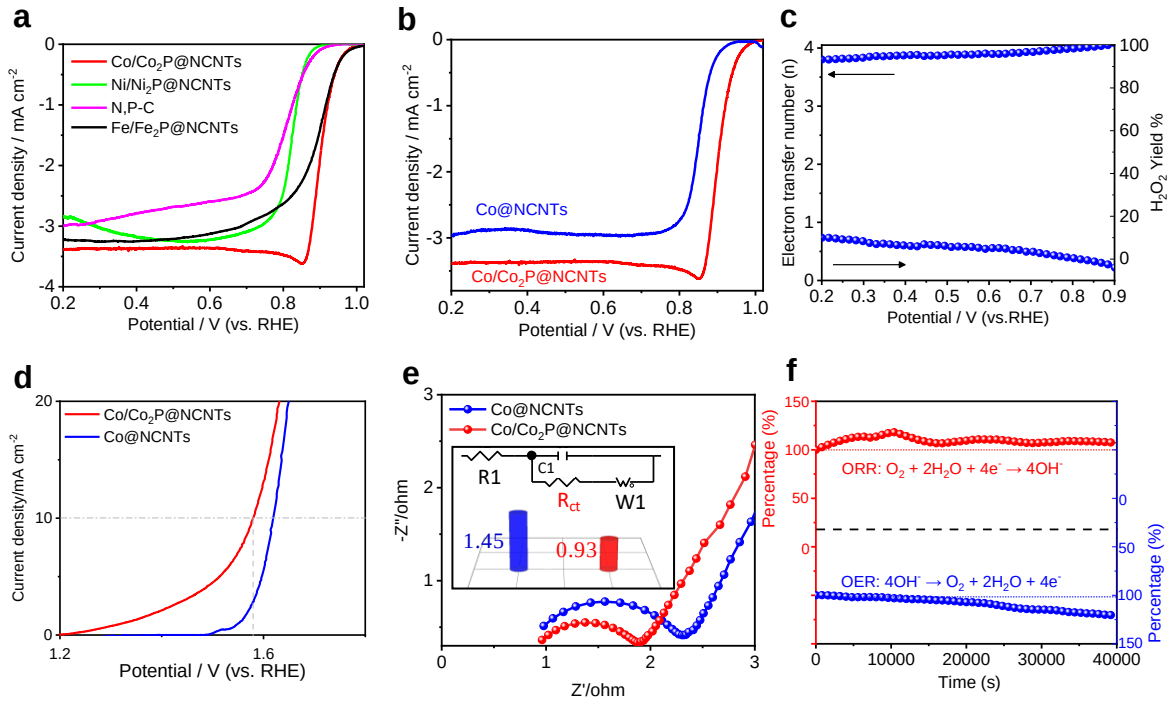

Figure 4-5 (a) ORR polarization plots of the M/M_2P@NCNTs (M= Co, Ni, Fe) and the N,P-C (rotation rate: 1600 rpm) in O_2-saturated 1.0 M KOH solution. (b) ORR polarization plots of the Co/Co_2P@NCNTs and the Co@NCNTs. (c) Percentages of H_2O_2 produced and ORR electron transfer numbers catalyzed by the Co/Co_2P@NCNTs before and after the OER process in 1.0 M KOH solution. (d) OER polarization plots of the Co/Co_2P@NCNTs and the Co@NCNTs (inset). (e) The electrochemical impedance spectra (EIS) are based on a three-electrode system. The inset of (e) is the value of the Faradaic charge-transfer resistance (R_{ct}) and the simulated equivalent circuit. (f) Chronoamperometric responses of the Co/Co_2P@NCNTs at 0.7 V for ORR and 1.7 V for OER.

The high performance is also illustrated by electrochemical impedance spectroscopy (EIS) in Figure 4-5e. The EIS curve can be well fitted using a typical equivalent electrical circuit (the inset of Figure 4-5e), where the Co/Co_2P@NCNTs exhibits a smaller Faradaic charge-transfer resistance (R_{ct}) (0.93 Ω) than Co@NCNTs (1.45 Ω), demonstrating a higher charge transfer efficiency benefitting from the rich active sites and unique structure. Chronoamperometry was used to study the ORR and OER stability of the Co/Co_2P@NCNTs composite. Figure 4-5f shows the chronoamperometric response curve at a constant voltage (0.8 V vs RHE for ORR, 1.7 V vs RHE for OER) in 1.0 M KOH electrolyte. The Co/Co_2P@NCNTs showed both excellent ORR and OER stability without losses in the activity after 40000 s. It even exhibited a significant

increase in both ORR and OER performance with a current increase of nearly 7.1% and 20.5% after 40000 s, respectively. These results indicate the high performance of the Co/Co_2P@NCNTs in terms of activity and stability. We infer that the greatly improved ORR/OER activities of the Co/Co_2P@NCNTs catalyst can be related to the increased electrochemically active surface area (ECSA) and the structural stability of the NCNTs.[21]

We have previously reported that the high potential operation can result in irreversible structural damage to the amorphous carbon materials, which can result in significantly increased charge transfer and mass-transport resistance.[22] Therefore, to confirm the strong structure stability toward high oxidation potentials of the Co/Co_2P@NCNTs, we then proceeded to evaluate its ORR catalytic activity after the OER process (1.1 V-2.1 V vs RHE). After the OER process, Co/Co_2P@NCNTs electrode demonstrated a greatly enhanced stability with high activity retained ($E_{1/2}$ = 0.87 V for the Co/Co_2P@NCNTs) (Figure 4-6a), which further confirms the high anti-oxidization ability of the unique structure. The Tafel slope at the diffusion-controlled and mixed kinetic-diffusion controlled regions was even lower than that of the Co/Co_2P@NCNTs without the OER process (Figure 4-6b). Moreover, to compare and analyze the influence of the OER process, EIS analyses were performed to characterize changes in the kinetics of the electrode reactions before and after the OER process. The EIS shows that there was no obvious change in the EIS spectra in the kinetically controlled region after the OER process, with a slight change in the mass transfer controlled region reflected by the increased Warburg impedance (W1) from 1.04 Ω to 1.20 Ω (Figure 4-6c). The results indicate that there is no obvious negative effect on the charge-transport resistances after undergoing a strong oxidation condition. Furthermore, the irreversible structural damage of the carbon materials could result in a significant decrease in ECSA (or abundant active sites) and mass activity. Theoretically, the double-layer capacitance (C_{dl}) is proportional to ECSA (supporting information). The C_{dl} was obtained by measuring the

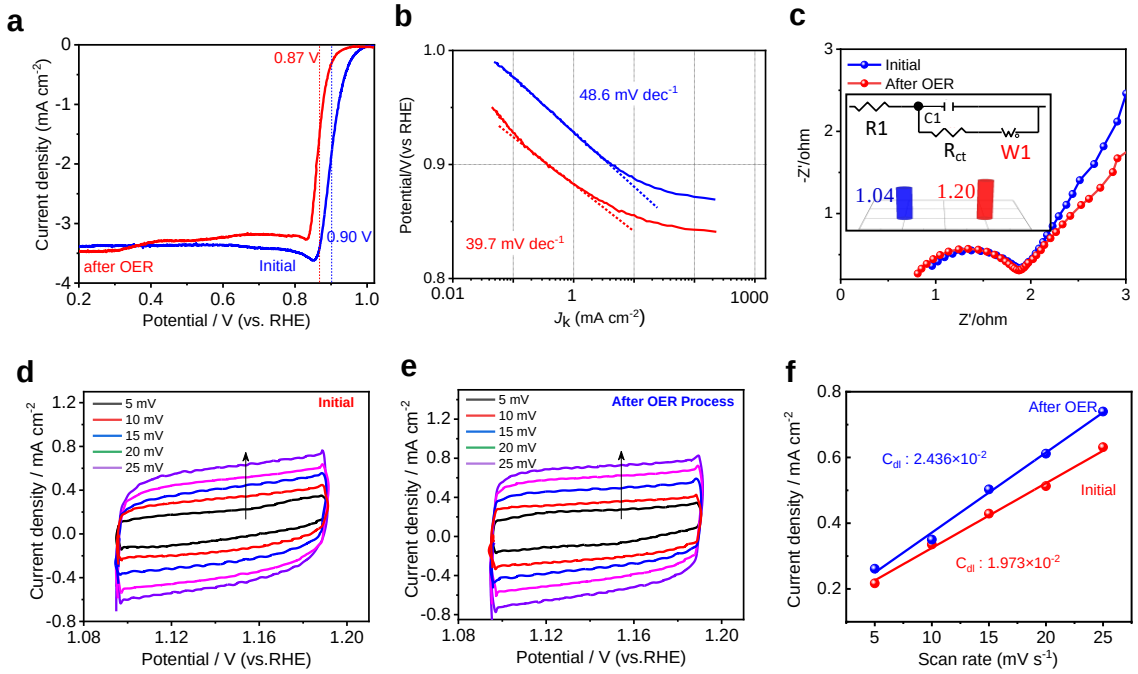

Figure 4-6 (a) ORR polarization plots of the Co/Co_2P@NCNTs before/after the OER process (in the potential range of 0-2 V vs RHE). (b) Tafel plots of Co/Co_2P@NCNTs before and after the OER process. (c) Electrochemical impedance spectra (EIS) based on a three-electrode system before and after the OER process. The inset of (c) is the value of the Warburg impedance (W1) and the simulated equivalent circuit. (d, e) CV curves of Co/Co_2P@NCNTs at different scan rates before and after the OER process. (f) The plots of the current density at 1.15 V versus the scan rate to obtain the double-layer capacitance (C_{dl}) before and after the OER process for the Co/Co_2P@NCNTs.

capacitive current, which is associated with double-layer charging. The Co/Co_2P@NCNTs catalyst has a large C_{dl} (1.973 × 10^{-2} F cm^{-2}) (Figure 4-6d-f), suggesting that the larger ECSA is due to the lower charge transfer resistance and optimized structure of NCNTs. Impressively, after the OER process, the improved ECSA of Co/Co_2P@NCNTs may be one of the critical factors in the increase of the Tafel slope. The increase in ECSA after the OER process could be caused by the slight corrosion of the carbon surface, contributing to the exposition of fresh active sites.[23] Additionally, the larger ECSA, remaining after the OER process, has ensured the outstanding stability of the Co/Co_2P@NCNTs. It has been reported that Co^{2+} oxides will be transformed into

Co^{3+} Oh-containing $CoO_x(OH)_y$ irreversibly during the OER process.[8, 24] The structural transformation occurs predominantly near the surface, and the formed cross-linked $CoO_x(OH)_y$ with lower crystallinity is believed to be the active species for the OER.[8] For the metal phosphides, the dephosphorization during the OER process accompanying surface oxidation has been widely reported.[25] To characterize and observe the dynamic catalytically active state of Co/Co_2P in the continuous charge and discharge process, the accelerated cycling durability test (ADT) was operated in a large potential window ranging (0.0 V-1.6 V versus RHE) in 1.0 M KOH solution to simulate the process of charge and discharge of the zinc-air battery (Figure 4-7a). By studying redox electrochemistry and electrocatalytic activity of the Co/Co_2P@NCNTs during the ADT test, we have attempted to establish structure-activity correlations of the bifunctional electrocatalysts. Here, we also observed a similar phenomenon of restructuring for the diphasic Co/Co_2P active materials during the OER. The two distinct redox transitions are commonly caused by the Co^{2+}/Co^{3+} couple (A1 and B1, E_{A1} = ~1.12 V) and the Co^{3+}/Co^{4+} couple (A2 and B2, E_{A2} = ~1.51 V). Thus, the local atomic structure of the surface Co-O sites at ~1.12V show a mean oxidation state of +3 for the CoOOH. Then, the Co^{3+}OOH was transformed into $Co^{3+/4+}O_x(OH)_y$ through Co^{3+}/Co^{4+} redox electrochemistry at ~1.51V. During the first 50 cycles of the ADT test, it was found that the intensity of the A1 peak gradually increased and reached its maximum. More importantly, it was noticed that the ORR performance was slightly influenced by the redox electrochemistry of the Co/Co_2P. After 50 cycles, the intensity of the A1 peak was gradually reduced. This phenomenon is attributed to the detachment of formed metal oxides/hydroxides nanocrystals from the NCNT surfaces. Meanwhile, the ORR performance showed a slight decay, and the double-layer capacitor exhibited a reduction, which suggests that the weakened chemical coupling effects between metal compounds and NCNTs surface do not influence much the ORR performance. The O K-edge XAS (Figure 4-7b,c) further reveals the

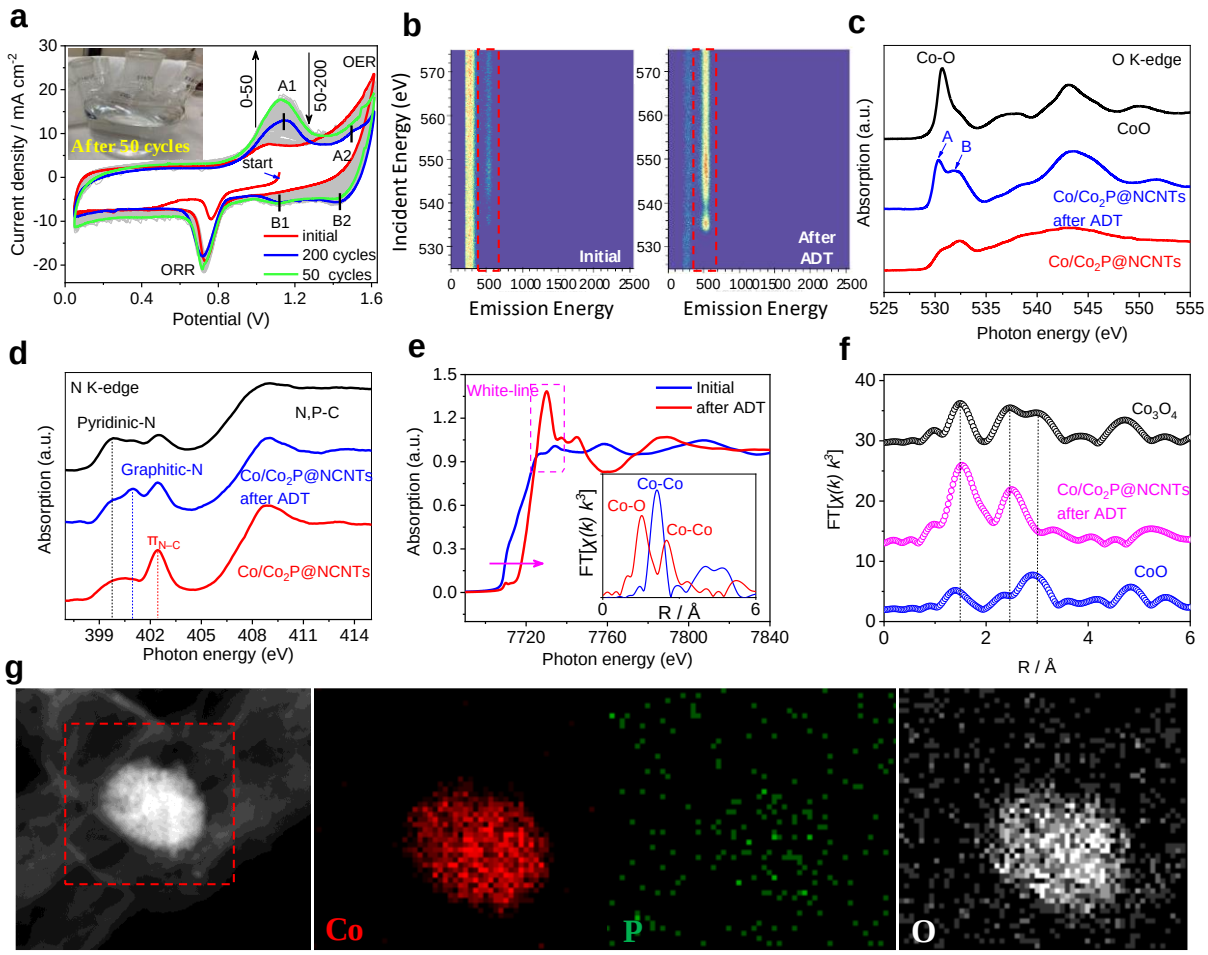

Figure 4-7 (a) CV curves (200 cycles) of the Co/Co_2P@NCNTs with a wide potential window (0.05 V-1.6 V versus RHE). The inset of (a) is the electrolyte after 50 cycles. (b) O K-edge emission line of the excitation-emission matrix spectrum before and after the ADT test. (c, d) O K-edge and N K-edge XAS spectra. e) The normalized Co K-edge XANES spectra of the Co/Co_2P@NCNTs before and after the ADT test. (f) The corresponding magnitude Fourier transforms of Co K-edge EXAFS oscillations $k^3\chi(k)$. The dashed vertical lines show the distance of Co^{3+}-O, Co^{3+} Oh-Co^{3+} Oh, and Co^{2+} Td-Co^{3+} Oh, at 1.48, 2.44, and 3.03 Å, respectively. (g) TEM images of the Co/Co_2P particles within the Co/Co_2P@NCNTs peeled off from the glassy carbon electrode after the ADT test, and the elemental mapping of the Co, P, and O.

changes in surface chemistry after the ADT test. The O K-edge XAS spectra of the Co/Co_2P@NCNTs after ADT in Figure 4-6c can be divided into two areas. One area (529 ~ 535 eV) is mainly attributed to the O 1s to unoccupied O 2p-TM 3d hybridized states. The other area (above 535 eV) is the result of the excitation of O 1s to O 2p-TM 4sp states.[26] Significantly, a

sharp peak at ~531.0 eV and a broad peak at ~544 eV, similar to that in the spectrum of CoO, appears in the O K-edge XAS of Co/Co_2P@NCNTs after ADT. This is also a result of the dynamic transformation from the Co/Co_2P to Co (oxy)hydroxide during the electrochemical OER process.[8] These results agree well with the analysis of redox electrochemistry mentioned above and in the literature. For the N K-edge XAS spectra (Figure 4-7d), we can observe four peaks at 399.6, 401.7, 402.5, and 405-412 eV, corresponding to the pyridinic-N ($\pi_{C=N-C}$), graphitic-N (π_{N-3C}), sp^3 N-C bridging among tri-*s*-triazine moieties (π_{N-C}), and 1s-σ_{N-C} transition, respectively.[27] Interestingly, the spectra of N K-edge reveal the transformation from π_{N-C} to graphitic-N after the ADT test, which confirms the restructuring of N active sites. The increase of graphitic-N active sites with high ORR activity would not have a negative effect on the ORR performance of the Co/Co_2P@NCNTs.

To further investigate the electronic and geometric structures of the Co/Co_2P nanocrystals under the ADT test, in situ electrochemical XAS with a homemade electrochemical cell was carried out (Figure 4-7e). We can directly observe that the shape of the Co K-edge XANES spectrum after the ADT test was very analogous with the CoOOH reported earlier.[28] The obvious reduction of the pre-edge peak intensity at 7710 eV and a sharp enhancement of the white-line peak intensity are noticed (Figure 4-7b). Meanwhile, a positive shift of the absorption edge (~ 3 eV) relative to the Co_3O_4 reference indicates an oxidation state of Co higher than 2+. These changes are all indications of the formation of $CoO_x(OH)_y$ phase, which is usually the real active species for OER. In addition, the dark-field TEM of Co/Co_2P has shown that there is an obvious change in morphology after the ADT test, following the formation of well-defined cross-linked $CoO_x(OH)_y$ of lower crystallinity (Figure 4-7g). These results give a rational interpretation of the significant increase in OER performance. The electrochemical influence on the coordination environment of the Co for the Co/Co_2P@NCNTs after the ADT test was further captured by

using operando EXAFS measurements (the inset of Fig 4-6e and Figure 4-7f). The spinel Co_3O_4 reference contains two types of geometrical cobalt ions, which are tetrahedral site Co^{2+} (Co^{2+} Td) and octahedral site (Co^{3+} Oh). respectively.[29] As expected, two distinctly different peaks centered at 1.48 Å (Co-O) and 2.44 Å (Co-Co) are observed for the ADT sample, which are typical characteristics of CoOOH,[30] providing further evidence for the irreversible transformation of Co/Co_2P into Co^{3+} Oh-containing $CoO_x(OH)_y$ after the ADT test. The triggered $CoO_x(OH)_y$ component as revealed by the in-situ electrochemical process under high oxidation potentials plays a dominant role in the OER process.

The excellent OER catalytic activity of the catalytically active species of Co(oxyhydr)oxides and the robust structure with the high anti-oxidization ability of NCNTs encourages us to believe that the Co/Co_2P@NCNTs would be an ideal catalyst for the rechargeable zinc-air battery. Moreover, the rechargeable zinc-air flow battery has attracted considerable attention due to its higher cycling stability compared with the conventional zinc-air battery with a static electrolyte. This configuration can dramatically inhibit the dendrite growth of the Zn electrode. Meanwhile, precipitated carbonates or other unwanted solid products formed during the charge and discharge processes can be rinsed away by the flowing electrolyte. To assess the potential application of the Co/Co_2P@NCNTs in energy storage and conversion devices, a rechargeable zinc-air flow battery was assembled by applying the Co/Co_2P@NCNTs as the bifunctional catalyst of air cathode and zinc foil as the anode (Figure 4-8a). As shown in Figure 4-8b, the Co/Co_2P@NCNTs-based battery exhibited a very promising open-circuit voltage of 1.45 V. Figure 4-8b shows the discharge performance from 1.0 mA cm^{-2} to a high current density of 20 mA cm^{-2}, indicating a good rate performance of the Co/Co_2P@NCNTs-based battery. The peak power density of the Co/Co_2P@NCNTs could be as high as 330 mW cm^{-2} (Figure 4-8c). The rechargeability and cycle stability of the Co/Co_2P@NCNTs catalyst in rechargeable zinc-air flow batteries are also vital for

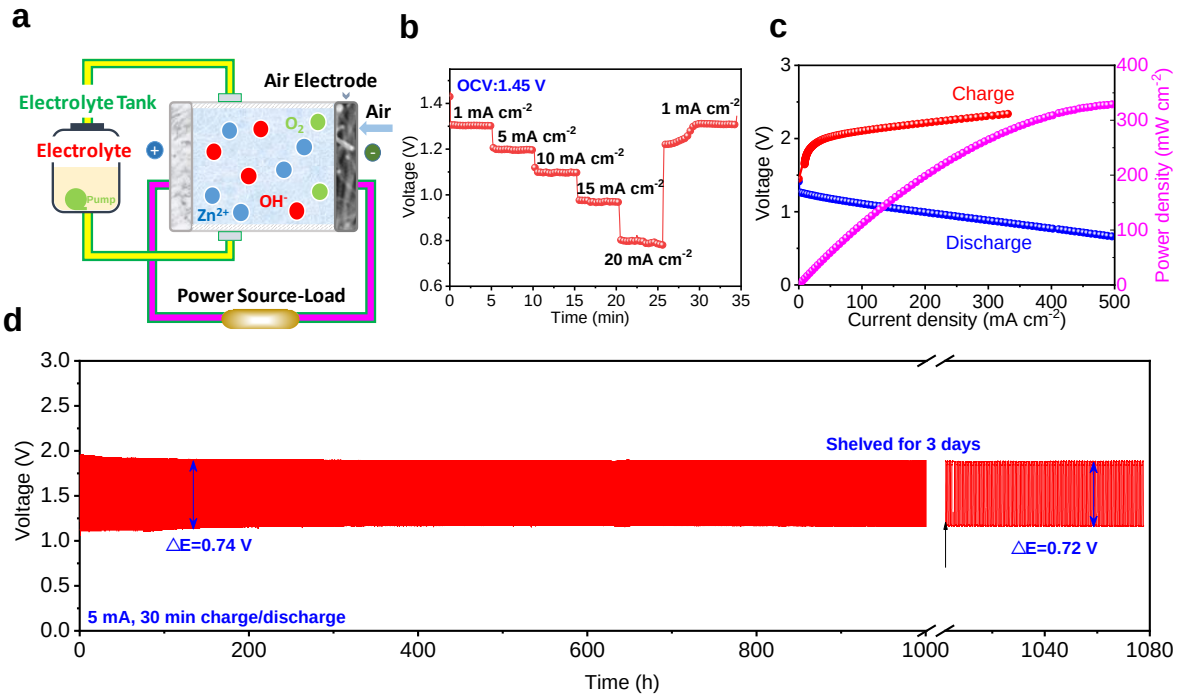

Figure 4-8 (a) A schematic configuration of the rechargeable zinc-air flow battery. (b) Discharge curves at different current densities of the zinc-air flow battery. (c) Galvanostatic charge/discharge cycling performance of the Co/Co_2P@NCNTs and the corresponding power density curves of the zinc-air batteries without circulating the electrolyte. (d) Cycling performance of the zinc-air flow battery using the Co/Co_2P@NCNTs at a current density of 5.0 mA cm^{-2} with each cycle being 1 h.

its practical applications. As shown in Figure 4-8c, the voltage gap is only 0.99 V at 100 mA cm^{-2}, which contributes to high energy efficiency (52.8% at 100 mA cm^{-2}). The cycling performance of the rechargeable battery with the Co/Co_2P@NCNTs was also evaluated (Figure 4-8d). The zinc-air flow battery with the Co/Co_2P@NCNTs delivered a decreasing charge-discharge voltage gap, indicating better charge-discharge performance. This is consistent with its improved electrochemically active surface area and the triggered $CoO_x(OH)_y$ active component. Significantly, the Co/Co_2P@NCNTs-based battery has demonstrated the highest lifetimes (1080 h over 1000 cycles) reported to date for rechargeable zinc-air flow batteries, suggesting its outstanding long-term durability. Moreover, during longtime charge and discharge operations in

zinc-air flow batteries, by adopting a flowing-electrolyte design, the frequent replacement of the zinc electrode (thickness: 0.7mm) is not necessary. After being shelved for 3 days, there are no obvious changes in both the voltage gap and energy efficiency (0.72 V and 62.5%), demonstrating the superior practicality of the Co/Co_2P@NCNTs in a real work environment of a rechargeable zinc-air flow battery.

4.4 Conclusions

In summary, we developed a facile strategy for the large-scale fabrication of heterojunction Co/Co_2P confined in N-doped CNTs (Co/Co_2P@NCNTs) as a pre-catalyst for the oxygen electrocatalysis. The NCNTs with a high degree of graphitization and increased graphitic-N active sites catalyzed by the unique Co/Co_2P heterojunction demonstrated excellent intrinsic electrical conductivity, which significantly accelerates the ORR kinetics and effectively reduces the negative effects of high oxidation potential (during the OER process) on the ORR performance in alkaline media. Meanwhile, the dynamic active state transformation from the heterojunction Co/Co_2P into Co^{3+} Oh-containing $CoO_x(OH)_y$ active species contributes to the significantly increased OER performance. Consequently, the developed Co/Co_2P@NCNTs with self-reconstruction in the assembled zinc-air flow battery displays a high-energy efficiency with a superior cycle life of 1080 h in an ambient environment. The large-scale synthesis of such a catalyst with outstanding electrochemical performance thereby makes it very promising in the industrialized application for metal-air batteries.

Chapter 5 Fe/Co Double Hydroxide/Oxide Nano-sheets on N-Doped CNTs for Rechargeable Zinc-air Batteries

5.1 Introduction

Advanced energy-storage technologies, including electrically rechargeable zinc-air batteries (ZABs), have attracted tremendous interest due to their great potential to offer high energy density while maintaining a long operational life.[199] Compared with the well developed lithium-ion batteries (~250 W h kg^{-1}), ZABs possess impressively high specific energy densities (~1218 W h kg^{-1}) mainly due to their unique "half-open" system in which the active component (i.e., oxygen) on the cathode is from the air.[200] Additionally, the other advantages including eco-friendliness, abundant materials, safe operation, and low cost make ZABs a promising candidate for practical applications in various areas ranging from small portable electric devices to large power systems such as electric vehicles (EVs). However, the insufficient performance of the bifunctional oxygen electrocatalysts that can catalyze both oxygen evolution reaction (OER) and oxygen reduction reaction (ORR) at the air electrodes seriously limit the development of rechargeable ZABs. Noble metals, like platinum (Pt) and ruthenium (Ru)- or iridium (Ir)-oxides have been commonly used for ORR and OER in alkaline solutions, respectively.[201] Unfortunately, their insufficient bifunctional catalytic activity, scarcity, high cost, and electrochemical instability inevitably hinder the scalable implementation of ZABs. In this context, the low-cost and earth-abundant transition metal hydroxides and oxides have emerged as bifunctional oxygen electrocatalysts to replace the expensive and rare noble-metal catalysts.[202] Recently, through engineering the anion chemistry of metal hydroxides or oxides to adjust the composition, morphology and crystallographic orientation of nanostructures has been proved to be an effective way to tune their physicochemical properties and to improve their catalytic performance.[203]

Among numerous transition metals compounds, versatile Fe/Co hydroxides and oxides have been used in supercapacitors and lithium-ion batteries (LIBs).[204-205] Recently, Fe/Co compounds have also been reported for use as effective OER catalysts.[206] However, the exploration of Fe/Co hydroxides or oxides for both ORR and OER is still rarely reported. Additionally, it has been demonstrated that the formation of amorphous metal hydroxides and oxides is beneficial for the OER.[207] Meanwhile, the studies of bimetal or multi-metal systems reveal that the incorporation of Fe^{3+} ions into the metal oxides is beneficial to enhance catalyst conductivity and can dramatically improve catalytic activity for OER.[208] Moreover, to further enhance the catalyst charging-discharging performance and lifetime, extensive efforts have been made by assembling metal-based materials on carbon materials, which own high electrical conductivity, strong chemical stability, large surface areas, such as porous carbon[209], graphene[210], and nanotubes (CNTs)[211]. These unique properties assure fast electron transport and the diffusion of ORR/OER-relevant species (H^+/OH^-, e^-, O_2, H_2O). Meanwhile, metal hydroxides or oxides supported on carbon materials by chemical attachment and electrical coupling have been reported to be an efficient strategy to improve activity and durability toward ORR and OER.[212-213] Unfortunately, although some progress has been achieved by carefully choosing suitable carbon supports and optimizing the nano-structures of transition metal oxides, the chemical instability of these metal species due to cation segregation and phase precipitation at the surface still limits their ORR/OER activity and durability.[214]

In this work, we develop a unique facile bimetal coupling approach to synthesize Fe/Co double hydroxide/oxide nano-sheets cladding layer on N-doped multiwall carbon nanotubes (FeCo-DHO/NCNTs). Through the direct nucleation, growth, and anchoring, the Fe/Co double hydroxide/oxide nano-sheets (FeCo-DHO) are uniformly inlaid on the surface of NCNTs, which provide high electrical contact area and strong adhesion on the conductive carbon support (Figure

5-1). The strong interactions of the FeCo-DHO nano-sheets with NCNTs (possibly due to the formation of M-O-C (M=Co, Fe) chemical bonding) not only greatly facilitate the charge transfer and mass transport, but also lead to high chemical stability to resist the corrosion during charge and discharge operation.[215] Consequently, the as-synthesized FeCo-DHO/NCNTs with the unique physiochemical properties exhibits superior bifunctional ORR/OER activity and stability, with a potential gap of 0.7 V between $E_{j=10}$ (OER, potential at 10.0 mA cm^{-2}) and $E_{1/2}$ (ORR, half-wave potential). When the FeCo-DHO/NCNTs were applied as the catalyst assembly in liquid and quasi-solid-state ZABs, excellent charging-discharging performance and ultra-long cycling lifetime have been achieved. The outstanding electrochemical performance of such catalysts thereby makes it very promising to replace the noble-metal catalysts (Pt group metals for ORR, and Ir/Ru group metals for OER) in metal-air batteries.

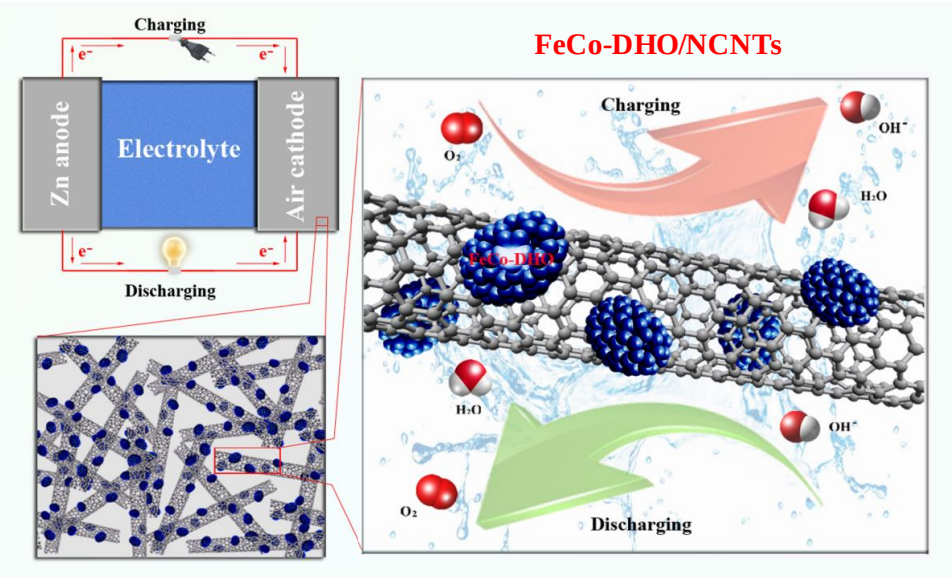

Figure 5-1 Schematic illustration of the ZAB configuration and the proposed mechanism for the synthesis of NCNTs Inlaid with uniform Fe/Co hydroxides/oxides cladding layer catalyst (FeCo-DHO/NCNTs).

5.2 Experimental Section

5.2.1 Synthesis

Synthesis of N-doped CNTs encapsulated in Fe/Co hydroxide/oxide nano-sheets cladding layer (FeCo-DHO/NCNTs): In a typical synthesis process, 40 mg of CNTs were dispersed in 30 ml ammonia assisted by sonication for 30 min. After that, 8 ml 0.2 M $Co(NO_3)_2$ $6H_2O$ and 1.6ml 0.2 M $FeSO_4$ aqueous solution were added. The solution was vigorously stirred for 30 min. Then, the obtained product was transferred to a 100 ml Teflon-lined stainless steel autoclave for solvothermal reaction at 180 °C for 4 hours. The resulting powder was washed with deionized water for neutralization and then dried overnight. Then, the final product FeCo-DHO/NCNTs was pyrolyzed at 400 °C for 1 hour under an argon atmosphere. For comparison, Fe-NCNTs without adding $Co(NO_3)_2$ $6H_2O$ and Co-NCNTs without adding $FeCl_2$ were prepared by a similar procedure.

5.2.2 Fabrication of the liquid and quasi-solid-state Zn-air battery

The liquid Zn-air batteries were tested in home-built electrochemical cells, the electrolyte was 6 M KOH with 0.2 M zinc acetate solution (Figure 5-2). The zinc-air battery was assembled with current collectors (copper foil for the anode and cathode), a polished zinc plate, and a catalyst layer (GL) coated gas diffusion electrode (GDE). To prepare the air electrode, a definite volume of homogeneous catalyst ink consisting of FeCo-DHO/NCNTs catalyst, Nafion solution (5 wt.%), and isopropanol was dropped onto a gas diffusion layer (GDL) (loading: 2 mg cm^{-2}) with an exposed active area of 1.13 cm^2 (Figure 5-2a). Then Ni Foam, GDL, and hydrophobic and breathable membrane were pressed together to form an integrated air electrode. As a comparison, the battery using 20 wt.% Pt/C (loading: 0.5 mg cm^{-2}), and Pt/C+RuO_2 (loading: 0.5

mg cm^{-2}) mixture catalyst with the same loading was fabricated through the same method. Polarization data was collected using the galvanodynamic method at a scan rate of 1.0 mA s^{-1} with the cut-off voltages of 0.6 V for the discharge and 2.2 V for the charge. Single-cell discharge and charge cycling tests were operated by the battery testing system.

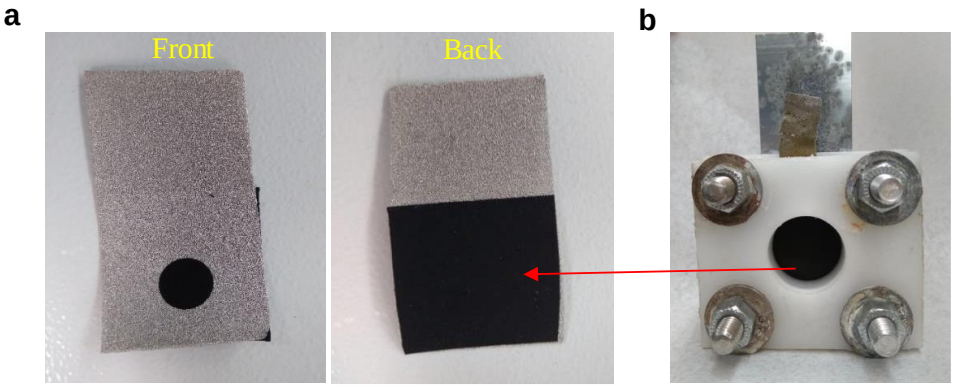

Figure 5-2 (a) The optical pictures of the air electrode for a liquid, and rechargeable zinc-air battery. (b) A demonstration of the liquid and rechargeable ZAB.

For the quasi-solid-state Zn-air battery, a flexible zinc electrode material consisting of (wt.%) 80% zinc (purum powder, Sigma-Aldrich), 8% ZnO, 3% CNF (Pyrograf III, Pyrograf Products, Inc.), 1% CB (Vulcan XC 72R), 8% PVDF (average Mw 455 000, Sigma-Aldrich) polymer binder, and Cu foil as the current collector. The CNF and CB were added to improve the electrical conductivity of the electrode. The PVDF was well dissolved in acetone to make a 10% solution. The mixture of the active materials and binder solution was magnetically stirred for 2 h. The resulting slurry was spread by doctor blading on a Cu foil substrate and further dried in a vacuum at 60 °C for 5 min. The air electrode was made by dropping a certain volume of catalyst ink onto a gas diffusion layer (GDL) (1.13 cm^2) with a catalyst loading of 2.0 mg cm^{-2}. The gel polymer electrolyte was prepared as follows: 1.0 g polyvinyl alcohol (PVA) powder (MW 19500, Aladdin) was dissolved in 10.0 mL deionized water at 95 ^oC under magnetic stirring for 2.0 h. Then 1.0 mL of 18.0 M NaOH filled with 0.10 M $ZnCl_2$ (dissolved in NaOH to form zincate, $Zn(OH)_4^{2-}$) was

added and the electrolyte solution was kept stirring at 95 °C for 60 min. Then pour it into plastic petri dishes, and water was evaporated under ambient conditions. When it is visually dry, the membranes were peeled from the plastic substrates and put soaked into 6 M KOH. Then the flexible solid-state Zn-air battery was assembled with air electrode and zinc electrode (1.13 cm^2) placed on the two sides of PVA gel, and a piece of Cu foil was used as the current collector next to the air electrolyte (Figure 5-3).

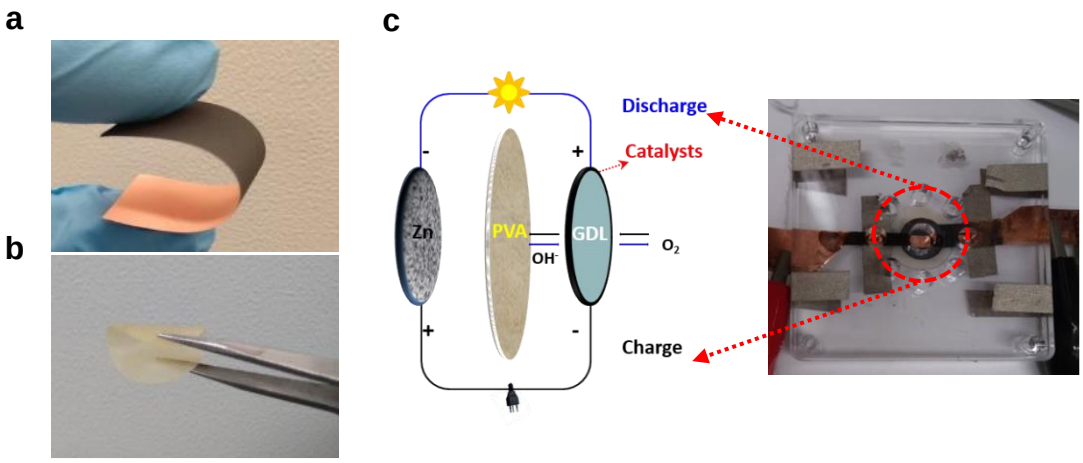

Figure 5-3 (a) The optical pictures of the bendable zinc electrode, and (b) the gelled PVA electrolyte membrane. (c) A schematic image of the solid-state, and rechargeable ZAB.

5.2.3 Material characterizations

The morphological structures of the catalysts were investigated by transmission electron microscopy (TEM) and high-resolution TEM (HRTEM) (JEOL JEM-2100F, operated at 200 kV). Energy Dispersive Spectroscopy (EDS) analysis was carried out on Tecnai TEM with EDS detector under scanning unit electron microscopy (STEM) mode. The crystal structure of the catalysts was analyzed by X-ray diffraction (XRD) (40 kV, 25 mA, Cu Kα radiation, λ=1.5418 Å); The surface properties were analyzed by X-ray photoelectron spectroscopy (XPS, VG ESCALAB 220i-XL) equipped with a hemispherical analyzer for a Twin Anode X-ray Source. The C 1s peak

(BE = 284.6 eV) was used as the reference line to accurately determine the positions of other spectral lines. The fine structure of the photoelectron lines was treated using Casa XPS software (2.3.15 Version). The surface areas of the catalysts were measured through N_2 sorption isotherms that were collected using Quantachrome Instruments Autosorb-1 at liquid nitrogen temperature. The Fe and Co K-edge X-ray absorption near-edge structure (XANES) and Extended X-ray Absorption Fine Structure (EXAFS) data were collected on the 06ID-1 Hard X-ray MicroAnalysis (HXMA) beamline at the Canadian Light Source.

5.2.4 Electrochemical measurements

The electrocatalytic performance for oxygen reduction (ORR) and evolution (OER) reactions was carried out in a standard three-electrode cell with a bipotentiostat (Pine, Model PGSTAT-72637) workstation at room temperature. All electrochemical tests were carried out in either O_2-saturated or N_2-saturated 0.1 M KOH electrolyte solution controlled at room temperature. To subtract the background capacitive current, linear sweep voltammetry was conducted under the same conditions in an N_2-saturated electrolyte. Catalyst powders cast on the rotating ring-disk electrode (RRDE, PINE Research Instrumentation) was used as the working electrode. A Pt wire and a saturated calomel electrode (SCE) were used as the counter and reference electrodes, respectively. When conducting accelerated durability tests (ADTs), a graphite rod was used as the counter electrode. In this paper, all potentials were converted to reversible hydrogen electrode (RHE) using the equation, $E_{(RHE)} = E_{(SCE)} + 0.0591pH + 0.24$. A rotating ring-disk electrode (RRDE) with a Pt ring and a GC disk (5.61 mm diameter) was used as the substrate for the working electrodes. Before use, the GC electrodes in RDE/RRDE are polished using aqueous alumina suspension on felt polishing pads. The catalyst ink was prepared by ultrasonically mixing 2.0 mg catalyst with 0.4 mL of isopropyl alcohol and 10 mL of 5 wt.% Nafion® for more

than 30 minutes. For comparison, commercially available Pt/C (20 wt.% Pt) and ruthenium dioxide (RuO_2, 99%) catalysts were used as the baseline.

5.3 Results and Discussion

5.3.1 Structural and morphological characterization

Figure 5-4 shows the XRD pattern of the CNTs (black line) with diffraction peaks at 26.4 (002) and 42.8 (100). When certain amounts of $Co(NO_3)_2$ $6H_2O$ and $FeSO_4$ $7H_2O$ were added, respectively, monometallic Fe-NCNTs and Co-NCNTs composites were obtained. In the case of Fe-NCNTs (red line), the diffraction peaks at 30.1, 37.09, 43.1, 56.9, 62.6 are assigned to the crystal planes (311), (222), (511), and (440), respectively, of Fe_3O_4 (JCPDF# 65-3107). For Co-NCNT (blue line), the diffraction peaks at 36.6, 42.4, 61.5, 61.9, 73.7, and 77.8 are assigned to the crystal planes (101), (110), (200), (112), (211), and (202), respectively, of CoO (JCPDF# 65-5474). The diffraction peaks (at 26.4 and 42.8) of CNTs for Fe-NCNTs and Co-NCNTs are only slightly weakened. However, the diffraction peaks (at 26.4 and 42.8) for CNTs are almost undetectable by XRD for FeCo-DHO/NCNTs, implying that the NCNTs have been covered by a large amount of FeCo-DHO. Moreover, the crystallization peaks of FeCo-DHO/NCNTs are very weak, suggesting a predominant amorphous structure.[216] The very weak diffraction peaks at 31.3, 36.8, and 44.8 can be assigned to the crystal planes (220), (311), and (400) of Co_3O_4 (JCPDF# 50-1350), respectively. These results indicate that Fe/Co bimetal synergetic coupling interactions can appropriately suppress the formation of the crystalline phase under the same conditions. The Fe/Co oxides or hydroxides with both crystalline and amorphous phases may result in more transportation channels than that of the highly crystalline phase, which consequently facilitates the sluggish oxygen electrochemical reactions.[217]

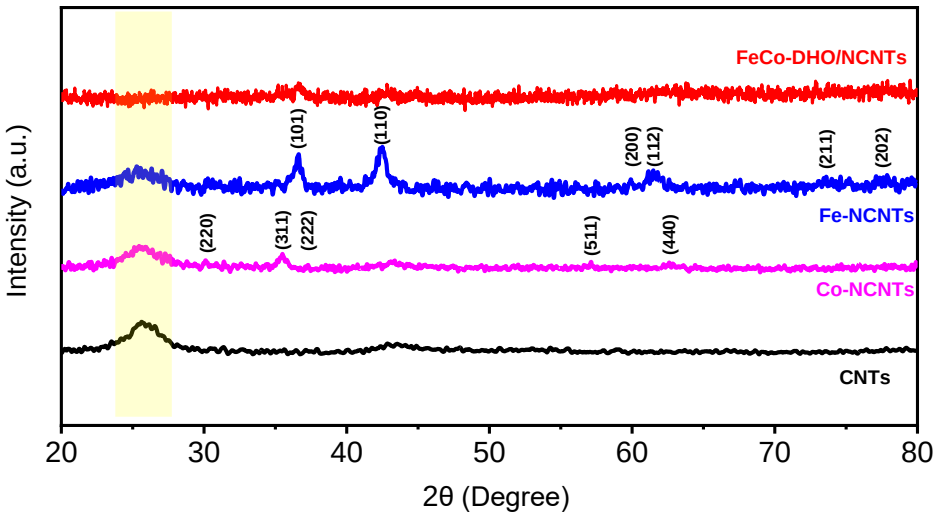

Figure 5-4 XRD spectra of the as-prepared CNTs, Fe-NCNTs, Co-NCNTs, and FeCo-DHO/NCNTs catalysts.

The morphology and structure of the catalysts were characterized by scanning electron microscopy (SEM) and transmission electron microscopy (TEM). The SEM images show that the as-prepared monometallic Fe-NCNTs and Co-NCNTs composites maintain the pristine morphology of the CNTs, with a low density of particle deposition. (Figure 5-5a,b). Interestingly, when both Fe precursor and Co precursor were employed, the NCNTs are covered by a large amount of Fe/Co nanocluster particles (Figure 5-5c). This indicates that the strong bimetal Fe/Co synergetic interaction promotes the formation of size-defined Fe/Co nano-sheets and their strong adhesion on the NCNTs. This unique interwoven network structure consisting of Fe/Co nano-sheets on the NCNTs can provide intimate interfacial contact between Fe/Co species and NCNTs, which is favoring a low-resistance pathway for a high flux of charge transfer during ORR and OER.[218] The TEM images of the FeCo-DHO/NCNTs (Figure 5-5d-f) show clearly that the Fe/Co nano-sheets (5-10 nm) homogeneously distribute across the entire network. The high-resolution TEM images and the corresponding selected area electron diffraction (SAED) patterns (Figure 5-5e,f) show the (220) and (111) facets of Co_3O_4.

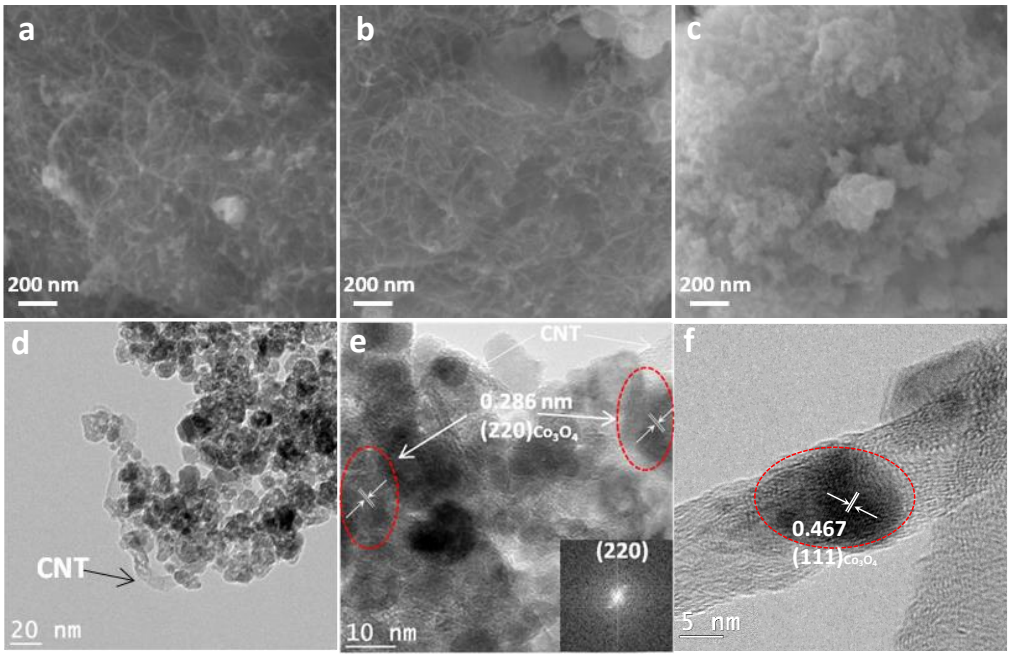

Figure 5-5 SEM images of Fe-NCNTs (a), Co-NCNTs (b) and FeCo-DHO/NCNTs (c). TEM images of the FeCo-DHO/NCNTs (d). HRTEM images of the FeCo-DHO/NCNTs (e, f) (inset: FFT patterns).

To further confirm the chemical composition and valence state of the as-prepared FeCo-DHO/NCNTs, X-ray photoelectron spectroscopy (XPS) measurements were conducted. As shown in Figure 5-6a, the XPS survey spectrum revealed the presence of Co, Fe, O, N, and C elements. The C 1s spectrum confirms the existence of C-C (284.6 eV), C=OH (285.6 eV), C=N (287.1 eV), C-OOH (288.9 eV) and π-π* (290.8 eV) bonds in FeCo-DHO/NCNTs (Figure 5-6b).[219] In addition, Figure 5-6c presents the high-resolution O1s spectra for FeCo-DHO/NCNTs sample. The peak at ~530.1 eV corresponds to the lattice O (O^{2-}) arising from Co-O or Fe-O bonds, and the peak at ~531.5 eV is assigned to the bound hydroxide groups (OH^-). The hydroxide groups imply that the incorporation of bimetal Fe/Co precursors induced the formation of the Fe/Co hydroxide structure. High-resolution N 1s spectrum (Figure 5-6d) can be deconvoluted into four peaks at 398.6, 400.1, 401.1, and 404.0 eV, which are assigned to pyridinic N (43.74%), pyrrolic N (21.89%), graphitic N (12.65%), and oxidized N (21.71%),

respectively. Peak fitting analyses of the Fe 2p spectra for the FeCo-DHO/NCNTs identified only one chemical state of Fe, i.e., Fe^{3+} at 713.8 and 711.0 eV (Figure 5-6e), which may be attributed to Fe^{3+} bonded with the hydroxyl group (-OH) and oxygen (-O), respectively. The high-resolution Co 2p spectrum (Figure 5-6f) shows four binding energies located at 780.4, 782.8, 786.3, and 790.5 eV, which match well with the previously reported $Co(OH)_2$ spectra.[220]

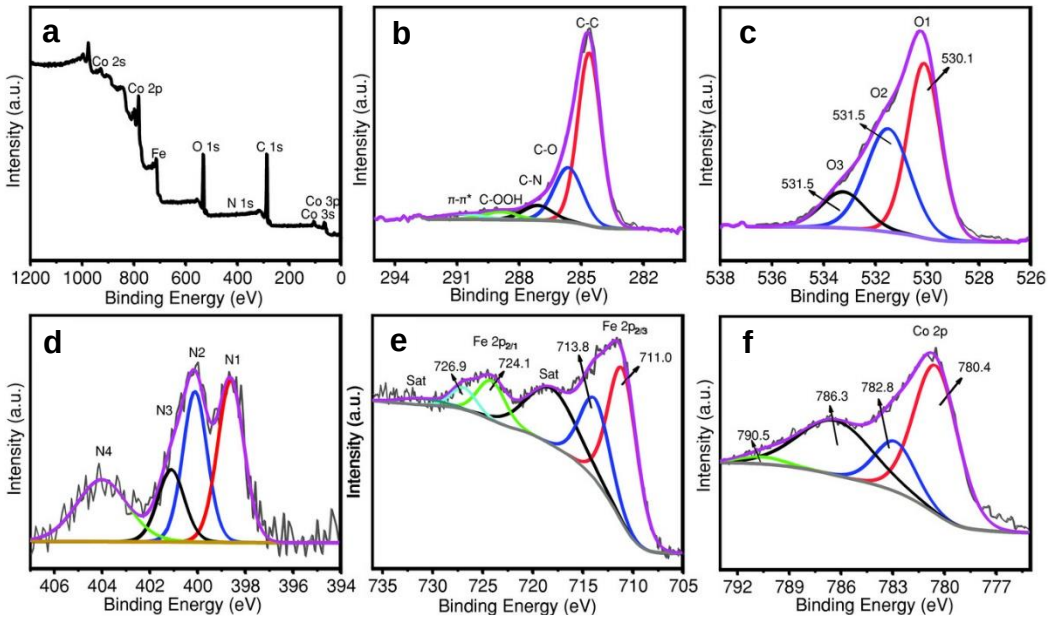

Figure 5-6 (a) XPS survey scan and the corresponding high-resolution spectra of (b) C 1s, (c) O 1s, (d) N 1s, (e) Fe 2p, and (f) Co $2p_{3/2}$ for FeCo-DHO/NCNTs.

5.3.2 Electrochemical characterization

Metal-oxygen hybridization and strong coupling between metal hydroxides/oxides and NCNTs play key roles in promoting fast exchange kinetics of O^{2-}/OH^- for ORR and OER reactivity.[45] To reveal the textural properties and catalytic performance for ORR and OER, rotating ring-disk electrode (RRDE) measurements were performed at 1600 rpm to further reveal the ORR catalytic activity and pathways of the hybrid catalysts in 0.1 M KOH (Figure 5-7). It can be seen that the FeCo-DHO/NCNTs showed the best activity in terms of the most positive

onset potential (E_{onset}; 0.91 V, vs 0.83 and 0.84 V for Fe-NCNTs and Co-NCNTs, respectively, determined as the potential at 0.1 mA cm^{-2}) and half-wave potential ($E_{1/2}$; 0.80 V, vs 0.72 and 0.73 V for Fe-NCNTs and Co-NCNTs, respectively). By comparison, the polarization curves for the Fe-NCNTs and Co-NCNTs electrodes are stretched out toward less positive potentials, suggesting that Fe-NCNTs and Co-NCNTs suffer larger overpotentials due to the slow ORR kinetics. The bifunctional catalytic activity can be evaluated by the variance of OER and ORR metrics ($\Delta E=E_{j=10}-E_{1/2}$). The smaller ΔE represents a superior bifunctional catalytic activity. As shown in Figure 5-7, the FeCo-DHO/NCNTs exhibits a small ΔE value of 0.93 V, which largely surpassed Fe-NCNTs (ΔE=1.21 V) and Co-NCNTs (ΔE=1.18 V). Here, what we should note is that the process of OER has a negative effect on the ORR process, which might be attributed to the fact that the chemical structure of metal oxides may be changed after the OER process.[221] We can see that, after the OER process, the onset potential and $E_{1/2}$ of ORR for all catalysts exhibit different degrees of negative shift. However, FeCo-DHO/NCNTs displays a lower potential downshift (74 mV) at 3 mA cm^{-2} than those for Fe-NCNTs (94 mV) and Co-NCNTs (93 mV), after suffering from the OER process, indicating that FeCo-DHO/NCNTs catalyst has a better bifunctional catalytic stability than M-NCNTs (M= Fe, Co).

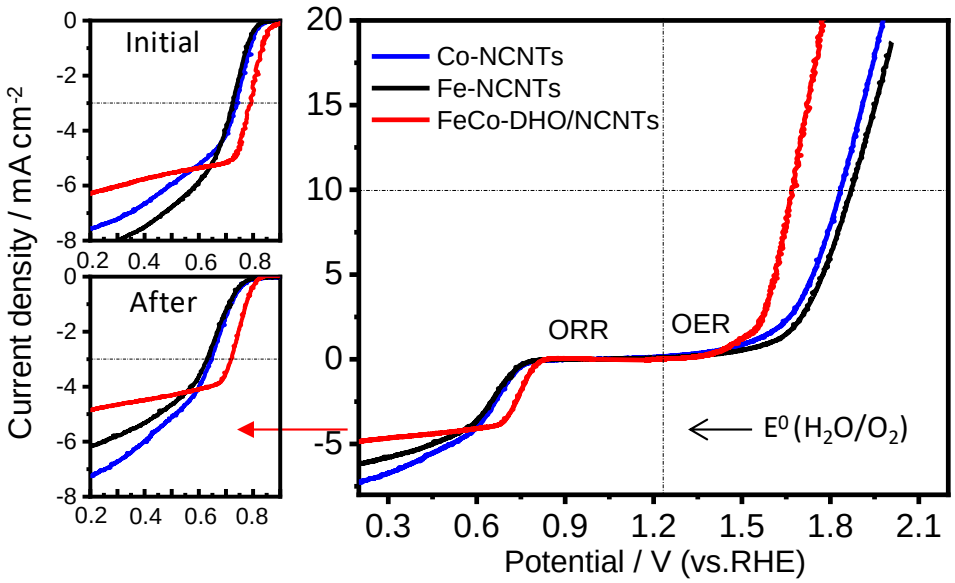

Figure 5-7 The ORR for Fe-NCNTs, Co-NCNTs, and FeCo-DHO/NCNTs catalysts before and after the OER process.

Furthermore, it is reported that KOH concentration has a significant effect on O_2 solubility, ionic conductivity, O_2 diffusion coefficient, and viscosity, which correlates closely with ORR and OER activity. Therefore, the ORR and OER kinetics catalyzed by FeCo-DHO/NCNTs catalyst were also studied by using RRDE techniques in 1.0 M KOH electrolyte (Figure 5-8a,b). In 1.0 M KOH, the performance of FeCo-DHO/NCNTs catalyst (loading: 1.0 mg cm^{-2}) was greatly enhanced compared with that in 0.1 M electrolyte. The half-wave potential of FeCo-DHO/NCNTs catalyst ($E_{1/2}$: 0.85 V) increases considerably by more than 50 mV. The diffusion-limiting current of FeCo-DHO/NCNTs catalyst decreased slightly, with less than 1.0 mA cm^{-2} (~17%) decrement (Figure 5-8a), which is the result of the reductions in O_2 solubility and the O_2 diffusion coefficient, as well as the increase in KOH solution viscosity. On the other hand, the FeCo-DHO/NCNTs displays low OER potential ($E_{j=10}$) (~1.55 V) in 1.0 M KOH, which is ~110 mV more negative than that of FeCo-DHO/NCNTs in 0.1 M KOH (~1.66 V) (Figure 5-8b).

Therefore, the as-prepared FeCo-DHO/NCNTs presents excellent bifunctional catalytic activity in 1.0 M KOH, with a potential gap of 0.7 V, strongly comparable to the performance of the best reported non-precious Fe/Co-based bifunctional catalysts.[222] In addition to the high bifunctional catalytic activity, the durability of FeCo-DHO/NCNTs also plays a critical role in achieving a long cycling lifetime for rechargeable ZABs. To evaluate the stability of FeCo-DHO/NCNTs catalyst, the ORR and OER performance change before and after the accelerated durability tests

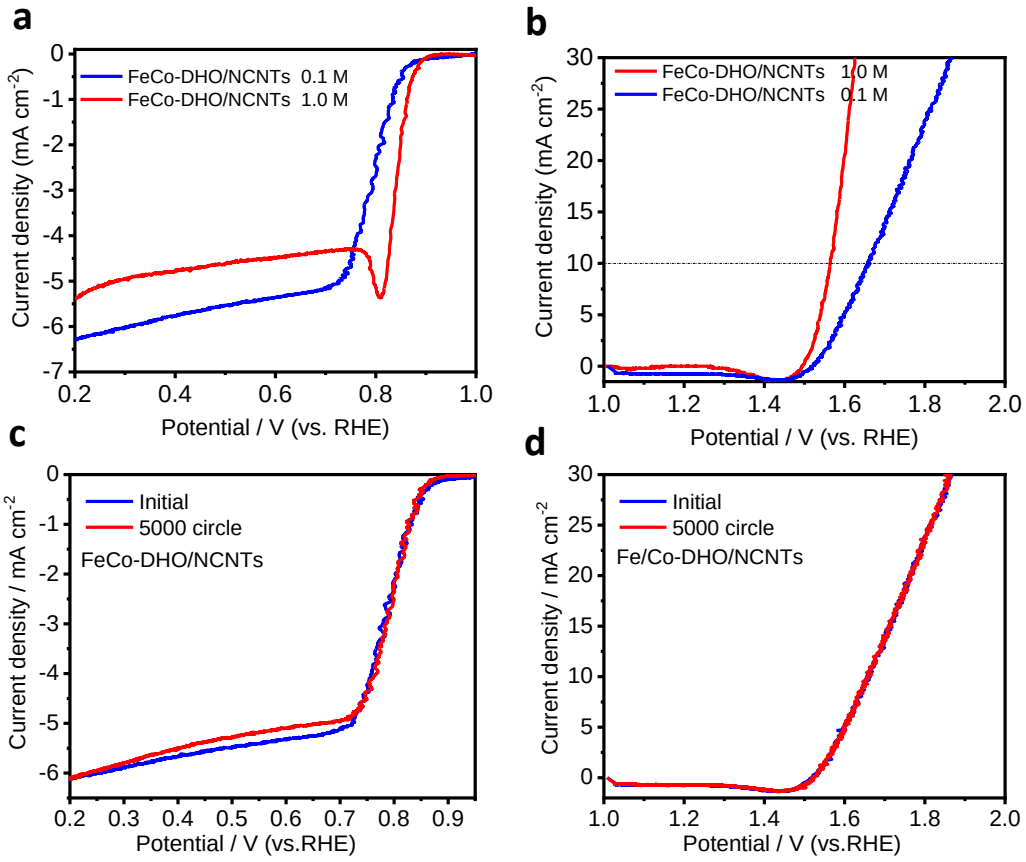

Figure 5-8 (a) ORR polarization curves for FeCo-DHO/NCNTs electrode (rotation rate: 1600 rpm) in O_2-saturated 0.1 and 1.0 m KOH at a scan rate of 5 mV s^{-1}, respectively. (b) LSV of OER for FeCo-DHO/NCNTs electrode (rotation rate: 1600 rpm) in O_2-saturated 0.1 and 1.0 m KOH at a scan rate of 5 mV s^{-1}. (c) Comparative ORR activities of FeCo-DHO/NCNTs before and after 5000 cycles of cyclic voltammetry (CV) between 0.6 and 1.8 V in O_2-saturated 0.1 m KOH solution at 50 mV s^{-1}. (d) Comparative OER activities of FeCo-DHO/NCNTs before and after 5000 cycles of CV between 0.6 and 1.8 V in O_2-saturated 0.1 m KOH solution at 50 mV s^{-1}.

(ADTs) were performed with cycling within a potential range of 0.6-1.0 V and 1.3-1.8 V in O_2-saturated 0.1 M KOH, respectively (Figure 5-8c,d). The ORR and OER overpotentials of FeCo-DHO/NCNTs exhibited almost no change after 5000 continuous cycles. These results highlight the outstanding performance of FeCo-DHO/NCNTs on both activity and stability. We infer that the salient bifunctional catalytic activity and durability of the FeCo-DHO/NCNTs catalyst can be associated with the covalency-reinforced hybrid structure of the catalyst as well as the structural stability of Fe/Co hydroxides/oxides with crystalline and amorphous phases, which may result in more transportation channels facilitating the diffusion of ORR/OER-relevant species than that of a highly crystalline one. Meanwhile, the interwoven NCNTs network can provide a rapid electro-conduction pathway for charge transport and consequently facilitate the sluggish oxygen electrochemical reaction kinetics.

To demonstrate the potential application of FeCo-DHO/NCNTs catalyst in real zinc-air battery devices, a rechargeable liquid ZAB was first assembled. Ni Foam, GDL, and hydrophobic/breathable membrane were pressed together to form an integrated air electrode. Highly conducting and porous Ni foam is a much better current collector than carbon fiber paper for OER electrocatalysis. Additionally, the hydrophobic and breathable membrane can effectively reduce seepage and evaporation of the electrolyte. For comparison, the battery using Pt/C+RuO_2 mixture catalyst (with the same mass ratio) was examined under the same discharge-charge protocol. Figure 5-9a displays discharge and charge polarization curves of the rechargeable battery using the FeCo-DHO/NCNTs and Pt/C+RuO_2 air electrodes. It reveals that the charge/discharge performance of the FeCo-DHO/NCNTs exhibit a lower overpotential, particularly at high current densities, than that of Pt/C+RuO_2. We can see that the voltage gap between charge and discharge is only 1.003 V at 60 mA cm^{-2}, far outperforming Pt/C+RuO_2 catalyst. The specific capacity was tested at a discharge current density of 20.0 mA cm^{-2} and was

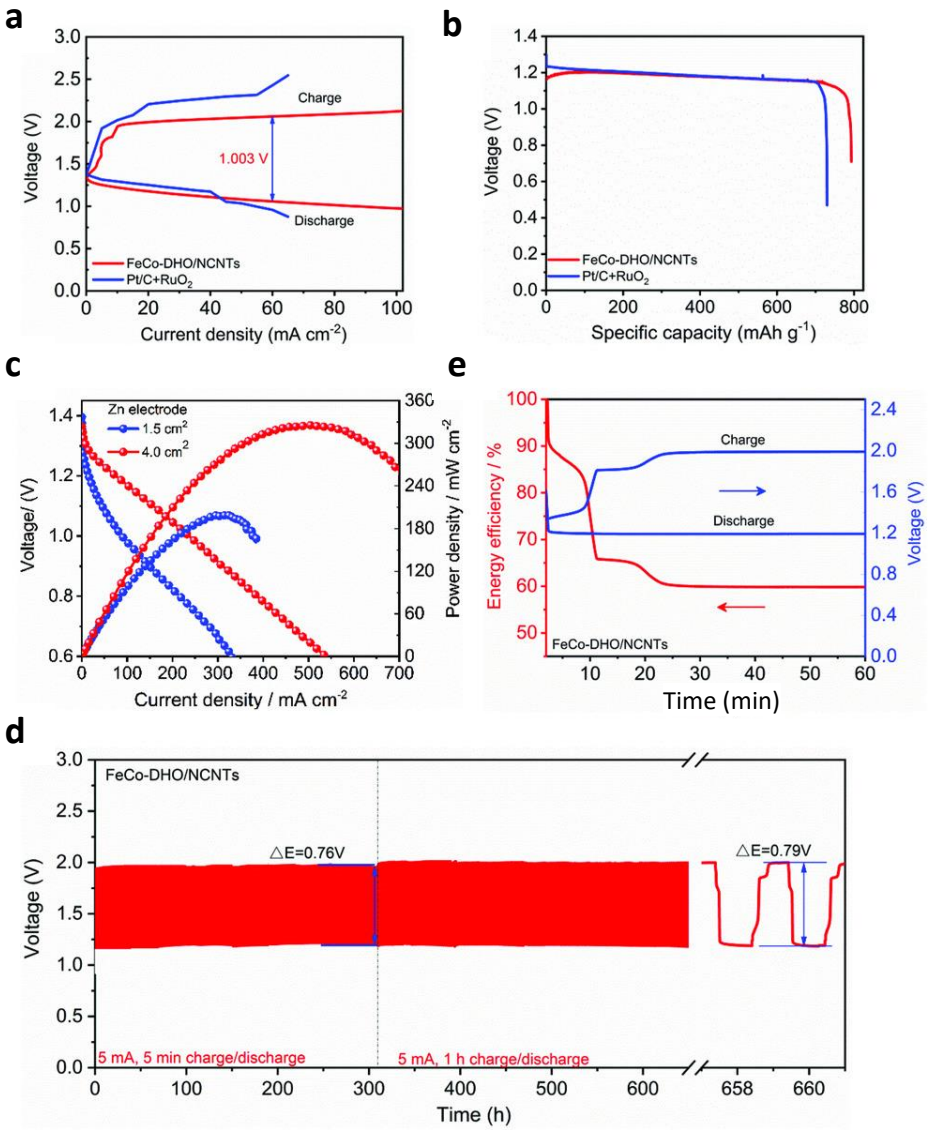

Figure 5-9 (a) Galvanodynamic discharge and charge polarization curves of FeCo-DHO/NCNTs and commercial Pt/C + RuO_2 catalysts. (b) Discharge curves under continuous discharge until complete consumption of Zn at a constant current density of 20 mA cm^{-2}. (c) A polarization curves (V ~ i) and corresponding power density plots of the liquid ZABs with different Zn electrode areas. (d) Galvanostatic discharge and charge cycling stability of FeCo-DHO/NCNTs. (e) Discharge/charge polarization and energy efficiency after cycling stability test.

normalized to the mass of Zn (Figure 5-9b). The specific capacity of FeCo-DHO/NCNTs was measured to be 793.0 mAh g^{-1}, corresponding to large gravimetric energy densities of 930.6 Wh kg^{-1}, which are higher than that of Pt/C+RuO_2 catalyst (854.3 Wh kg^{-1}), indicating that ZAB with

FeCo-DHO/NCNTs catalyst as air electrode has a higher zinc utilization. Additionally, to study the influence of Zn electrode area on the power density for FeCo-DHO/NCNTs battery, we tested the battery performance using a zinc plate with 1.5 and 4.0 cm^2, respectively. As shown in Figure 5-9c, the peak power density of FeCo-DHO/NCNTs with 4.0 cm^2 Zn electrode area could be as high as ~326 mW cm^{-2}, significantly superior to that with 1.5 cm^2 Zn electrode area (193 mW cm^{-2}), suggesting that increasing the specific surface area of Zn electrode is an effective way to improve practical power density. To investigate the charge-discharge cycling performance using the FeCo-DHO/NCNTs air electrode, we performed galvanostatic charge and discharge testing at low (5 mA cm^{-2}) and high (20 mA cm^{-2}) current density, respectively. Meanwhile, the cycling test in a short cycle time is an appropriate way to evaluate the rechargeability of the FeCo-DHO/NCNTs air electrode, while alleviating irreversible impacts from the zinc electrode. The battery with FeCo-DHO/NCNTs catalyst was first cycled at 5 mA cm^{-2} with each cycle being 10 min. As shown in Figure 5-9d, after 1800 cycles (300 h of operation time), the final discharge-charge voltage gap is only 0.76 V without visible voltage losses. Importantly, we continued to cycle the same FeCo-DHO/NCNTs air electrode at 5 mA cm^{-2} with a longer cycle period (2 h). After about 350 h, the voltage gap and energy efficiency (determined by dividing the discharge potential by the charge potential at a certain current density) remain nearly unchanged (0.79 V and >60.0%) (Figure 5-9d,e). Furthermore, to elucidate the impact of cycling at high current density with a long cycle period, we reassembled a battery with FeCo-DHO/NCNTs air electrode and performed galvanostatic charge and discharge testing at 20 mA cm^{-2} with each cycle being 2 h. As shown in Figure 5-10a, the initial discharge-charge voltage gap is only 0.83 V for FeCo-DHO/NCNTs, contributing to energy efficiency of 58.0%. After 175 h of rigorous measurement, the voltage gap and energy efficiency are 0.88 V and 55.0%, respectively. These results indicate that the FeCo-DHO/NCNTs catalyst exhibited excellent stability for ORR and

OER. The slight performance degradation can be ascribed to the loss of strong coupling between FeCo-DHO and NCNTs under the positive potentials.

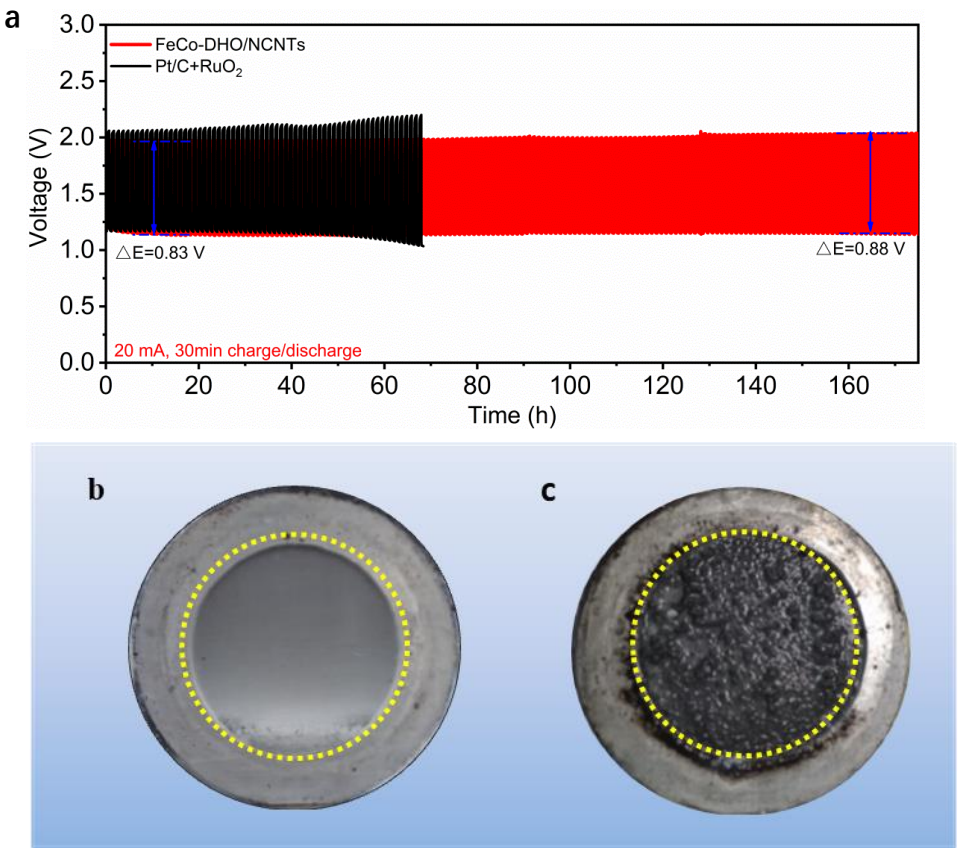

Figure 5-10 (a) Galvanostatic discharge and charge cycling stability of FeCo-DHO/NCNTs and commercial Pt/C@RuO_2 catalysts at a current density of 20 mA cm^{-2} with each cycle being 1.0 hour, for over 170 hrs. The optical pictures of zinc electrodes surface of ZAB using (b) FeCo-DHO/NCNTs and (c) Pt/C@RuO_2 air electrode.

In addition to the catalyst's intrinsic stability, the reversibility of the zinc electrode also plays a significant role in enhancing ZAB systemic stability. During longtime charge and discharge operation in ZABs, we commonly have no alternative but to replace the zinc electrode frequently or adopt a flowing-electrolyte design to guarantee the system normal operation, which mainly due to the major issues that zinc electrode faced (e.g., dendrite growth, shape change, surface passivation). Previous studies of zinc electrodeposition in alkaline solutions have identified that low overpotential can effectively suppress dendrite growth. As we expected, there were no visible

phenomenons of shape change and dendrite growth under low charge potential after a long time charge-discharge process for the battery using FeCo-DHO/NCNTs (Figure 5-10b). Zn-dendrite formation only occurred on the bottom of the zinc electrode due to the positively sloped concentration gradient of $Zn(OH)_4^{2-}$. In contrast, after 60 cycles for the battery using $Pt/C+RuO_2$, obvious shape change and dendrite growth can be observed for the zinc electrode (Figure 5-10c).

Building on the outstanding catalytic activity and liquid battery performance present above, we further demonstrated its potential application in a quasi-solid-state ZAB, which was fabricated using FeCo-DHO/NCNTs catalyst coated carbon paper as air electrode, flexible Zn electrode as

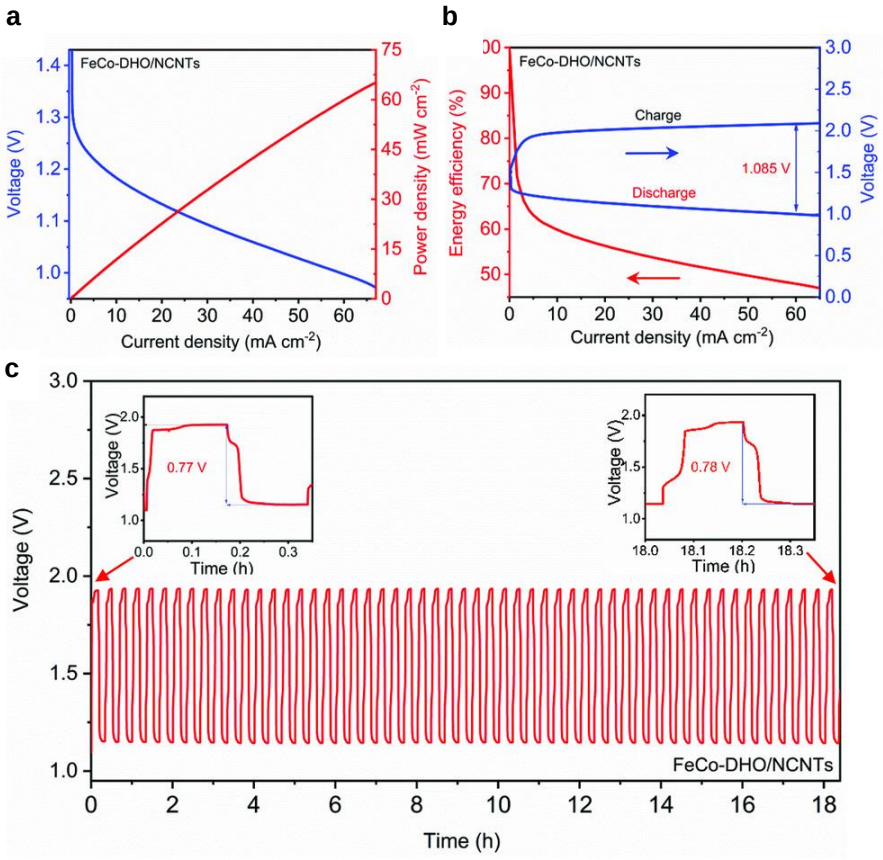

Figure 5-11 (a) A polarization curve (V ~ i) and the corresponding power density plot of the quasi-solid-state ZAB using FeCo-DHO/NCNTs as the cathode catalyst. (b) Galvanodynamic discharge/charge polarization curves and energy efficiency of FeCo-DHO/NCNTs. (c) Galvanostatic discharge/charge cycling stability of FeCo-DHO/NCNTs at a current density of 5 mA cm^{-2} with each cycle being 10 min, for over 18 h.

anode, and alkaline gel electrolyte. Figure 5-11a shows that the open-circuit voltage is measured to be as high as 1.48 V. The FeCo-DHO/NCNTs all-solid-state battery yields a high power density of 60 mW cm^{-2} at 1.0 V. Figure 5-11b exhibits discharge and charge polarization curves of all-solid-state battery with FeCo-DHO/NCNTs air electrode operated under ambient conditions. The voltage gap (1.085 V at 60 mA cm^{-2}) and energy efficiency (60% at 10 mA cm^{-2}) are very close to that in liquid ZAB (1.003 V at 60 mA cm^{-2}, 60% at 10 mA cm^{-2}). Furthermore, to examine the stability of all-solid-state battery, it was cycled at a current density of 5 mA cm^{-2} with each cycle staying 5 min. As shown in Figure 5-11c, the initial discharge-charge voltage gap is only 0.77 V. After 100 cycles (18 h of operation time), the voltage gap remains nearly unchanged (0.78 V), indicating the superior stability of FeCo-DHO/NCNTs in the all-solid-state battery. These results highlight strongly comparable catalytic activity and stability to the liquid battery.

5.4 Conclusion

In summary, for the first time, a simple strategy was developed to fabricate novel nanostructured bimetal Fe/Co hydroxide/oxide nanosheets coupled with NCNTs, which exhibit excellent bifunctional catalytic performance for both ORR and OER. Through the bimetal synergetic coupling interactions, Fe/Co-DHO nano-sheets are strongly anchored on the carbon nanotubes, which provides high electrical contact areas. The formation of FeCo-DHO with dual phases can be ascribed to the Fe/Co bimetal synergetic coupling interactions and specific experimental conditions, which may effectively suppress the formation of the crystalline phase. The obtained FeCo-DHO/NCNTs with unique structure greatly facilitates the sluggish oxygen reaction kinetics and shows excellent activities for both OER and ORR, with a potential gap of 0.7 V for bifunctional oxygen electrocatalysis in 1.0 M KOH, outperforming most reported

bifunctional oxygen electrocatalysts. Importantly, when the FeCo-DHO/NCNTs were applied in reversible liquid and all-solid-state ZABs, excellent charging-discharging performance and cycling behaviors have been achieved, demonstrating their promising potential applications in practical all-solid-state ZABs devices.

Chapter 6 A Self-supported Electrode as a Binder- and Carbon-Free Cathode for Rechargeable Hybrid Zinc Batteries

6.1 Introduction

Recently, flexible electronic devices have gained much attention due to their advantages, such as being lightweight, bendable, rugged, portable, rollable, and potentially foldable.[223-224] To meet the ever-growing demands of the flexible electronics market, a few promising flexible energy storage and conversion systems have been developed, including flexible lithium-ion batteries, sodium-ion batteries, supercapacitors, and solar cells.[146] Very recently, rechargeable Zn-air batteries (ZABs) have emerged as one of the most promising next-generation electrochemical energy storage technologies due to their high theoretical energy density and safety.[5, 135, 224] However, there remain many scientific and technological challenges to be overcome towards the commercialization of rechargeable ZABs, much less the flexible type. Particularly, the main challenge is the development of air-breathing electrodes with high electrocatalytic activity and stability toward both oxygen reduction reaction (ORR) and oxygen evolution reaction (OER).[121, 172, 225] Previous electrode fabrication always involved the use of powder catalysts, gas diffusion layers, and polymer binders together with conductive carbon black.[14, 135] One critical issue faced by the carbonaceous cathode is the carbon corrosion during charging, resulting in a gradual performance decay.[20, 198] Moreover, the introduction of low conductive binders will limit electron conductance and mass transport due to some undesirable consequences, such as limited active surface area, microstructure destruction, a decrease of volume.[154] Meanwhile, the binder degradation over long charge/discharge cycling operation eventually leads to detachment of catalysts from the substrates. Therefore, there is an urgent need to design and fabricate electrochemically stable and highly effective binder-free air electrodes.

Meanwhile, to meet the severe requirements of flexible devices, binder-free self-supported electrocatalysts directly growing on conductive and flexible substrates have attracted tremendous interest. Electroactive species grown on conductive substrates show many structural advantages compared with the conventional electrode fabrication process: 1) greatly simplifying the design and fabrication procedure of air electrodes, 2) the strong adhesion between the electrocatalysts and the conductive substrates can effectively reduce catalysts' mechanical shedding from supporting substrates during continuous O_2 evolution, 3) the advanced nanostructures like nanowire/plate/pillar/flower arrays afford large electroactive surface area, plenty of exposed active sites, and efficient mass transport, consequently promoting reaction kinetics. Up to date, extensive research work on self-supported carbon-free air cathodes, mostly focusing on the modification of non-carbon 3D porous Ni foam and stainless steel (SS) substrates by various technologies, such as hydrothermal process and electro-deposition.[226-227] However, the influences of the Ni substrate on the electroactive species are always ignored.[228-233] Sometimes, the Ni foam not only acts as a substrate but also serves as a slow-releasing nickel precursor that is induced by redox-etching of oxidant species. Another non-carbon SS support is an iron-based alloy that is low-cost and oxidation resistant. SS often contains Ni, Cr, and S as an additive, which is prone to induce additional catalytic active species (e.g., FeCr alloy, FeNi alloy, NiS_x, NiO_x) and thus greatly improves the kinetics OER.[149 234]

Here, we report a strategy to fabricate a flexible self-supported sandwich structured electrode with $Co_{3-x}Ni_xO_4/Co_3O_4$ nanowire arrays by simply pressing two NF@$Co_{3-x}Ni_xO_4$ and one SS@Co_3O_4 air cathodes together. The novel structure exhibited excellent catalytic ORR/OER activity and stability, as well as the Zn-air battery performance due to the following reasons: (1) At the atomic scale, the uniform Ni doping significantly remodels the surface structure of the porous $Co_{3-x}Ni_xO_4$ nanowire and consequently increases the intrinsic electrochemical

performance; (2) The abundant Co^{2+}/Ni^{2+} and oxygen vacancies on the surface significantly improve the ORR and OER performance. Meanwhile, combining the super mechanical flexibility and intrinsic high OER activity of SS, the assembled porous air electrode can take full advantage of the sandwich structure to promote the energy efficiency of NS@$Co_{3-x}Ni_xO_4$/Co_3O_4; (3) Rechargeable ZAB is assembled by employing NS@$Co_{3-x}Ni_xO_4$/Co_3O_4 as both a new class of cathode and current collector to replace the conventional rigid and bulky counterparts. Consequently, the ZAB with NS@$Co_{3-x}Ni_xO_4$/Co_3O_4 electrode demonstrates a much lower charge-discharge potential gap than that of NF@$Co_{3-x}Ni_xO_4$ and SS@Co_3O_4 electrodes, respectively; (4) Additionally, the multifunctional $Co_{3-x}Ni_xO_4$ shows good redox electrochemical performance, providing a Zn-based battery with two electrochemical processes: process I, the first plateau at 1.92 V ascribed to Zn-$Co_{3-x}Ni_xO_4$ battery, and process II, the second plateau at 1.25 V resulting from ZAB. The Zn-air battery part offers a low potential gap of 0.696 V, high energy efficiency of 62.2%, and long-cycling stability of 200 h for 200 cycles at a current density of 5 mA cm^{-2}. This protocol undoubtedly opens a new avenue to strategically design high-efficiency and stable self-supported air electrodes for electrochemical energy storage devices.

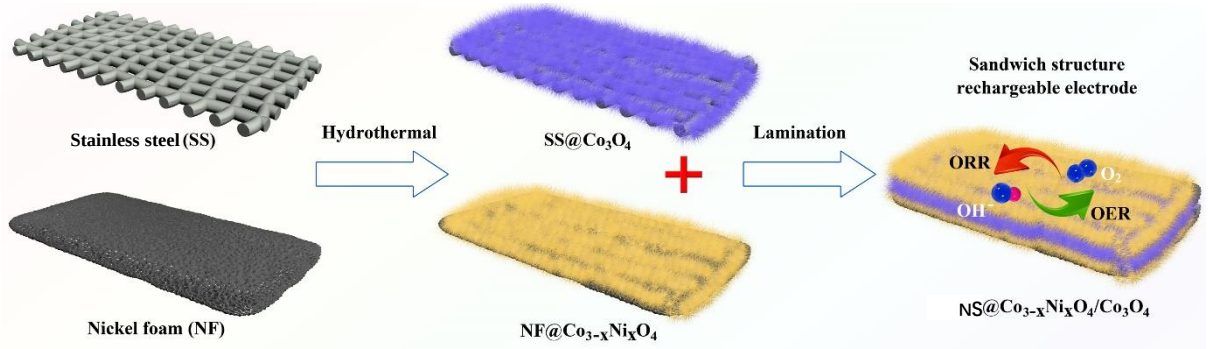

Figure 6-1 Schematic illustration toward the synthetic process of NS@$Co_{3-x}Ni_xO_4$/Co_3O_4. The sandwich structure consists of two pieces of NF@$Co_{3-x}Ni_xO_4$ separated by one piece of SS@ Co_3O_4.

6.2 Experimental Section

6.2.1 Synthesis of NF@$Co_{3-x}Ni_xO_4$ electrode

The $Co_3Ni_{3-x}O_4/Co_3O_4$ nanowire on Ni foam (the thickness of 1.7 mm) was obtained by a facile hydrothermal method followed by the calcination method. First, the Ni foam, 2 cm × 4 cm, was treated with 2 M HCl solution with ultrasonic for 10 min to remove the surface oxide layer, and it was washed with ethanol and water several times. Then, 2.5 g of $Co(NO_3)_2$ $6H_2O$, 2.5 mmol of $CO(NH_2)_2$, and 0.3 g NH_4F were dissolved in 40 mL of distilled water. Next, the resulting solution was transferred into a 50 mL Teflon-lined stainless steel autoclave, and the Ni foam was immersed into the precursor solution. The Ni foam not only acts as a substrate but also serves as a slow-releasing nickel precursor. The autoclave was sealed and heated at 90 °C for 12 h and then cooled to room temperature naturally. The pink-colored cobalt carbonated hydroxide nanowire arrays grown on Ni foam were obtained and then were rinsed with distilled water. Finally, the NF@$Co_{3-x}Ni_xO_4$ was obtained by calcinating under 400 ^oC for 2 h in the air (loading: ~ 2mg/cm^2). The substrate is in strong contact with the active material, which contributes to the low internal resistance of the electrode.

6.2.2 Synthesis of SS@Co_3O_4 electrode

To elucidate the effect of substrate on the composition and electrocatalytic activity, the SS@Co_3O_4 were prepared by the same procedure. The stainless steel wire cloth (SS) (Geo. Renteln Inc.), 2 cm × 4 cm, was etched with 2 M HCl solution with ultrasonic for 10 min to remove the surface oxide layer and make the SS surface rougher. Because SS support is an iron-based alloy that is oxidation resistant, SS only acts as a substrate without involving in the synthesis of active species. Finally, the mono-metallic Co_3O_4 nanowire arrays supported on the

SS (SS@Co_3O_4) were obtained by calcinating under 400 ^oC for 2 h in the air (loading: ~ 0.8mg/cm^2).

6.2.3 Synthesis of NS@$Co_{3-x}Ni_xO_4$/Co_3O_4 electrode

To obtain high catalyst loading and combine the super mechanical flexibility and intrinsic high OER activity of SS, the self-supported sandwich structure air electrode (NS@$Co_{3-x}Ni_xO_4$/Co_3O_4) was prepared by pressing NF@$Co_{3-x}Ni_xO_4$ and SS@Co_3O_4 air cathodes together to form a dense, interconnected, and conducting network (Figure 6-1).

6.2.4 Fabrication of the liquid Zn-air battery

The Zn-air batteries were tested in home-built electrochemical cells, the electrolyte was 6 M KOH with 0.2 M zinc acetate solution. The liquid rechargeable hybrid zinc battery was assembled with prepared self-supported electrodes, a polished zinc plate. Then, self-supported electrodes and hydrophobic/breathable membrane were pressed together. Polarization data was collected using the galvanodynamic method at a scan rate of 1.0 mA s^{-1}. Single-cell discharge and charge cycling tests were operated by the battery testing system.

6.2.5 Material characterizations

The morphologies and structures of the samples were characterized using a high-resolution transmission electron microscope (HRTEM, JEM-2100) operated at 200 kV and a scanning electron microscope (SEM, Quanta 450 ESEM, FEI) operated at 10 kV. Energy Dispersive Spectroscopy (EDS) analysis was carried out on Tecnai TEM with EDS detector under scanning unit electron microscopy (STEM) mode. The crystal structure of the catalysts was analyzed by X-

ray diffraction (XRD) (40 kV, 25 mA, Cu Kα radiation, λ=1.5418 Å); The surface properties were analyzed by X-ray photoelectron spectroscopy (XPS, VG ESCALAB 220i-XL) equipped with a hemispherical analyzer for a Twin Anode X-ray Source. The fine structure of the photoelectron lines was treated using Casa XPS software (2.3.15 Version). The surface areas of the catalysts were measured through N_2 sorption isotherms that were collected using Quantachrome Instruments Autosorb-1 at liquid nitrogen temperature. The Co K-edge X-ray absorption near-edge structure (XANES) and Extended X-ray Absorption Fine Structure (EXAFS) data were collected on the 06ID-1 Hard X-ray MicroAnalysis (HXMA) beamline at the Canadian Light Source. During data collection, the CLS storage ring (2.9 GeV) was operated under 250 mA mode and the HXMA superconducting wiggler was run at 1.9 T. Measurements were made at room temperature in fluorescence mode using a 32-element Ge detector. Data collection configuration was using metal Co foil as energy calibration by in step calibration for every data set. The spectra were normalized with respect to the edge height after subtracting the pre-edge and post-edge backgrounds, and then convert the data from energy space to k space using Athena software.

6.2.4 Electrochemical measurements

The electrocatalytic performance for oxygen reduction (ORR) and evolution (OER) reactions was carried out in a standard three-electrode cell with a bipotentiostat (Pine, Model PGSTAT-72637) workstation at room temperature. All electrochemical tests were carried out in either O_2-saturated or N_2-saturated 1.0 M KOH electrolyte solution controlled at room temperature. To subtract the background capacitive current, linear sweep voltammetry was conducted under the same conditions in an N_2-saturated electrolyte. Catalyst powder cast on the glass carbon (GC) disk electrode (RDE, PINE Research Instrumentation) was used as the

working electrode. A Pt wire and a Hg/HgO (KOH, (20%)) were used as the counter and reference electrodes, respectively. In this paper, all potentials were converted to a reversible hydrogen electrode (RHE). Before use, the GC electrodes are polished using aqueous alumina suspension on felt polishing pads. The catalyst ink was prepared by ultrasonically mixing 2.0 mg catalyst with 0.4 mL of isopropyl alcohol and 10 mL of 5 wt.% Nafion® for more than 30 minutes.

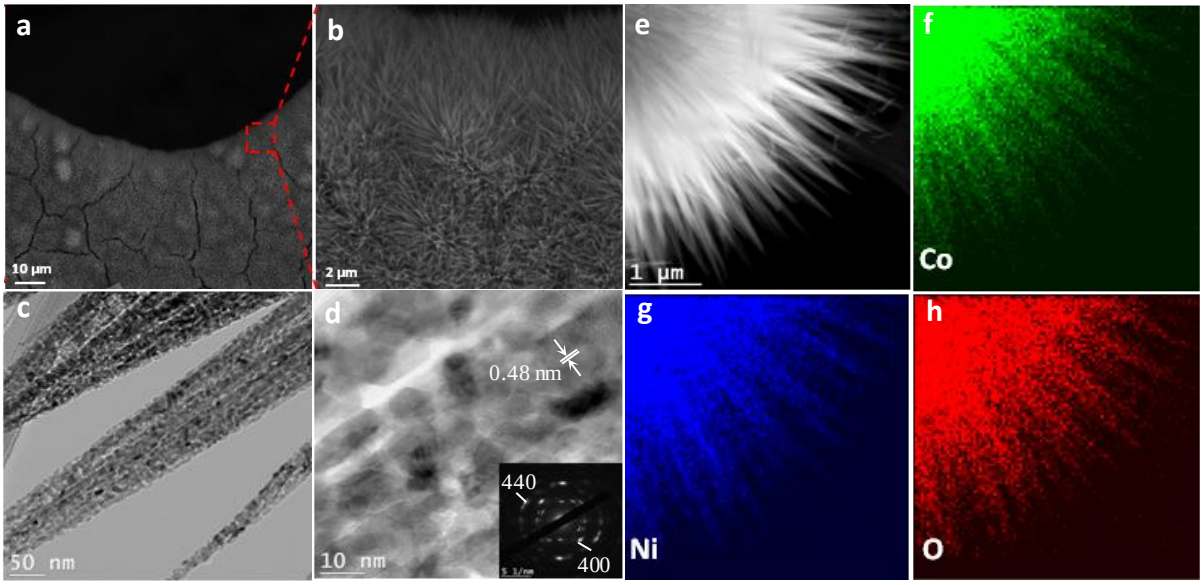

Figure 6-2 (a, b) SEM images of NF@$Co_{3-x}Ni_xO_4$. (c, d) Bright-field TEM images of NF@$Co_{3-x}Ni_xO_4$. Inset: the corresponding FFT diffraction pattern of the NF@$Co_{3-x}Ni_xO_4$. (e-h) Dark-field TEM image of NF@$Co_{3-x}Ni_xO_4$ and the corresponding elemental mapping of Co, Ni, and O.

6.3 Results and Discussion

6.3.1 Synthesis and Characterization

The electrode fabrication strategy for NF@$Co_{3-x}Ni_xO_4$ and SS@Co_3O_4 electrodes is schematically illustrated in the Experimental Section. The substituted cobalt oxides ($Co_{3-x}Ni_xO_4$) nanowire on Ni foam (NF@$Co_{3-x}Ni_xO_4$) was obtained by a facile hydrothermal followed by a

calcination method. Metal nickel can be gradually oxidized under hydrothermal conditions. Figure 6-2a,b show the scanning electron microscopy (SEM) images of the NF@$Co_{3-x}Ni_xO_4$ and $Co_{3-x}Ni_xO_4$ nanowire. It can be seen that aligned $Co_{3-x}Ni_xO_4$ grown nearly vertically to the macroscopic 3D skeleton of Ni foam, forming needle nanowires arrays. To elucidate the effect of substrate on the composition and electrocatalytic activity, the SS@Co_3O_4 were prepared by the same procedure. Because SS support is an iron-based alloy that is strongly oxidation resistant, so SS only acts as a substrate without involving in the synthesis of active species. The EDS shows a relatively low metal to oxygen atom ratio (0.67 to 1) for the $Co_{3-x}Ni_xO_4$ scraped from NF@$Co_{3-x}Ni_xO_4$, which implies the formation of oxygen vacancies in the $Co_{3-x}Ni_xO_4$ and Co_3O_4. The structure and morphology of the $Co_{3-x}Ni_xO_4$ were further investigated by TEM. As illustrated in Figure 6-2c,d, the $Co_{3-x}Ni_xO_4$ is composed of nanocrystallites of 8-10 nm in size, forming a highly porous surface morphology. The nanostructure can increase the electroactive area for ORR/OER reactions, providing effective electrolyte-accessible channels for mass transportation. Figure 6-2d is an HRTEM image of the nanowire. The spacing between the adjacent fringes is ~0.48 nm, slightly higher than the theoretical interplane spacing of spinel Co_3O_4 (111) planes (0.47 nm), which can be ascribed to the Ni doping into the lattice structure of Co_3O_4. TEM

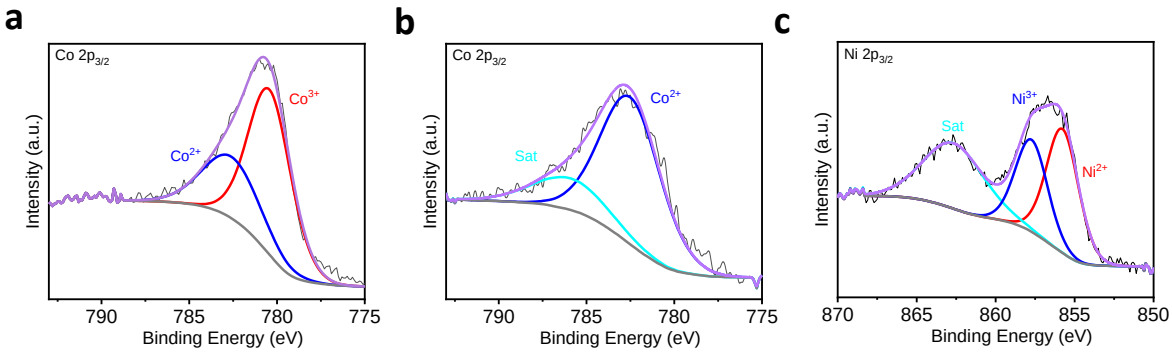

Figure 6-3 The high-resolution XPS spectra of (a) Co $2p_{3/2}$ for Co_3O_4 nanowire, (b) Co $2p_{3/2}$ and (c) Ni $2p_{3/2}$ for $Co_{3-x}Ni_xO_4$.

elemental mapping images further reveal that Co, Ni, and O are uniformly distributed along the needle nanowires of $Co_{3-x}Ni_xO_4$ (Figure 6-2e-h).

Since the O_2 electrocatalytic reaction mainly occurs on the surface of catalysts, it is essential to investigate the surface composition and structure of $Co_{3-x}Ni_xO_4$ and Co_3O_4 nanowire by XPS analysis. Figure 6-3a,b show the high-resolution Co $2p_{3/2}$ spectra of $Co_{3-x}Ni_xO_4$ and Co_3O_4 nanowire. In Co_3O_4 nanowire, the spectrum of Co $2p_{3/2}$ consists of two spin-orbit doublets characteristic of Co^{2+} and Co^{3+}. The relative atomic ratio of Co^{2+}/Co^{3+} could be obtained by comparing the area that the fitted curve covered. It could be obtained that the atomic ratio of Co^{2+}/Co^{3+} on the surface of the $Co_{3-x}Ni_xO_4$ is 1:2. In $Co_{3-x}Ni_xO_4$, the peak fitting analyses of the Co $2p_{3/2}$ identifies only one chemical state of Co, i.e., Co^{2+} at 782.5, indicating that complete Ni substitution of Co^{3+} took place in the $Co_{3-x}Ni_xO_4$ surface and lead to the change of local environment of the Co site. In contrast to Co_3O_4 nanowire, the Co $2p_{3/2}$ signal of $Co_{3-x}Ni_xO_4$ also exhibits a strong satellite structure on the higher binding energy side. This satellite structure can be ascribed to the shake-up process of the Co^{2+} compound in the high spin state. Figure 6-3c shows the high-resolution Ni $2p_{3/2}$ spectra of $Co_{3-x}Ni_xO_4$ nanowire. The spectrum of Ni is also best fitted with two spin-orbit doublets that are corresponding to Ni^{2+} and Ni^{3+}, but the strong satellite peaks indicate that Ni^{2+} represents a significant proportion of the Ni^{2+} in the $Co_{3-x}Ni_xO_4$ sample. Ni^{2+} has been suggested to be a more effective active site for the OER.[235]

X-ray absorption fine structure spectroscopy (XAFS) measurements at the Co K-edge were also carried out to investigate the local chemistry changes of the Co atom. Figure 6-4a shows the normalized X-ray absorption near-edge structure (XANES) spectra at the Co K-edge of NF@$Co_{3-x}Ni_xO_4$ and SS@Co_3O_4. The XANES spectra of commercial Co_3O_4 are also included for reference. Spinel Co_3O_4 is composed of two types of geometrical cobalt ions with different oxidation states: one Co^{2+} ion in the tetrahedral site and two Co^{3+} ions in the octahedral site

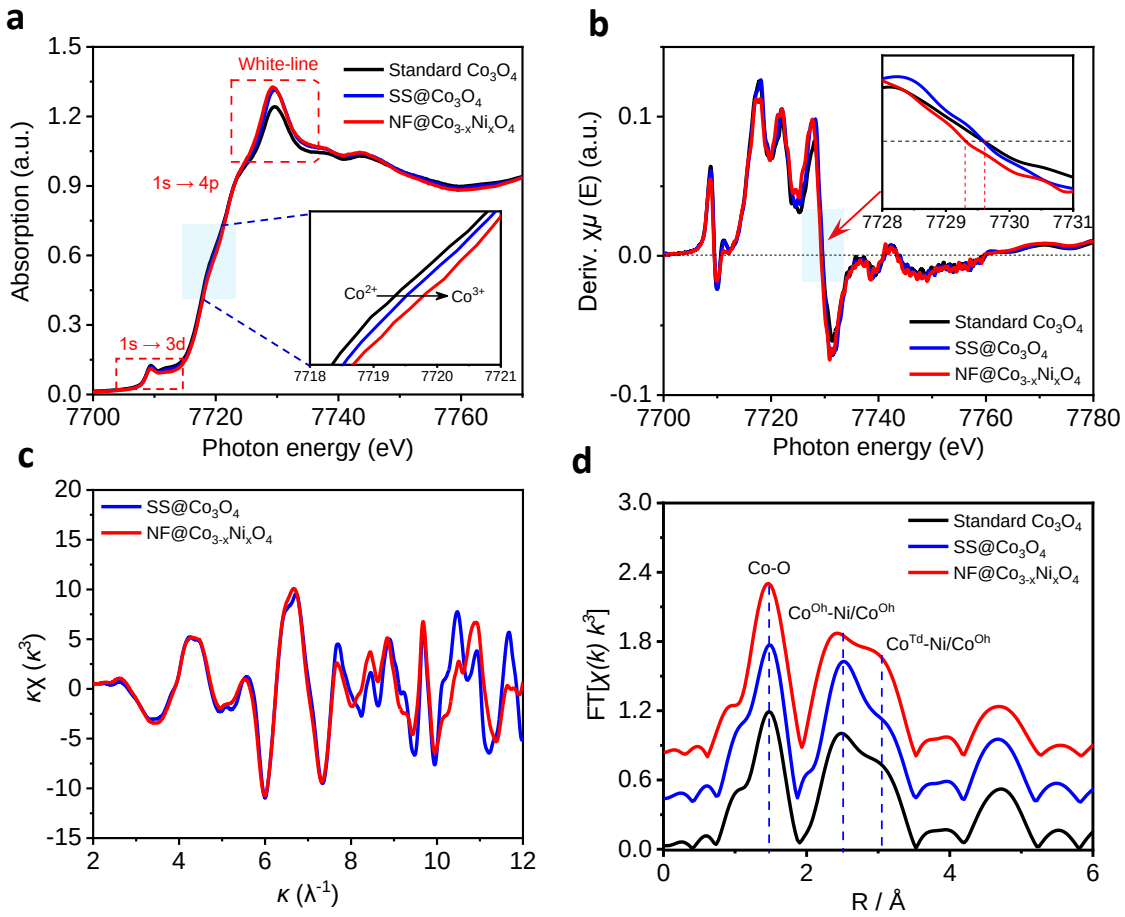

Figure 6-4 (a) Normalized Co K-edge XANES spectra of SS@Co_3O_4, NF@$Co_{3-x}Ni_xO_4$, and Co_3O_4 standard sample with their magnified inset. (b) The corresponding first derivatives of XANES spectra of SS@Co_3O_4 and NF@$Co_{3-x}Ni_xO_4$. (c) Normalized Co K-edge EXAFS oscillation of SS@Co_3O_4 and NF@$Co_{3-x}Ni_xO_4$. (d) The Fourier transforms (FT) spectra of standard Co_3O_4, SS@Co_3O_4, and NF@$Co_{3-x}Ni_xO_4$.

(denoted as Co^{Td} and Co^{Oh}, respectively).[236-237] As shown in Figure 6-4a, the pre-edge peak is associated with the photoelectron transitions to the unoccupied 3d states (1s-3d) hybridized with Co 4p and O 2p states, whereas the main absorption peak relates the transitions from Co 1s core level to unoccupied 4p states (1s-4p).[238-240] The main absorption edge position and peak shapes of NF@$Co_{3-x}Ni_xO_4$ and SS@Co_3O_4 are very similar to the commercial Co_3O_4. However, the pre-edge absorption peak at ≈7709.5 eV and the shoulder of NF@$Co_{3-x}Ni_xO_4$ is lower than those of the SS@Co_3O_4 and commercial Co_3O_4. Additionally, the white-line peak position of NF@Co_{3-}

$_xNi_xO_4$ slightly shifted to lower energy compared to the SS@Co_3O_4 and commercial Co_3O_4 spectra (Figure 6-4b). These changes upon Ni incorporation can be ascribed to the change of the local geometry and environment of the Co site, such as the ratio of Co^{2+}/Co^{3+} or the partial substitution of Co atom with Ni atom. Furthermore, the Co K-edge spectra of NF@$Co_{3-x}Ni_xO_4$ are slightly shifted to higher energy compared to the SS@Co_3O_4 and commercial Co_3O_4 spectra (Figure 6-4a inset). Because the energy shift is below 1 eV, the estimated difference between oxidation states of cobalt is less than 0.1 unit,[237] the average Co oxidation states for NF@$Co_{3-x}Ni_xO_4$ are slightly higher than +2.67, indicating that internal Co^{3+} was preserved in $Co_{3-x}Ni_xO_4$. The structural position of NF@$Co_{3x}Ni_xO_4$ was also probed by extended X-ray absorption fine structure spectroscopy (EXAFS). As displayed in Figure 6-4a, the Co K-edge extended EXAFS oscillation of NF@$Co_{3-x}Ni_xO_4$ and SS@Co_3O_4 presented a similar oscillation and amplitude intensity, indicating the similar local atomic arrangements of the nanowire. The partial replacement of Co by Ni atom is clearly shown by the phase shift in the part of the EXAFS Fourier transforms (FT) (Figure 6-4b). For the SS@Co_3O_4 and commercial Co_3O_4, the first peak at 1.5 Å can be corresponding to single scattering paths of the metal ion to the closest neighboring crystal oxygen. The second and third peaks at 2.5 and 3.0 Å, respectively, are assigned to the scattering paths of the cobalt ion to its closest neighboring cobalt ion in the octahedral or tetrahedral site, depending on the position where the cobalt ion initially stays.[236] Positions of the Co-O pairs of the three samples are almost identical. However, compare with the SS@Co_3O_4, the intensities of the Co^{Oh}-Ni/Co^{Oh} and Co^{Td}-Ni/Co^{Oh} peaks of NF@$Co_{3x}Ni_xO_4$ weaken and strengthen, respectively, which indicate the substitution of Co^{3+} by Ni and the increase of the Co^{2+}. These results are consistent with XPS results. The coordination of two metal species and disordered structure attributed to the Ni substitution commonly provide both-way rich active sites to improve bifunctional catalytic activities.[241]

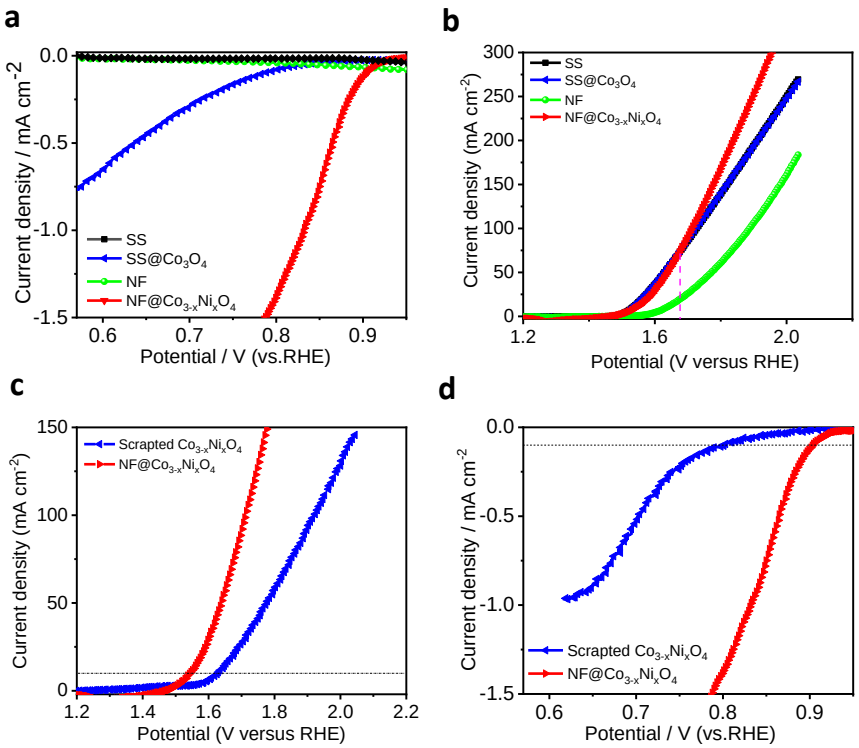

Figure 6-5 (a) ORR and (b) OER polarization curves of SS, NF, SS@Co_3O_4, and NF@$Co_{3-x}Ni_xO_4$ in O_2-saturated 1.0 M KOH at a scan rate of 5 mV s^{-1}. (c) ORR and (d) OER polarization curves of NF@$Co_{3-x}Ni_xO_4$ and scraped $Co_{3-x}Ni_xO_4$.

6.3.2 Oxygen electrocatalysis performance evaluation for ORR and OER

Electrocatalysts in situ grown on conductive substrates with novel architectures like nanowire arrays as binder-free air electrodes have many structural advantages in comparison with their powdery counterparts. To evaluate the O_2 electrocatalytic performance of the NF, SS, NF@$Co_{3-x}Ni_xO_4$, and SS@Co_3O_4 electrodes, we performed linear sweep voltammetry (LSV) measurements without rotation in a 1.0 M KOH solution using a standard three-electrode system with a Hg/HgO reference electrode. NF@$Co_{3-x}Ni_xO_4$ shows the best activity in terms of the most positive onset potential (E_{onset}; 0.91 V, vs 0.83 V for SS@Co_3O_4, determined as the potential at 0.1 mA cm^{-2}) and much higher current density at 0.80 V (1.4 mA cm^{-2}) for NF@$Co_{3-x}Ni_xO_4$ than that of SS@Co_3O_4 (0.1 mA cm^{-2}, 0.80 V) (Figure 6-5a). Meanwhile, we found that simple NF

and SS don't show ORR activity. Figure 6-5b shows the LSV curves of the electrodes for OER at 5 mV s^{-1} in 1.0 M KOH solution. It can be seen that the NF@$Co_{3-x}Ni_xO_4$ electrode exhibits the highest OER catalytic activity (highest levels of current density) in the high potential window (1.675-2.2 V). An overpotential of only 310 mV is required for the NF@$Co_{3-x}Ni_xO_4$ electrode to reach a current density of 10 mA cm^{-2}. The NF and SS were also tested for comparison. The poor OER activity of the Ni foam suggests that the high catalytic activity of the NF@$Co_{3-x}Ni_xO_4$ electrode originates from the $Co_{3-x}Ni_xO_4$ nanowire. Moreover, for the SS and SS@Co_3O_4, the OER polarization curves are almost coincided with each other, indicating that Co_3O_4 grown on the SS does not change the intrinsic OER catalytic activity of iron-based SS alloy. An overpotential of only 300 mV is required for the SS and SS@Co_3O_4 electrodes to reach a current density of 10 mA cm^{-2}. Additionally, to elucidate the practical benefit of NF@$Co_{3-x}Ni_xO_4$ as the binder-free electrode, the electrocatalytic activity of powder-ink based $Co_{3-x}Ni_xO_4$ for ORR and OER sprayed on the carbon paper with the same catalyst loading was also evaluated in 1.0 M KOH solution for comparison. The powder-ink-based catalyst slurry composed of Nafion® binders and $Co_{3-x}Ni_xO_4$ nanostructures scraped from the NF substrate was prepared by ultrasonically mixing 2.0 mg catalyst with 0.4 mL of isopropyl alcohol and 10 mL of 5 wt.% Nafion® for more than 30 minutes. Figure 6-5c,d compares the powder-ink-based $Co_{3-x}Ni_xO_4$ and NF@$Co_{3-x}Ni_xO_4$ electrodes tested under the same conditions. In terms of onset potential for ORR and the overpotential at the current density of 10 mA cm^{-2}, NF@$Co_{3-x}Ni_xO_4$ exhibited much better catalytic performance than that of the ink-based $Co_{3-x}Ni_xO_4$ with the binder.

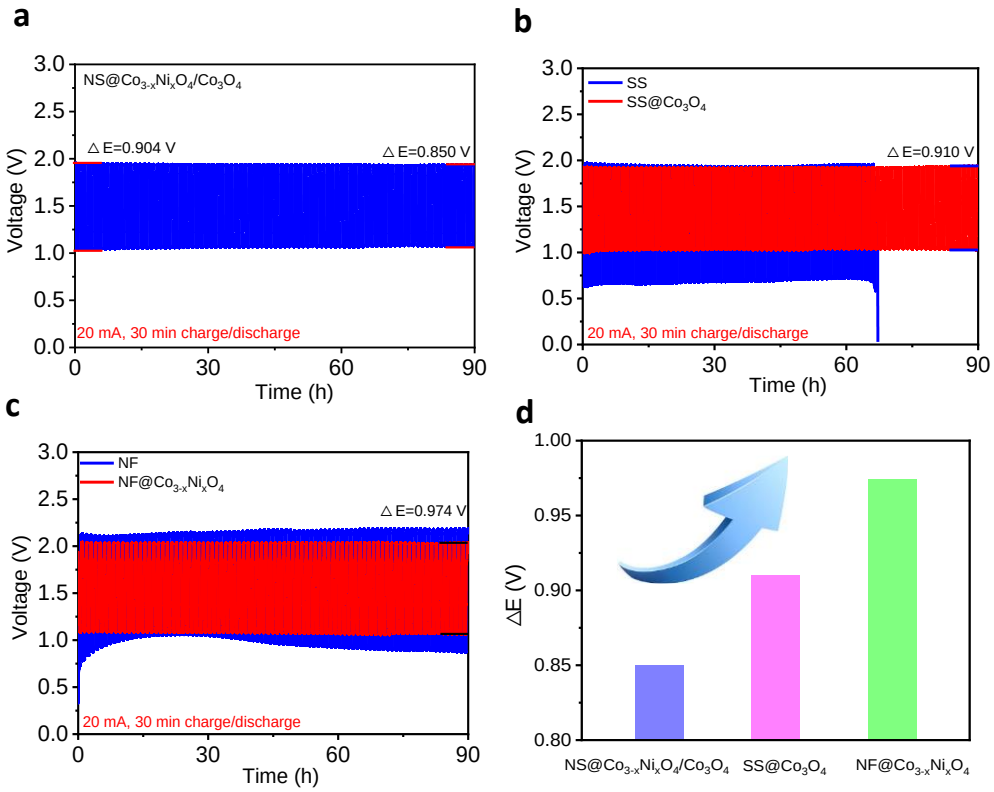

Figure 6-6 (a-c) Galvanostatic discharge and charge cycling stability of $NS@Co_{3-x}Ni_xO_4/Co_3O_4$, $SS@Co_3O_4$, SS, NF, and $NF@Co_{3-x}Ni_xO_4$ electrodes at a current density of 20 mA cm^{-2} with a cycle being 1 h. (d) The voltage gap △E (E_{charge}-$E_{discharge}$) after 90 h cycling operation.

To explore the feasibility of the self-supported and binder-free electrode for future practical applications, a single-cell practical liquid ZAB was assembled using the $NF@Co_{3-x}Ni_xO_4$ and $SS@Co_3O_4$ as the air electrode and oxygen in atmospheric air as the main source of fuel. Additionally, liquid ZABs with NF and SS electrodes were also assembled for comparison. Furthermore, to obtain high catalyst loading and combine the super mechanical flexibility and intrinsic high OER activity of SS, self-supported sandwich structure air electrode ($NS@Co_{3-x}Ni_xO_4/Co_3O_4$) prepared by pressing $NF@Co_{3-x}Ni_xO_4$ and $SS@Co_3O_4$ air cathodes together to form a dense, interconnected, and conducting network was also tested in the practical liquid ZAB system (Figure 6-6a).[242] Figure 6-6b shows that SS exhibits very poor discharge performance at a

current density of 20 mA cm^{-2}. After operating only about 70 cycles, it displays severely enlarged overpotentials derived from decreased discharge potential. However, SS shows similar initial charge performance (the charge potential of 1.968 V) with SS@Co_3O_4 (the charge potential of 1.924 V), consistent with the half-cell testing results. The SS@Co_3O_4 electrode exhibits a superior initial charge potential of 1.92 V (Figure 6-6b), which can contribute to excellent rechargeability. Even after 90 h cycling operation, the bifunctional performance of the NS@$Co_{3-x}Ni_xO_4/Co_3O_4$ and SS@Co_3O_4 electrodes show a slight decrease in the voltage gap △E. In contrast, the performance of the NF@$Co_{3-x}Ni_xO_4$ electrode shows a slight increase after 90 h cycling operation due to the high initial charge potential (2.04 V). The energy efficiency of the battery can be determined by dividing the discharge potential by the charge potential at a certain current density. As shown in Figure 6-6a, after 90 cycles (90 h of operation time), the discharge-charge voltage gap of NS@$Co_{3-x}Ni_xO_4/Co_3O_4$ is only 0.85 V, contributing to energy efficiency of 60.4%, which are better than that of SS@Co_3O_4 (0.91 V and 60.0%), NF@$Co_{3-x}Ni_xO_4$ (0.974 V and 60.0%) and NF (1.31 V and 39.0%), respectively (Figure 6-6b,c). The significantly improved bifunctional performances of NS@$Co_{3-x}Ni_xO_4/Co_3O_4$ indicate the assembled porous air electrode can take full advantage of the sandwich structure to promote the electrocatalytic reaction kinetics of NS@$Co_{3-x}Ni_xO_4/Co_3O_4$. Furthermore, ZAB was also cycled at a current density of 5.0 mA cm^{-2} with each cycle being 1 h. As shown in Figure 6-7a, the initial discharge-charge voltage gap is only 0.696 V, contributing to energy efficiency of 62.9%. After 200 cycles (200 h of operation time), both the voltage gap and energy efficiency remain nearly unchanged (0.711 V and 62.2%), indicating the superior stability of NS@$Co_{3-x}Ni_xO_4/Co_3O_4$ in ZAB. The Zn-air battery with NS@$Co_{3-x}Ni_xO_4$ can be discharged from 1.0 to a high current density of 20 mA cm^{-2} (Figure 6-7b), suggesting that it can be operated at a wide range of current densities. The superior performance of the NS@$Co_{3-x}Ni_xO_4/Co_3O_4$ electrocatalyst is mainly attributed to the unique

composite architecture, high loading of active catalyst per unit volume, and intrinsic high OER activity of SS.

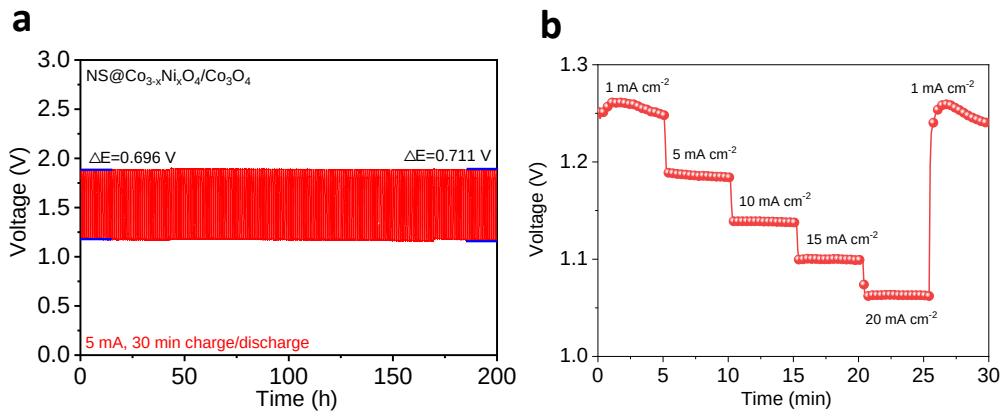

Figure 6-7 (a) Galvanostatic discharge and charge cycling stability of NS@$Co_{3-x}Ni_xO_4/Co_3O_4$ catalyst at a current density of 5 mA cm^{-2} with a cycle being 1 h. (b) Discharge curves at different current densities.

6.3.3 Faradaic redox reaction performance evaluation

Furthermore, the ZAB system, as a semiclosed system, cannot work under an oxygen-free environment. To solve these problems, the integration of multiple electrochemical reactions in one system has been demonstrated for hybridizing nickel/cobalt-zinc-based batteries and ZAB to achieve both high energy and power density.[243-244] Compared with the ZABs, nickel/cobalt-zinc-based batteries exhibit high-operating voltage and can remain operational in oxygen-free environments. However, the aqueous nickel/cobalt-zinc-based batteries cannot continuously discharge for a long time due to their relatively low energy density and restricted energy release.[245] Considering the features of ZABs and nickel/cobalt-zinc-based batteries, they are complementary in many aspects, including energy density, power density, voltage output, and usage scenario. As shown in Figure 6-8a, the galvanodynamic charge/discharge voltage behaviors of the battery using NF@$Co_{3-x}Ni_xO_4$ show obvious features of a hybrid zinc battery.[246-247] For the battery using NF@$Co_{3-x}Ni_xO_4$ electrode, the initial charge voltage profiles exhibit a flat plateau at

1.38 V, which is different from that of an individual ZAB. In the following charge process, the charge voltage profiles exhibit a flat plateau at 1.82 V, similar to typical discharge curves of ZABs. The plateau at 1.38 V is assigned to the oxidation reaction of CoNi-O → CoNi-O-OH, whereas the plateau at 1.82 V is attributed to the OER process. Correspondingly, the discharge plateau at 1.67 V originates from the cation reduction reaction of CoNi-O-OH → CoNi-O and the voltage plateau at 1.10 V stems from ORR behavior. As a comparison, the battery using SS, NF, and SS@Co_3O_4 were examined under the same test condition. As expected, SS and NF only show the features of ZAB (Figure 6-8c,d). For the battery using the SS@Co_3O_4 electrode (Figure 6-8b), despite the similar initial charge trend curve, the discharge potential decreases much faster than that of NF@$Co_{3-x}Ni_xO_4$. These results indicate that NF@$Co_{3-x}Ni_xO_4$

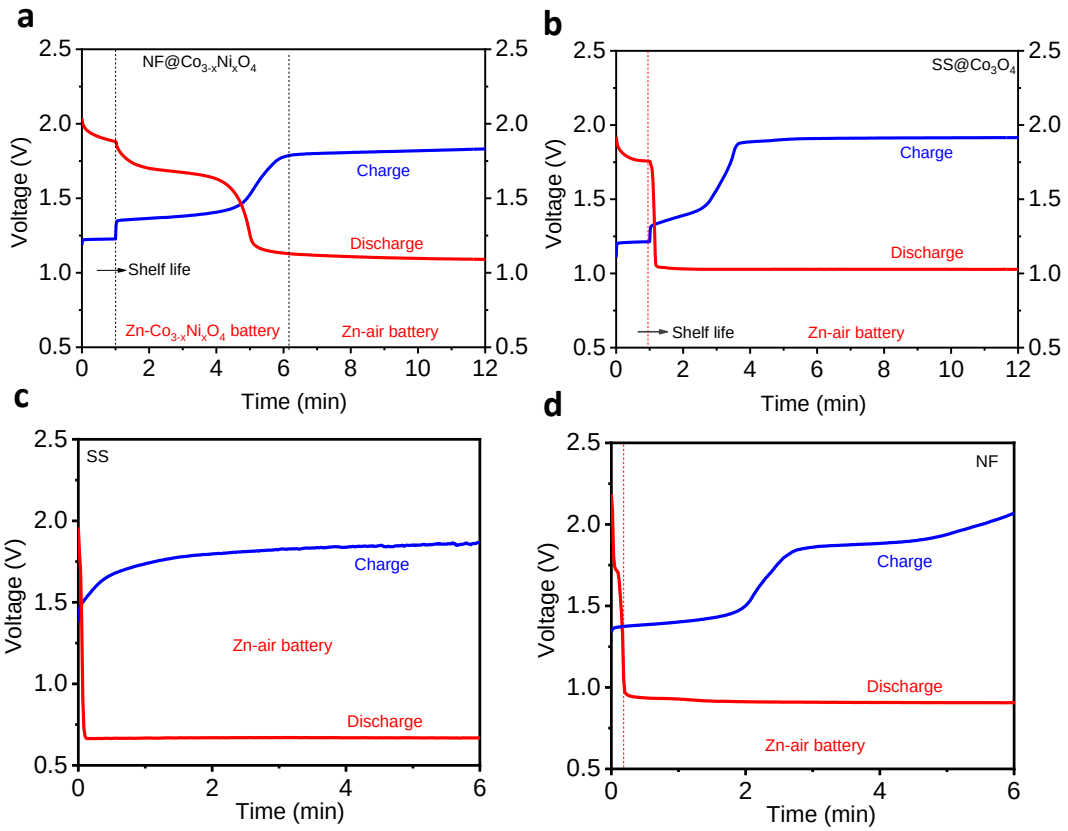

Figure 6-8 Galvanostatic discharge and charge of (a) NF@$Co_{3-x}Ni_xO_4$, (b) SS@Co_3O_4, (c) SS, and (d) NF electrodes at a current density of 20 mA cm^{-2}.

can possess a longer discharging time, which can be attributed to the structural engineering of Ni-doped Co_3O_4 ($Co_{3-x}Ni_xO_4$) and relatively high catalyst loading.

To investigate the structural stabilities of NF@$Co_{3-x}Ni_xO_4$ after durability test, the possible changes in the valence states and local coordination of cobalt in substituted cobalt oxides are revealed using XANES. After ultra-long cycling operation (600 h of operation time), the ZAB displays enlarged overpotentials due to decreased discharge potential and increased charge potential (Figure 6-9a). As shown in Figure 6-9b, there was a shift of the Co K-edge to approximately 1.4 eV higher energy after cycling operation. These all indicate an increase in the Co oxidation state. The intensity of the main peak at approximately 1.47 Å in the Fourier transform of the EXAFS spectrum (Figure 6-9c) increased slightly; this may be ascribed to the decrease of oxygen vacancies and result in more Co-O bonds. Compared with that without cycling test, the main peak shifted (~ 0.09 Å) to shorter lengths after cycling operation, which suggests shrink of the Co-O bond. The SEM images of NF@$Co_{3-x}Ni_xO_4$ after cycling operation showed detachment of $Co_{3-x}Ni_xO_4$ needle nanowires from NF@$Co_{3-x}Ni_xO_4$ accompanied by aggregation (Figure 6-9d). The performance degradation may be attributed to the decrease of oxygen vacancies, an increase of the Co oxidation state, and the detachment of $Co_{3-x}Ni_xO_4$ from the electrode.

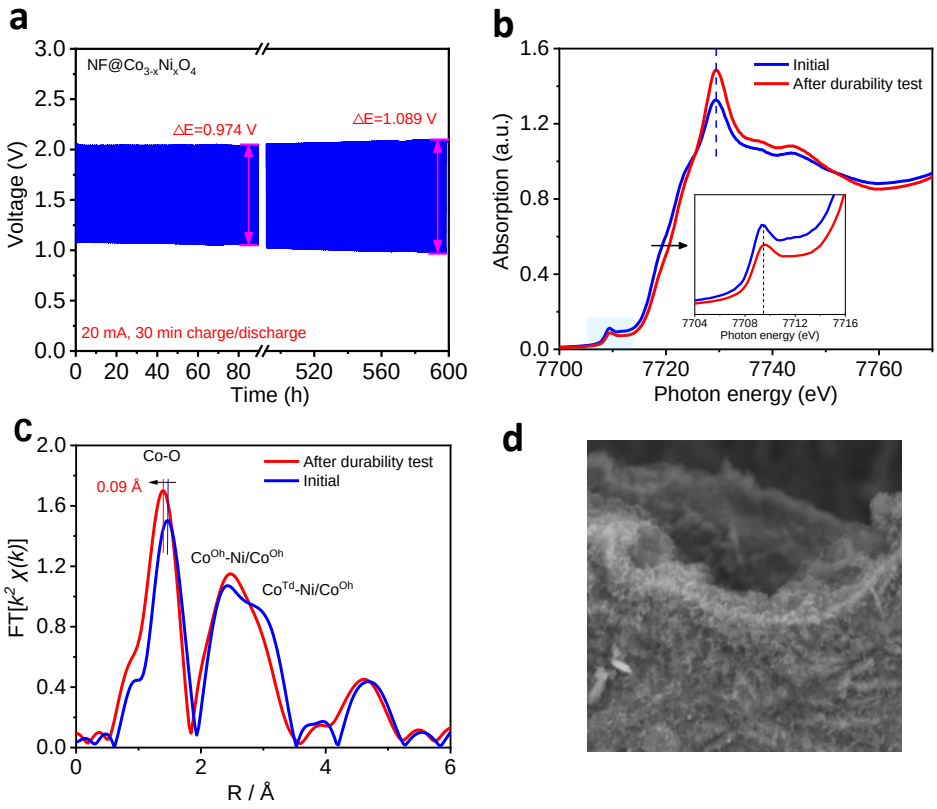

Figure 6-9 (a) Galvanostatic discharge and charge cycling stability of NF@$Co_{3-x}Ni_xO_4$ catalyst at a current density of 20 mA cm^{-2} with a cycle being 1 h. (b) Normalized Co K-edge XANES spectrum of initial NF@$Co_{3-x}Ni_xO_4$ and after 600 h cycling test (20 mA cm^{-2} with a cycle being 1 h). (c) The corresponding Fourier transforms (FT) spectrum. (d) SEM image of NF@$Co_{3-x}Ni_xO_4$ after charge/discharge cycling test.

6.4 Conclusion

By using Ni foam as both the substrate and nickel precursor to control the surface structure of the Co_3O_4, we successfully endow Ni-doped Co_3O_4 (NF@$Co_{3-x}Ni_xO_4$) with the ability to carry out multiple electrochemical reactions, including ORR/OER electrocatalysis and Faradaic CoNi-O ↔ CoNi-O-OH redox reactions. Moreover, combining the 3D porous structure of NF and intrinsic high OER activity of SS, we synthesized a self-supported sandwich structure electrode (NS@$Co_{3-x}Ni_xO_4$/Co_3O_4) with a dense and interconnected sandwich structure by pressing NF@$Co_{3-x}Ni_xO_4$ and SS@Co_3O_4 air cathodes together. The as-prepared electrode can take full

advantage of the sandwich structure to promote the electrocatalytic reaction toward both reversible Faradaic redox reaction of CoNi-O ↔ CoNi-O-OH and excellent ORR/OER performance. Moreover, the resulting hybrid system using NS@$Co_{3-x}Ni_xO_4/Co_3O_4$ electrode exhibits excellent cycle stability (200 cycles over 8 days at 5 $mA \cdot cm^{-2}$ for hybrid battery) and high energy efficiency (62.2% at 5 mA cm^{-2} for ZABs). We believe this protocol undoubtedly opens a new avenue to design high-efficiency and stable developed hybrid energy-storage devices.

Chapter 7 Conclusions and recommendation

7.1 Conclusions

This thesis has presented great efforts to develop conventional powdery (Chapters 3, 4, 5) catalysts and self-supported carbon-free electrodes (Chapters 6) as bifunctional oxygen cathodes to improve the performance of the rechargeable zinc-air batteries. In Chapter 3, the graphitic-shell encapsulated FeNi alloy/nitride nanocrystals supported on N-doped porous carbon fabricate were fabricated. The porous architecture can provide abundant accessible active sites and improved mass transfer. Benefitting from the strong catalyst-support interactions between the graphite-coated nanocrystals and the N-doped porous carbon, it promotes the electrocatalytic reaction kinetics and stability for both ORR and OER. In addition, the bulk structure of the Fe_xNi_yN nanocrystals shows strong stability against the harsh OER electrochemical corrosion process. The assembled electrode with this catalyst demonstrated high stability over 400 hours at 5.0 mA/cm^2 in rechargeable zinc-air batteries. To further enhance the carbon corrosion resistance, in Chapter 4, the Co/Co_2P heterojunctions confined in N-doped CNTs (Co/Co_2P@NCNTs) as a precatalyst for oxygen electrocatalysis are developed. The NCNTs with a high degree of graphitization and an increased number of graphitic-N active sites catalyzed by the unique Co/Co_2P heterojunctions significantly accelerate the ORR kinetics and effectively weakens the negative effects of high oxidation potential (during the OER process) on ORR performance in alkaline media. Meanwhile, the operando XAS reveals the dynamic active state transformation from the Co/Co_2P heterojunctions into $CoO_x(OH)_y$ active species, which contributes to the significantly improved OER performance. The assembled zinc-air flow battery with Co/Co_2P@NCNTs catalysts display a high energy efficiency and a superior cycle life of 1080 h. In Chapter 5, a facile bimetal coupling approach to synthesize Fe/Co double hydroxide/oxide

nano-sheets supported on NCNTs (FeCo-DHO/NCNTs) is proposed. The Fe/Co double hydroxide/oxide nano-sheets (FeCo-DHO) with dual phases are uniformly supported on the surface of NCNTs through direct nucleation, growth, and anchoring. This structure provides a high electrical contact area and strong adhesion on the conductive carbon support. The strong interaction of the FeCo-DHO nano-sheets with NCNTs facilitates charge transfer and mass transport. It also leads to high chemical stability to resist corrosion during charge and discharge operation. The high bifunctional ORR/OER activity and stability of FeCo-DHO/NCNTs in liquid and quasi-solid-state ZABs both shown a long cycling lifetime and improved charge/discharge performance. Previous electrode fabrication always involved the use of powder catalysts, gas diffusion layers, and polymer binders. One critical issue faced by the carbonaceous cathode is the carbon corrosion and binder degradation during charging, resulting in a gradual performance decay. In Chapter 6, by using Ni foam as both the substrate and nickel precursor to control the surface structure of the Co_3O_4, it successfully endows Ni-doped Co_3O_4 (NF@$Co_{3-x}Ni_xO_4$) with the ability to carry out multiple electrochemical reactions, including ORR/OER electrocatalysis and Faradaic CoNi-O ↔ CoNi-O-OH redox reactions. Moreover, combining the 3D porous structure of NF and intrinsic high OER activity of SS, the fabricated self-supported sandwich structure electrode (NS@$Co_{3-x}Ni_xO_4$/Co_3O_4) by pressing Ni foam NF@$Co_{3-x}Ni_xO_4$ and stainless steel SS@Co_3O_4 air cathodes together shows a dense and interconnected sandwich structure. The sandwich structure promotes the electrocatalytic reaction toward both reversible Faradaic redox reaction of CoNi-O ↔ CoNi-O-OH and excellent ORR/OER performance. Consequently, the NS@$Co_{3-x}Ni_xO_4$/Co_3O_4 electrode in rechargeable zinc-air batteries exhibits high cycle stability and high energy efficiency (62.2% at 5 mA cm^{-2}).

7.2 Recommended future work

Based on the research results of this thesis, the following recommendations are proposed for future work.

1. *Further investigations on the encapsulation effect on the performance of bifunctional oxygen cathode.* In chapters 3 and 4, carbon-encapsulated transition metal nanoparticles have been synthesized successfully. The encapsulation structure effectively inhibits particle aggregation, resulting in excellent durability. The electron transfer between transition metals (TMs) and the surface carbon layer have a synergetic role in activating molecular oxygen during ORR. Importantly, the structural modulation of the carbon layer or TMs usually has an important effect on its electronic properties and thereby the corresponding catalytic performance. Therefore, the factors influencing the electron transfer process from TMs through carbon shell, such as the thickness of carbon shell, heteroatom doping within carbon surface, TM type, size, the curvature of carbon shell, etc.[248]

2. *Further investigations on the self-reconstruction effect on the performance of TMs.* In chapter 4, the operando X-ray absorption spectroscopy and electrochemical measurements were conducted to investigate the dynamic structural evolution of the Co/Co_2P heterojunctions during electrocatalytic operation. The enhanced OER performance is mainly due to the generation of the $CoO_x(OH)_y$ active species. In a specific electrocatalytic reaction, the initial active sites at a given potential could be oxidized or reduced into other species and would undergo structural self-reconstruction owing to electrically driven structural oxidation or reduction processes.[249] Understanding catalytic processes and identifying active sites explicitly is vital to clarify the catalytic mechanism and develop advanced electrocatalysts. In situ or operando characterization techniques (e.g., XAS, XRD, Raman) have been demonstrated as valid tools to track dynamic structure and analyze real-time reaction products. A systematic understanding in terms of the self-

reconstruction of TMs-based materials is still urgently needed. Here, it is recommended that an investigation on factors determine the self-reconstruction behavior, which providing guidelines for the understanding of the true catalytically active sites.

3. *Further investigations on the defects control of catalyst towards high catalytic performance.* The improvement of intrinsic activity and active site density will directly lead to increases in electrode activity. The intrinsic ORR and OER activities highly depend on the properties of defects structure, such as lattice-strain control, crystallographic structure control, vacancy defect control, and metal-carbon support interaction control. In Chapter 5, the role of metal-carbon support interaction control was demonstrated to be positive in catalyst improvement. To further improve the multifunctional catalytic activity, the reinforcement of metal-carbon interaction can be realized by the structural surface defects, substitutional-doping, and/or chemical functionalization of the carbon surfaces. Moreover, in Chapter 6, the Ni-modified Co_3O_4 surface with oxygen vacancy defects carried out multiple electrochemical reactions, and significantly improved the reversibility of CoNi-O ↔ CoNi-O-OH. However, in Chapters 3 and 4, the electrochemical measurements have demonstrated that the FeNi alloy/nitride nanocrystals and Co/Co_2P heterojunctions exhibited poor reversibility. Therefore, it is also strongly recommended that an investigation on factors determine the reversibility behavior.

4. *Further investigations on the strategies for improving catalysts' stability.* For the carbon-based materials, carbon corrosion, especially under the hash OER process, will results in significant charge- and mass-transport resistances. Physicochemical characteristics of the carbon substrate significantly affect their catalytic activity and stability, such as degree of graphitization, carbon structure, surface area, and morphology. However, the pyrolysis of organic materials commonly leads to unpredictable structural changes in the support, and the formed amorphous carbon limits their stability. The carbon substrates with a high degree of graphitization play a key

role in enhancing their stability. In addition, developing new advanced support materials or with high conductivity and corrosion resistance are highly desired.

References

1. Wang, H.; Xu, S.; Tsai, C.; Li, Y.; Liu, C.; Zhao, J.; Liu, Y.; Yuan, H.; Abild-Pedersen, F.; Prinz, F. B.; Norskov, J. K.; Cui, Y., Direct and continuous strain control of catalysts with tunable battery electrode materials. *Science* **2016,** *354* (6315), 1031-1036.
2. Fu, J.; Cano, Z. P.; Park, M. G.; Yu, A.; Fowler, M.; Chen, Z., Electrically Rechargeable Zinc-Air Batteries: Progress, Challenges, and Perspectives. *Adv. Mater.* **2017,** *29* (7).
3. Yang, D.; Zhang, L.; Yan, X.; Yao, X., Recent Progress in Oxygen Electrocatalysts for Zinc-Air Batteries. *Small Methods* **2017,** *1* (12), 1700209.
4. Lee, J.-S.; Tai Kim, S.; Cao, R.; Choi, N.-S.; Liu, M.; Lee, K. T.; Cho, J., Metal-Air Batteries with High Energy Density: Li-Air versus Zn-Air. *Advanced Energy Materials* **2011,** *1* (1), 34-50.
5. Wu, M.; Tang, Q.; Dong, F.; Wang, Y.; Li, D.; Guo, Q.; Liu, Y.; Qiao, J., The design of Fe, N-doped hierarchically porous carbons as highly active and durable electrocatalysts for a Zn-air battery. *Phys. Chem. Chem. Phys.* **2016,** *18* (28), 18665-9.
6. Tang, Q.; Wang, L.; Wu, M.; Xu, N.; Jiang, L.; Qiao, J., Achieving high-powered Zn/air fuel cell through N and S co-doped hierarchically porous carbons with tunable active-sites as oxygen electrocatalysts. *J. Power Sources* **2017,** *365*, 348-353.
7. Li, L.; Liu, C.; He, G.; Fan, D.; Manthiram, A., Hierarchical pore-in-pore and wire-in-wire catalysts for rechargeable Zn- and Li-air batteries with ultra-long cycle life and high cell efficiency. *Energy & Environmental Science* **2015,** *8* (11), 3274-3282.
8. Pei, P.; Wang, K.; Ma, Z., Technologies for extending zinc-air battery's cycle life: A review. *Applied Energy* **2014,** *128*, 315-324.
9. Xu, M.; Ivey, D. G.; Xie, Z.; Qu, W., Rechargeable Zn-air batteries: Progress in electrolyte development and cell configuration advancement. *J. Power Sources* **2015,** *283*, 358-371.
10. Cheng, F.; Shen, J.; Peng, B.; Pan, Y.; Tao, Z.; Chen, J., Rapid room-temperature synthesis of nanocrystalline spinels as oxygen reduction and evolution electrocatalysts. *Nat. Chem.* **2011,** *3* (1), 79-84.
11. Wang, H.-F.; Tang, C.; Zhang, Q., A Review of Precious-Metal-Free Bifunctional Oxygen Electrocatalysts: Rational Design and Applications in Zn−Air Batteries. *Adv. Funct. Mater.* **2018,** *28* (46), 1803329.
12. Li, M.; Zhang, L.; Xu, Q.; Niu, J.; Xia, Z., N-doped graphene as catalysts for oxygen

reduction and oxygen evolution reactions: Theoretical considerations. *J. Catal.* **2014,** *314*, 66-72.

13. Yuan, S.-J.; Dai, X.-H., An efficient sewage sludge-derived bi-functional electrocatalyst for oxygen reduction and evolution reaction. *Green Chemistry* **2016,** *18* (14), 4004-4011.
14. Wu, M.; Tang, Q.; Dong, F.; Bai, Z.; Zhang, L.; Qiao, J., Fe/N/S-composited hierarchically porous carbons with optimized surface functionality, composition and nanoarchitecture as electrocatalysts for oxygen reduction reaction. *J. Catal.* **2017,** *352*, 208-217.
15. Jiang, S.; Li, J.; Fang, J.; Wang, X., Fibrous-Structured Freestanding Electrodes for Oxygen Electrocatalysis. *Small* **2019**, e1903760.
16. Wu, M.; Zhang, G.; Du, L.; Yang, D.; Yang, H.; Sun, S., Defect Electrocatalysts and Alkaline Electrolyte Membranes in Solid-State Zinc–Air Batteries: Recent Advances, Challenges, and Future Perspectives. *Small Methods* **2020**, *5 (1)*, 2000868.
17. Wen, Z.; Shen, C.; Lu, Y., Air Electrode for the Lithium-Air Batteries: Materials and Structure Designs. *ChemPlusChem* **2015,** *80* (2), 270-287.
18. Sathiskumar, C.; Ramakrishnan, S.; Vinothkannan, M.; Karthikeyan, S.; Yoo, D. J.; Rhan Kim, A., Nitrogen-Doped Porous Carbon Derived from Biomass Used as Trifunctional Electrocatalyst toward Oxygen Reduction, Oxygen Evolution and Hydrogen Evolution Reactions. *Nanomaterials* **2019,** *10* (1).
19. Tao, H. B.; Zhang, J.; Chen, J.; Zhang, L.; Xu, Y.; Chen, J. G.; Liu, B., Revealing Energetics of Surface Oxygen Redox from Kinetic Fingerprint in Oxygen Electrocatalysis. *J. Am. Chem. Soc.* **2019,** *141* (35), 13803-13811.
20. Hong, W. T.; Risch, M.; Stoerzinger, K. A.; Grimaud, A.; Suntivich, J.; Shao-Horn, Y., Toward the rational design of non-precious transition metal oxides for oxygen electrocatalysis. *Energy & Environmental Science* **2015**, *8 (5)*, 1404-1427.
21. Guan, Y.; Liu, G.; Li, J.; Wang, Y.; Zhang, Z., Surface-engineered cobalt nitride composite as efficient bifunctional oxygen electrocatalyst. *Nanotechnology* **2019,** *30* (49), 495406.
22. Cui, Z.; Li, Y.; Fu, G.; Li, X.; Goodenough, J. B., Robust Fe_3Mo_3C Supported IrMn Clusters as Highly Efficient Bifunctional Air Electrode for Metal-Air Battery. *Adv. Mater.* **2017,** *29* (40).
23. Li, H.; Guo, Z.; Wang, X., Atomic-layer-deposited ultrathin Co_9S_8 on carbon nanotubes: an efficient bifunctional electrocatalyst for oxygen evolution/reduction reactions and

rechargeable Zn-air batteries. *J. Mater. Chem. A* **2017,** *5* (40), 21353-21361.

24. Sutton, J. E.; Guo, W.; Katsoulakis, M. A.; Vlachos, D. G., Effects of correlated parameters and uncertainty in electronic-structure-based chemical kinetic modeling. *Nat. Chem.* **2016,** *8* (4), 331-7.
25. Stohr, M.; Van Voorhis, T.; Tkatchenko, A., Theory and practice of modeling van der Waals interactions in electronic-structure calculations. *Chem. Soc. Rev.* **2019,** *48* (15), 4118-4154.
26. Harvey, J. N.; Himo, F.; Maseras, F.; Perrin, L., Scope and Challenge of Computational Methods for Studying Mechanism and Reactivity in Homogeneous Catalysis. *ACS Catalysis* **2019,** *9* (8), 6803-6813.
27. Wu, M.; Zhang, G.; Hu, Y.; Wang, J.; Sun, T.; Regier, T.; Qiao, J.; Sun, S., Graphitic-shell encapsulated FeNi alloy/nitride nanocrystals on biomass-derived N-doped carbon as an efficient electrocatalyst for rechargeable Zn-air battery. *Carbon Energy* **2020**.
28. Wu, M.; Zhang, G.; Wu, M.; Prakash, J.; Sun, S., Rational design of multifunctional air electrodes for rechargeable Zn-Air batteries: Recent progress and future perspectives. *Energy Storage Materials* **2019,** *21*, 253-286.
29. Li, J.; Chen, M.; Cullen, D. A.; Hwang, S.; Wang, M.; Li, B.; Liu, K.; Karakalos, S.; Lucero, M.; Zhang, H.; Lei, C.; Xu, H.; Sterbinsky, G. E.; Feng, Z.; Su, D.; More, K. L.; Wang, G.; Wang, Z.; Wu, G., Atomically dispersed manganese catalysts for oxygen reduction in proton-exchange membrane fuel cells. *Nature Catalysis* **2018,** *1* (12), 935-945.
30. Wu, M. J.; Zhang, G. X.; Chen, N.; Chen, W. F.; Qiao, J. L.; Sun, S. H., A self-supported electrode as a high-performance binder- and carbon-free cathode for rechargeable hybrid zinc batteries. *Energy Storage Materials* **2020,** *24*, 272-280.
31. Huang, K., An Active and Robust Bifunctional Oxygen Electrocatalyst through Carbon-Free Hierarchical Functionalization. *Angew. Chem. Int. Ed. Engl.* **2017,** *56* (42), 12826-12827.
32. Lu, X.; Yin, Y.; Zhang, L.; Huang, S.; Xi, L.; Liu, L.; Oswald, S.; Schmidt, O. G., 3D Ag/NiO-Fe2O3/Ag nanomembranes as carbon-free cathode materials for Li-O_2 batteries. *Energy Storage Materials* **2019,** *16*, 155-162.
33. Huang, Z.-F.; Wang, J.; Peng, Y.; Jung, C.-Y.; Fisher, A.; Wang, X., Design of Efficient Bifunctional Oxygen Reduction/Evolution Electrocatalyst: Recent Advances and Perspectives. *Advanced Energy Materials* **2017,** *7* (23), 1700544.
34. Wang, X. X.; Swihart, M. T.; Wu, G., Achievements, challenges and perspectives on cathode

catalysts in proton exchange membrane fuel cells for transportation. *Nature Catalysis* **2019,** *2* (7), 578-589.

35. Rousseau, R.; Glezakou, V.-A.; Selloni, A., Theoretical insights into the surface physics and chemistry of redox-active oxides. *Nature Reviews Materials* **2020,** *5* (6), 460-475.
36. Zhang, H.; Chung, H. T.; Cullen, D. A.; Wagner, S.; Kramm, U. I.; More, K. L.; Zelenay, P.; Wu, G., High-performance fuel cell cathodes exclusively containing atomically dispersed iron active sites. *Energy & Environmental Science* **2019,** *12* (8), 2548-2558.
37. He, Y.; Liu, J. C.; Luo, L.; Wang, Y. G.; Zhu, J.; Du, Y.; Li, J.; Mao, S. X.; Wang, C., Size-dependent dynamic structures of supported gold nanoparticles in CO oxidation reaction condition. *Proc Natl Acad Sci USA* **2018,** *115* (30), 7700-7705.
38. Seh, Z. W.; Kibsgaard, J.; Dickens, C. F.; Chorkendorff, I.; Norskov, J. K.; Jaramillo, T. F., Combining theory and experiment in electrocatalysis: Insights into materials design. *Science* **2017,** *355* (6321).
39. Wei, C.; Feng, Z.; Scherer, G. G.; Barber, J.; Shao-Horn, Y.; Xu, Z. J., Cations in Octahedral Sites: A Descriptor for Oxygen Electrocatalysis on Transition-Metal Spinels. *Adv. Mater.* **2017,** *29* (23).
40. Wang, X. T.; Ouyang, T.; Wang, L.; Zhong, J. H.; Ma, T.; Liu, Z. Q., Redox-Inert Fe^{3+} Ions in Octahedral Sites of Co-Fe Spinel Oxides with Enhanced Oxygen Catalytic Activity for Rechargeable Zinc-Air Batteries. *Angew. Chem.* **2019,** *131* (38), 13425-13430.
41. Wang, X. T.; Ouyang, T.; Wang, L.; Zhong, J. H.; Liu, Z. Q., Surface Reorganization on Electrochemically-Induced Zn-Ni-Co Spinel Oxides for Enhanced Oxygen Electrocatalysis. *Angew. Chem.* **2020,** *132* (16), 6554-6561.
42. Zhao, Q.; Yan, Z.; Chen, C.; Chen, J., Spinels: Controlled Preparation, Oxygen Reduction/Evolution Reaction Application, and Beyond. *Chem. Rev.* **2017,** *117* (15), 10121-10211.
43. Gerber, I. C.; Serp, P., A Theory/Experience Description of Support Effects in Carbon-Supported Catalysts. *Chem. Rev.* **2020,** *120* (2), 1250-1349.
44. Shi, Q.; Zhu, C.; Du, D.; Lin, Y., Robust noble metal-based electrocatalysts for oxygen evolution reaction. *Chem. Soc. Rev.* **2019,** *48* (12), 3181-3192.
45. Wang, H.; Dai, H., Strongly coupled inorganic-nano-carbon hybrid materials for energy storage. *Chem. Soc. Rev.* **2013,** *42* (7), 3088-113.

46. Kou, Z.; Zang, W.; Ma, Y.; Pan, Z.; Mu, S.; Gao, X.; Tang, B.; Xiong, M.; Zhao, X.; Cheetham, A. K.; Zheng, L.; Wang, J., Cage-confinement pyrolysis route to size-controlled molybdenum-based oxygen electrode catalysts: From isolated atoms to clusters and nanoparticles. *Nano Energy* **2020,** *67*, 104288.
47. Li, Z.; Zhang, Y.; Feng, Y.; Cheng, C. Q.; Qiu, K. W.; Dong, C. K.; Liu, H.; Du, X. W., Co_3O_4 Nanoparticles with Ultrasmall Size and Abundant Oxygen Vacancies for Boosting Oxygen Involved Reactions. *Adv. Funct. Mater.* **2019,** *29* (36), 1903444.
48. Han, X.; Ling, X.; Wang, Y.; Ma, T.; Zhong, C.; Hu, W.; Deng, Y., Generation of Nanoparticle, Atomic-Cluster, and Single-Atom Cobalt Catalysts from Zeolitic Imidazole Frameworks by Spatial Isolation and Their Use in Zinc-Air Batteries. *Angew. Chem.* **2019,** *131* (16), 5413-5418.
49. Lu, Q.; Guo, Y.; Mao, P.; Liao, K.; Zou, X.; Dai, J.; Tan, P.; Ran, R.; Zhou, W.; Ni, M.; Shao, Z., Rich atomic interfaces between sub-1 nm RuO_x clusters and porous Co_3O_4 nanosheets boost oxygen electrocatalysis bifunctionality for advanced Zn-air batteries. *Energy Storage Materials* **2020,** *32*, 20-29.
50. Seo, B.; Sa, Y. J.; Woo, J.; Kwon, K.; Park, J.; Shin, T. J.; Jeong, H. Y.; Joo, S. H., Size-Dependent Activity Trends Combined with in Situ X-ray Absorption Spectroscopy Reveal Insights into Cobalt Oxide/Carbon Nanotube-Catalyzed Bifunctional Oxygen Electrocatalysis. *Acs Catalysis* **2016,** *6* (7), 4347-4355.
51. Xu, N.; Qiao, J.; Zhang, X.; Ma, C.; Jian, S.; Liu, Y.; Pei, P., Morphology controlled $La_2O_3/Co_3O_4/MnO_2$-CNTs hybrid nanocomposites with durable bi-functional air electrode in high-performance zinc-air energy storage. *Applied Energy* **2016,** *175*, 495-504.
52. Li, Y.; Cheng, G.; Zhou, Z.; Liao, X.; Han, S.; Ye, F.; Sun, M.; Yu, L., Shape-Controlled Synthesis of $NiCo_2O_4$-rGO as Bifunctional Electrocatalyst for Zn-Air Battery. *ChemElectroChem* **2019,** *6* (17), 4429-4436.
53. Hwang, J.; Ejsmont, A.; Freund, R.; Goscianska, J.; Schmidt, B.; Wuttke, S., Controlling the morphology of metal-organic frameworks and porous carbon materials: metal oxides as primary architecture-directing agents. *Chem. Soc. Rev.* **2020,** *49* (11), 3348-3422.
54. Ling, T.; Yan, D. Y.; Jiao, Y.; Wang, H.; Zheng, Y.; Zheng, X.; Mao, J.; Du, X. W.; Hu, Z.; Jaroniec, M.; Qiao, S. Z., Engineering surface atomic structure of single-crystal cobalt (II) oxide nanorods for superior electrocatalysis. *Nat. Commun.* **2016,** *7*, 12876.

55. Zhang, Y.; Hao, F.; Liu, C.; Chen, X., Band gap and oxygen vacancy diffusion of anatase (101) surface: the effect of strain. *Theor. Chem. Acc.* **2016,** *135* (7).
56. Heo, S.; Oh, C.; Son, J.; Jang, H. M., Influence of tensile-strain-induced oxygen deficiency on metal-insulator transitions in $NdNiO_3$-delta epitaxial thin films. *Sci. Rep.* **2017,** *7* (1), 4681.
57. Liu, J.; Zhang, J., Nanointerface Chemistry: Lattice-Mismatch-Directed Synthesis and Application of Hybrid Nanocrystals. *Chem. Rev.* **2020,** *120* (4), 2123-2170.
58. Miao, Z.; Wang, X.; Tsai, M. C.; Jin, Q.; Liang, J.; Ma, F.; Wang, T.; Zheng, S.; Hwang, B. J.; Huang, Y.; Guo, S.; Li, Q., Atomically Dispersed Fe-N_x/C Electrocatalyst Boosts Oxygen Catalysis via a New Metal-Organic Polymer Supramolecule Strategy. *Advanced Energy Materials* **2018,** *8* (24), 1801226.
59. Bai, L.; Duan, Z.; Wen, X.; Si, R.; Guan, J., Atomically dispersed manganese-based catalysts for efficient catalysis of oxygen reduction reaction. *Applied Catalysis B: Environmental* **2019,** *257*, 117930.
60. Zhang, X.; Han, X.; Jiang, Z.; Xu, J.; Chen, L.; Xue, Y.; Nie, A.; Xie, Z.; Kuang, Q.; Zheng, L., Atomically dispersed hierarchically ordered porous Fe-N-C electrocatalyst for high performance electrocatalytic oxygen reduction in Zn-Air battery. *Nano Energy* **2020,** *71*, 104547.
61. Huang, K.; Wang, R.; Zhao, S.; Du, P.; Wang, H.; Wei, H.; Long, Y.; Deng, B.; Lei, M.; Ge, B.; Gou, H.; Zhang, R.; Wu, H., Atomic species derived CoO_x clusters on nitrogen doped mesoporous carbon as advanced bifunctional electro-catalysts for Zn-air battery. *Energy Storage Materials* **2020,** *29*, 156-162.
62. Fei, H.; Dong, J.; Feng, Y.; Allen, C. S.; Wan, C.; Volosskiy, B.; Li, M.; Zhao, Z.; Wang, Y.; Sun, H.; An, P.; Chen, W.; Guo, Z.; Lee, C.; Chen, D.; Shakir, I.; Liu, M.; Hu, T.; Li, Y.; Kirkland, A. I.; Duan, X.; Huang, Y., General synthesis and definitive structural identification of MN_4C_4 single-atom catalysts with tunable electrocatalytic activities. *Nature Catalysis* **2018,** *1* (1), 63-72.
63. Yang, X. F.; Wang, A.; Qiao, B.; Li, J.; Liu, J.; Zhang, T., Single-atom catalysts: a new frontier in heterogeneous catalysis. *Acc. Chem. Res.* **2013,** *46* (8), 1740-8.
64. Zhang, K.; Zhang, Y.; Zhang, Q.; Liang, Z.; Gu, L.; Guo, W.; Zhu, B.; Guo, S.; Zou, R., Metal-organic framework-derived Fe/Cu-substituted Co nanoparticles embedded in

CNTs-grafted carbon polyhedron for Zn-air batteries. *Carbon Energy* **2020,** *2* (2), 283-293.

65. Wang, H. F.; Chen, L.; Pang, H.; Kaskel, S.; Xu, Q., MOF-derived electrocatalysts for oxygen reduction, oxygen evolution and hydrogen evolution reactions. *Chem. Soc. Rev.* **2020,** *49* (5), 1414-1448.
66. Liu, J.; Zhu, D.; Guo, C.; Vasileff, A.; Qiao, S.-Z., Design Strategies toward Advanced MOF-Derived Electrocatalysts for Energy-Conversion Reactions. *Advanced Energy Materials* **2017,** *7* (23), 1700518.
67. Qin, R.; Liu, P.; Fu, G.; Zheng, N., Strategies for Stabilizing Atomically Dispersed Metal Catalysts. *Small Methods* **2018,** *2* (1), 1700286.
68. Liu, M.; Wang, L.; Zhao, K.; Shi, S.; Shao, Q.; Zhang, L.; Sun, X.; Zhao, Y.; Zhang, J., Atomically dispersed metal catalysts for the oxygen reduction reaction: synthesis, characterization, reaction mechanisms and electrochemical energy applications. *Energy & Environmental Science* **2019,** *12* (10), 2890-2923.
69. Li, J.; Pršlja, P.; Shinagawa, T.; Martín Fernández, A. J.; Krumeich, F.; Artyushkova, K.; Atanassov, P.; Zitolo, A.; Zhou, Y.; García-Muelas, R.; López, N.; Pérez-Ramírez, J.; Jaouen, F., Volcano Trend in Electrocatalytic CO_2 Reduction Activity over Atomically Dispersed Metal Sites on Nitrogen-Doped Carbon. *ACS Catalysis* **2019,** *9* (11), 10426-10439.
70. Liang, Z.; Guo, W.; Zhao, R.; Qiu, T.; Tabassum, H.; Zou, R., Engineering atomically dispersed metal sites for electrocatalytic energy conversion. *Nano Energy* **2019,** *64*, 103917.
71. Yan, D.; Li, Y.; Huo, J.; Chen, R.; Dai, L.; Wang, S., Defect Chemistry of Nonprecious-Metal Electrocatalysts for Oxygen Reactions. *Adv. Mater.* **2017,** *29* (48).
72. Zhu, Y.; Liu, X.; Jin, S.; Chen, H.; Lee, W.; Liu, M.; Chen, Y., Anionic defect engineering of transition metal oxides for oxygen reduction and evolution reactions. *Journal of Materials Chemistry A* **2019,** *7* (11), 5875-5897.
73. Lee, H.; Gwon, O.; Choi, K.; Zhang, L.; Zhou, J.; Park, J.; Yoo, J.-W.; Wang, J.-Q.; Lee, J. H.; Kim, G., Enhancing Bifunctional Electrocatalytic Activities via Metal d-Band Center Lift Induced by Oxygen Vacancy on the Subsurface of Perovskites. *ACS Catalysis* **2020,** *10* (8), 4664-4670.
74. Yang, M. Q.; Wang, J.; Wu, H.; Ho, G. W., Noble Metal-Free Nanocatalysts with Vacancies for Electrochemical Water Splitting. *Small* **2018,** *14* (15), e1703323.
75. Grimaud, A.; Diaz-Morales, O.; Han, B.; Hong, W. T.; Lee, Y. L.; Giordano, L.; Stoerzinger,

K. A.; Koper, M. T. M.; Shao-Horn, Y., Activating lattice oxygen redox reactions in metal oxides to catalyze oxygen evolution. *Nat. Chem.* **2017,** *9* (5), 457-465.

76. Li, G.; Blake, G. R.; Palstra, T. T., Vacancies in functional materials for clean energy storage and harvesting: the perfect imperfection. *Chem. Soc. Rev.* **2017,** *46* (6), 1693-1706.
77. Yang, C.; Laberty-Robert, C.; Batuk, D.; Cibin, G.; Chadwick, A. V.; Pimenta, V.; Yin, W.; Zhang, L.; Tarascon, J. M.; Grimaud, A., Phosphate Ion Functionalization of Perovskite Surfaces for Enhanced Oxygen Evolution Reaction. *J. Phys. Chem. Lett.* **2017,** *8* (15), 3466-3472.
78. Chen, D.; Qiao, M.; Lu, Y. R.; Hao, L.; Liu, D.; Dong, C. L.; Li, Y.; Wang, S., Preferential Cation Vacancies in Perovskite Hydroxide for the Oxygen Evolution Reaction. *Angew. Chem. Int. Ed. Engl.* **2018,** *57* (28), 8691-8696.
79. Deng, D.; Novoselov, K. S.; Fu, Q.; Zheng, N.; Tian, Z.; Bao, X., Catalysis with two-dimensional materials and their heterostructures. *Nat Nanotechnol* **2016,** *11* (3), 218-30.
80. Jin, W.; Chen, J.; Liu, B.; Hu, J.; Wu, Z.; Cai, W.; Fu, G., Oxygen Vacancy-Rich In-Doped CoO/CoP Heterostructure as an Effective Air Cathode for Rechargeable Zn-Air Batteries. *Small* **2019,** *15* (46), e1904210.
81. Xu, W.; Lyu, F.; Bai, Y.; Gao, A.; Feng, J.; Cai, Z.; Yin, Y., Porous cobalt oxide nanoplates enriched with oxygen vacancies for oxygen evolution reaction. *Nano Energy* **2018,** *43*, 110-116.
82. Dong, G.; Hu, H.; Huang, X.; Zhang, Y.; Bi, Y., Rapid activation of Co_3O_4 cocatalysts with oxygen vacancies on TiO_2 photoanodes for efficient water splitting. *Journal of Materials Chemistry A* **2018,** *6* (42), 21003-21009.
83. Wu, M.; Zhang, G.; Tong, H.; Liu, X.; Du, L.; Chen, N.; Wang, J.; Sun, T.; Regier, T.; Sun, S., Cobalt (II) oxide nanosheets with rich oxygen vacancies as highly efficient bifunctional catalysts for ultra-stable rechargeable Zn-air flow battery. *Nano Energy* **2021,** *79*, 105409.
84. Xiao, Z.; Wang, Y.; Huang, Y.-C.; Wei, Z.; Dong, C.-L.; Ma, J.; Shen, S.; Li, Y.; Wang, S., Filling the oxygen vacancies in Co_3O_4 with phosphorus: an ultra-efficient electrocatalyst for overall water splitting. *Energy & Environmental Science* **2017,** *10* (12), 2563-2569.
85. Ji, D.; Fan, L.; Tao, L.; Sun, Y.; Li, M.; Yang, G.; Tran, T. Q.; Ramakrishna, S.; Guo, S., The Kirkendall Effect for Engineering Oxygen Vacancy of Hollow Co_3O_4 Nanoparticles toward High-Performance Portable Zinc-Air Batteries. *Angew. Chem. Int. Ed. Engl.* **2019,** *58* (39),

13840-13844.

86. Tsai, C.; Li, H.; Park, S.; Park, J.; Han, H. S.; Norskov, J. K.; Zheng, X.; Abild-Pedersen, F., Electrochemical generation of sulfur vacancies in the basal plane of MoS_2 for hydrogen evolution. *Nat. Commun.* **2017,** *8*, 15113.
87. Yin, Y.; Han, J.; Zhang, Y.; Zhang, X.; Xu, P.; Yuan, Q.; Samad, L.; Wang, X.; Wang, Y.; Zhang, Z.; Zhang, P.; Cao, X.; Song, B.; Jin, S., Contributions of Phase, Sulfur Vacancies, and Edges to the Hydrogen Evolution Reaction Catalytic Activity of Porous Molybdenum Disulfide Nanosheets. *J. Am. Chem. Soc.* **2016,** *138* (25), 7965-72.
88. Wang, F.; Li, K.; Li, J.; Wolf, L. M.; Liu, K.; Zhang, H., A bifunctional electrode engineered by sulfur vacancies for efficient electrocatalysis. *Nanoscale* **2019,** *11* (35), 16658-16666.
89. Chattot, R.; Le Bacq, O.; Beermann, V.; Kuhl, S.; Herranz, J.; Henning, S.; Kuhn, L.; Asset, T.; Guetaz, L.; Renou, G.; Drnec, J.; Bordet, P.; Pasturel, A.; Eychmuller, A.; Schmidt, T. J.; Strasser, P.; Dubau, L.; Maillard, F., Surface distortion as a unifying concept and descriptor in oxygen reduction reaction electrocatalysis. *Nat. Mater.* **2018,** *17* (9), 827-833.
90. Krishnamurthy, D.; Sumaria, V.; Viswanathan, V., Maximal Predictability Approach for Identifying the Right Descriptors for Electrocatalytic Reactions. *J. Phys. Chem. Lett.* **2018,** *9* (3), 588-595.
91. E. Pérez, A.; Ribadeneira, R., Modeling with DFT and Chemical Descriptors Approach for the Development of Catalytic Alloys for PEMFCs. **2019**.
92. Yuk, S. F.; Cooper, V. R., Tuning oxygen electrocatalysis via strain on LaNiO3(001). *Phys. Chem. Chem. Phys.* **2019,** *21* (9), 4738-4745.
93. Hwang, J.; Feng, Z.; Charles, N.; Wang, X. R.; Lee, D.; Stoerzinger, K. A.; Muy, S.; Rao, R. R.; Lee, D.; Jacobs, R.; Morgan, D.; Shao-Horn, Y., Tuning perovskite oxides by strain: Electronic structure, properties, and functions in (electro)catalysis and ferroelectricity. *Mater. Today* **2019,** *31*, 100-118.
94. Yao, Y.; Hu, S.; Chen, W.; Huang, Z.-Q.; Wei, W.; Yao, T.; Liu, R.; Zang, K.; Wang, X.; Wu, G.; Yuan, W.; Yuan, T.; Zhu, B.; Liu, W.; Li, Z.; He, D.; Xue, Z.; Wang, Y.; Zheng, X.; Dong, J.; Chang, C.-R.; Chen, Y.; Hong, X.; Luo, J.; Wei, S.; Li, W.-X.; Strasser, P.; Wu, Y.; Li, Y., Engineering the electronic structure of single atom Ru sites via compressive strain boosts acidic water oxidation electrocatalysis. *Nature Catalysis* **2019,** *2* (4), 304-313.
95. Nørskov, J. K.; Rossmeisl, J.; Logadottir, A.; Lindqvist, L.; Kitchin, J. R.; Bligaard, T.;

Jónsson, H., Origin of the Overpotential for Oxygen Reduction at a Fuel-Cell Cathode. *The Journal of Physical Chemistry B* **2004,** *108* (46), 17886-17892.

96. Lima, F. H. B.; Zhang, J.; Shao, M. H.; Sasaki, K.; Vukmirovic, M. B.; Ticianelli, E. A.; Adzic, R. R., Catalytic Activity−d-Band Center Correlation for the O2Reduction Reaction on Platinum in Alkaline Solutions. *The Journal of Physical Chemistry C* **2007,** *111* (1), 404-410.
97. Yamada, I.; Takamatsu, A.; Asai, K.; Shirakawa, T.; Ohzuku, H.; Seno, A.; Uchimura, T.; Fujii, H.; Kawaguchi, S.; Wada, K.; Ikeno, H.; Yagi, S., Systematic Study of Descriptors for Oxygen Evolution Reaction Catalysis in Perovskite Oxides. *The Journal of Physical Chemistry C* **2018,** *122* (49), 27885-27892.
98. Wang, X.; Gao, X. J.; Qin, L.; Wang, C.; Song, L.; Zhou, Y. N.; Zhu, G.; Cao, W.; Lin, S.; Zhou, L.; Wang, K.; Zhang, H.; Jin, Z.; Wang, P.; Gao, X.; Wei, H., eg occupancy as an effective descriptor for the catalytic activity of perovskite oxide-based peroxidase mimics. *Nat. Commun.* **2019,** *10* (1), 704.
99. Lee, Y. L.; Gadre, M. J.; Shao-Horn, Y.; Morgan, D., Ab initio GGA+U study of oxygen evolution and oxygen reduction electrocatalysis on the (001) surfaces of lanthanum transition metal perovskites $LaBO_3$ (B = Cr, Mn, Fe, Co and Ni). *Phys. Chem. Chem. Phys.* **2015,** *17* (33), 21643-63.
100. Xie, W.; Lee, Y. L.; Shao-Horn, Y.; Morgan, D., Oxygen Point Defect Chemistry in Ruddlesden-Popper Oxides $(La_{1-x}Sr_x)_2MO_{4\pm\sigma}$ (M = Co, Ni, Cu). *J. Phys. Chem. Lett.* **2016,** *7* (10), 1939-44.
101. Mayeshiba, T.; Morgan, D., Strain effects on oxygen migration in perovskites. *Phys. Chem. Chem. Phys.* **2015,** *17* (4), 2715-21.
102. Kubicek, M.; Cai, Z.; Ma, W.; Yildiz, B.; Hutter, H.; Fleig, J., Tensile lattice strain accelerates oxygen surface exchange and diffusion in $La_{1-x}Sr_xCoO_{3-\sigma}$ thin films. *ACS Nano* **2013,** *7* (4), 3276-86.
103. Stemmer, S.; Jacobson, A. J.; Chen, X.; Ignatiev, A., Oxygen vacancy ordering in epitaxial $La_{0.5}Sr_{0.5}CoO_{3-\partial}$ thin films on (001) $LaAlO_3$. *J. Appl. Phys.* **2001,** *90* (7), 3319-3324.
104. Strasser, P.; Koh, S.; Anniyev, T.; Greeley, J.; More, K.; Yu, C.; Liu, Z.; Kaya, S.; Nordlund, D.; Ogasawara, H.; Toney, M. F.; Nilsson, A., Lattice-strain control of the activity in dealloyed core-shell fuel cell catalysts. *Nat. Chem.* **2010,** *2* (6), 454-60.
105. Liu, Q.; Chen, Z.; Yan, Z.; Wang, Y.; Wang, E.; Wang, S.; Wang, S.; Sun, G., Crystal-Plane-

Dependent Activity of Spinel Co_3O_4 Towards Water Splitting and the Oxygen Reduction Reaction. *ChemElectroChem* **2018,** *5* (7), 1080-1086.

106. Wang, Y.; Hu, T.; Chen, Y.; Yuan, H.; Qiao, Y., Crystal facet-dependent activity of α-Mn_2O_3 for oxygen reduction and oxygen evolution reactions. *Int. J. Hydrogen Energy* **2020**.
107. Su, D.; Dou, S.; Wang, G., Single crystalline Co_3O_4 nanocrystals exposed with different crystal planes for Li-O_2 batteries. *Sci Rep* **2014,** *4*, 5767.
108. Lv, G.; Wu, Y.; Wang, Y.; Kang, W.; Zhang, H.; Zhou, M.; Huang, Z.; Li, J.; Guo, Z.; Wang, Y., Rational design of perfect interface coupling to boost electrocatalytical oxygen reduction. *Nano Energy* **2020,** *76*, 105055.
109. Han, X.; He, G.; He, Y.; Zhang, J.; Zheng, X.; Li, L.; Zhong, C.; Hu, W.; Deng, Y.; Ma, T.-Y., Engineering Catalytic Active Sites on Cobalt Oxide Surface for Enhanced Oxygen Electrocatalysis. *Advanced Energy Materials* **2018,** *8* (10), 1702222.
110. Liu, B.; Sun, Y.; Liu, L.; Xu, S.; Yan, X., Advances in Manganese-Based Oxides Cathodic Electrocatalysts for Li-Air Batteries. *Adv. Funct. Mater.* **2018,** *28* (15), 1704973.
111. Cheng, F.; Su, Y.; Liang, J.; Tao, Z.; Chen, J., MnO2-Based Nanostructures as Catalysts for Electrochemical Oxygen Reduction in Alkaline Media†. *Chem. Mater.* **2010,** *22* (3), 898-905.
112. Meng, Y.; Song, W.; Huang, H.; Ren, Z.; Chen, S. Y.; Suib, S. L., Structure-property relationship of bifunctional MnO2 nanostructures: highly efficient, ultra-stable electrochemical water oxidation and oxygen reduction reaction catalysts identified in alkaline media. *J. Am. Chem. Soc.* **2014,** *136* (32), 11452-64.
113. Kuo, C. H.; Mosa, I. M.; Thanneeru, S.; Sharma, V.; Zhang, L.; Biswas, S.; Aindow, M.; Pamir Alpay, S.; Rusling, J. F.; Suib, S. L.; He, J., Facet-dependent catalytic activity of MnO electrocatalysts for oxygen reduction and oxygen evolution reactions. *Chem Commun* **2015,** *51* (27), 5951-4.
114. Gao, R.; Zhu, J.; Xiao, X.; Hu, Z.; Liu, J.; Liu, X., Facet-Dependent Electrocatalytic Performance of Co3O4for Rechargeable Li-O2Battery. *The Journal of Physical Chemistry C* **2015,** *119* (9), 4516-4523.
115. Wang, Y.-J.; Long, W.; Wang, L.; Yuan, R.; Ignaszak, A.; Fang, B.; Wilkinson, D. P., Unlocking the door to highly active ORR catalysts for PEMFC applications: polyhedron-engineered Pt-based nanocrystals. *Energy & Environmental Science* **2018,** *11* (2), 258-275.

116. Moldovan, M. S.; Bulou, H.; Dappe, Y. J.; Janowska, I.; Bégin, D.; Pham-Huu, C.; Ersen, O., On the Evolution of Pt Nanoparticles on Few-Layer Graphene Supports in the High-Temperature Range. *The Journal of Physical Chemistry C* **2012,** *116* (16), 9274-9282.
117. Settem, M.; Rajak, P.; Islam, M.; Bhattacharyya, S., Influence of supporting amorphous carbon film thickness on measured strain variation within a nanoparticle. *Nanoscale* **2017,** *9* (43), 17054-17062.
118. Yan, Q. Q.; Wu, D. X.; Chu, S. Q.; Chen, Z. Q.; Lin, Y.; Chen, M. X.; Zhang, J.; Wu, X. J.; Liang, H. W., Reversing the charge transfer between platinum and sulfur-doped carbon support for electrocatalytic hydrogen evolution. *Nat. Commun.* **2019,** *10* (1), 4977.
119. Wan, Q.; Xia, J.; Lu, W.; Yang, J.; Che, C. M., Kinetically Controlled Self-Assembly of Phosphorescent Au(III) Aggregates and Ligand-to-Metal-Metal Charge Transfer Excited State: A Combined Spectroscopic and DFT/TDDFT Study. *J. Am. Chem. Soc.* **2019,** *141* (29), 11572-11582.
120. Ro, I.; Resasco, J.; Christopher, P., Approaches for Understanding and Controlling Interfacial Effects in Oxide-Supported Metal Catalysts. *ACS Catalysis* **2018,** *8* (8), 7368-7387.
121. Wu, M. J.; Zhang, G. X.; Qiao, J. L.; Chen, N.; Chen, W. F.; Sun, S. H., Ultra-long life rechargeable zinc-air battery based on high-performance trimetallic nitride and NCNT hybrid bifunctional electrocatalysts. *Nano Energy* **2019,** *61*, 86-95.
122. Wu, M. J.; Wei, Q. L.; Zhang, G. X.; Qiao, J. L.; Wu, M. X.; Zhang, J. H.; Gong, Q. J.; Sun, S. H., Fe/Co Double Hydroxide/Oxide Nanoparticles on N-Doped CNTs as Highly Efficient Electrocatalyst for Rechargeable Liquid and Quasi-Solid-State Zinc-Air Batteries. *Advanced Energy Materials* **2018,** *8* (30), 1801836.
123. Ahmadi, M.; Mistry, H.; Roldan Cuenya, B., Tailoring the Catalytic Properties of Metal Nanoparticles via Support Interactions. *The Journal of Physical Chemistry Letters* **2016,** *7* (17), 3519-3533.
124. Liu, L.; Corma, A., Metal Catalysts for Heterogeneous Catalysis: From Single Atoms to Nanoclusters and Nanoparticles. *Chem. Rev.* **2018,** *118* (10), 4981-5079.
125. Serp, P., Carbon. **2013**, 323-369.
126. Lin, Y.; Feng, Z.; Yu, L.; Gu, Q.; Wu, S.; Su, D. S., Insights into the surface chemistry and electronic properties of sp2 and sp3-hybridized nanocarbon materials for catalysis. *Chem. Commun.* **2017,** *53* (35), 4834-4837.

127. Banhart, F.; Kotakoski, J.; Krasheninnikov, A. V., Structural Defects in Graphene. *ACS Nano* **2010,** *5* (1), 26-41.
128. Zhu, J.; Huang, Y.; Mei, W.; Zhao, C.; Zhang, C.; Zhang, J.; Amiinu, I. S.; Mu, S., Effects of Intrinsic Pentagon Defects on Electrochemical Reactivity of Carbon Nanomaterials. *Angew. Chem. Int. Ed. Engl.* **2019,** *58* (12), 3859-3864.
129. Cheng, W.; Yuan, P.; Lv, Z.; Guo, Y.; Qiao, Y.; Xue, X.; Liu, X.; Bai, W.; Wang, K.; Xu, Q.; Zhang, J., Boosting defective carbon by anchoring well-defined atomically dispersed metal-N4 sites for ORR, OER, and Zn-air batteries. *Applied Catalysis B: Environmental* **2020,** *260*, 118198.
130. Zhang, Z.; Chen, Y.; Zhou, L.; Chen, C.; Han, Z.; Zhang, B.; Wu, Q.; Yang, L.; Du, L.; Bu, Y.; Wang, P.; Wang, X.; Yang, H.; Hu, Z., The simplest construction of single-site catalysts by the synergism of micropore trapping and nitrogen anchoring. *Nat. Commun.* **2019,** *10* (1), 1657.
131. Mohideen, M. M.; Liu, Y.; Ramakrishna, S., Recent progress of carbon dots and carbon nanotubes applied in oxygen reduction reaction of fuel cell for transportation. *Applied Energy* **2020,** *257*, 114027.
132. Ramakrishnan, S.; Balamurugan, J.; Vinothkannan, M.; Kim, A. R.; Sengodan, S.; Yoo, D. J., Nitrogen-doped graphene encapsulated FeCoMoS nanoparticles as advanced trifunctional catalyst for water splitting devices and zinc-air batteries. *Applied Catalysis B: Environmental* **2020,** *279*, 119381.
133. Ramakrishnan, S.; Karuppannan, M.; Vinothkannan, M.; Ramachandran, K.; Kwon, O. J.; Yoo, D. J., Ultrafine Pt Nanoparticles Stabilized by MoS_2/N-Doped Reduced Graphene Oxide as a Durable Electrocatalyst for Alcohol Oxidation and Oxygen Reduction Reactions. *ACS Appl Mater Interfaces* **2019,** *11* (13), 12504-12515.
134. Fu, K.; Wang, Y.; Mao, L.; Yang, X.; Peng, W.; Jin, J.; Yang, S.; Li, G., Rational assembly of hybrid carbon nanotubes grafted on the carbon nanofibers as reliable and robust bifunctional catalyst for rechargeable zinc-air battery. *J. Power Sources* **2019,** *421*, 68-75.
135. Wu, M.; Qiao, J.; Li, K.; Zhou, X.; Liu, Y.; Zhang, J., A large-scale synthesis of heteroatom (N and S) co-doped hierarchically porous carbon (HPC) derived from polyquaternium for superior oxygen reduction reactivity. *Green Chemistry* **2016,** *18* (9), 2699-2709.
136. Liu, J.; Wu, X.; Yang, L.; Wang, F.; Yin, J., Unprotected Pt nanoclusters anchored on ordered

mesoporous carbon as an efficient and stable catalyst for oxygen reduction reaction. *Electrochim. Acta* **2019,** *297*, 539-544.

137. Shrestha, S.; Liu, Y.; Mustain, W. E., Electrocatalytic Activity and Stability of Pt clusters on State-of-the-Art Supports: A Review. *Catalysis Reviews* **2011,** *53* (3), 256-336.
138. Sadeghifar, H.; Djilali, N.; Bahrami, M., Effect of Polytetrafluoroethylene (PTFE) and micro porous layer (MPL) on thermal conductivity of fuel cell gas diffusion layers: Modeling and experiments. *J. Power Sources* **2014,** *248*, 632-641.
139. Park, J.; Oh, H.; Ha, T.; Lee, Y. I.; Min, K., A review of the gas diffusion layer in proton exchange membrane fuel cells: Durability and degradation. *Applied Energy* **2015,** *155*, 866-880.
140. Ma, Z.; Pei, P.; Wang, K.; Wang, X.; Xu, H.; Liu, Y.; peng, G., Degradation characteristics of air cathode in zinc air fuel cells. *J. Power Sources* **2015,** *274*, 56-64.
141. Park, J.-H.; Kim, J.-M.; Kim, J.-S.; Shim, E.-G.; Lee, S.-Y., Polyimide/carbon black composite nanocoating layers as a facile surface modification strategy for high-voltage lithium ion cathode materials. *Journal of Materials Chemistry A* **2013,** *1* (40), 12441.
142. Bockelmann, M.; Kunz, U.; Turek, T., Electrically rechargeable zinc-oxygen flow battery with high power density. *Electrochem. Commun.* **2016,** *69*, 24-27.
143. Li, X.; Pletcher, D.; Russell, A. E.; Walsh, F. C.; Wills, R. G. A.; Gorman, S. F.; Price, S. W. T.; Thompson, S. J., A novel bifunctional oxygen GDE for alkaline secondary batteries. *Electrochem. Commun.* **2013,** *34*, 228-230.
144. Zhang, E.; Wu, M.; Tang, Q.; Gong, Q.; Sun, S.; Qiao, J.; Zhang, L., Using aminopyrine as a nitrogen-enriched small molecule precursor to synthesize high-performing nitrogen doped mesoporous carbon for catalyzing oxygen reduction reaction. *RSC Advances* **2017,** *7* (2), 669-677.
145. Zhou, X.; Bai, Z.; Wu, M.; Qiao, J.; Chen, Z., 3-Dimensional porous N-doped graphene foam as a non-precious catalyst for the oxygen reduction reaction. *Journal of Materials Chemistry A* **2015,** *3* (7), 3343-3350.
146. Liu, Q. C.; Xu, J. J.; Xu, D.; Zhang, X. B., Flexible lithium-oxygen battery based on a recoverable cathode. *Nat. Commun.* **2015,** *6*, 7892.
147. Tan, P.; Chen, B.; Xu, H.; Zhang, H.; Cai, W.; Ni, M.; Liu, M.; Shao, Z., Flexible Zn- and Li-air batteries: recent advances, challenges, and future perspectives. *Energy Environ. Sci.* **2017,**

10 (10), 2056-2080.

148. Pan, J.; Xu, Y. Y.; Yang, H.; Dong, Z.; Liu, H.; Xia, B. Y., Advanced Architectures and Relatives of Air Electrodes in Zn-Air Batteries. *Advanced Science* **2018**, 1700691.
149. Ng, J. W. D.; Tang, M.; Jaramillo, T. F., A carbon-free, precious-metal-free, high-performance O_2 electrode for regenerative fuel cells and metal-air batteries. *Energy & Environmental Science* **2014,** *7* (6), 2017.
150. Zhao, Z.; Wu, H.; He, H.; Xu, X.; Jin, Y., Self-standing non-noble metal (Ni-Fe) oxide nanotube array anode catalysts with synergistic reactivity for high-performance water oxidation. *Journal of Materials Chemistry A* **2015,** *3* (13), 7179-7186.
151. Xia, X.; Zhu, C.; Luo, J.; Zeng, Z.; Guan, C.; Ng, C. F.; Zhang, H.; Fan, H. J., Synthesis of free-standing metal sulfide nanoarrays via anion exchange reaction and their electrochemical energy storage application. *Small* **2014,** *10* (4), 766-73.
152. Ma, T. Y.; Dai, S.; Jaroniec, M.; Qiao, S. Z., Metal-organic framework derived hybrid Co_3O_4-carbon porous nanowire arrays as reversible oxygen evolution electrodes. *J. Am. Chem. Soc.* **2014,** *136* (39), 13925-31.
153. Jiang, P.; Liu, Q.; Liang, Y.; Tian, J.; Asiri, A. M.; Sun, X., A cost-effective 3D hydrogen evolution cathode with high catalytic activity: FeP nanowire array as the active phase. *Angew. Chem. Int. Ed. Engl.* **2014,** *53* (47), 12855-9.
154. Ma, T. Y.; Dai, S.; Qiao, S. Z., Self-supported electrocatalysts for advanced energy conversion processes. *Mater. Today* **2016,** *19* (5), 265-273.
155. Davari, E.; Johnson, A. D.; Mittal, A.; Xiong, M.; Ivey, D. G., Manganese-cobalt mixed oxide film as a bifunctional catalyst for rechargeable zinc-air batteries. *Electrochim. Acta* **2016,** *211*, 735-743.
156. Xiong, M.; Ivey, D. G., Electrodeposited Co-Fe as an oxygen evolution catalyst for rechargeable zinc-air batteries. *Electrochemistry Communications* **2017,** *75*, 73-77.
157. Faber, M. S.; Dziedzic, R.; Lukowski, M. A.; Kaiser, N. S.; Ding, Q.; Jin, S., High-performance electrocatalysis using metallic cobalt pyrite (CoS_2) micro- and nanostructures. *J. Am. Chem. Soc.* **2014,** *136* (28), 10053-61.
158. Chen, S.; Duan, J.; Zheng, Y.; Chen, X.; Du, X. W.; Jaroniec, M.; Qiao, S.-Z., Ionic liquid-assisted synthesis of N/S-double doped graphene microwires for oxygen evolution and Zn-air batteries. *Energy Storage Materials* **2015,** *1*, 17-24.

159. Liu, Q.; Wang, Y.; Dai, L.; Yao, J., Scalable Fabrication of Nanoporous Carbon Fiber Films as Bifunctional Catalytic Electrodes for Flexible Zn-Air Batteries. *Adv. Mater.* **2016,** *28* (15), 3000-6.
160. Zeng, S.; Tong, X.; Zhou, S.; Lv, B.; Qiao, J.; Song, Y.; Chen, M.; Di, J.; Li, Q., All-in-One Bifunctional Oxygen Electrode Films for Flexible Zn-Air Batteries. *Small* **2018,** *14* (48), e1803409.
161. Konno, H., X-ray Photoelectron Spectroscopy. **2016**, 153-171.
162. Wang, Z. L., New Developments in Transmission Electron Microscopy for Nanotechnology. *Adv. Mater.* **2003,** *15* (18), 1497-1514.
163. Vernon-Parry, K. D., Scanning electron microscopy: an introduction. *III-Vs Review* **2000,** *13* (4), 40-44.
164. Bunaciu, A. A.; Udristioiu, E. G.; Aboul-Enein, H. Y., X-ray diffraction: instrumentation and applications. *Crit. Rev. Anal. Chem.* **2015,** *45* (4), 289-99.
165. de Groot, F., High-resolution X-ray emission and X-ray absorption spectroscopy. *Chem. Rev.* **2001,** *101* (6), 1779-808.
166. Zitolo, A.; Ranjbar-Sahraie, N.; Mineva, T.; Li, J.; Jia, Q.; Stamatin, S.; Harrington, G. F.; Lyth, S. M.; Krtil, P.; Mukerjee, S.; Fonda, E.; Jaouen, F., Identification of catalytic sites in cobalt-nitrogen-carbon materials for the oxygen reduction reaction. *Nat. Commun.* **2017,** *8* (1), 957.
167. Li, Y.; Li, Q.; Wang, H.; Zhang, L.; Wilkinson, D. P.; Zhang, J., Recent Progresses in Oxygen Reduction Reaction Electrocatalysts for Electrochemical Energy Applications. *Electrochemical Energy Reviews* **2019,** *2* (4), 518-538.
168. Liu, C.; Dong, F.; Wu, M.; Wang, Y.; Xu, N.; Wang, X.; Qiao, J.; Shi, P.; Huang, H., Dual-active-sites design of CoSx anchored on nitrogen-doped carbon with tunable mesopore enables efficient Bi-Functional oxygen catalysis for ultra-stable zinc-air batteries. *J. Power Sources* **2019,** *438*, 226953.
169. Lin, Y.; Yang, L.; Zhang, Y.; Jiang, H.; Xiao, Z.; Wu, C.; Zhang, G.; Jiang, J.; Song, L., Defective Carbon-CoP Nanoparticles Hybrids with Interfacial Charges Polarization for Efficient Bifunctional Oxygen Electrocatalysis. *Advanced Energy Materials* **2018,** *8* (18), 1703623.
170. Wu, M.; Zhang, G.; Chen, N.; Chen, W.; Qiao, J.; Sun, S., A self-supported electrode as a

high-performance binder- and carbon-free cathode for rechargeable hybrid zinc batteries. *Energy Storage Materials* **2020,** *24*, 272-280.

171. Wang, Y.-J.; Fang, B.; Zhang, D.; Li, A.; Wilkinson, D. P.; Ignaszak, A.; Zhang, L.; Zhang, J., A Review of Carbon-Composited Materials as Air-Electrode Bifunctional Electrocatalysts for Metal-Air Batteries. *Electrochemical Energy Reviews* **2018,** *1* (1), 1-34.
172. Zhang, X.; Luo, J.; Lin, H.-F.; Tang, P.; Morante, J. R.; Arbiol, J.; Wan, K.; Mao, B.-W.; Liu, L.-M.; Fransaer, J., Tailor-made metal-nitrogen-carbon bifunctional electrocatalysts for rechargeable Zn-air batteries via controllable MOF units. *Energy Storage Materials* **2019,** *17*, 46-61.
173. Li, Y.; Liu, Y.; Qian, Q.; Wang, G.; Zhang, G., Supramolecular assisted one-pot synthesis of donut-shaped CoP@PNC hybrid nanostructures as multifunctional electrocatalysts for rechargeable Zn-air batteries and self-powered hydrogen production. *Energy Storage Materials* **2020,** *28*, 27-36.
174. Su, C.-Y.; Cheng, H.; Li, W.; Liu, Z.-Q.; Li, N.; Hou, Z.; Bai, F.-Q.; Zhang, H.-X.; Ma, T.-Y., Atomic Modulation of FeCo-Nitrogen-Carbon Bifunctional Oxygen Electrodes for Rechargeable and Flexible All-Solid-State Zinc-Air Battery. *Advanced Energy Materials* **2017,** *7* (13), 1602420.
175. Dong, F.; Liu, C.; Wu, M.; Guo, J.; Li, K.; Qiao, J., Hierarchical Porous Carbon Derived from Coal Tar Pitch Containing Discrete Co-Nx-C Active Sites for Efficient Oxygen Electrocatalysis and Rechargeable Zn-Air Batteries. *ACS Sustainable Chemistry & Engineering* **2019,** *7* (9), 8587-8596.
176. Wu, M. J.; Zhang, E. G.; Guo, Q. P.; Wang, Y. Z.; Qiao, J. L.; Li, K. X.; Pei, P. C., N/S-Me (Fe, Co, Ni) doped hierarchical porous carbons for fuel cell oxygen reduction reaction with high catalytic activity and long-term stability. *Applied Energy* **2016,** *175*, 468-478.
177. Zhu, C.; Li, H.; Fu, S.; Du, D.; Lin, Y., Highly efficient nonprecious metal catalysts towards oxygen reduction reaction based on three-dimensional porous carbon nanostructures. *Chem. Soc. Rev.* **2016,** *45* (3), 517-31.
178. Cai, W.; Zhang, Y.; Jia, Y.; Yan, J., Flexible heteroatom-doped porous carbon nanofiber cages for electrode scaffolds. *Carbon Energy* **2020**.
179. Alegre, C.; Modica, E.; Lo Vecchio, C.; Sebastián, D.; Lázaro, M. J.; Aricò, A. S.; Baglio, V., Carbon Nanofibers as Advanced Pd Catalyst Supports for the Air Electrode of Alkaline

Metal-Air Batteries. *ChemPlusChem* **2015,** *80* (9), 1384-1388.

180. Fabbri, E.; Nachtegaal, M.; Cheng, X.; Schmidt, T. J., Superior Bifunctional Electrocatalytic Activity of $Ba_{0.5}Sr_{0.5}Co_{0.8}Fe_{0.2}O_{3-\delta}$/Carbon Composite Electrodes: Insight into the Local Electronic Structure. *Advanced Energy Materials* **2015,** *5* (17), 1402033.
181. Barman, B. K.; Nanda, K. K., Prussian blue as a single precursor for synthesis of Fe/Fe_3C encapsulated N-doped graphitic nanostructures as bi-functional catalysts. *Green Chemistry* **2016,** *18* (2), 427-432.
182. Chang, J.; Liang, L.; Li, C.; Wang, M.; Ge, J.; Liu, C.; Xing, W., Ultrathin cobalt phosphide nanosheets as efficient bifunctional catalysts for a water electrolysis cell and the origin for cell performance degradation. *Green Chemistry* **2016,** *18* (8), 2287-2295.
183. He, G.; Han, X.; Moss, B.; Weng, Z.; Gadipelli, S.; Lai, F.; Kafizas, A. G.; Brett, D. J. L.; Guo, Z. X.; Wang, H.; Parkin, I. P., Solid solution nitride/carbon nanotube hybrids enhance electrocatalysis of oxygen in zinc-air batteries. *Energy Storage Materials* **2018,** *15*, 380-387.
184. Pandey, J.; Hua, B.; Ng, W.; Yang, Y.; van der Veen, K.; Chen, J.; Geels, N. J.; Luo, J.-L.; Rothenberg, G.; Yan, N., Developing hierarchically porous MnO_x/NC hybrid nanorods for oxygen reduction and evolution catalysis. *Green Chemistry* **2017,** *19* (12), 2793-2797.
185. Xue, Z.-H.; Su, H.; Yu, Q.-Y.; Zhang, B.; Wang, H.-H.; Li, X.-H.; Chen, J.-S., Janus Co/CoP Nanoparticles as Efficient Mott-Schottky Electrocatalysts for Overall Water Splitting in Wide pH Range. *Advanced Energy Materials* **2017,** *7* (12), 1602355.
186. Yang, L.; Zeng, X.; Wang, D.; Cao, D., Biomass-derived FeNi alloy and nitrogen-codoped porous carbons as highly efficient oxygen reduction and evolution bifunctional electrocatalysts for rechargeable Zn-air battery. *Energy Storage Materials* **2018,** *12*, 277-283.
187. Liang, Y.; Li, Y.; Wang, H.; Zhou, J.; Wang, J.; Regier, T.; Dai, H., Co_3O_4 nanocrystals on graphene as a synergistic catalyst for oxygen reduction reaction. *Nat. Mater.* **2011,** *10* (10), 780-6.
188. Zhang, X.; Lu, P.; Cui, X.; Chen, L.; Zhang, C.; Li, M.; Xu, Y.; Shi, J., Probing the electro-catalytic ORR activity of cobalt-incorporated nitrogen-doped CNTs. *J. Catal.* **2016,** *344*, 455-464.
189. Khani, H.; Grundish, N. S.; Wipf, D. O.; Goodenough, J. B., Graphitic-Shell Encapsulation of Metal Electrocatalysts for Oxygen Evolution, Oxygen Reduction, and Hydrogen Evolution in Alkaline Solution. *Advanced Energy Materials* **2019**, 1903215.

190. Liu, W.; Zhang, J.; Bai, Z.; Jiang, G.; Li, M.; Feng, K.; Yang, L.; Ding, Y.; Yu, T.; Chen, Z.; Yu, A., Controllable Urchin-Like $NiCo_2S_4$ Microsphere Synergized with Sulfur-Doped Graphene as Bifunctional Catalyst for Superior Rechargeable Zn-Air Battery. *Adv. Funct. Mater.* **2018**, 1706675.
191. Lin, F.; Liu, Y.; Yu, X.; Cheng, L.; Singer, A.; Shpyrko, O. G.; Xin, H. L.; Tamura, N.; Tian, C.; Weng, T. C.; Yang, X. Q.; Meng, Y. S.; Nordlund, D.; Yang, W.; Doeff, M. M., Synchrotron X-ray Analytical Techniques for Studying Materials Electrochemistry in Rechargeable Batteries. *Chem. Rev.* **2017,** *117* (21), 13123-13186.
192. Zhang, Y.; Ouyang, B.; Xu, J.; Jia, G.; Chen, S.; Rawat, R. S.; Fan, H. J., Rapid Synthesis of Cobalt Nitride Nanowires: Highly Efficient and Low-Cost Catalysts for Oxygen Evolution. *Angew. Chem. Int. Ed. Engl.* **2016,** *55* (30), 8670-4.
193. Meng, N.; Ren, J.; Liu, Y.; Huang, Y.; Petit, T.; Zhang, B., Engineering oxygen-containing and amino groups into two-dimensional atomically-thin porous polymeric carbon nitrogen for enhanced photocatalytic hydrogen production. *Energy & Environmental Science* **2018,** *11* (3), 566-571.
194. Chen, C.; Cheng, D.; Liu, S.; Wang, Z.; Hu, M.; Zhou, K., Engineering the multiscale structure of bifunctional oxygen electrocatalyst for highly efficient and ultrastable zinc-air battery. *Energy Storage Materials* **2019**.
195. Li, M.; Wang, Y.; Zheng, Y.; Fu, G.; Sun, D.; Li, Y.; Tang, Y.; Ma, T., Gadolinium-Induced Valence Structure Engineering for Enhanced Oxygen Electrocatalysis. *Advanced Energy Materials* **2020**, 1903833.
196. Wang, X.; Sunarso, J.; Lu, Q.; Zhou, Z.; Dai, J.; Guan, D.; Zhou, W.; Shao, Z., High-Performance Platinum-Perovskite Composite Bifunctional Oxygen Electrocatalyst for Rechargeable Zn-Air Battery. *Advanced Energy Materials* **2019,** *10* (5), 1903271.
197. Yang, L.; Wang, D.; Lv, Y.; Cao, D., Nitrogen-doped graphitic carbons with encapsulated CoNi bimetallic nanoparticles as bifunctional electrocatalysts for rechargeable Zn-Air batteries. *Carbon* **2019,** *144*, 8-14.
198. Wu, M.; Wei, Q.; Zhang, G.; Qiao, J.; Wu, M.; Zhang, J.; Gong, Q.; Sun, S., Fe/Co Double Hydroxide/Oxide Nanoparticles on N-Doped CNTs as Highly Efficient Electrocatalyst for Rechargeable Liquid and Quasi-Solid-State Zinc-Air Batteries. *Advanced Energy Materials* **2018**, 1801836.

199. Sun, W.; Wang, F.; Zhang, B.; Zhang, M.; Kupers, V.; Ji, X.; Theile, C.; Bieker, P.; Xu, K.; Wang, C.; Winter, M., A rechargeable zinc-air battery based on zinc peroxide chemistry. *Science* **2021,** *371* (6524), 46-51.
200. Li, Y.; Dai, H., Recent advances in zinc-air batteries. *Chem. Soc. Rev.* **2014,** *43* (15), 5257-75.
201. Wang, Z. L.; Xu, D.; Zhong, H. X.; Wang, J.; Meng, F. L.; Zhang, X. B., Gelatin-derived sustainable carbon-based functional materials for energy conversion and storage with controllability of structure and component. *Sci Adv* **2015,** *1* (1), e1400035.
202. Zhou, T.; Zhang, N.; Wu, C.; Xie, Y., Surface/interface nanoengineering for rechargeable Zn-air batteries. *Energy & Environmental Science* **2020,** *13* (4), 1132-1153.
203. Caban-Acevedo, M.; Stone, M. L.; Schmidt, J. R.; Thomas, J. G.; Ding, Q.; Chang, H. C.; Tsai, M. L.; He, J. H.; Jin, S., Efficient hydrogen evolution catalysis using ternary pyrite-type cobalt phosphosulphide. *Nat. Mater.* **2015,** *14* (12), 1245-51.
204. Pourfarzad, H.; Shabani-Nooshabadi, M.; Ganjali, M. R.; Kashani, H., Synthesis of Ni-Co-Fe layered double hydroxide and Fe2O3/Graphene nanocomposites as actively materials for high electrochemical performance supercapacitors. *Electrochim. Acta* **2019,** *317*, 83-92.
205. Zheng, M.; Tang, H.; Li, L.; Hu, Q.; Zhang, L.; Xue, H.; Pang, H., Hierarchically Nanostructured Transition Metal Oxides for Lithium-Ion Batteries. *Adv Sci* **2018,** *5* (3), 1700592.
206. He, J.; Wu, T.; Chen, S.-Y.; Miao, R.; Dang, Y.; Zhong, W.; Wang, M.; Jiang, T.; Suib, S. L., Structure-property relationship of graphene coupled metal (Ni, Co, Fe) (oxy)hydroxides for efficient electrochemical evolution of oxygen. *J. Catal.* **2019,** *377*, 619-628.
207. Duan, Y.; Yu, Z. Y.; Hu, S. J.; Zheng, X. S.; Zhang, C. T.; Ding, H. H.; Hu, B. C.; Fu, Q. Q.; Yu, Z. L.; Zheng, X.; Zhu, J. F.; Gao, M. R.; Yu, S. H., Scaled-Up Synthesis of Amorphous NiFeMo Oxides and Their Rapid Surface Reconstruction for Superior Oxygen Evolution Catalysis. *Angew. Chem.* **2019,** *131* (44), 15919-15924.
208. Wang, X. T.; Ouyang, T.; Wang, L.; Zhong, J. H.; Ma, T.; Liu, Z. Q., Redox-Inert Fe3+Ions in Octahedral Sites of Co-Fe Spinel Oxides with Enhanced Oxygen Catalytic Activity for Rechargeable Zinc-Air Batteries. *Angew. Chem.* **2019,** *131* (38), 13425-13430.
209. Jiang, H.; Liu, Y.; Li, W.; Li, J., Co Nanoparticles Confined in 3D Nitrogen-Doped Porous Carbon Foams as Bifunctional Electrocatalysts for Long-Life Rechargeable Zn-Air Batteries.

Small **2018,** *14* (13), e1703739.

210. Niu, W.; Li, Z.; Marcus, K.; Zhou, L.; Li, Y.; Ye, R.; Liang, K.; Yang, Y., Surface-Modified Porous Carbon Nitride Composites as Highly Efficient Electrocatalyst for Zn-Air Batteries. *Advanced Energy Materials* **2018,** *8* (1), 1701642.
211. Lei, H.; Wang, Z.; Yang, F.; Huang, X.; Liu, J.; Liang, Y.; Xie, J.; Javed, M. S.; Lu, X.; Tan, S.; Mai, W., NiFe nanoparticles embedded N-doped carbon nanotubes as high-efficient electrocatalysts for wearable solid-state Zn-air batteries. *Nano Energy* **2020,** *68*, 104293.
212. Long, X.; Li, J.; Xiao, S.; Yan, K.; Wang, Z.; Chen, H.; Yang, S., A Strongly Coupled Graphene and FeNi Double Hydroxide Hybrid as an Excellent Electrocatalyst for the Oxygen Evolution Reaction. *Angew. Chem.* **2014,** *126* (29), 7714-7718.
213. Chen, D.; Zhu, J.; Mu, X.; Cheng, R.; Li, W.; Liu, S.; Pu, Z.; Lin, C.; Mu, S., Nitrogen-Doped carbon coupled $FeNi_3$ intermetallic compound as advanced bifunctional electrocatalyst for OER, ORR and zn-air batteries. *Applied Catalysis B: Environmental* **2020,** *268*, 118729.
214. Feng, Z.; Hong, W. T.; Fong, D. D.; Lee, Y. L.; Yacoby, Y.; Morgan, D.; Shao-Horn, Y., Catalytic Activity and Stability of Oxides: The Role of Near-Surface Atomic Structures and Compositions. *Acc. Chem. Res.* **2016,** *49* (5), 966-73.
215. Lu, X. F.; Gu, L. F.; Wang, J. W.; Wu, J. X.; Liao, P. Q.; Li, G. R., Bimetal-Organic Framework Derived $CoFe_2O_4$/C Porous Hybrid Nanorod Arrays as High-Performance Electrocatalysts for Oxygen Evolution Reaction. *Adv. Mater.* **2017,** *29* (3).
216. Dong, C.; Liu, Z. W.; Liu, J. Y.; Wang, W. C.; Cui, L.; Luo, R. C.; Guo, H. L.; Zheng, X. L.; Qiao, S. Z.; Du, X. W.; Yang, J., Modest Oxygen-Defective Amorphous Manganese-Based Nanoparticle Mullite with Superior Overall Electrocatalytic Performance for Oxygen Reduction Reaction. *Small* **2017,** *13* (16).
217. Zou, H.; Li, G.; Duan, L.; Kou, Z.; Wang, J., In situ coupled amorphous cobalt nitride with nitrogen-doped graphene aerogel as a trifunctional electrocatalyst towards Zn-air battery deriven full water splitting. *Applied Catalysis B: Environmental* **2019,** *259*, 118100.
218. Hao, Y.; Xu, Y.; Liu, W.; Sun, X., Co/CoP embedded in a hairy nitrogen-doped carbon polyhedron as an advanced tri-functional electrocatalyst. *Materials Horizons* **2018,** *5* (1), 108-115.
219. Liang, J.; Jiao, Y.; Jaroniec, M.; Qiao, S. Z., Sulfur and nitrogen dual-doped mesoporous

graphene electrocatalyst for oxygen reduction with synergistically enhanced performance. *Angew. Chem. Int. Ed. Engl.* **2012,** *51* (46), 11496-500.

220. Yang, J.; Liu, H.; Martens, W. N.; Frost, R. L., Synthesis and Characterization of Cobalt Hydroxide, Cobalt Oxyhydroxide, and Cobalt Oxide Nanodiscs. *The Journal of Physical Chemistry C* **2009,** *114* (1), 111-119.
221. Fu, Y.; Yu, H.-Y.; Jiang, C.; Zhang, T.-H.; Zhan, R.; Li, X.; Li, J.-F.; Tian, J.-H.; Yang, R., NiCo Alloy Nanoparticles Decorated on N-Doped Carbon Nanofibers as Highly Active and Durable Oxygen Electrocatalyst. *Adv. Funct. Mater.* **2018,** *28* (9), 1705094.
222. Zhang, Y. L.; Goh, K.; Zhao, L.; Sui, X. L.; Gong, X. F.; Cai, J. J.; Zhou, Q. Y.; Zhang, H. D.; Li, L.; Kong, F. R.; Gu, D. M.; Wang, Z. B., Advanced non-noble materials in bifunctional catalysts for ORR and OER toward aqueous metal-air batteries. *Nanoscale* **2020,** *12* (42), 21534-21559.
223. Park, J.; Park, M.; Nam, G.; Lee, J. S.; Cho, J., All-solid-state cable-type flexible zinc-air battery. *Adv. Mater.* **2015,** *27* (8), 1396-401.
224. Guan, C.; Sumboja, A.; Zang, W.; Qian, Y.; Zhang, H.; Liu, X.; Liu, Z.; Zhao, D.; Pennycook, S. J.; Wang, J., Decorating Co/CoN_x nanoparticles in nitrogen-doped carbon nanoarrays for flexible and rechargeable zinc-air batteries. *Energy Storage Materials* **2019,** *16*, 243-250.
225. Zhou, T.; Xu, W.; Zhang, N.; Du, Z.; Zhong, C.; Yan, W.; Ju, H.; Chu, W.; Jiang, H.; Wu, C.; Xie, Y., Ultrathin Cobalt Oxide Layers as Electrocatalysts for High-Performance Flexible Zn-Air Batteries. *Adv. Mater.* **2019,** *31* (15), e1807468.
226. Ren, J.; Hu, Z.; Chen, C.; Liu, Y.; Yuan, Z., Integrated Ni2P nanosheet arrays on three-dimensional Ni foam for highly efficient water reduction and oxidation. *Journal of Energy Chemistry* **2017,** *26* (6), 1196-1202.
227. Wang, B.; Tang, C.; Wang, H. F.; Li, B. Q.; Cui, X.; Zhang, Q., Anion-Regulated Hydroxysulfide Monoliths as OER/ORR/HER Electrocatalysts and their Applications in Self-Powered Electrochemical Water Splitting. *Small Methods* **2018,** *2* (12), 1800055.
228. Guo, X.; Zheng, T.; Ji, G.; Hu, N.; Xu, C.; Zhang, Y., Core/shell design of efficient electrocatalysts based on $NiCo_2O_4$ nanowires and NiMn LDH nanosheets for rechargeable zinc-air batteries. *Journal of Materials Chemistry A* **2018,** *6* (22), 10243-10252.
229. Zhang, H. L.; Hirschmann, M. M.; Cottrell, E.; Newville, M.; Lanzirotti, A., Structural

environment of iron and accurate determination of $Fe^{3+}/\Sigma Fe$ ratios in andesitic glasses by XANES and Mössbauer spectroscopy. *Chemical Geology* **2016,** *428*, 48-58.

230. Lin, X.; Shang, Y.; Li, L.; Yu, A., Sea-Urchin-like Cobalt Oxide Grown on Nickel Foam as a Carbon-Free Electrode for Lithium-Oxygen Batteries. *ACS Sustainable Chemistry & Engineering* **2015,** *3* (5), 903-908.
231. Zhong, X.; Jiang, Y.; Chen, X.; Wang, L.; Zhuang, G.; Li, X.; Wang, J.-g., Integrating cobalt phosphide and cobalt nitride-embedded nitrogen-rich nanocarbons: high-performance bifunctional electrocatalysts for oxygen reduction and evolution. *Journal of Materials Chemistry A* **2016,** *4* (27), 10575-10584.
232. Wang, Z.-L.; Xu, D.; Xu, J.-J.; Zhang, L.-L.; Zhang, X.-B., Graphene Oxide Gel-Derived, Free-Standing, Hierarchically Porous Carbon for High-Capacity and High-Rate Rechargeable Li-O_2 Batteries. *Adv. Funct. Mater.* **2012,** *22* (17), 3699-3705.
233. Wang, Y.; Zhou, T.; Jiang, K.; Da, P.; Peng, Z.; Tang, J.; Kong, B.; Cai, W.-B.; Yang, Z.; Zheng, G., Reduced Mesoporous Co_3O_4 Nanowires as Efficient Water Oxidation Electrocatalysts and Supercapacitor Electrodes. *Advanced Energy Materials* **2014,** *4* (16), 1400696.
234. Wu, M.; Zhang, G.; Wu, M.; Prakash, J.; Sun, S., Rational design of multifunctional air electrodes for rechargeable Zn-Air batteries: Recent progress and future perspectives. *Energy Storage Materials* **2019**.
235. Chen, J.; Zheng, F.; Zhang, S.-J.; Fisher, A.; Zhou, Y.; Wang, Z.; Li, Y.; Xu, B.-B.; Li, J.-T.; Sun, S.-G., Interfacial Interaction between FeOOH and Ni-Fe LDH to Modulate the Local Electronic Structure for Enhanced OER Electrocatalysis. *ACS Catalysis* **2018,** *8* (12), 11342-11351.
236. Wang, H. Y.; Hung, S. F.; Chen, H. Y.; Chan, T. S.; Chen, H. M.; Liu, B., In Operando Identification of Geometrical-Site-Dependent Water Oxidation Activity of Spinel Co_3O_4. *Journal of the American Chemical Society* **2016,** *138* (1), 36-9.
237. Rosen, J.; Hutchings, G. S.; Jiao, F., Synthesis, structure, and photocatalytic properties of ordered mesoporous metal-doped Co_3O_4. *J. Catal.* **2014,** *310*, 2-9.
238. Liu, X.; Liu, W.; Ko, M.; Park, M.; Kim, M. G.; Oh, P.; Chae, S.; Park, S.; Casimir, A.; Wu, G.; Cho, J., Metal (Ni, Co)-Metal Oxides/Graphene Nanocomposites as Multifunctional Electrocatalysts. *Advanced Functional Materials* **2015,** *25* (36), 5799-5808.

239. Friebel, D.; Louie, M. W.; Bajdich, M.; Sanwald, K. E.; Cai, Y.; Wise, A. M.; Cheng, M. J.; Sokaras, D.; Weng, T. C.; Alonso-Mori, R.; Davis, R. C.; Bargar, J. R.; Norskov, J. K.; Nilsson, A.; Bell, A. T., Identification of highly active Fe sites in (Ni,Fe)OOH for electrocatalytic water splitting. *J. Am. Chem. Soc.* **2015,** *137* (3), 1305-13.

240. Wu, M.; Shi, J.; Wang, Q.; Qiao, J.; Liu, Y., Nitrogen-Doped Hierarchical Mesoporous/Macroporous Carbon (H-C) Prepared from the Combined Silica Templates with Different Size for Oxygen Reduction. *ECS Transactions* **2015,** *66* (3), 79-86.

241. Xu, K.; Chen, P.; Li, X.; Tong, Y.; Ding, H.; Wu, X.; Chu, W.; Peng, Z.; Wu, C.; Xie, Y., Metallic nickel nitride nanosheets realizing enhanced electrochemical water oxidation. *Journal of the American Chemical Society* **2015,** *137* (12), 4119-25.

242. Li, Y.; Li, H.; Cao, K.; Jin, T.; Wang, X.; Sun, H.; Ning, J.; Wang, Y.; Jiao, L., Electrospun three dimensional Co/CoP@nitrogen-doped carbon nanofibers network for efficient hydrogen evolution. *Energy Storage Materials* **2018,** *12*, 44-53.

243. Ma, L.; Chen, S.; Pei, Z.; Li, H.; Wang, Z.; Liu, Z.; Tang, Z.; Zapien, J. A.; Zhi, C., Flexible Waterproof Rechargeable Hybrid Zinc Batteries Initiated by Multifunctional Oxygen Vacancies-Rich Cobalt Oxide. *ACS nano* **2018**.

244. Huang, Y.; Ip, W. S.; Lau, Y. Y.; Sun, J.; Zeng, J.; Yeung, N. S. S.; Ng, W. S.; Li, H.; Pei, Z.; Xue, Q.; Wang, Y.; Yu, J.; Hu, H.; Zhi, C., Weavable, Conductive Yarn-Based NiCo//Zn Textile Battery with High Energy Density and Rate Capability. *ACS nano* **2017,** *11* (9), 8953-8961.

245. Wang, X.; Wang, F.; Wang, L.; Li, M.; Wang, Y.; Chen, B.; Zhu, Y.; Fu, L.; Zha, L.; Zhang, L.; Wu, Y.; Huang, W., An Aqueous Rechargeable Zn//Co_3O_4 Battery with High Energy Density and Good Cycling Behavior. *Advanced materials* **2016,** *28* (24), 4904-11.

246. Tan, P.; Chen, B.; Xu, H.; Cai, W.; He, W.; Liu, M.; Shao, Z.; Ni, M., Co_3O_4 Nanosheets as Active Material for Hybrid Zn Batteries. *Small* **2018,** *14* (21), e1800225.

247. Li, B.; Quan, J.; Loh, A.; Chai, J.; Chen, Y.; Tan, C.; Ge, X.; Hor, T. S.; Liu, Z.; Zhang, H.; Zong, Y., A Robust Hybrid Zn-Battery with Ultralong Cycle Life. *Nano Lett.* **2017,** *17* (1), 156-163.

248. Deng, J.; Deng, D.; Bao, X., Robust Catalysis on 2D Materials Encapsulating Metals: Concept, Application, and Perspective. *Adv. Mater.* **2017,** *29* (43).

249. Jiang, H.; He, Q.; Zhang, Y.; Song, L., Structural Self-Reconstruction of Catalysts in

Electrocatalysis. *Acc. Chem. Res.* **2018,** *51* (11), 2968-2977.

250. Larcher, D.; Tarascon, J. M., Towards greener and more sustainable batteries for electrical energy storage. *Nat. Chem.* **2015,** *7* (1), 19-29.

251. Ren, J.; Huang, Y.; Zhu, H.; Zhang, B.; Zhu, H.; Shen, S.; Tan, G.; Wu, F.; He, H.; Lan, S.; Xia, X.; Liu, Q., Recent progress on MOF-derived carbon materials for energy storage. *Carbon Energy* **2020**.

252. Feng, X.; Ouyang, M.; Liu, X.; Lu, L.; Xia, Y.; He, X., Thermal runaway mechanism of lithium ion battery for electric vehicles: A review. *Energy Storage Materials* **2018,** *10*, 246-267.

Appendix A: Résumé

Les batteries rechargeables zinc-air (ZAB) sont considérées comme l'un des candidats les plus prometteurs en tant que source d'énergie pour les appareils électroniques portables, les véhicules électriques (VE) et le stockage sur réseau, en raison de leur haute densité d'énergie (1218 Wh kg^{-1}), leur avantage écologique, leur caractéristiques opérationnelles sûres et leur faible coût de production. L'un des plus grands défis dans le développement de ZAB rechargeables haute performance est la conception appropriée d'électrodes à air bifonctionnelles, avec des compositions chimiques contrôlées et des architectures bien conçues qui permettent la catalyse efficacede la réaction clé de réduction de l'oxygène (ORR) et la réaction de dégagement d'oxygène (OER). La fabrication des électrodes à air ayant une activité catalytique bifonctionnelle (ORR et OER) est la partie la plus compliquée mais la plus importante pour la mise au point des ZAB rechargeables puisqu'elles déterminent leur performance électrochimique et la stabilité au niveau du cyclage. Cette thèse décrit des stratégies de synthèse faciles pour la fabrication d'électrodes à oxygène bifonctionnelles pour les ZAB rechargeables.

Dans la première étude, j'ai développé une méthode facile pour fabriquer la structure de nanocristaux binaires en alliage FeNi/nitrure encapsulés dans une coquille graphitique et hybride de carbone dopé en azote (NC) dérivé de la biomasse (Fe_xNi_yN@C/NC). Son architecture poreuse fournit une abondance de sites actifs accessibles et une amélioration du transfert de masse. Bénéficiant des fortes interactions catalyseur-support entre les nanocristaux Fe_xNi_yN revêtus de graphite et le carbone poreux dopé N, le matériau hybride (Fe_xNi_yN@C/NC) peut tirer pleinement avantage des structures uniques formées pour favoriser la cinétique et la stabilité des réactions électrocatalytiques de ORR et OER. Comme prévu, le catalyseur Fe_xNi_yN@C/NC obtenu présente une activité ORR/OER bifonctionnelle élevée, indiquée par la petite différence

de potentiel (ΔE) de 0,67 V entre $E_{j = 10}$ (1,54 V) et $E_{1/2}$ (0,87 V) à 1,0 M KOH. Les tests électrochimiques et les analyses par spectroscopie d'absorption des rayons X (XAS) ont révélé qu'il n'y a pratiquement pas de changement dans la structure en vrac des nanocristaux Fe_xNi_yN après avoir subi le dur processus de corrosion électrochimique de OER. Lorsqu'il est intégré dans une électrode à air pour les batteries rechargeables Zn-air, le catalyseur hybride a démontré une excellente stabilité élevée pendant 400 heures à 5,0 mA/cm^2.

En outre, une approche de couplage bimétallique facile a été utilisée pour synthétiser la couche de revêtement de nanoparticules d'hydroxyde/oxyde double Fe/Co sur des nanotubes de carbone multi-parois dopés N (FeCo-DHO/NCNTs). Grâce à la nucléation directe, la croissance et l'ancrage, les nanoparticules d'hydroxyde/oxyde double Fe/Co (FeCo-DHO) sont uniformément incrustées à la surface des NCNTs, qui fournit une zone de contact électrique élevée et une forte adhérence au support de carbone conducteur. La forte interaction des nanoparticules amorphes de FeCo-DHO avec les NCNTs (due possiblement en raison de la formation d'une liaison chimique M-O-C (M = Co, Fe)) non seulement facilite grandement le transfert de charge et le transport de masse, mais conduit également à une stabilité chimique élevée permettant de résister à la corrosion pendant l'opération de charge et de décharge de la batterie. Par conséquent, le FeCo-DHO/NCNTs tel que synthétisé, présente une activité et une stabilité ORR/OER bifonctionnelle élevée, avec un écart de potentiel de 0,7 V entre $E_{j = 10}$ (OER, potentiel à 10,0 mA cm^{-2}) et $E_{1/2}$ (ORR, potentiel demi- vague). De plus, des performances de charge-décharge exceptionnelles et une longue durée de vie en cyclage, ont été obtenues dans les ZAB à l'état liquide et quasi solide. Les performances électrochimiques élevées d'un tel catalyseur rendent ainsi très prometteur le remplacement des catalyseurs à métaux nobles (métaux du groupe Pt pour ORR et métaux du groupe Ir/Ru pour OER) dans les batteries métal-air.

En outre, une stratégie facile formée de deux étapes a été développée pour synthétiser des nanoparticules diphasiques à base de métal/phosphure métallique encapsulées dans les CNTs dopés en N en forme de bambou (M/M_2P@NCNTs). Parmi eux, l'unique structure de l'hétérojonction du Co/Co_2P induit à la construction de NCNTs hautement ordonnés ayant des sites actifs riches en groupement pyridinique-N et graphitique-N. Cette stratégie simple est une mesure valable pour éviter la destruction des sites actifs nécessaires pour l'ORR dû aux conditions d'oxydation du processus de OER qui nécessite un potentiel élevé. De façon générale, le Co/Co_2P@NCNTs ($E_{1/2}$ = 0,90 V) a présenté des performances ORR exceptionnelles avec un $E_{1/2}$ de 0,87 V par rapport à RHE après avoir subi une condition d'oxydation à potentiel élevé, qui, à notre connaissance, parmi les catalyseurs ORR précédemment rapportés n'a jamais été atteint. Tandis que, l'auto-reconstruction profonde de l'hétérojonction Co/Co_2P confinée dans les NCNTs montre une augmentation des performances de OER en raison de la génération en grand nombre à l'espèce active soit le $CoO_x(OH)_y$, à l'état actif dynamique, ce qui est différent de la transformation structurelle rapportée précédemment qui ne se produit qu'à la région de la surface proche des oxydes de cobalt. Bénéficiant de la résistance élevée observée aux potentiels d'oxydation du NCNTs et de la transformation de l'hétérojonction Co/Co_2P en espèces actives $CoO_x(OH)_y$ contenant du Co^{3+} Oh, les Co/Co_2P@NCNTs peuvent être utilisés comme pré-catalyseur bifonctionnel efficace pour les batteries rechargeables à flux zinc-air. La batterie à flux zinc-air assemblée avec le catalyseur développé démontre une efficacité de cellule élevée avec une durée de vie de 1000 h dans un environnement ambiant, indiquant l'application prometteuse de ces catalyseurs dans les batteries métal-air.

Enfin, une électrode autoportée en tant que cathode haute performance sans liant et sans carbone pour les batteries au zinc hybrides rechargeables est explorée. Dans ce travail, la mousse de Ni dans ce travail agit non seulement comme un substrat, mais sert également de précurseur de

nickel pour la formation du catalyseur $Co_{3-x}Ni_xO_4$. Ainsi, en combinant la structure poreuse 3D de NF et l'activité OER intrinsèque élevée de SS, l'électrode à air poreux assemblée peut tirer pleinement avantage de la structure sandwich pour promouvoir la cinétique de réaction électrocatalytique de $NS@Co_{3-x}Ni_xO_4/Co_3O_4$. Cette nouvelle nanostructure démontre une réaction redox faradique réversible très élevée de CoNi-O ↔ CoNi-O-OH et une activité bifonctionnelle élevée à la fois vers la réaction de réduction de l'oxygène (ORR) et la réaction de dégagement d'oxygène (OER). De plus, la cathode à air, préparée par pressage de l'acier inoxydable $(SS)@Co_3O_4$ prise en sandwich entre deux mousses de $Ni(NF)@Co_{3-x}Ni_xO_4$, possède une structure dense et interconnectée avec une charge élevée de catalyseur actif. Le système de batterie hybride rechargeable assemblé à partir de cette électrode $NS@Co_{3-x}Ni_xO_4/Co_3O_4$ basée à la fois sur des réactions électrochimiques $Zn\text{-}Co_{3-x}Ni_xO_4$ et Zn-air présente une efficacité énergétique et une durabilité beaucoup plus élevée que celles des électrocatalyseurs commerciaux Pt/C et RuO_2. Ce protocole ouvre une nouvelle voie pour la conception rationnelle d'électrode à air autoportée hautement efficace et stable pour les batteries métal-air.

Appendix B: Synopsis

Développement d'électrocatalyseurs d'oxygène bifonctionnels à hautes performances pour les batteries rechargeables Zn-air

L'Introduction

De nos jours, la crise énergétique et les problèmes environnementaux ont propulsé et accéléré l'utilisation des énergies vertes et renouvelables.[250] L'énergie renouvelable (par exemple, l'énergie solaire, l'énergie éolienneet l'hydroélectricité) a été largement étudiée comme une alternative prometteuse pour remplacer les combustibles fossiles traditionnels.[45] Cependant, ces énergies varient considérablement selon les saisons, les climats et les lieux. Cette caractéristique d'instabilité rend les énergies renouvelables difficiles à intégrerle réseau électrique périodique.[8] Par conséquent, des dispositifs de stockage d'énergie efficaces sont nécessaires pour améliorer l'efficacité énergétique et optimiser la répartition des charges du réseau électrique.[251] À ce jour, les batteries Li-ion sont devenues la solution la plus efficace pour la conversion et le stockage d'énergie, et elles sont largement utilisées pour les applications desélectroniques portables et les véhicules électriques (VE).[33] Cependant, leur inconvénients de longue date incluent leur coût élevé, leur densité d'énergie insuffisante, de la rareté du lithium et les problèmes de sécurité ce qui limitent considérablement leurs applications à grande échelle dans l'industrie automobile, en particulier pour les véhicules électriques à autonomie étendue.[252] Par comparaison aux batteries Li-ion, les batteries métal-air (MAB) avec un système semi-ouvert unique ont attirés une grande attention en raison de leur énergie spécifique élevée. En particulier, au cours de la dernière décennie, les batteries zinc-air (ZAB) ont suscité un intérêt croissant de la part des chercheurs, ce qui peut être clairement indiqué par la forte augmentation du nombre d'articles publiés ces

dernières années. Cela souligne que la technologie ZAB pour le stockage d'énergie est en effet un candidat prometteur. Différents du mécanisme d'intercalation des batteries métal-ion, les MAB impliquent le processus de dissolution-dépôt sur l'électrode d'anode métallique et la réaction de réduction de l'oxygène (ORR) et la réaction de dégagement d'oxygène (OER) sur l'électrode de cathode à air. Parmi les MAB secondaires, la batterie lithium-air fait l'objet d'une attention particulière en raison de son énergie spécifique théorique la plus élevée (5928 W h kg^{-1}) et d'une tension de cellule élevée (normalement 2,96 V). Cependant, le lithium n'est pas stable lorsqu'il est exposé à l'air et aux électrolytes aqueux. Les batteries au magnésium et aluminium-air présentent des densités d'énergie plus élevées que les batteries Zn-air. Cependant, ils montrent une rechargeabilité faible en raison de leur grave auto-décharge et de leur faible efficacité de charge coulombique.[2] Heureusement, le Zn et le Fe sont plus stables et peuvent être chargés plus efficacement dans un électrolyte alcalin, et le zinc, ayant une énergie spécifique (1218 Wh kg^{-1}) et une tension de cellule (1,66 V) plus élevée, a reçu beaucoup plus d'attention. En outre, les batteries zinc-air (ZAB) présentent de nombreux autres avantages tels qu’un faible coût, écologique et haute sécurité, et sont donc considérées comme l'un des dispositifs de stockage d'énergie de nouvelle génération les plus prometteurs.[3, 234]

La majorité de la perte d'énergie dans les ZAB est due à la cinétique lente de l'ORR et de l'OER.[15] L'utilisation de catalyseurs hautement actifs et rentables pour réduire l'énergie libre de la ou des étapes de détermination du potentiel joue un rôle central dans la large distribution de ces dispositifs.[16] Afin d'obtenir une densité de puissance et une stabilité élevées pour les ZAB rechargeables, les électrodes à air bifonctionnelles avec une activité ORR et OER catalytique élevée et une durabilité supérieure sont des propriétés essentielles.[17] Cependant, le développement d'une électrode à air bifonctionnelle, avec les propriétés souhaitées qui est capable de résister aux conditions difficiles lors de décharges et de charges répétitives dans des

électrolytes alcalins, est assez difficile. La recherche sur les catalyseurs bifonctionnels s'est principalement concentrée sur des alternatives non précieuses telles que les composés de métaux de transition (par exemple, les oxydes, les sulfures, les nitrures, les carbures et les macrocycles), les matériaux à base de carbone et les composites hybrides.[20-23] Cependant, la plupart des catalyseurs métalliques non précieux sont toujours moins performants que les métaux précieux, bien que les chercheurs aient essayé de développer des modèles cinétiques et des paramètres de structure électronique qui peuvent potentiellement régir la force de liaison de l'adsorbat pour prédire les catalyseurs avec une activité améliorée.[16, 24-26] La méthodologie synthétique efficace et polyvalente pour réguler de manière contrôlable l'activité intrinsèque des catalyseurs est toujours un défi important pour les processus ORR et OER. De plus, les performances des électrodes à air bifonctionnelles doivent être stables dans une large plage de potentiel de travail de ~ 0,6 V (par rapport à l'électrode à hydrogène réversible (RHE), pH = 14) pendant la décharge à ~ 2,0 V pendant la charge.[27-28] En particulier pour les matériaux à base de carbone, les changements de structure et de morphologie dus à la corrosion du carbone dans des conditions hautement oxydantes induisent facilement l'augmentation significative des résistances de transport de charge et de masse, ce qui limite considérablement leur densité de puissance.[29] Les problèmes critiques liés à la corrosion de l'électrode à air pendant la réaction de charge ont ralenti le développement du ZAB et l'ont rendu moins compétitif que les batteries Li-ion vers la fin du 20e siècle. L'utilisation d'électrodes à air sans carbone ou de substrats à base de carbone avec un degré de graphitisation élevé est efficace pour améliorer la stabilité du cyclage de la batterie.[30-32]

Objectifs

Dans ce travail de thèse, différents types d'électrocatalyseurs ou d'électrodes à oxygène

bifonctionnels ont été conçus et étudiés; leurs propriétés de structure et leurs performances électrochimiques pertinentes ont été améliorées, puis contribuent à des ZAB rechargeables haute performance. Les objectifs spécifiques de cette étude sont:

i) développer des matériaux cathodiques haute performance pour les ZAB rechargeables;

ii) révéler la relation entre la nanostructure/composition et les performances électrochimiques;

iii) suivre l'évolution structurelle pendant le fonctionnement électrocatalytique et comprendre l'état actif réel;

iv) offrir une solution innovante et précieuse pour le développement d'électrocatalyseurs à faible coût, très durable et efficace pour les ZAB rechargeables.

Résultats

Dans la première étude, j'ai développé une méthode facile pour fabriquer la structure de nanocristaux binaires en alliage FeNi/nitrure encapsulés dans une coquille graphitique et hybride de carbone dopé N (NC) dérivé de la biomasse (Fe_xNi_yN@C/NC). Cette nouvelle structure présente plusieurs avantages. Premièrement, les couches de carbone graphitique peuvent protéger les noyaux métalliques de la corrosion électrochimique sévère. Deuxièmement, cette architecture morphologique unique permet également de fournir une voie de transfert d'électrons direct, améliorer la stabilité de la structure, ainsi qu'améliorer l'activité catalytique. L'architecture poreuse permet de fournir d'abondants sites actifs accessibles et améliore le transfert de masse. Bénéficiant des fortes interactions catalyseur-support entre les nanocristaux Fe_xNi_yN revêtus de graphite et le carbone poreux dopé N, le matériau hybride (Fe_xNi_yN@C/NC) peut tirer pleinement avantage des structures uniques pour favoriser la cinétique et la stabilité de la réaction

électrocatalytique pour ORR et OER. Comme prévu, le catalyseur Fe_xNi_yN@C/NC obtenu présente une activité ORR / OER bifonctionnelle élevée, indiquée par le faible écart de potentiel (ΔE) de 0,67 V entre $E_{j = 10}$ (1,54 V) et $E_{1/2}$ (0,87 V) à 1,0 M KOH. Les tests électrochimiques et les analyses par spectroscopie d'absorption des rayons X (XAS) ont révélé qu'il n'y a pratiquement pas de changement dans la structure en vrac des nanocristaux Fe_xNi_yN après avoir subi le dur processus de corrosion électrochimique des REL. Lorsqu'il est intégré dans une électrode à air pour les batteries rechargeables Zn-air, le catalyseur hybride a démontré une excellente stabilité élevée pendant 400 heures à 5,0 mA/cm^2.

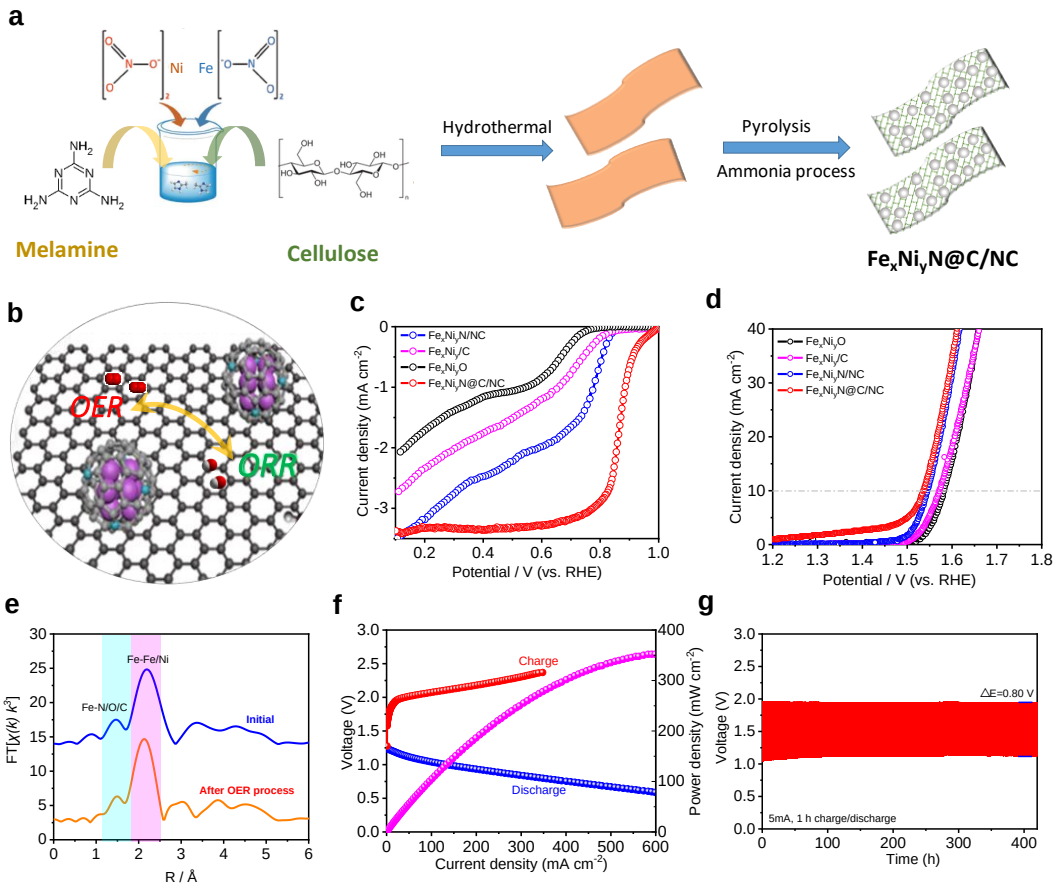

Figure 1 (a) Illustration schématique de la synthèse de Fe_xNi_yN @ C/NC. (b) Illustration de l'électrocatalyseur bifonctionnel de l'alliage binaire FeNi/nitrure encapsulé avec une coque graphitique supportée sur du carbone dopé N (NC). (c) Tracés de polarisation de la réaction de réduction de l'oxygène (ORR) et (d) de la réaction de dégagement d'oxygène (OER) dans du KOH 1,0 M saturé en O_2. (e) Les transformées de Fourier des oscillations à structure fine d'absorption des rayons X étendues de Fe K-edge $k^3\chi$ (k) de Fe_xNi_yN@C/NC avant et après le processus OER. (f)

Courbes de polarisation de décharge et de charge du catalyseur Fe_xNi_yN@C/NC et tracé de densité de puissance correspondant de la batterie Zn-air liquide. (g) Décharge galvanostatique et stabilité du cycle de charge du Fe_xNi_yN@/NC dans la batterie Zn-air liquide.

L'article décrit ci-dessus est le suivant:

Mingjie Wu, Gaixia Zhang, Ning Chen, Weifeng Chen, Jinli Qiao, Shuhui Sun. Encapsulation de coquille graphitique de nanocristaux à base de NiFe décorés sur du carbone poreux dopé N dérivé de la biomasse pour améliorer le dégagement d'oxygène et la catalyse de réduction. Carbon Energy, 3 (2020) 176-187.

En outre, une stratégie facile en deux étapes a été développée pour synthétiser des nanoparticules diphasiques de métal/phosphure métallique encapsulées dans les CNTs dopés N en forme de bambou (M/M_2P@NCNTs). Parmi eux, l'unique structure de l'hétérojonction du Co/Co_2P induit à la construction de NCNTs hautement ordonnés ayant des sites actifs riches en groupement pyridinique-N et graphitique-N. Cette stratégie simple est une mesure valable pour éviter la destruction des sites actifs ORR dû aux conditions d'oxydation du processur de OER qui nécessite un potentiel élevé. De façon générale, le Co/Co_2P@NCNT ($E_{1/2}$ = 0,90 V) a démontré des performances ORR exceptionnelles avec un $E_{1/2}$ de 0,87 V par rapport à RHE après avoir subi une condition d'oxydation à potentiel élevé, qui, à notre connaissance parmi les catalyseurs ORR précédemment rapportés, n'a jamais été atteint. Tandis que, l'auto-reconstruction profonde de l'hétérojonction Co/Co_2P confinée dans les NCNTs montre une augmentation des performances des OER en raison de la génération en grand nombre de l'espèce active soit le $CoO_x(OH)_y$, l'état actif dynamique, ce qui est différent de la transformation structurelle rapportée précédemment qui ne se produit qu'à la région de la surface proche des oxydes de cobalt. Bénéficiant de la résistance élevée observées aux potentiels d'oxydation du NCNTs et de la transformation de l'hétérojonction Co/Co_2P en espèces actives $CoO_x(OH)_y$ contenant du Co^{3+} Oh, les

Co/Co_2P@NCNTs peuvent être utilisés comme pré-catalyseurs bifonctionnels efficaces pour les batteries rechargeables à flux zinc-air. La batterie à flux zinc-air assemblée avec le catalyseur développé, affiche une efficacité de cellule élevée avec une durée de vie sans précédent de 1000 h dans un environnement ambiant, indiquant l'application prometteuse de ces catalyseurs dans les batteries métal-air.

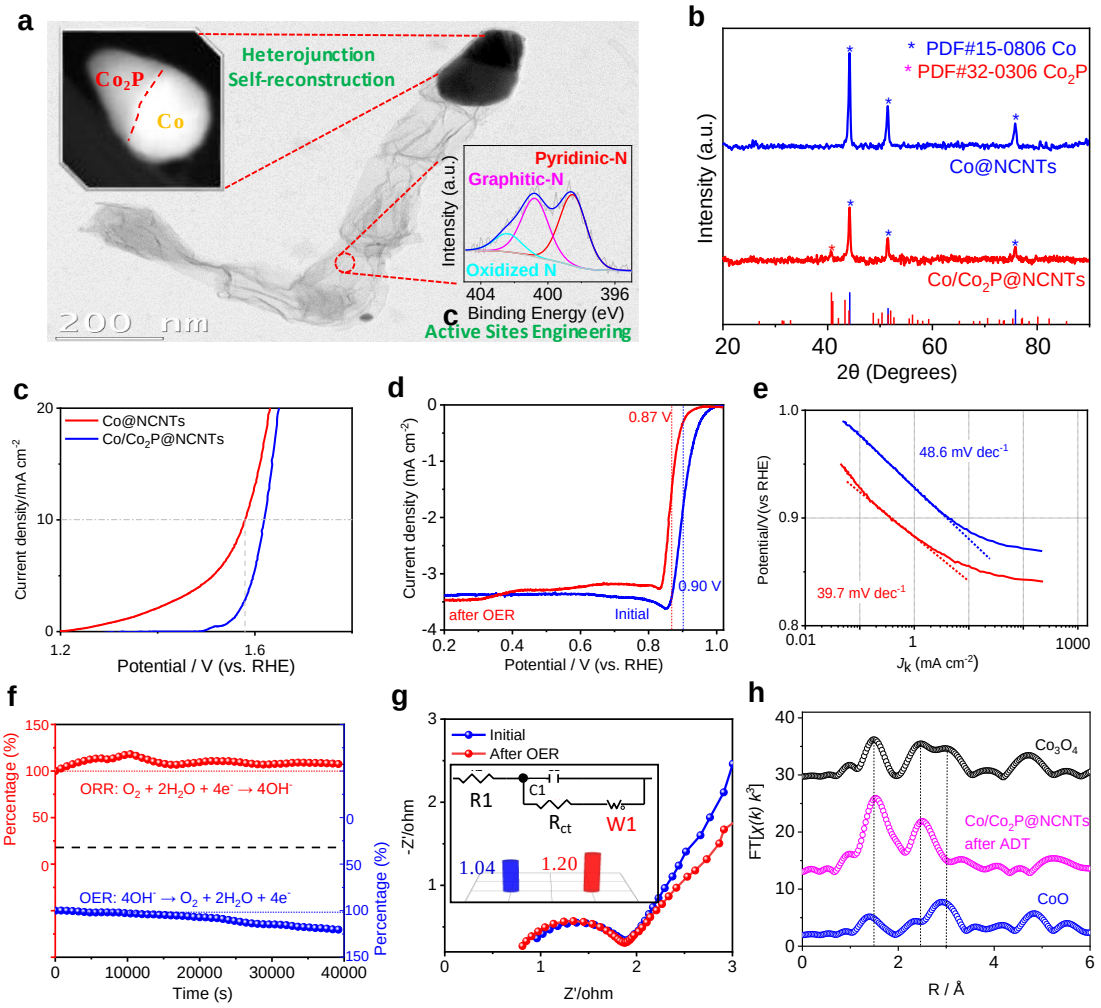

Figure 2 (a) Image TEM et XPS haute résolution des N 1 des Co/Co_2P@NCNTs. (b) Les spectres XRD des Co/Co_2P@NCNTs et Co@NCNTs. (c) Tracés de polarisation OER des Co/Co_2P@NCNT et Co@NCNTs. (d) Tracés de polarisation ORR des Co/Co_2P@NCNTs avant / après le processus OER (dans la plage de potentiel de 0-2 V par rapport à RHE). (e) Tracés Tafel de Co/Co_2P@NCNT avant et après le processus OER. (f) Réponses chronoampérométriques des Co/Co_2P@NCNTs à 0,7 V pour ORR et 1,7 V pour OER. (g) Spectres d'impédance électrochimique (EIS) basés sur un système à trois électrodes avant et après le processus OER. (h) Les transformées

de Fourier de magnitude correspondante des oscillations EXAFS du bord K de Co $k^3\chi$ (k).

L'article décrit ci-dessus est le suivant:

Mingjie Wu, Gaixia Zhang, Ning Chen, Tom Regier, Yongfeng Hu, Diane Rawach, Shuhui Sun, Auto-Reconstruction of Co/Co_2P Heterojonctions Confined in N-Doped Carbon Nanotubes for Zinc-Air Flow Batteries. ACS Energy Letters, 6 (2021) 1153-1161.

En outre, une approche de couplage bimétallique facile a été utilisée pour synthétiser la couche de revêtement de nanoparticules d'hydroxyde/oxyde double Fe/Co sur des nanotubes de carbone multi-parois dopés N (FeCo-DHO/NCNTs). Grâce à la nucléation directe, la croissance et l'ancrage, les nanoparticules d'hydroxyde/oxyde double Fe/Co (FeCo-DHO) sont uniformément incrustées sur la surface des NCNTs, qui fournissent une zone de contact électrique élevée et une forte adhérence sur le support de carbone conducteur. Les fortes interactions des nanoparticules amorphes de FeCo-DHO avec les NCNTs (probablement en raison de la formation d'une liaison chimique M-O-C (M = Co, Fe)) non seulement facilitent grandement le transfert de charge et le transport de masse, mais conduisent également à une stabilité chimique élevée permettant de résister à la corrosion pendant l'opération de charge et de décharge de la batterie. Par conséquent, le FeCo-DHO/NCNTs tel que synthétisé présente une activité et une stabilité ORR/OER bifonctionnelle élevée, avec un écart de potentiel de 0,7 V entre $E_{j = 10}$ (OER, potentiel à 10,0 mA cm^{-2}) et $E_{1/2}$ (ORR, potentiel demi-onde). De plus, des performances de charge-décharge exceptionnelles et une longue durée de vie en cyclage ont été obtenues dans les ZAB à l'état liquide et quasi solide. Les performances électrochimiques élevées d'un tel catalyseur rendent ainsi très prometteur le remplacement des catalyseurs à métaux nobles (métaux du groupe Pt pour ORR et métaux du groupe Ir/Ru pour OER) dans les batteries métal-air.

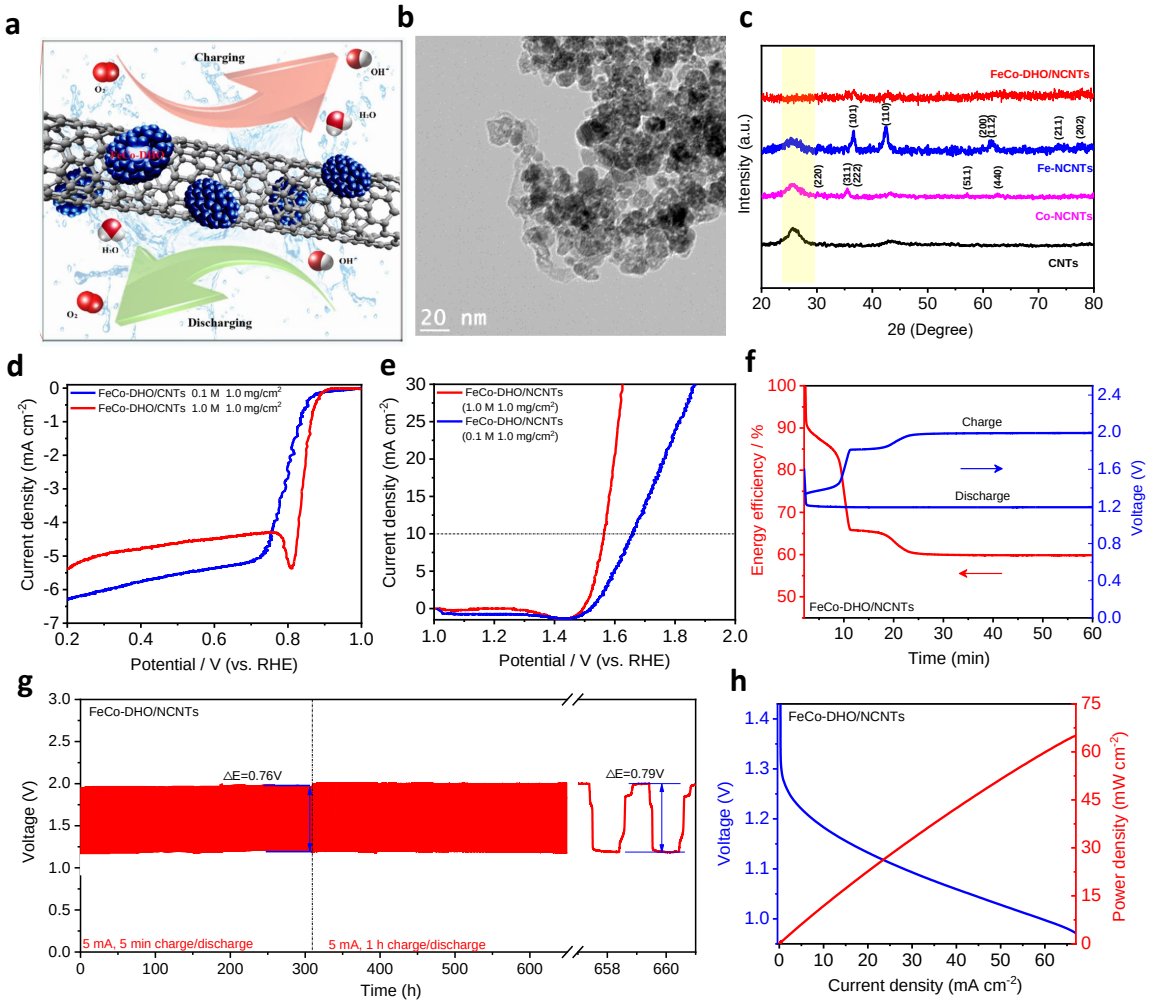

Figure 3 (a) Illustration de l'électrocatalyseur bifonctionnel de la couche de gaine de nanoparticules d'hydroxyde/oxyde double Fe/Co sur nanotubes de carbone multi-parois dopés N (FeCo-DHO/NCNTs). (b) Images HRTEM des FeCo-DHO/NCNTs. (c) Spectres XRD des catalyseurs CNTs, Fe-NCNTs, Co-NCNTs et FeCo-DHO/NCNTs tels que préparés. (d) Courbes de polarisation ORR pour l'électrode FeCo-DHO/NCNTs dans O_2 saturé 0,1 et 1,0 m KOH, respectivement. (e) LSV de l'OER pour l'électrode FeCo-DHO/NCNTs en O_2 saturé 0,1 et 1,0 m KOH. (f) Polarisation de décharge/charge et efficacité énergétique. (g) Décharge galvanostatique et stabilité du cycle de charge des FeCo-DHO/NCNTs. (h) Une courbe de polarisation (V ~ i) et le tracé de densité de puissance correspondant du ZAB quasi-solide en utilisant FeCo-DHO/NCNTs comme catalyseur de cathode.

L'article décrit ci-dessus est le suivant:

Mingjie Wu, Gaixia Zhang, Ning Chen, Weifeng Chen, Jinli Qiao, Shuhui Sun. Nanoparticules double hydroxyde/oxyde de Fe/Co sur les N-Doped CNTs comme

électrocatalyseur hautement efficace pour les batteries rechargeables zinc-air liquides et quasi-solides. Matériaux énergétiques avancés, 8 (2018) 1801836.

Enfin, une électrode flexible et autoportée en structure de sandwich avec des réseaux de nanofils $Co_{3-x}Ni_xO_4/Co_3O_4$ est développée en appuyant simplement deux cathodes à air NF@$Co_{3-x}Ni_xO_4$ et une SS@Co_3O_4 ensemble. La nouvelle structure développée a démontré une excellente activité et stabilité catalytiques ORR / OER, ainsi que les performances de la batterie Zn-air pour les raisons suivantes: (1) À l'échelle atomique, le dopage Ni uniforme change significativement la structure de surface du nanofil poreux $Co_{3-x}Ni_xO_4$ et augmente par conséquent les performances électrochimiques intrinsèques; (2) Les lacunes abondantes en Co^{2+}/Ni^{2+} et en oxygène à la surface améliorent considérablement les performances ORR et OER. Alors, en combinant la flexibilité super mécanique et l'activité intrinsèque élevée OER des solides solubles, l'électrode à air poreux assemblée peut tirer pleinement avantage de la structure sandwich pour promouvoir l'efficacité énergétique de NS@$Co_{3-x}Ni_xO_4/Co_3O_4$; (3) La ZAB rechargeable est assemblée en utilisant NS@$Co_{3-x}Ni_xO_4/Co_3O_4$ à la fois comme une nouvelle classe de cathode et de collecteur de courant pour remplacer les homologues conventionnels rigides et encombrants. Par conséquent, la ZAB avec électrode NS@$Co_{3-x}Ni_xO_4/Co_3O_4$ présente un écart de potentiel de charge-décharge beaucoup plus faible que celui des électrodes NF@$Co_{3-x}Ni_xO_4$ et SS@Co_3O_4, respectivement; (4) De plus, le $Co_{3-x}Ni_xO_4$ multifonctionnel présente de bonnes performances électrochimiques redox, fournissant une batterie à base de Zn avec deux processus électrochimiques: le processus I, le premier plateau à 1,92 V attribué à la batterie Zn-$Co_{3-x}Ni_xO_4$, et le processus II, le deuxième plateau à 1,25 V résultant de ZAB. La partie batterie Zn-air offre un faible écart de potentiel de 0,696 V, un rendement énergétique élevé de 62,2% et une stabilité de 200 h pendant 200 cycles à une densité de courant de 5 mA cm^{-2}. Ce protocole ouvre sans

aucun doute une nouvelle voie pour concevoir stratégiquement des électrodes à air autoportées à haut rendement et stables pour les dispositifs de stockage d'énergie électrochimique.

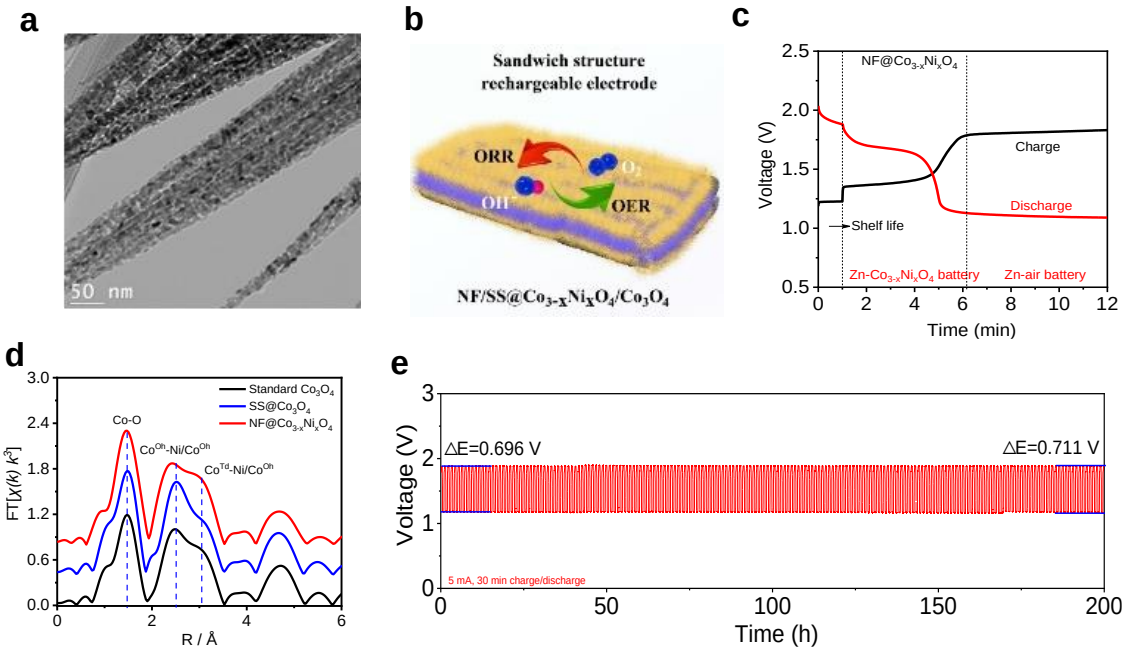

Figure 4 (a) Images TEM en champ clair de NF@$Co_{3-x}Ni_xO_4$. (b) Illustration de l'électrode NS@$Co_{3-x}Ni_xO_4$/Co_3O_4 à structure sandwich pour favoriser la cinétique de la réaction électrocatalytique. (c) Décharge et charge des électrodes NF@$Co_{3-x}Ni_xO_4$ à une densité de courant de 20 mA cm^{-2}. (d) Les spectres de transformées de Fourier (FT) des standards Co_3O_4, SS@Co_3O_4 et NF@$Co_{3-x}Ni_xO_4$. (e) Décharge galvanostatique et stabilité du cycle de charge de l'électrode NS@$Co_{3-x}Ni_xO_4$/Co_3O_4 à une densité de courant de 5 mA cm^{-2} avec un cycle de 1 h.

L'article décrit ci-dessus est le suivant:

Mingjie Wu, Gaixia Zhang, Ning Chen, Weifeng Chen, Jinli Qiao, Shuhui Sun. Une électrode autoportée en tant que cathode haute performance sans liant et sans carbone pour les batteries au zinc hybrides rechargeables. Matériaux de stockage d'énergie, 24 (2020) 272-280.